

UNIVERSITY OF CALGARY

MEASUREMENT AND MODELLING METHODOLOGY FOR HEAVY OIL  
AND BITUMEN VAPOUR PRESSURE

by

ORLANDO CASTELLANOS DÍAZ

A THESIS

SUBMITTED TO THE FACULTY OF GRADUATE STUDIES  
IN PARTIAL FULFILMENT OF THE REQUIREMENTS FOR THE  
DEGREE OF DOCTOR OF PHILOSOPHY IN CHEMICAL ENGINEERING

DEPARTMENT OF CHEMICAL AND PETROLEUM ENGINEERING  
CALGARY, ALBERTA

APRIL, 2012

© Orlando Castellanos Díaz, 2012

UNIVERSITY OF CALGARY  
FACULTY OF GRADUATE STUDIES

The undersigned certify that they have read, and recommend to the Faculty of Graduate Studies for acceptance, a thesis entitled "Measurement and Modelling Methodology for Heavy Oil and Bitumen Vapour Pressure" submitted by Orlando Castellanos Díaz in partial fulfilment of the requirements of the degree of Doctor of Philosophy in Chemical Engineering.

---

*Supervisor, Harvey W. Yarranton  
Department of Chemical and Petroleum Engineering*

---

*Dr. William Y. Svrcek  
Department of Chemical and Petroleum Engineering*

---

*Dr. Michael Foley  
Department of Chemical and Petroleum Engineering*

---

*Internal/External Examiner, Dr. Larry R. Lines  
Department of Geosciences*

---

*External/External Examiner, Dr. Milind Deo  
College of Engineering, University of Utah  
Salt Lake City, Utah*

---

*Date*

## Abstract

Both the refining of heavy oil and solvent-based recovery processes for heavy oil require the prediction of phase behaviour. Petroleum fluids are typically characterized using distillation (or gas chromatography based assays correlated to boiling points); however, the heaviest fraction (residue) of the oil is left undetermined because the components in this fraction have boiling points higher than the cracking temperature. Current commercial methods are capable of distilling about 25 to 30 wt% of heavy oil and bitumen which leaves about 70% of the oil undetermined. To improve this characterization, true boiling point and vapour pressure of residue cuts are required. At present, few data are available in the open literature. Neither a standard procedure nor appropriate equipment is available commercially for direct vapour pressure measurement and deep vacuum distillation of heavy hydrocarbons.

A high vacuum vapour pressure measurement system was designed, constructed, and tested. The system operates at medium to high vacuum conditions (atmospheric to  $10^{-7}$  kPa) and temperatures ranging from 25 to 300 °C. The apparatus was used to measure the vapour pressure of three pure components, seven biodiesel samples, and three bitumen fractions with repeatability and reproducibility of literature data, when available, within 4%. The apparatus was also used to systematically fractionate 58 wt% of a bitumen sample with repeatability within 5%. The amount fractionated more than doubles that obtained by commercial spinning band distillation (25 wt%).

In addition, a methodology was proposed to extrapolate the vapour pressure of heavy oil fractions beyond the accurate-measurable range (below  $10^{-4}$  kPa) using calorimetric data. The vapour pressure was modeled with a correlation, such as the Cox equation, or an equation of state, such as the Advanced Peng Robinson EoS (APR EoS) implemented by Virtual Materials Group Inc. The heat capacity is related to the vapour pressure through the Clausius-Clapeyron relationship and was used to constrain the correlation or equation of state parameters. Both the correlation and equation of state approaches were tested on the biodiesel samples. Both approaches fit the vapour pressures and heat capacities to within 8% and 3%, respectively.

The equation of state approach was used for the heavy oil. The non-distillable maltene fractions were represented with a Gaussian distribution and the asphaltene fraction was represented with a Gamma distribution to account for asphaltene self-association. The vapour pressure and heat capacity were predicted to within 7% and 4%, respectively.

A preliminary protocol was developed for deep vacuum fractionation of heavy oil and bitumen. An experimental procedure was defined and an inter-conversion method to obtain atmospheric equivalent boiling points was formulated. Specifications for additional experimental vapour pressure and heat capacity of fractions obtained with the protocol were laid out to standardize and validate the inter-conversion method. The high vacuum vapour pressure measurement system and associated modeling methodologies

expand the capability to characterize heavy oils for phase behaviour modelling from approximately 30 wt% of the oil to 60 wt% of the oil.

## Acknowledgements

This thesis is a product of the efforts of a lot of people to which I own all my gratitude. They gave me the courage, the support, and the energy to go through this fulfilling enterprise. Of course this couple of pages cannot encompass my appreciation, but I will give it a try.

I would like express my profound gratitude and admiration for my supervisor, Dr. Harvey Yarranton, who provided guidance and support for this project and a lot of patience, I should say. His ideas and our insightful discussions helped developed a very promising apparatus, a very robust method, and a better engineer and person.

I shall never forget and I am eternally grateful for the tremendous vision, support and charisma of Dr. William Svrcek, who started this all and believed in a young foreign recently graduated engineer.

I also would like to acknowledge and say (or write) a humongous thank you to Mr. Florian Schoeggl (technical manager), Dr. Marco Satyro (Virtual Materials Group Inc.), and Dr. Michal Fulem (Institute of Chemical Technology, Prague), because they turned the light on when the night was darkest. They helped consolidate the project, and having them around was a relief.

Let's not forget that this would not have been possible without the framework provided by the University of Calgary and the Department of Chemical and Petroleum Engineering; in particular, I would like to acknowledge the collaboration of Mr. Bernie Then, Mr. Mike Grigg, and Ms. Elaine Baydak for their collaboration on the design and construction of the apparatus. Moreover, the funding support provided by NSERC, Shell Canada, Schlumberger, and Petrobras, through the Asphaltene and Emulsion Research Group and the Heavy Oil Properties and Processing chair, is mostly appreciated.

Usually in these thesis acknowledgments, family and friends come last, which I think is not fair. If I could I would write this section simultaneously, but certain things you need to respect to blend in. I strongly believe that if my parents would not have raised me I would not be writing this, so I own them everything, including this thesis of course. By the same token, I own mother nature a huge hug and an "I'm sorry, I'll try harder". I would like to thank my few friends for making this journey more interesting. And finally, but diametrically oppositely not the last thing that I would like to say, thanks for this world we are living in and many more to come, to my beautiful green.

## Dedication

Alguna vez escribí una frase que describía una situación desconocida, y de alguna forma, como mi camino hasta ahora, tiene más sentido una vez la repaso por trigésima vez: *“Siempre tratando de intentar sin obtener lo que tratas de obtener; no trates de atrapar lo que no tiene forma”*. Probablemente tardaré varias vidas en entenderlo completamente, pero en este instante puedo decir que las mejores cosas que me han pasado, me han pasado porque las he dejado fluir. Es así como en estos instantes me encuentro sentado, en frente de un computador, con la satisfacción parcial de logros cumplidos, con la energía para seguir aprendiendo de esta vida, y con la alegría de estar reunido y compartiendo estos momentos con las pocas personas por las que daría mi vida, en persona y a la distancia.

Y es así mí querida hermanita, como la perseverancia, la paciencia, algo de lógica, amor, y el hecho de que dejes fluir las cosas te pueden traer cosas muy bonitas. Como alguien diría *“Todo llega al que sabe esperar”*.

This thesis and my works are dedicated to my little sister, as a sign that perseverance, patience, love, and a little bit of logic bring about beautiful things.

## Table of Contents

CHAPTER ONE: INTRODUCTION.....	1
1.1 Overview.....	1
1.2 Objectives .....	7
1.3 Thesis Structure .....	9
CHAPTER TWO: LITERATURE REVIEW.....	10
2.1 Petroleum Characterization.....	11
2.1.1 Definition of Petroleum .....	11
2.1.2 Heavy Oil and Bitumen Chemistry and Phase Behaviour.....	14
2.1.3 Oil Characterization Methods.....	18
2.2 Biodiesel Definition.....	23
2.3 Vapour Pressure Modeling .....	28
2.3.1 Vapour Pressure Of Pure Substances.....	28
2.3.2 Vapour Pressure of Mixtures .....	32
2.3.3 Extrapolation of Vapour Pressure.....	35
2.3.4 Vapour Pressure of Biodiesels.....	37
2.3.5 Vapour Pressure of Heavy Oil.....	38
2.4 Measurement Methods for Vapour Pressure.....	40
2.4.1 Static Methods .....	40
2.4.2 Dynamic Methods.....	41
2.4.3 Effusion Methods.....	42
2.4.4 Transpiration Methods.....	42
2.4.5 Calorimetric Methods .....	43
2.5 Vacuum Physics.....	43
2.5.1 Rarefied Gas Theory .....	44
2.5.2 Gas Flow Rate at Low Pressures .....	45
2.5.3 Thermal Transpiration .....	48
2.6 Summary.....	51

CHAPTER THREE: EXPERIMENTAL METHOD.....	52
3.1 EXPERIMENTAL MATERIALS .....	52
3.2 Apparatus Design.....	54
3.2.1 Apparatus Design Criteria .....	56
3.2.2 Vapour Pressure Measurement Apparatus.....	63
3.2.3 Degassing Apparatus .....	70
3.3 Apparatus Testing and Calibration .....	73
3.4 Experimental Procedure.....	82
3.4.1 Degassing.....	82
3.4.2 Vapour Pressure Measurement .....	85
3.4.3 Fractionation .....	86
3.5 Apparatus Testing on Pure Components.....	88
3.5.1 Assessment of Literature Vapour Pressure Data .....	89
3.5.2 Regression of Literature Vapour Pressure Data .....	92
3.5.3 Vapour Pressure of Naphthalene and Hexadecane .....	93
3.6 Liquid Heat Capacity Experimental Procedure .....	94
3.7 Summary.....	97
 CHAPTER FOUR: CONSTRAINED EXTRAPOLATION OF VAPOR PRESSURE ...	99
4.1 Introduction.....	99
4.2 Analytical Approach .....	103
4.3 Equation of State Approach .....	105
4.3.1 Peng-Robinson Equation of State .....	106
4.3.2 Vapour pressure of a pure component .....	108
4.3.3 Vapour Pressure of mixtures.....	110
4.3.4 Heat Capacities and Heat of Vaporization.....	112
4.3.5 Adjustment of the Peng-Robinson EoS to Experimental Data .....	114
4.4 Summary .....	114
 CHAPTER FIVE: MODELLING THE VAPOR PRESSURE OF FATTY ACID METHYL ESTERS .....	116
5.1 Introduction.....	116
5.2 FAMES Physical Properties .....	117

5.3 Phase Transition Heat Capacity .....	118
5.3.1 Ideal Gas Heat Capacity .....	119
5.3.2 Liquid Heat Capacity .....	120
5.4 Analytical Vapour Pressure Correlation for FAMES.....	125
5.5 Predictive Vapour Pressure Equation for FAMES .....	131
5.5.1 Saturated FAMES Vapour Pressure Equation.....	132
5.5.2 Unsaturated FAMES Vapour Pressure Equation .....	134
5.6 Equation of State Approach for FAMES Vapour Pressure .....	137
5.6.1 FAMES Critical Properties and Acentric Factor.....	138
5.6.2 Vapour Pressure Calculation and Optimization of Critical Properties and Acentric Factor for FAMES .....	141
5.6.3 Liquid Heat Capacity Calculation of FAMES.....	143
5.7 Summary .....	149
CHAPTER SIX: MODELLING BIODIESEL VAPOR PRESSURE AND CALORIMETRIC DATA .....	150
6.1 Experimental Data of Biodiesels .....	151
6.1.1 Composition of Biodiesels.....	152
6.1.2 Water Content of Biodiesels .....	155
6.1.3 Vapour Pressure of Biodiesels.....	156
6.1.4 Liquid Heat Capacity and Cloud Point of Biodiesels .....	157
6.2 Modelling Results of Biodiesel Vapour Pressure and Heat Capacity.....	159
6.2.1 Analytical Approach.....	159
6.2.2 Equation of State Approach.....	163
6.3 Summary .....	168
CHAPTER SEVEN: MODELLING HEAVY OIL VAPOUR PRESSURE AND CALORIMETRIC DATA .....	170
7.1 Experimental Data and Modelling Results for Western Canadian Bitumen .....	171
7.1.1 Vapour Pressure Experimental Data of WC_B1 Bitumen.....	171
7.1.2 Liquid Heat Capacity of Alberta Region Heavy Oil.....	172
7.2 Modelling Approach for Heavy Oil Vapour Pressure using Equation of State.....	173
7.2.1 General Characterization of Heavy Oils .....	174
7.2.2 Vapour Pressure Calculation .....	186
7.3 Modelling the WC_B1 Sample.....	187

7.4 Equation of State Model for Alberta Region Heavy Oil Vapour Pressure .....	190
7.5 Summary .....	194
CHAPTER EIGHT: HEAVY OIL DEEP VACUUM RACTIONATION .....	196
8.1 Preliminary Fractionation Test .....	198
8.2 High Vacuum Fractionation of Heavy Oil.....	201
8.2.1 Identifying Initial Temperature of Fractionation .....	202
8.2.2 Collection of Heavy Oil and Bitumen Fractions .....	205
8.3 Inter-conversion of Reduced-Pressure Boiling Point Curves .....	211
8.3.1 Maxwell-Bonnell Inter Conversion Method.....	212
8.3.2 Equation-of-State Based Inter Conversion Method.....	216
8.3.3 Inter-Conversion Based on Measured Vapour Pressures .....	217
8.3.4 Comparison to Other Distillation Techniques .....	222
8.4 Fractionation Results .....	224
8.4.1 Reproducibility of Fractionation Data .....	225
8.4.2 Density Profiles.....	226
8.5 Recommended Design Improvements .....	230
8.6 Summary .....	233
CHAPTER NINE: CONCLUSIONS AND RECOMMENDATIONS .....	235
9.1 Dissertation Contributions and Conclusions.....	235
9.1.1 High Vacuum – Vapour Pressure Measurement System.....	235
9.1.2 Vapour Pressure Experimental Data.....	236
9.1.3 Vapour Pressure Extrapolation Technique .....	237
9.1.4 Heavy Oil and Bitumen Characterization Method .....	238
9.1.5 Fractionation of Heavy Oil and Bitumen.....	239
9.2 Recommendations.....	239
References.....	243
APPENDIX A.....	257
APPENDIX B.....	273
APPENDIX C.....	317

## List of Tables

Table 2.1 Composition* of selected biodiesel from a variety of sources (composition in mass fraction).....	24
Table 2.2 Selected physical properties of most common fatty acid methyl esters. ....	25
Table 3.1 Selected physical properties of naphthalene, n-hexadecane, and n-eicosane. ..	53
Table 3.2 Selected physical properties of biodiesel samples.....	53
Table 3.3 Selected physical properties of bitumen sample from the Western Canadian Bitumen (WC_B1). ....	54
Table 3.4 Temperature operational range for the HV-VPMS.....	57
Table 3.5 Pressure operational range for the different gauges in the HV-VPMS.....	65
Table 3.6 Factors influencing the pump down time and ultimate pressure on a vacuum system. ....	75
Table 3.7 Cox equation constants for naphthalene and n-hexadecane vapour pressure...	93
Table 4.8 Constants for the saturation pressure calculation of pure substances using Peng-Robinson Equation of state.....	109
Table 5.9 Experimental data for selected FAMES and temperature range in °C .....	117
Table 5.10 Regressed constants for liquid heat capacity for FAMES according to.....	120
Table 5.11 Modified parameters of the Dadgostar-Shaw equation for FAMES.....	123
Table 5.12 Performance of Dadgostar-Shaw method, Equation 5.8, and Equation 5.13 for known FAMES liquid heat capacity .....	124
Table 5.13 Cox equation parameters for all data and constrained data for FAMES.....	126
Table 5.14 Performance of the vapour pressure and heat capacity equations for various FAMES. ....	126
Table 5.15 Experimental and Calculated normal boiling point of different FAMES .....	129
Table 5.16 Critical properties and acentric factor of selected FAMES.....	139
Table 5.17 Performance of the Peng-Robinson EoS for the prediction of vapour pressure and enthalpy of vaporization for various FAMES .....	140

Table 5.18 AARD values for the Peng-Robinson EoS for the prediction of liquid heat capacity for various FAMES with three different methods for the ideal gas heat capacity prediction. ....	148
Table 6.19 Temperature range of vapour pressure and heat capacity data for selected biodiesel fuels. ....	152
Table 6.20 Mole fraction percentage of fatty acid methyl esters in different biodiesel fuels. ....	153
Table 6.21 Moisture content in studied biodiesels. ....	156
Table 6.22 Polynomial regression coefficients for liquid heat capacity of selected biodiesels. ....	158
Table 6.23 Experimental and literature cloud points (CP) of selected biodiesels .....	158
Table 6.24 Performance of “All-data” and “Constrained” scenarios in the prediction of biodiesel fuel vapour pressure and liquid heat capacity. ....	160
Table 6.25 Performance of APR-EoS prediction of biodiesel fuel vapour pressure and liquid heat capacity. ....	164
Table 7.1 Physical properties of WC_B1 maltenes and asphaltenes .....	187
Table 7.2 Physical property correlations used in WC_B1 bitumen modelling .....	188
Table 7.3 Pseudo-component physical properties of WC_B1 bitumen. ....	189
Table 7.4 Parameters for the three-degree regressed polynomial for ideal gas heat capacity calculation of WC_B1 bitumen pseudo-components. ....	189
Table 8.5 Parameter values and absolute and relative deviation values (AAD and AARD) of Equation 8.2 and 8.3 describing the volume profiles of different WC_B1 maltene fractions. ....	208
Table 8.6 Simulated composition of WC-B1 and fractions. ....	219
Table 8.7 WC_B1 maltene fractions obtained using the HV-VPMS. ....	225
Table 8.8 Extrapolated values of density for the different WC_B1 maltene fractions using ideal and non-ideal density models .....	228
Table A.1 Experimental Vapour Pressure of Hexadecane. ....	260
Table A.2 Experimental Vapour Pressure of Eicosane. ....	260
Table A.3 Experimental Vapour Pressure of Naphthalene .....	260

Table A.4 Experimental Vapour Pressure of Palm Oil Biodiesel.....	264
Table A.5 Experimental Vapour Pressure of Rapeseed Oil Biodiesel.....	264
Table A.6 Experimental Vapour Pressure of Canola I25 Oil Biodiesel .....	265
Table A.7 Experimental Vapour Pressure of Canola CB Oil Biodiesel .....	265
Table A.8 Experimental Vapour Pressure of Soy S-B100 Oil Biodiesel .....	265
Table A.9 Experimental Vapour Pressure of Soy MG-B100 Oil Biodiesel .....	265
Table A.10 Experimental Vapour Pressure of Coconut Oil Biodiesel .....	266
Table A.11 Liquid heat capacity of Canola CB-01 biodiesel .....	266
Table A.12 Liquid heat capacity of Canola I25 biodiesel .....	266
Table A.13 Liquid heat capacity of Soy MG-B100 biodiesel .....	267
Table A.14 Liquid heat capacity of Soy S-B100 biodiesel.....	267
Table A.15 Liquid heat capacity of Rapeseed biodiesel S090824.....	267
Table A.16 Liquid heat capacity of Palm biodiesel S102550.....	268
Table A.17 Liquid heat capacity of Coconut biodiesel S102550 .....	268
Table A.18 Experimental High Vacuum Distillation Data for WC-B1 Maltenes .....	270
Table A.19 Experimental SBD Data for WC-B1 Maltenes.....	270
Table A.20 Experimental SimDist Data for WC-B1 Maltenes.....	271
Table A.21 Experimental Vapour Pressure of WC-B1 Bitumen.....	271
Table A.22 Experimental Vapour Pressure of WC-B1 Maltenes .....	271
Table A.23 Experimental Vapour Pressure of WC-B1 85% wt Maltenes Residue.....	272
Table A.24 Experimental Vapour Pressure of WC-B1 78% wt Maltenes Residue.....	272
Table A.25 Liquid heat capacity of WC-B1 maltenes.....	272
Table B1 List of parts comprising the HV-VPMS .....	314
Table C.1 Constants for Joback methods for relevant molecular groups .....	317

## List of Figures and Illustrations

Figure 1.1 Recorded and expected world energy demand; source: World Energy Council and Institut Francais du Petrole .....	2
Figure 1.2 World total resources of oil in-place (OIP) .....	2
Figure 1.3 Schematic true boiling point (TBP) curve of bitumen .....	5
Figure 2.1 Petroleum classification according to specific gravity and viscosity .....	12
Figure 2.2 IFP schematic ternary diagram for crude oil classification .....	12
Figure 2.3 Evolution chart of molecular structures as a function of boiling point .....	13
Figure 2.4 Simplified representation of crude oil by solvent fractionation .....	14
Figure 2.5 Phase envelope of the system Athabasca bitumen – propane – carbon dioxide.....	18
Figure 2.6 Normal boiling point of a crude oil and compartmentalization based on equal mass fraction distilled.....	20
Figure 2.7 Simulated molecular distribution of Athabasca bitumen using a Gaussian distribution on maltenes and a Gamma distribution on asphaltenes using VMGSim.....	22
Figure 2.8 Gamma molecular distribution and the determination of the $i^{\text{th}}$ pseudo-component.....	22
Figure 2.9 A triglyceride: a combination of three fatty acids and a glycerol molecule....	24
Figure 2.10 Methanolysis reaction equation.....	26
Figure 2.11 Isothermal vapour-liquid equilibrium diagram of a binary mixture.....	32
Figure 2.12 Molecular trajectories in various flow types .....	46
Figure 2.13 Pressure reading as a function of flow regime .....	46
Figure 2.14 Chamber representation for thermal transpiration phenomenon.....	49
Figure 3.15 Schematic of a static vapour pressure apparatus.....	55
Figure 3.16 High Vacuum Vapour Pressure Measurement system (HV-VPMS); Vapour Pressure Measurement Apparatus VPMA (above) and Degassing Apparatus DA (below).....	56

Figure 3.17 Experimental and modeled vapour pressure data for Athabasca residue and hexadecane. ....	59
Figure 3.18 Knudsen number as a function of pressure at 200 °C with an inner diameter of 1 in. and a 1nm molecule.....	62
Figure 3.19 Transition pressure for thermal transpiration as a function of pipe inner diameter, molecule size, and temperature.....	62
<b>Figure 3.20</b> Vapour Pressure Measurement Apparatus (VPMA).....	64
Figure 3.21 Sample Chamber Schematic.....	66
Figure 3.22 Pressure gauges applicability ranges and literature and expected vapour pressure values for hexadecane and WC_B1 bitumen, respectively. ....	67
Figure 3.23 Cold Finger schematic.....	70
Figure 3.24 Degassing Apparatus (DA).....	71
Figure 3.25: VPMA pressure rise profile before and after out gassing. ....	74
Figure 3.26 Experimental pump down time of DA and VPMA before out gassing.....	75
Figure 3.27 Calibration chart for RTD against F251 HTP. ....	77
Figure 3.28 Calibration chart for Cold Cathode- Pirani gauge against GOR diaphragm gauge. ....	79
Figure 3.29 Calibration chart for DG1 diaphragm gauges. ....	79
Figure 3.30 Experimental and literature data for eicosane measured with DG1 .....	81
Figure 3.31 Literature and measured vapour pressure data of eicosane with linear calibration and with linear + non-linear calibration.....	81
Figure 3.32 Simplified VPMA schematics .....	83
Figure 3.33 A typical degassing cycle. ....	84
Figure 3.34 Complete cycle of hexadecane degassing at 25°C. ....	84
Figure 3.35 Simplified schematic of the vapour pressure measurement apparatus, VPMA. ....	85
Figure 3.36 Vapour pressure measurement cycle.....	86
Figure 3.37 Pump down time for early fractionation stage .....	87

Figure 3.38 n-Hexadecane literature data plotted with Korsten equation axes. ....	91
Figure 3.39 Complete set of n-Hexadecane literature data plotted with the Oonk-van Linde coordinates. ....	92
Figure 3.40 Experimental vapour pressure data for n-hexadecane and naphthalene. ....	94
Figure 3.41 Heat flow and temperature ramp for differential scanner calorimeter assay on a biodiesel fuel sample -4 to 8 °C .....	95
Figure 3.42 Heat capacity as a function of temperature. ....	96
Figure 3.43 Heat flow as a function of temperature for a biodiesel fuel .....	97
Figure 4.1 Vapour pressure and heat capacity of methyl oleate; constrained extrapolation of vapour pressure is backed up by liquid heat capacity data above the freezing point. ....	100
Figure 4.2 Optimization function for vapour pressure determination. ....	112
Figure 5.1 Experimental and regressed liquid heat capacities for selected FAMES. ....	121
Figure 5.2 Experimental and predicted liquid heat capacity for methyl palmitate. ....	123
Figure 5.3 Experimental and regressed vapour pressure of methyl palmitate. ....	128
Figure 5.4 Experimental and regressed vapour pressure of methyl caprylate .....	128
Figure 5.5a Cox parameter $a_{PV1}$ as a function of carbon number for saturated FAMES. ....	130
Figure 5.6 Vapour pressure as a function of carbon number for saturated FAMES at 70 °C. ....	133
Figure 7 Parameters $a_{CN,0}$ and $a_{CN,1}$ as a function of temperature and fitted with Equations 5.17 and 5.18. ....	133
Figure 5.8 Experimental and predicted values for the training set (left) and the tester, methyl nonadecanoate (right). ....	134
Figure 5.9 Experimental and correlated vapour pressure data for unsaturated C18 family of FAMES at 30 °C. ....	135
Figure 5.10 Departure function for unsaturated C18 family of FAMES at 30 °C. ....	136
Figure 5.11 Experimental and predicted values for methyl palmitoleate. ....	137
Figure 5.12 Experimental and predicted vapour pressure and heat of vaporization data for methyl caprate, C10:0 using initial critical properties and acentric factor. ....	141

Figure 5.13 Algorithm to adjust critical properties and acentric factor of FAMES for the Peng-Robinson equation of state.....	142
Figure 5.14 Experimental and predicted vapour pressure and heat of vaporization data for methyl caprate, C10:0 using adjusted critical properties and acentric factor....	143
Figure 5.15 Algorithm to adjust ideal gas heat capacity of FAMES for the Peng-Robinson equation of state.....	144
Figure 5.16 Calculated and regressed ideal gas heat capacity for methyl caprylate, C10:0.....	145
Figure 5.17 Parameters of Equation 2 as a function of molecular weight.....	146
Figure 5.18 Experimental and predicted liquid heat capacity data for methyl caprate, C10:0.....	148
Figure 6.1 Comparison between measured and literature molecular weight profile for Canola biodiesel.....	154
Figure 6.2 Comparison between measured and literature molecular weight profile for Rapeseed biodiesel.....	154
Figure 6.3 Experimental vapour pressure of rapeseed biodiesel; dotted line is drawn to show the tendency and does not represent any particular model.....	157
Figure 6.4 Experimental and predicted vapour pressure of coconut biodiesel S170717 with analytical “All-data” and “Constrained” scenarios.....	161
Figure 6.5 Experimental and predicted liquid heat capacity of coconut biodiesel S170717 with analytical “All-data” and “Constrained” scenarios.....	162
Figure 6.6 Experimental and predicted vapour pressure of biodiesel fuels listed in Table 6.1 with the analytical “Constrained” scenario.....	162
Figure 6.7 Experimental and predicted liquid heat capacity of biodiesel fuels listed in Table 6.1 with the analytical “Constrained” scenario.....	163
Figure 6.8 Experimental and predicted vapour pressure of biodiesel fuels listed in Table 6.1 with the Advanced Peng-Robinson equation of state.....	164
Figure 6.9 Experimental and predicted liquid heat capacity of biodiesel fuels listed in Table 6.1 with the Advanced Peng-Robinson equation of state.....	165
Figure 6.10 Experimental and predicted vapour pressure of coconut biodiesel with the n values ranging from Zc to -5.....	166
Figure 6.11 Experimental and predicted liquid heat capacity of coconut biodiesel with the n values ranging from Zc to -5.....	168

Figure 7.1 Vapour pressure of WC_B1 bitumen and maltenes – lines are drawn to show the tendency and do not represent any specific model. ....	172
Figure 7.2 Experimental and regressed liquid heat capacity of WC_B1 maltenes and fractions.....	173
Figure 7.3 Algorithm schematics for the modelling of heavy oil and bitumen based on the measured and extrapolated normal boiling point.....	175
Figure 7.4 Experimental normal boiling point of WC_B1 maltenes .....	176
Figure 7.5 Gaussian extrapolation of the normal boiling point of maltenes based on the Medium region.....	178
Figure 7.6 Experimental and extrapolated normal boiling point of WC_B1 maltenes ..	178
Figure 7.7 GMDF schematic; compartmentalization of one molecular weight-based pseudo-component is shown. ....	181
Figure 7.8 Modelled normal boiling point for asphaltene fraction with $\alpha=2.5$ and $\eta=735$ . ....	183
Figure 7.9 Complete experimental and extrapolation normal boiling point of a bitumen .....	184
Figure 7.10 Complete experimental and extrapolated normal boiling point of WC_B1 bitumen .....	188
Figure 7.11 Experimental and predicted vapour pressure of WC_B1 bitumen and maltene fraction using the APR-EoS. ....	192
Figure 7.12 Experimental and predicted liquid heat capacity of WC_B1 bitumen and maltene fraction using the APR-EoS and the Lastovka-Shaw correlation. ....	192
Figure 7.13 Experimental and predicted vapour pressure values for WC_B1 maltene fraction at different n-values for the Gao et al. interaction parameter correlation..	194
Figure 8.1 Schematics of distillation performance on a heavy oil or bitumen at different operating pressures.....	197
Figure 8.2 Simplified schematics of the vapour pressure measurement apparatus (VPMA). ....	199
Figure 8.3 WC_B1 maltene fractions and residue obtained through deep vacuum fractionation. ....	200
Figure 8.4 Boiling point cuts for WC_B1maltenes. ....	201

Figure 8.5 Pressure profile for the fractionation of WC_B1 maltenes at temperatures from 60 °C to 115°C.....	203
Figure 8.6 Condensation blockage in the form of oil droplet formation and its pressure profile at 150 °C.....	204
Figure 8.7 Pressure profile for the fractionation procedure on WC_B1 maltenes at a temperature range of 60°C to 150 °C. ....	204
Figure 8.8 Pressure profile for the fractionation of WC_B1 maltenes at 150 °C. ....	206
Figure 8.9 Volume profiles for five WC_B1 maltene cuts – lines are drawn to show the tendency and do not represent any particular model.....	206
Figure 8.10 Cumulative volume profiles for five WC_B1 maltene cuts .....	209
Figure 8.11 Cumulative volume profiles for five WC_B1 maltene cuts .....	209
Figure 8.12 Values of $t_{95}$ for five fractions from WC_B1 maltenes.....	210
Figure 8.13 Predicted values of $t_{95}$ for five fractions from WC_B1 maltenes.....	211
Figure 8.14 Boiling point profiles for WC_B1 maltenes _ Inter-converted values of high vacuum boiling points in the SBD experimental data region. ....	213
Figure 8.15 Correlated operating pressures for the first two high vacuum boiling points using the Maxwell-Bonnell equations.....	214
Figure 8.16 Boiling point profiles for WC_B1 maltenes – volume based.....	214
Figure 8.17 Boiling point profiles for WC_B1 maltenes – mass based.....	215
Figure 8.18 Flash schematics for simulated production of deep vacuum cuts. ....	216
Figure 8.19 Vapour pressure of WC_B1 bitumen and fractions. ....	218
Figure 8.20 Experimental and predicted vapour pressure of WC_B1 bitumen and fractions using the APR-EoS – original compositions. ....	220
Figure 8.21 Experimental and predicted vapour pressure of WC_B1 bitumen and fractions using the APR-EoS – compositions have been relaxed to within experimental error. ....	221
Figure 8.22 Experimental and extrapolated normal boiling point of WC_B1 maltenes – a representation of the extrapolated NBP of three cuts is also shown. ....	222
Figure 8.23 Boiling point profiles for WC_B1 maltenes – mass based.....	223

Figure 8.24 Photograph of five the different fractions and residue of WC_B1 maltenes deep vacuum fractionation.....	224
Figure 8.25 Boiling point profiles for WC_B1 maltenes – mass based.....	226
Figure 8.26 Density profile of WC_B1 maltene residue (after high vacuum distillation) at different concentrations with toluene .....	228
Figure 8.27 Measured and predicted density of WC_B1 maltenes fractions as a function of cumulative mass distilled. ....	230
Figure 8.28 Schematics of sample vessel and cold finger and possible mass transfer limitations involved in deep vacuum fractionation.....	231
Figure 8.29 Cold finger tip – Current (right) and Tapered (left). ....	233
Figure A.1 Comparison between open literature and experimental molecular weight distributions for soybean biodiesels.....	263
Figure A.2 Comparison between open literature and experimental molecular weight distributions for coconut biodiesels .....	263
Figure A.3 Comparison between open literature and experimental molecular weight distributions for palm biodiesels.....	264
Figure A.4a Heat flow for different biodiesels: a) CB01 Canola, b) I25 Canola, c) MG-B100 Soy, d) S-B100 Soy .....	269
Figure A.5b Heat flow for different biodiesels: e) S080824 Palm, f) S071707 Coconut, g) Sylfat9014 Tallow, h) I26 Tallow .....	269
Figure B.1 High Vacuum Vapour Pressure Measurement system (HV-VPMS); Vapour Pressure Measurement Apparatus VPMA (above) and Degassing Apparatus DA (below) .....	275
Figure B2 Vapour Pressure Measurement Apparatus (VPMA) .....	277
Figure B3 Sample Chamber Schematic .....	278
Figure B4 Schematics of the Inficon diaphragm gauge.....	279
Figure B5 Schematics of the Pfeiffer Compact FullRange™ gauge .....	280
Figure B6 Picture of the Pfeiffer HiCube 80 pumping station (modified from Pfeiffer Vacuum [2009]) .....	281
Figure B7 Connection schematics from the pump station suction point to the Cold cathode-Pirani gauge with KF flanges .....	282

Figure B8 Cold Finger schematic .....	283
Figure B9 Degassing Apparatus (DA).....	284
Figure B10 DA Cold Finger schematic .....	286
Figure B11 ConFlat (CF) Flange Schematic- Recommended tighten up order.....	288
Figure B12 DCU display and main constituents (modified from Pfeiffer [2004]).....	290
Figure B13 Differences with non-outgassed and outgassed pressure profile .....	293
Figure B14 LabView main window for HV-VPMS data acquisition.....	294
Figure B15 LabView main window for saving files and the HV-VPMS “File Tree” ....	295
Figure B16 DA simplified schematic .....	297
Figure B17 DA degassing cycles for a hexadecane sample .....	298
Figure B18 VPMA simplified schematic.....	299
Figure B19: Vapour pressure measurement cycle .....	301
Figure B20: Volume vs. Time profile of fractionate crude oil – shown.....	303
Figure B21 Raw pressure profile of a single cycle using DG01.....	305
Figure B22 Single pressure profile cycle processing.....	306
Figure B23 Processed pressure profile .....	307
Figure B24 Calibration chart for RTD against F251 HTP.....	308
Figure B.25 Calibration chart for Cold Cathode- Pirani gauge against GOR diaphragm gauge. ....	310
Figure B.26 Calibration chart for DG1 diaphragm gauges.....	310
Figure B.27 Experimental and literature data for eicosane measured with DG1 .....	312
Figure B.28 Literature and measured vapour pressure data of eicosane with linear calibration and with linear + non-linear calibration.....	312
Figure B29 Leak detector configuration with single dry mechanical pump.....	313

## List of Symbols, Abbreviations and Nomenclature

<b>Symbol</b>	<b>Definition</b>	<b>Units</b>
$a_i$	Adjustable Parameters	[-]
a, b, c, d...	Adjustable Parameters	[-]
a	Attractive Parameter in Equation of State	[-]
A	Area	[m <sup>2</sup> ]
A, B	Cubic Equation of State Form Parameters	[-]
AAD	Absolute Average Deviation	[-]
AARD	Absolute Average Relative Deviation	[-]
b	Exclusive Volume in Equation of State	[m <sup>3</sup> /mol]
$C_p$	Heat Capacity	[kJ/kmol.K]
$C_K$	Soave Vapour Pressure Equation Parameters	[-]
$d_M$	Average Diameter of a Molecule	[m]
$d_{eq}$	Equivalent Inner Pipe Diameter	[m]
f	Fugacity	[kPa]
$f_P$	Modified Pressure for Oonk Method	[kPa]
$f_w$	Acentric Factor Parameter in Equation of State	[-]
$H_v$	Enthalpy of Vaporization	[kJ/kmol]
j	Optimization Function	[-]
k	Boltzmann Constant	[m <sup>2</sup> .kg/s <sup>2</sup> .K]

$k_{ij}$	Interaction Parameter in Equation of State	[-]
$K_i$	Weight Factor for Optimization Function	[-]
$K_i$	Equilibrium K-value	[-]
$K_n$	Knudsen Number	[-]
$K_w$	Watson Factor	[-]
$m_M$	Mass of a Molecule	[kg/molecule]
$MW$	Molecular Mass (Weight)	[kg/kmol]
$n$	Exponent of Gao et al. correlation	[-]
$NBP$	Normal Boiling Point	[K]
$N_i$	Number of Molecules of Type “i”	[-]
$N_{UC}$	Number of Unsaturated Carbon Molecules	[-]
$P$	Pressure	[kPa]
$P_m$	Pressure at Measurement Conditions	[kPa]
$P_v$	Vapour or Saturation Pressure	[kPa]
$q_M$	Molecular Flow	[molecules/s]
$R$	Universal Gas Constant	[kJ.m <sup>3</sup> /kmol.K]
$Re$	Reynolds Number	[-]
$R_K$	Knudsen Value	[-]
$SG$	Specific Gravity	[-]
$T$	Temperature	[K]
$T_b$	Boiling Point	[K]
$v$	Velocity	[m/s]
$V, v$	Molar Volume	[m <sup>3</sup> /mol]

w	Weight Fraction	[kg/kg]
x	Mole Fraction in Liquid Phase	[kmol/kmol]
y	Mole Fraction in Vapour Phase	[kmol/kmol]
z	Normal Distribution Parameter	[-]
Z	Compressibility Factor	[-]

<b>Greek Symbols</b>	<b>Definition</b>	<b>Units</b>
$\alpha$	Adjustable Parameter in Equation of State	[-]
$\alpha_r$	Shape Factor of Gamma Distribution Function	[-]
$\alpha_{CP}$	Similarity Variable	[-]
$\beta$	Gamma Distribution Factor	[-]
$\beta_{12}$	Interaction Parameter	[-]
$\beta_{0,f}$	Adjustable Parameters for Oonk Method	[-]
$\Delta$	Change of Parameter Value	[-]
$\gamma$	Activity Coefficient	[-]
$\Gamma$	Gamma Function	[-]
$\eta$	Monomer Weight on Gamma Distribution Function	[-]
$\lambda$	Mean Free Path	[m]
$\mu$	Viscosity	[kg/m.s]
$\rho$	Density	[kg/m <sup>3</sup> ]

$\sigma$	Standard Deviation	[-]
$\nu$	Stoichiometric Number	[-]
$\Phi$	Fugacity Coefficient	[-]
$\Phi_M$	Molecular Incidence Rate	[moles/m <sup>2</sup> ]
$\omega$	Acentric Factor	[-]

### **Superscripts**

### **Definition**

calc	Calculated Value
exp	Experimental Data Value
L	Liquid Phase
Res	Residual Property from Equation of State
Sat	Value at Saturation Conditions
V	Vapour Phase
0	Ideal Gas Property

### **Subscripts**

### **Definition**

Avg	Average Value
c	Cumulative Property
C	Critical Property
C <sub>P</sub>	Adjusted Parameter of a Heat Capacity Equation
Frac	Property of a Fraction

i, j	Property of the Substance i or j
L	Property of the Liquid Phase
m	Property of Mixture in Equation of State
Mix	Property of Mixture
Pv	Adjusted Parameter of a Vapour Pressure Equation
R	Reduced Property
Ref	Reference Value
V	Property of the Vapour Phase

## Epigraph

*“It’s one of those inexplicable things  
How everything I’ve learned and experienced is brought to bear the problem.  
Pushing too hard will only make things freeze up.  
How many great problems have gone unsolved  
Because men didn’t know enough, or have enough faith in  
The creative process and in themselves,  
To let go for the whole mind to work at it?”*

Daniel Keyes

## CHAPTER ONE: INTRODUCTION

### 1.1 Overview

Petroleum is currently the most important source of energy and one of the most important substances used by mankind worldwide. It displaced coal as the main source of energy by 1965 [Enzer et al., 1975]. This transition is directly attributable to its relative ease of discovery, extraction, production, and utilization [Wiley, 2007]. It is also used as a feedstock for manufacturing industries in the areas of polymers, solvents, lubricants, cosmetics, petrochemicals, and a wide variety of other materials.

Oil demand continues to increase as energy demand increases (Figure 1.1); however, oil resources are finite (Figure 1.2). Oil production can be sustained if new oil resources or technologies are introduced. Currently, oil supply is based chiefly on conventional oil (medium to light oil produced from land based sandstone or carbonate reservoirs) and to a small extent on non-conventional oil (bitumen, heavy oil, and shale oil,). However, non-conventional oil reservoirs have been shown to be as vast as conventional oil reservoirs (Figure 1.2) and are relatively undeveloped. Hence, it is likely that there will be a transition from conventional to non-conventional oil [Green et al., 2003; Hedrick et al., 2006].

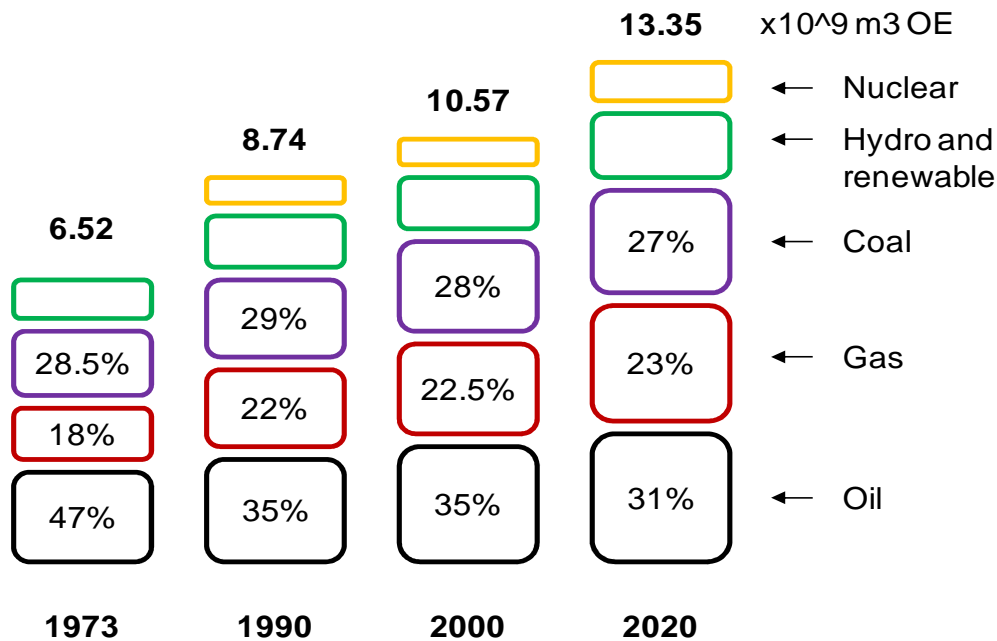


**Figure 1.1** Recorded and expected world energy demand; source: World Energy Council and Institut Francais du Petrole (Modified from Alazard and Montadert, 1993); OE: Oil Equivalent

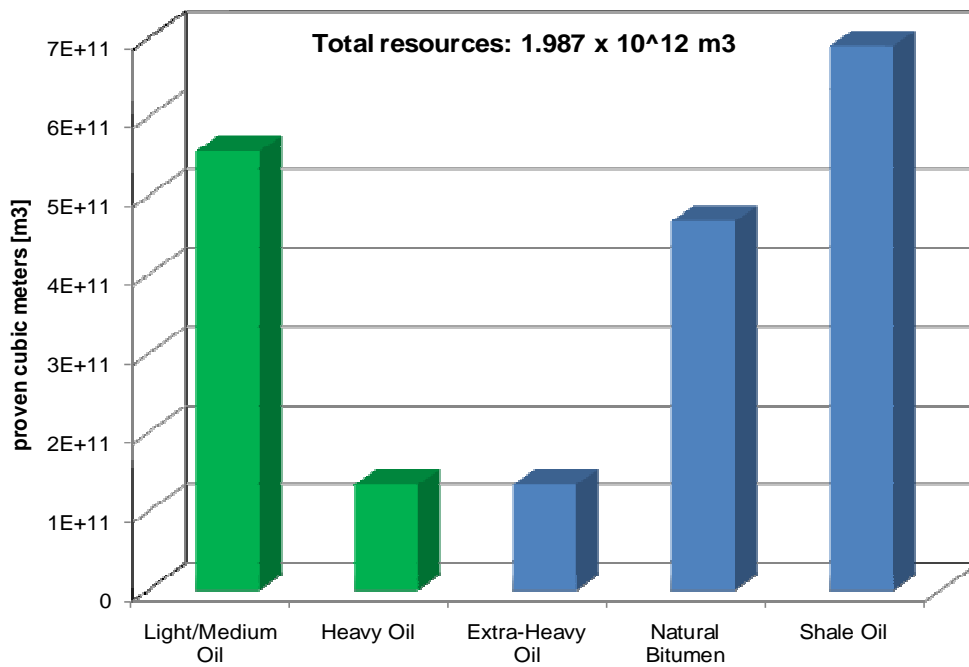


**Figure 1.2** World total resources of oil in-place (OIP); source: Institut Francais du Petrole (modified from Alazard and Montadert, 1993)

One of the largest bitumen and heavy oil deposits in the world are in Alberta, Canada, with an estimated oil in place (OOIP) of 2.7 trillion barrels of petroleum [Janisch, 1979; Butler, 1991], which equates to the total inventory (cumulative production, reserves, and undiscovered estimated resources) of the world conventional crude. However, by 1992, only about 10% of it was technically (not necessarily economically) recoverable [Alazard and Montadert, 1993; Wiley, 2007]. The other major deposit of heavy oil is the Orinoco belt reservoir in Venezuela with approximately 3 trillion barrels OOIP [UNITAR, 1979; Shaw and Zou, 2007; Janisch, 1979; Butler, 1991]. Russia and the United States also account for significant heavy oil and shale oil reservoirs, respectively, with approximately 0.15 trillion barrels OOIP each [Green et al, 2003; Janisch, 1979; Butler, 1991].

In Canada, since the 1970's, there has been an increasing interest in processing bitumen and heavy oil, stemming from the discoveries of non-conventional reservoirs in northern-eastern Alberta [AOSTRA, 1984]. Steam based methods have often been employed to improve heavy oil recovery [AEUB, 2006]; however, the industry is seeking alternatives to these methods because they are energy intensive and may be constrained by the available water supply. As well, some heavy oils are contained in carbonate reservoirs where adverse reactions can occur between the steam and the carbonate rock. Solvent based recovery methods are a potential alternative capable of providing high recovery factors without high water requirements or potential for high temperature reactions [Jiang, 1997].

The design, implementation, and optimization of such technologies rely upon good understanding of both reservoir and heavy oil characteristics [Speight, 1999], particularly the interaction of the solvents with the heavy oil which is expected to be complex [Shaw and Zou, 2007], showing multiple liquid phases [Mehrotra et al. 1985; Badamchi-Zadeh et al., 2009a] and asphaltene precipitation [Alboudwarej et al. 2005]. Since it is not practical to collect data for all possible combinations of heavy oil and solvent, a modelling framework is required to predict phase behaviour and physical properties based on the available data.

Cubic equations of state (CEoS) are used in most commercial simulators for predicting hydrocarbon phase behaviour. To obtain an accurate CEoS model, the fluid must first be characterized; that is, divided into a set of real and/or hypothetical components with assigned properties. Typically, in refinery applications, a petroleum fluid is characterized for a CEoS based on its distillation curve. A distillation curve is probably the most important assay in petroleum industry because it is easy to measure and a single assay provides a large amount of information. For reservoir fluids, a similar approach is used based on gas chromatography [Castellanos Diaz et al., 2011].

However, the use of CEoS for heavy oils and bitumen/solvent mixtures is more challenging than conventional oil modeling since the characterization of the petroleum fluid from the distillation curve is incomplete (Figure 1.3). Distillation techniques are limited by thermal cracking which occurs around 300°C. Most of a heavy oil or bitumen

will not distil below this temperature even with vacuum distillation. On average, the distillable fraction makes up to 50 wt% of a heavy oil and only about 25 wt% of a bitumen.

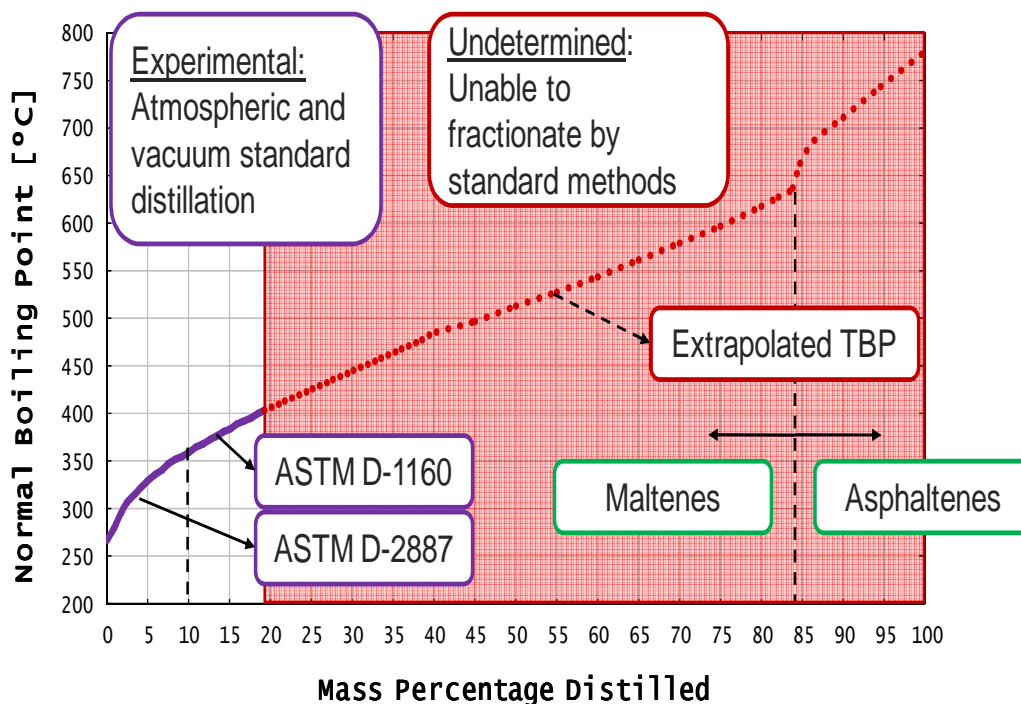


**Figure 1.3** Schematic true boiling point (TBP) curve of bitumen; shadowed region is left undetermined by standard distillation techniques

Flash calculations involving heavy oils pose another challenge since heavy oil/solvent interactions may lead to the appearance of multiple liquid phases over small pressure or composition changes [Shaw and Zou, 2007]. The liquid-liquid phase behaviour of bitumen is dominated by the non-distillable fraction, particularly the asphaltenes which are the highest boiling 10 to 20 wt% of the distillation assay, Figure 1-3 [Castellanos

Diaz et al., 2011]. Hence, it is essential to characterize the non-distillable fraction of heavy oil and bitumen based on measured experimental data.

Commercial atmospheric distillation techniques such as ASTM D86, TBP, and ASTM D2887 can distil about 10% of a bitumen whereas commercial vacuum distillation techniques such as ASTM D1160 and the Spinning Band Distillation technique generate fractions up to about 25 to 30 wt%. The latter techniques operate at pressures close to  $1.3 \times 10^{-1}$  kPa (1 mmHg) [Riazi, 2005].

Distillation behaviour is related to the relative volatility of the components comprising the fluid, which, in turn, is directly related to the vapour pressure of the substances. Therefore, vapour pressure data for the residue fraction of heavy oil and bitumen is a key property in characterizing and modeling heavy oil and bitumen in general, and in extrapolating the TBP curve in particular. While much research has been directed towards obtaining transport and thermodynamic properties of heavy oil and bitumen; there is a lack of reliable vapour pressure data [Schwarz et al., 1986].

Currently, neither a standard procedure nor appropriate equipment is available commercially for direct vapour pressure measurement of heavy hydrocarbons as well as for distillation of heavy hydrocarbon at pressures below  $10^{-1}$  kPa. Medium to high vacuum conditions (pressures below  $10^{-3}$  kPa) are required to obtain vapour-liquid-equilibria at temperatures below the cracking point. At these conditions, new methodologies are required to validate and extrapolate the data.

## 1.2 Objectives

The main goal of this thesis is to develop an apparatus to collect vapour pressure data at high vacuum conditions and to generate heavy oil and bitumen fractionation beyond commercial distillation techniques. This goal is complemented by the development of a new methodology using to characterize the non-distillable fraction of heavy oil and bitumen based in the data collected.

Specific objectives of this thesis are:

- Design, build, and commission a vapour pressure measurement system suitable of sub-atmospheric pressure measurements of substances at temperatures ranging from 20 to 200 °C
- Validate the apparatus with known pure component vapour pressure data
- Obtain and assess vapour pressure data of biodiesel samples to validate the performance of the apparatus with complex known mixtures. Biodiesel are better defined organic mixtures than heavy oils and bitumens and can provide a good test of the proposed apparatus and methodologies. The biodiesel compositions are determined using gas chromatography assays coupled with mass spectrometry (GC-MS)
- Obtain and assess heat capacity data of biodiesels to complement the vapour pressure data and proposed methodology. Heat capacities of biodiesels are

measured using a differential scanning calorimeter (DSC). These data are used to constrain extrapolations of the vapour pressures below  $10^{-4}$  kPa

- Develop a model to characterize heavy oil and bitumen based on experimental normal boiling point data. Extrapolation of the NBP curve is expected using Gaussian and Gamma distributions
- Obtain and assess vapour pressure of bitumen and fractions using the new apparatus. The methodology developed for the biodiesels and the proposed characterization for heavy oil and bitumen is applied
- Obtain and assess heat capacities for bitumen. The heat capacity is used to constrain the vapour pressure model for the bitumen
- Generate definite bitumen fractions beyond 30wt% using the new apparatus. The results from this objective, in the form of a boiling point curve, would surpass what commercial distillation techniques are capable of producing
- Generate an inter-conversion method of the boiling point generated with the new apparatus to normal boiling point based on the proposed bitumen characterization methodology.

The intended outcome is an apparatus to fractionate a significantly greater portion of heavy oils and bitumen than is possible with existing distillation methods. The apparatus is to be validated against literature data and biodiesels. Preliminary experimental protocols and an inter-conversion method are to be established laying the ground work for a standardized method to be developed in future work.

### 1.3 Thesis Structure

This thesis is divided into eight more chapters:

- Chapter Two provides a literature review of the basics of heavy oil characterization and the principles involved in the apparatus design
- Chapter Three presents the main features that were taken into account in the design and construction of the new apparatus, including testing procedures, validation, and an example of the data collection procedure
- Chapter Four develops the methodology used to correlate and extrapolate measured vapour pressure of pure components and mixtures using analytical vapour pressure equations as well as an equation of state
- Chapter Five introduces the modeling results of vapour pressure of fatty acid methyl esters, as main constituents of biodiesel fuels using the methodology developed in Chapter 4. The data in this section is collected from open literature sources
- Chapter Six presents experimental and modeling results of vapour pressure and heat capacity data for biodiesels
- Chapter Seven presents experimental and modeling results of vapour pressure and heat capacity data for bitumen and also discusses the significance of the data
- Chapter Eight presents experimental and modeling results of bitumen deep vacuum fractionation including inter-conversion methods
- Chapter Nine presents the dissertation conclusions and provides guidance for future studies

## CHAPTER TWO: LITERATURE REVIEW

This chapter provides a review of the principles underlying the design and construction of the new high vacuum vapour pressure measurement system (HV-VPMS) as well as the assessment of vapour pressure data. The chapter has four main topics: petroleum characterization, biodiesel characterization, vapour pressure modeling and measurement methodologies, and vacuum physics. While at first sight those topics might appear to be unrelated, they all play an important role in the development of the HV-VPMS.

The review of petroleum characterization provides a context for the HV-VPMS and illustrates the importance of deep fractionation of heavy oil and bitumens and how the vapour pressure is used for oil characterization. Biodiesels are also reviewed because they are well defined mixtures of complex components and provide a means to compare the results from the HV-VPMS with literature data and model predictions. Vapour pressure is discussed including definitions, treatment of vapour pressure data at vacuum conditions, the vapour pressure of heavy oil and biodiesel, and measurement techniques. Finally, the review of vacuum physics focuses on thermal transpiration which affects pressure measurements at deep vacuum conditions.

## **2.1 Petroleum Characterization**

### ***2.1.1 Definition of Petroleum***

Petroleum is a naturally-occurring complex mixture comprising mainly hydrocarbons and variable amounts of compounds containing nitrogen, oxygen, and sulphur together with small amounts of metals such as nickel and vanadium. The composition of petroleum varies depending on its origin and it may occur in the solid (asphalt), liquid (crude oil), or gas (natural gas) state.

Petroleum can be classified through bulk physical properties such as boiling point, specific gravity, viscosity, odour, or color. Crude oil is typically classified as light or heavy according to its specific gravity and viscosity (Figure 2.1). In particular, heavy petroleum (heavy oil and bitumen) is defined as a liquid or solid with specific gravity values lower than 22.3 °API and viscosity values greater than 100 cP at standard conditions (15.6 °C and 1 atm.), Figure 2.1. The average molecular weight is higher than 300 g/mol and the normal boiling point is often higher than 500 K (230 °C).

Light crude oil is known to be rich in low boiling and paraffinic compounds, whereas heavy crude has greater amounts of high boiling and asphalt-like molecules, is more aromatic, and contains larger amounts of hetero-atoms. Hence, there is a correlation between physical properties and composition [Bestougeff et al., 1984; Khayan, 1984; Wiley, 2007]. Figure 2.2 illustrates how the composition of some of the chemical families in a crude oil is distributed [Kinghorn, 1983, AOSTRA, 1984].

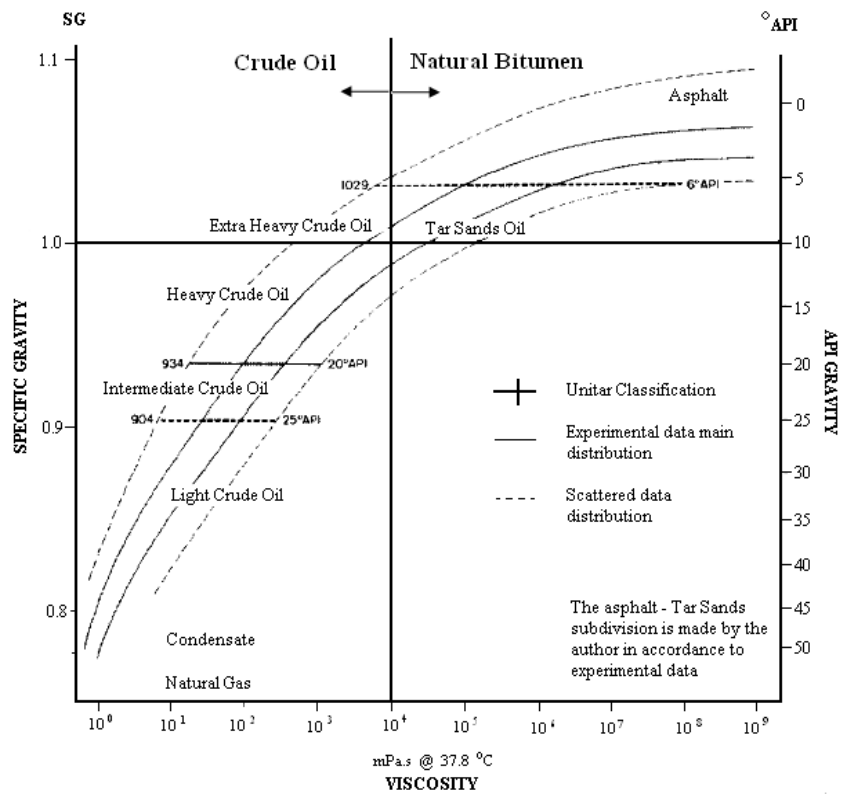


**Figure 2.1** Petroleum classification according to specific gravity and viscosity (Modified from Wiley, 2007).

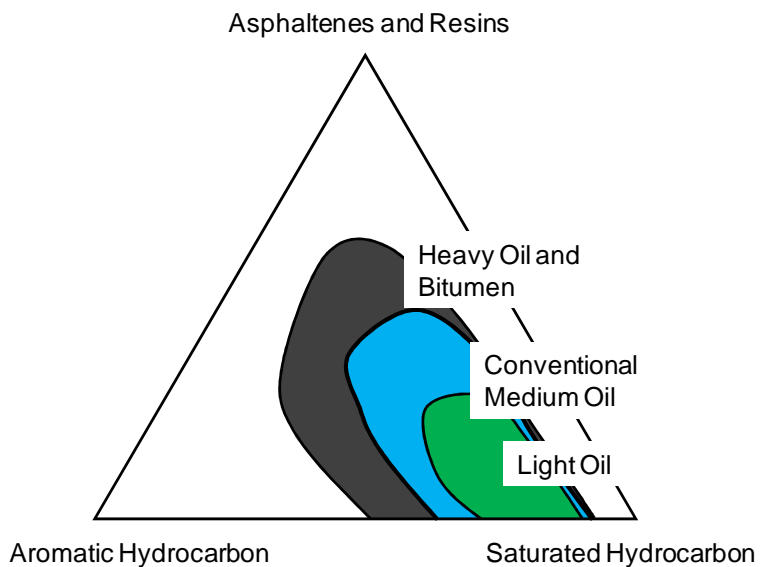


**Figure 2.2** IFP schematic ternary diagram for crude oil classification (Modified from AOSTRA, 1984).

The complexity of the molecules in crude oils increases with the boiling point as well as the density, viscosity, asphalt-like molecules content, refractive index (aromaticity), and polarity (content of hetero-atoms and metals), Figure 2.3 [Altget and Boduszynski, 1994; Merdrignac and Espinat, 2007]. Conventional crude oils consist of relatively lower carbon number species and are less complex mixtures than heavy oils. Most of a conventional oil sample is distillable and there are well-established methods to characterize these fluids for phase behaviour and property models [Riazi, 2005]. Characterization of heavy oils is more challenging because only a relatively small fraction of the oil is distillable.

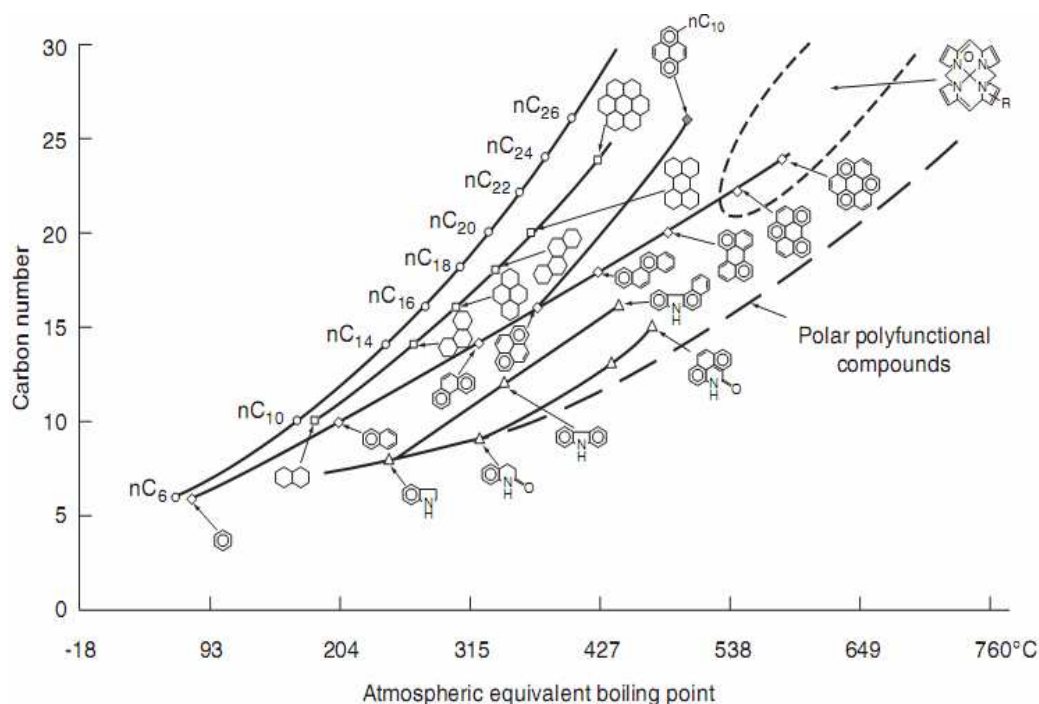


**Figure 2.3** Evolution chart of molecular structures as a function of boiling point (Modified from Merdrignac and Espinat, 2007).

### 2.1.2 Heavy Oil and Bitumen Chemistry and Phase Behaviour

There are few methods to describe heavy oil chemistry. One of the most common methods consists in defining its composition based on fractionation by solvent affinity [AOSTRA, 1984]; for example, the heavy oil can be divided into: saturates, aromatics, resins, asphaltenes, carbenes, and carboids, as shown in Figure 2.4. These groups consist of molecules with common solubility or adsorption properties. Note that the classification is arbitrary since no real boundaries in physical properties exist among the fractions [AOSTRA, 1984; McFarland, 2007]. A brief description of the main characteristics of these groups follows:

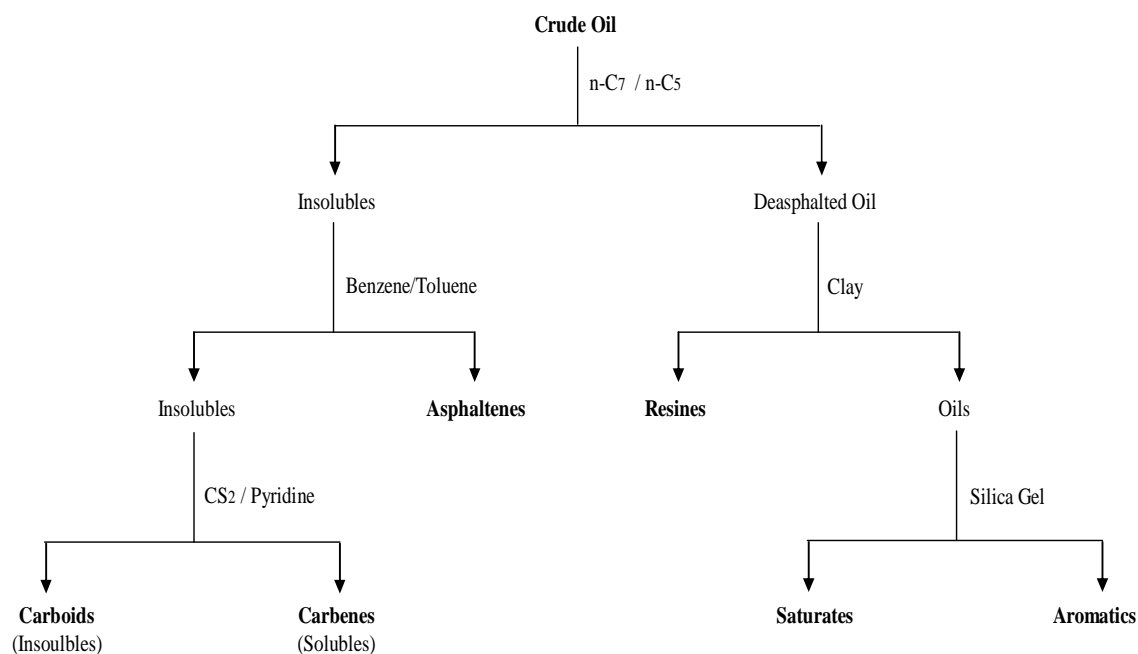


**Figure 2.4** Simplified representation of crude oil by solvent fractionation (Modified from Speight, 1999, Riazi, 2005).

Saturates: Saturates comprise, together with aromatics, the low and medium molecular weight fraction of heavy oil and bitumen. This fraction is soluble in low-boiling paraffins and ethers. The saturate fraction consists, mainly, on long non-polar carbon chains of linear, branched, and cyclic saturated hydrocarbons. The molecular weight of saturates ranges from 200 to 500 g/gmol approximately [Read and Whiteoak, 2003].

Aromatics: The aromatic fraction consists on aromatic ring aggregates with aliphatic substitutions. This fraction comprises the low and medium molecular weight hydrocarbons which are soluble in low-boiling paraffin and ethers. The molecular weight of oils ranges from 200 to 2000 g/gmol [Read and Whiteoak, 2003].

Resins: Resins are usually a dark viscous liquid, with molecular carbon to hydrogen ratio (C/H) of approximately 1.5. The majority of the carbon molecules are aromatic-bounded. The molecular weight values for resins are reported to range from 500 to 1200 g/gmol. These values do not seem to vary with the experimental conditions and therefore it is concluded that resins do not self-associate [Read and Whiteoak, 2003].

Asphaltenes: Asphaltenes are defined as material that is insoluble in non-polar solvents with surface tension lesser than 25 mN/m (such as n-pentane and n-heptane) and soluble in polar solvents with surface tension greater than 25 mN/m (such as benzene or toluene). Asphaltenes are classed according to the solvent that is used to separate the fraction; for example, n-C5 asphaltenes or n-C7 asphaltenes. The amount and composition of the asphaltene fraction vary depending on the type of solvent that is used.

Asphaltenes are black or brown highly viscous liquid that constitute the most polar fraction of the heavy oil. Their C/H ratio is approximately 1.15 and most of the carbon molecules are aromatic-bounded. The reported molecular weight of asphaltene is found to vary with the experimental conditions such as temperature and solvent polarity and concentration. This variation can be explained by self-associative behaviour of asphaltenes [Yarranton and Masliyah, 1996]. Molecular weight values ranging from 500 to 2000 g/mol have been reported for asphaltene monomers with an average value ranging from 800 to 1000 g/mol [AOSTRA, 1984].

Carbenes and Carboids: These fractions form a minor part of the heavy oil, representing highly associated and condensed products that are insoluble in most of the solvents used for petroleum assays. Their molecular weight and oxygen content are high. They may be oxidation products from asphaltenes [Read and Whiteoak, 2003].

The oil fractions that are soluble in low molecular weight hydrocarbons such as heptane and propane are termed maltenes. Hence, maltenes include saturates, aromatics, and resins. Conventional oil consists almost entirely of maltenes. Heavy oils and bitumen, on the other hand, consist of between 80 to 90% maltenes; the remaining fraction is primarily asphaltenes.

### Heavy Oil Phase Behaviour

The phase behaviour of heavy oil and bitumen is expected to be simple for the liquid-vapour region and somewhat complex for the liquid-solid region. This means that single liquid phases are expected on the Liquid-Vapour (LV) envelope whereas complex vitreous transitions may occur when the heavy oil solidifies [Shaw and Zou, 2007; Fulem et al, 2008].

The complexity of the phase behaviour increases when the heavy oil is mixed with solvents. For instance, when bitumen is mixed with supercritical fluids or solvents at conditions closed to or above its boiling point, phase behaviour such as Liquid-Liquid-Vapour (LLV) and asphaltene precipitation is expected [Speight, 1999]. Figure 2.5 shows saturation pressures of Athabasca bitumen with carbon dioxide and propane showing LV, LLV, and LL regions over narrow pressure range (relative to reservoir conditions) [Badamchi-zadeh et al., 2009; Castellanos-Diaz et al., 2011]. This type of phase behaviour is sensitive to the characterization of the medium and heavy fractions of the fluid. Hence, characterization of the non-distillable fraction of heavy oils plays a significant role when modeling processes involving heavy oil and solvents.

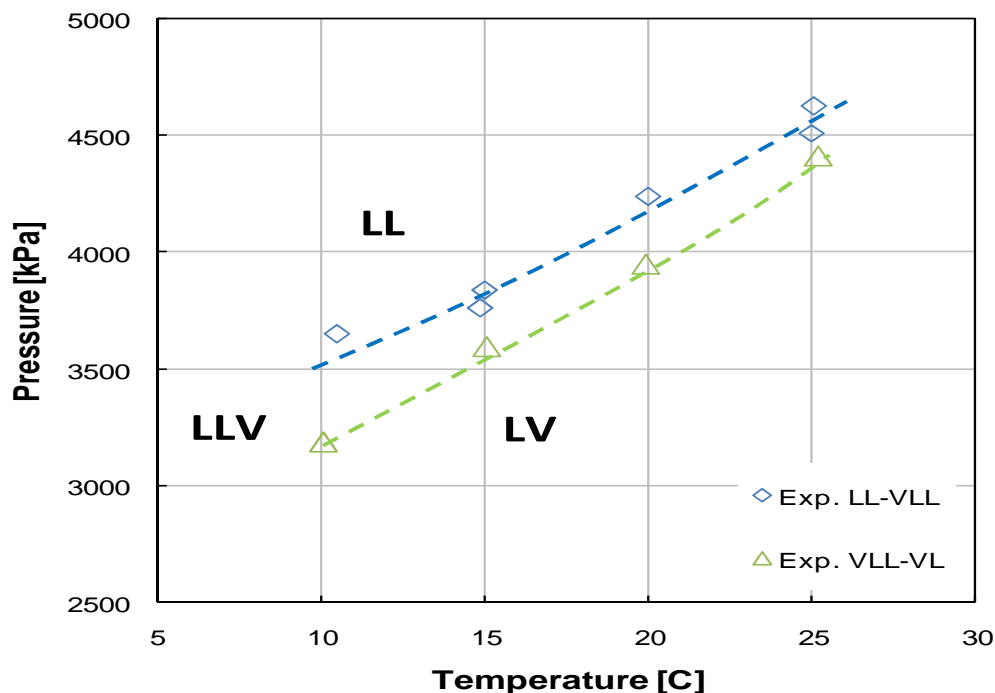


**Figure 2.5** Phase envelope of the system Athabasca bitumen – propane – carbon dioxide [Modified from Badamchi-zadeh et al., 2009]; lines are drawn to follow the trends and do not represent any specific model.

### 2.1.3 Oil Characterization Methods

The design, optimization, and operation of petroleum fluids processing require the characterization of the oil for modeling purposes. As mentioned before, an oil sample can be defined to some extent by its bulk properties; however, a more detailed knowledge of its composition is essential in order to predict physicochemical properties of the oil, such as calorimetric and phase equilibrium behaviour, in a reliable manner. However, the task of identifying every one of the millions of components that exist in a crude oil is impractical and virtually impossible.

Although considerable effort has been made to identify as many components as possible in an oil sample [Smith et al. 2008], the most common composition representation of crude oils is to lump certain components into pseudo-components that represent a narrow range of properties. Computational effort and laboratory techniques limitations restrict the actual number of pseudo-components. Typically, between five to twenty pseudo-components are considered sufficient to define a crude oil [Huang and Radosz, 1991; Whitson and Brulé, 2000; Riazi, 2005; Castellanos Diaz et al. 2011].

The choice of pseudo-components depends on the crude oil type, the characterization method, and the available equipment [Riazi, 2005]. Traditionally, pseudo-components are defined based on specific gravity, normal boiling point (TBP or GC assays), and average molecular weight [Gray et al, 1989]. Additional data such as PNA composition (Paraffins, Naphthenes, and Aromatics), SARA composition (Saturates, Aromatics, Resins, and Asphaltenes), density, viscosity, heat capacity, and/or vapour pressure are used to further define the fractions. For each pseudo-component, physical property correlations are used to predict the critical constants and thermodynamic properties (the former are especially important when modeling the oil with an equation of state). Mixing rules are used to obtain the full characterization of the fluid.

Distillation (TBP-curve, ASTM D-86, D-1160, etc), chromatography (ATSM D-2887, HPLC, HTGC-SIMDIST, SEC), and chemical class assays (PNA, SARA) are the most commonly used assays. Other methods are sometimes employed to supplement the characterization including: refractive index (RI), nuclear magnetic resonance (H-NMR,

C-NMR), infrared spectroscopy (IR, FTIR), etc. [Leelavanichkul, et al., 2004; Riazi, 2005; Merdrignac and Espinat, 2007]. However, distillation is the preferred choice in industry because of its practical and economical features and because it provides extensive information from a single assay. Figure 2.6 shows how the oil can be divided into pseudo-components of equal mass fraction of boiling point interval.

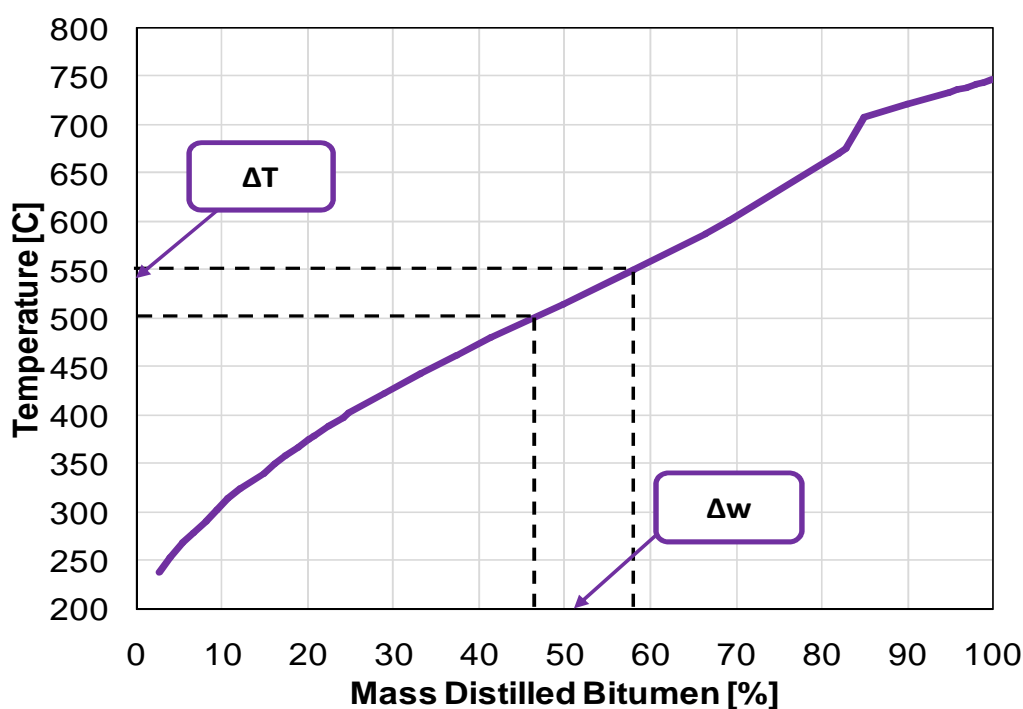


**Figure 2.6** Normal boiling point of a crude oil and compartmentalization based on equal mass fraction distilled.

Distillation methods are limited to temperatures below approximately 300 °C to avoid thermal cracking. Vacuum distillation (ASTM D-86, D-1160, D-2892, and D-5236) extends the atmospheric equivalent boiling points to approximately 838 K (565 °C). For conventional oils (light and medium oil – Figures 2.1 and 2.2), vacuum distillation

provides characterization of 80 to 95 wt% of the oil. However, only 20 to 30 wt% of heavy oil or bitumen is distillable with these methods, Figure 1.3. No standard methodology is yet available to extend a distillation assay to the remainder of a heavy oil [Batistella et al., 2005].

Due to this limitation, there is a need to extrapolate the distillation curve through the non-distillable fraction for characterization of heavy oils [Castellanos-Diaz et al, 2011]. One approach is to extrapolate based on molecular weight and/or boiling point. The molecular weight distribution and boiling point curves of conventional oils can be described using a Gaussian distribution [Huang and Radosz, 1991]. For heavy oils, the molecular distribution of maltenes can also be described using a normal (Gaussian) distribution. However, asphaltenes do not seem to follow the same property trends as the maltenes (Figure 2.3). The high molecular weight of these fractions does not arise from chemical bonding; rather, it seems to be a consequence of asphaltene self-association [Yarranton and Masliyah, 1996]. This property of the asphaltenes can be described by the Gamma probability distribution applied to its molecular weight as opposed to the Gaussian probability distribution of the maltene boiling points [Huang and Radosz, 1991; Castellanos-Diaz et al., 2011]. Figure 2.7 shows an example molecular weight distribution including both maltenes and asphaltenes. Figure 2.8 illustrates how the molecular weight distribution can be divided into pseudo-components of equal mole fraction or equal molecular weight interval.

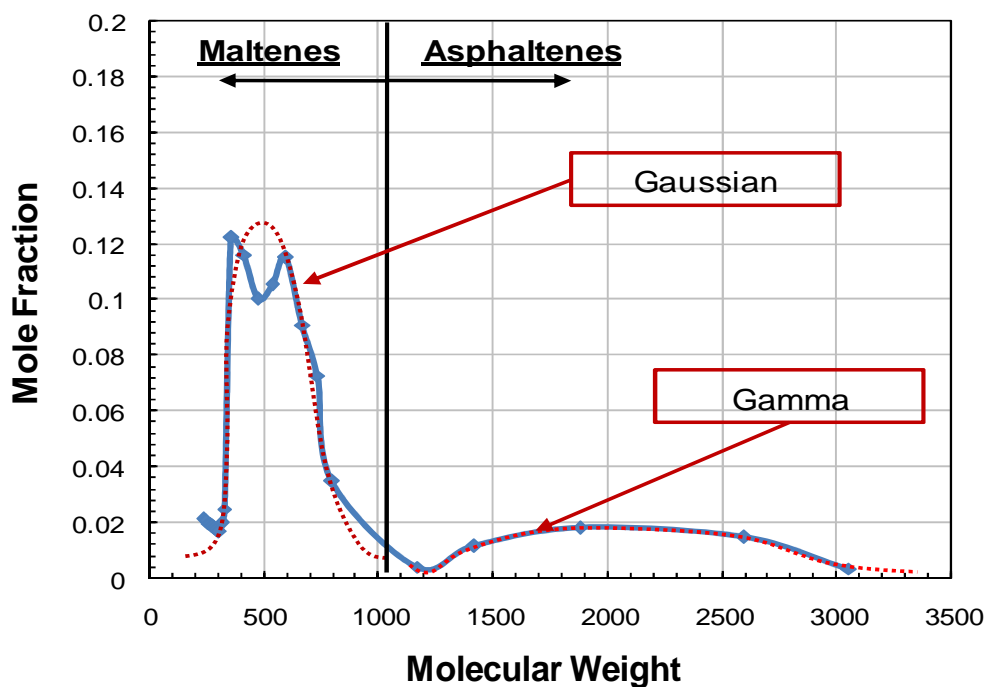


**Figure 2.7** Simulated molecular distribution of Athabasca bitumen using a Gaussian distribution on maltenes and a Gamma distribution on asphaltenes using VMGSim. Distortion on the distribution is due to the number of pseudo-components.

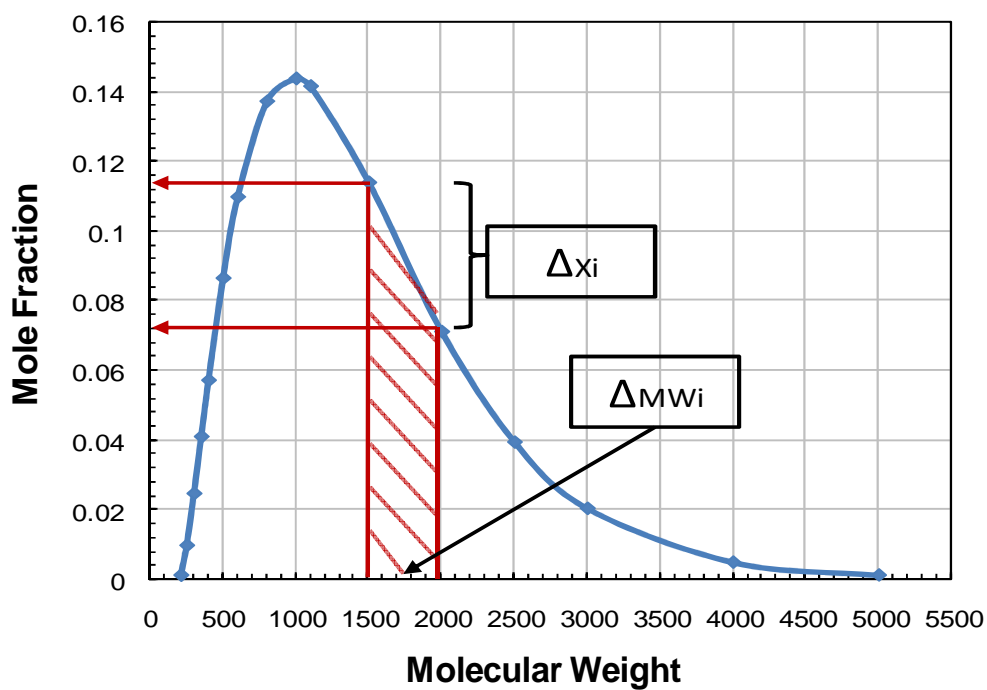


**Figure 2.8** Gamma molecular distribution and the determination of the  $i^{\text{th}}$  pseudo-component.

Although molecular weight provides a convenient method to distinguish between the maltenes and the asphaltenes, a number of challenges remain. The molecular weight distribution of the self-associated asphaltenes in the crude oil cannot be measured directly and must be estimated from indirect measurements such as fitting phase behaviour data to a model. Also, the correlations used for the physical properties were developed for lighter components and must be extrapolated for the non-distillable fraction. The reliability of the extrapolations is unknown *a priori*. Hence any technique applied to determine the heavy fraction's pseudo-components needs to be assessed using experimental data, such as vapour pressure, calorimetric data, or phase equilibria. Among these, vapour pressure is the most relevant property for distillation extrapolation.

## **2.2 Biodiesel Definition**

A biodiesel is the refined mixture of esters produced by the transesterification of fatty acids from vegetable oil and animal fat (fatty acid methyl esters or FAMES). Table 2.1 shows typical composition of biodiesels from different sources [Goodrum, 2002; Conceicao et al., 2007].

Extracted oil from vegetable and animal sources is composed of triglycerides, which are a combination of glycerol and fatty acids, as shown in Figure 2.9. The carbon radicals ( $R_i$ ) on the triglycerides corresponding to the fatty acids can be saturated (single bonding

between carbon molecules) or unsaturated (double bonding in some of the carbon molecules). Typically, one, two or three unsaturated carbon molecules are found in fatty acid radicals of vegetable and animal oils. The majority of these unsaturated molecules are found in radicals with 18 carbon molecules. Overall, the carbon number of fatty acids found in vegetable oils and animal fat ranges from C6 to C24 (Table 2.1 and 2.2). However, the majority of these oils are comprised of six fatty acids: myristic, palmitic, stearic, oleic, linoleic, and linolenic. [Allen et al., 1999; Goodrum, 2002; Ott and Bruno, 2008].

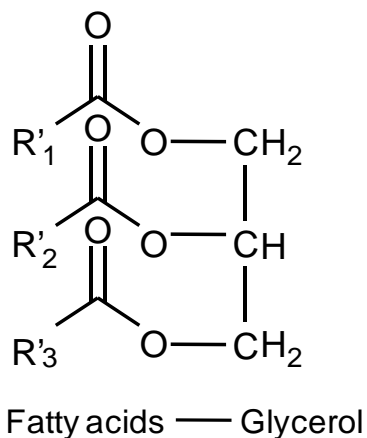


**Figure 2.9** A triglyceride: a combination of three fatty acids and a glycerol molecule.

**Table 2.1** Composition\* of selected biodiesel from a variety of sources (composition in mass fraction).

Source	6:0	8:0	10:0	12:0	14:0	15:0	16:0	16:1	17:0	18:0	18:1	18:2	18:3	20:0	20:1
Canola	-	-	-	-	-	-	8.6	0.8	0.3	4.5	60.7	16.0	7.5	0.5	1.1
Soy	-	-	-	-	-	-	10.6	-	-	3.3	23.1	55.3	7.4	0.3	-
Rapeseed	-	-	-	-	-	-	4.4	-	-	1.3	63.9	19.4	9.0	1.4	0.6
Palm	-	-	-	-	1.3	-	42.9	-	-	3.8	41.2	10.2	0.2	0.3	-

Coconut	0.6	9.1	6.6	47.4	18.4	-	8.3	-	-	2.1	6.0	1.5	-	-	-
Tallow	-	-	-	-	2.9	0.5	24.1	2.7	1.2	15.4	45.9	5.9	1.1	0.2	-

\* Nomenclature: C6:0 stands for an ester coming from the esterification of an acid with a carbon number equal to 6 and with a number of saturations equating to zero, Table 2.2

**Table 2.2** Selected physical properties of most common fatty acid methyl esters [NIST, 2010].

FAME	Formula*	NBP [K]	NFP [K]	MW	CN	C=C
M-hexanoate	C6:0	423	202.85	130	7	0
M-caprylate	C8:0	466.05	236.29	158	9	0
M-caprate	C10:0	502.1	257.66	186	11	0
M-laurate	C12:0	418.56	278.14	214	13	0
M-myristate	C14:0	423.46	291.72	242	15	0
M-pentadecanoate	C15:0	440.95	291.07	256	16	0
M-palmitate	C16:0	433.70	302.52	270	17	0
M-heptadecanoate	C17:0		302.64	284	18	0
M-stearate	C18:0	444.69	311.63	298	19	0
M-arachidate	C20:0	642.10	319.22	326	21	0
M-behenate	C22:0	666.10	326.21	354	23	0
M-lignocerate	C24:0	642.10	319.22	382	25	0
M-palmitoleate	C16:1		239.74	268	17	1
M-heptadecenoate	C17:1		246.55***	282	18	1
M-oleate	C18:1(11)	619.1	253.36	296	19	1
M-vaccenate	C18:1(9)				19	1
M-cis-11-eicosenoate	C20:1(11)		266.986***		21	1
M-erucate	C22:1	666.10	280.542***		23	1
M-linoleate	C18:2	619.10	233.92	294	19	2
M-linolenate	C18:3	620.10	229.29**	292	19	3

\*The formula for FAMES is related to the original fatty acid from which the ester is formed; for instance, C6:0 methyl hexanoate comes from hexanoic acid which have six carbon molecules

\*\* Obtained through linear extrapolated value using log MW vs. 1/T

\*\*\*Interpolated from vapour pressure model, Chapter 5

Transesterification of vegetable oil and animal fat is usually performed with methanol using potassium hydroxide as catalyst; this process is also known as methanolysis.

Methanol and potassium hydroxide react producing water and the radical methoxide; the latter attacks the triglyceride, dislocating the radicals and producing the ester mixture and the radical glycol oxide. Finally, water reacts with the oxide producing glycerol and regenerating the potassium hydroxide. The balanced reaction equation is shown in Figure 2.10

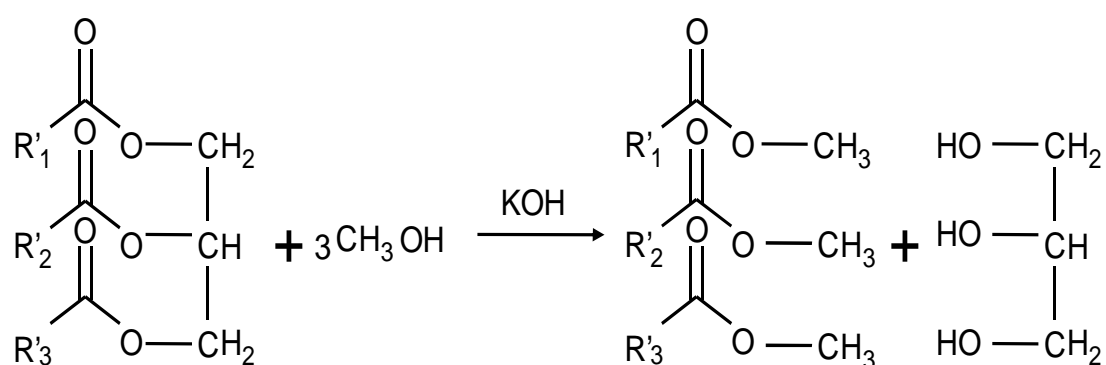


**Figure 2.10** Methanolysis reaction equation.

Biodiesels constitute one of the most promising alternatives for petroleum-based diesel fuel (petro-diesel). Furthermore, biodiesels can be used as lubricant additives, solvent, a substitute of chlorinated hydrocarbons for industrial cleaning, as detergents (biodiesel sulphonates), etc. [Starkey and Bruno, 2008; Narvaez et al., 2008]. For fuel usage, biodiesels can be used directly on an engine or can be blended with petro-diesel since they have similar calorific power [Conceicao et al., 2007].

As a blend, biodiesel adds lubricity to the petro-diesel, especially on low-sulphur fuels (characterized by low lubricity) without adding any sulphur source, hence, reducing the emission of particulate matter. Moreover, engine firing is improved since biodiesels are comprised by oxygenated molecules; it is a renewable, non-mutagenic, non-carcinogenic, biodegradable fuel that can be domestically produced (this is especially important when fuel sources need to be used in remote places where transportation of petro-diesel can increase fuel prices significantly) [Conceicao et al., 2007; Ott and Bruno, 2008].

Despite the multiple beneficial features of biodiesel as a fuel or as a fuel blend, there are some disadvantages that need to be assessed before implementing it. For instance,  $\text{NO}_x$  emissions may be increase due to injection properties of the biodiesel [Dzida et al., 2008], they have oxidative instability, have a tendency to absorb moisture during storage and have poor cold flow properties at winter conditions [Goodrum and Eitman, 1996; Ott and Bruno, 2008].

To account for these features and to use this valuable fuel in an optimal manner, biodiesels and biodiesels/petro-diesel blends physicochemical properties such as density, viscosity, and volatility, as well as the phase behaviour of these systems need to be assessed and modeled in a consistent manner with a strong experimental data background. However, the fact that biodiesels and petro-diesels are such chemically different substances makes this task difficult [Ott and Bruno, 2008].

Currently, experimental physical property data for fatty acids and fatty acids methyl esters and biodiesels are scarce and need further development.

## 2.3 Vapour Pressure Modeling

### 2.3.1 Vapour Pressure Of Pure Substances

When a liquid substance is in equilibrium with its vapour at a given temperature, the pressure exerted by the vapour is known as the vapour pressure of the substance. Vapour pressure data are used to generate thermodynamic property tables, develop isochoric equations of state, and design chemical processes. Reliable data are mandatory in order to fit and assess any proposed phase behaviour model.

The vapour pressure of a substance is a function of temperature, as stated by the Clapeyron equation [Wallas, 1985]

$$RT^2 \left( \frac{d}{dT} \ln P_v \right) = \frac{\Delta H_v}{\Delta Z}, \quad [2.1]$$

where  $P$  is the pressure,  $T$  is the absolute temperature,  $\Delta H_v$  is the enthalpy of vaporization, and  $\Delta Z$  is the difference between the compressibility factors of the coexisting phases. If the vapour phase is considered an ideal gas, Equation 2.1 simplifies to the Clausius-Clapeyron equation:

$$d \ln(P_v) = \frac{\Delta H_v}{R} d\left(\frac{1}{T}\right), \quad [2.2]$$

Integration of Equation 2.1 over the vapour-liquid equilibrium region of the substance (from the triple point to the critical point) provides the exact relationship of the vapour pressure with temperature. Expressions of the enthalpy of vaporization and the compressibility factor as a function of temperature must be available over the temperature range, which is usually not the case.

In general, a vapour pressure equation should be capable of reproducing experimental data and be able to extrapolate data beyond the temperature range of the method. It should be simple, smooth, provide reliable values of the enthalpy of vaporization, and account for considerations that stem from the thermodynamic consistency of the method [Waring, 1954; Wagner, 1973]. The first and the simplest attempt made to obtain a vapour pressure equation was to consider the ratio of  $\Delta H_v/\Delta Z$  as constant with respect to temperature, resulting in the Clapeyron equation for vapour pressure, Equation 2.3

$$\ln P_v = a_1 + \frac{a_2}{T}, \quad [2.3]$$

where  $a_i$  are adjustable constants for the vapour pressure equation. Equation 2.3 is reliable over a small temperature range in which the ratio  $\Delta H_v/\Delta Z$  remains constant [Wallas, 1985; Poling et al, 2001]. From this point on, many attempts have been made to obtain a more precise vapour pressure equation by adding adjustable parameters to

account for the non-constant behaviour of the  $\Delta H_V/\Delta Z$  ratio. One of the most common approaches is the Antoine equation, Equation 2.4

$$\ln P_V = a_1 + \frac{a_2}{a_3 + T}, \quad [2.4]$$

Note, even though the vapour pressure of a pure substance is a function only of the temperature, the distinct parameters of each equation,  $a_i$ , are often correlated with other physical properties. Hence, the equation may be applicable not only for a given substance but for a family of components. The correlative parameters utilized normally fall into two categories: 1) bulk properties of the substances such as molecular weight, specific gravity, carbon number; 2) critical properties.

Other correlations are available, usually derived from a statistical analysis of the data following the exponential trend given by the Clapeyron equation, Equation 2.1. These equations are likely to have additional parameters to better adjust the data for the specific substance at the specific temperature range [Jahangini et al. 1986]; however, they usually lack generality and the ability to be extrapolated [Wagner, 1973].

Wagner [1973] introduced an equation which is a product of a statistical algorithm applied to vapour pressure experimental data. Although his equation was originally developed for argon and nitrogen, it has been extensively used to model a wide variety of compounds and has become the most popular method for correlating vapour pressure

data. Wagner equations are shown in Equations 2.5 and 2.6; they are usually referred as Wagner 3-6 or Wagner 2.5-5, respectively:

$$\ln\left(\frac{P_V}{P_C}\right) = (a\tau + b\tau^{1.5} + c\tau^3 + d\tau^6)(1 - \tau)^{-1}, \quad [2.5]$$

$$\ln\left(\frac{P_V}{P_C}\right) = (a\tau + b\tau^{1.5} + c\tau^{2.5} + d\tau^5)(1 - \tau)^{-1}, \quad [2.6]$$

where  $\tau = (1-T_r)$ ,  $T_r = T/T_c$ , and  $T_c$  and  $P_c$  are the critical temperature and pressure of the substance, respectively. Another well known correlation is the Cox equation [Cox, 1923]:

$$\ln P_V = \ln P_{ref} + \left(1 - \frac{T_{ref}}{T}\right) \exp\left[\sum_i a_i T^i\right], \quad [2.7]$$

The Cox equation is independent of the critical properties of the substance, unlike the Wagner equation, and has proven to provide satisfactory performance on extrapolating vapour pressures towards the triple point [Růžička and Majer, 1996]. Usually, the equation is used with four parameters, three adjustable parameters plus the reference pressure,  $P_{ref}$ . A defined reference temperature,  $T_{ref}$ . For extrapolation purposes, the intention is that the reference state be close to the extrapolation target; that is, if extrapolating towards the triple point, it is recommended that the reference point be close to the triple point.

### 2.3.2 Vapour Pressure of Mixtures

In mixtures, the vapour pressure changes as a function of the composition. When the mixture is undergoing liquid-vapour phase transition at constant temperature and a fixed global composition, the vapour pressure changes as the liquid evaporates (Figure 2.11, process  $A_L$ -  $A_V$ ) or condenses (Figure 2.11, process  $B_V$ -  $B_L$ ); therefore, not a single point but a range of vapour pressure points exists.

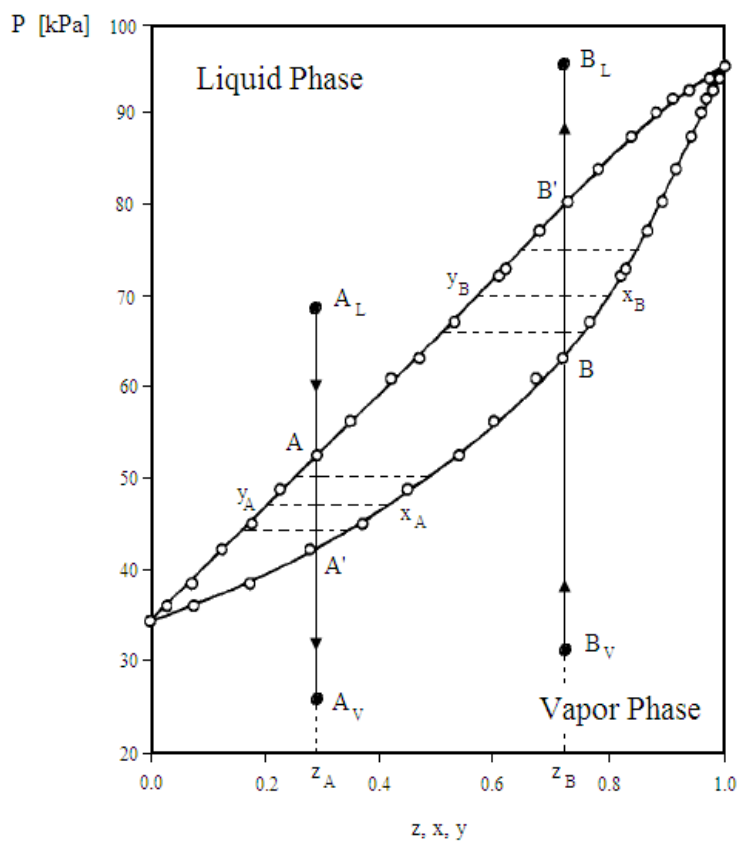


**Figure 2.11** Isothermal vapour-liquid equilibrium diagram of a binary mixture

Two of the points within the vapour pressure range are of special relevance: the bubble point and the dew point. The bubble point (Point A and B' in Figure 2.11) represents the

condition at which the first bubble of gas is formed in the liquid phase as it is evaporated. The dew point, on the other hand, represents the condition at which the first drop is formed when a given vapour is being condensed (Point B and A' in Figure 2.11).

In many process calculations, it is necessary to relate the pressure, temperature, and composition of a mixture at equilibrium. At thermodynamic equilibrium conditions in a closed system, the chemical potential of any component on a mixture is the same in all phases as well as the temperature of each phase (neglecting other forces, such as gravity, electromagnetism, or surface tension). This equilibrium condition is expressed by the equality of the fugacities of each component in each phase:

$$f_i^V = f_i^L, \quad [2.8]$$

The equality in Equation 2.8 can be written as [Wallas, 1985]:

$$y_i P = x_i P_i^{Sat} \frac{\phi_i^{Sat}}{\phi_i} \gamma_i PF_i, \quad [2.9]$$

where  $P_i^{Sat}$  is the saturation pressure,  $x_i$  and  $y_i$  are the mole fractions of the  $i$ -th component in the liquid and gas phase, respectively,  $\phi_i$  is the fugacity coefficient of the  $i^{\text{th}}$  component,  $\phi_i^{Sat}$  is the fugacity coefficient of the  $i^{\text{th}}$  component at saturation conditions,  $\gamma_i$  is the activity coefficient of the  $i^{\text{th}}$  component, and  $PF_i$  is the Poynting factor. For ideal mixtures, Equation 2.9 simplifies to Raoult's law:

$$y_i P = x_i P_i^{Sat}, \quad [2.10]$$

Equation 2.9 is the basis of vapour-liquid phase equilibrium calculations. Combined with a material balance the amount and composition of the vapour and liquid phases can be determined using the well known flash equations, such as the Rachford-Rice equation [Wallas, 1985; Smith et al., 1996]. Usually, flash calculations are coupled with phase stability tests based on the Gibbs free energy minimization approach [Michelsen, 1982a, b] to determine the number of stable phases under equilibrium.

As Equation 2.9 shows, vapour pressures are required for the flash calculation. The vapour pressure of each individual component can be calculated using an appropriate equation of state or a specific vapour pressure equation. Techniques, such as equations of state (EoS), group contribution methods (UNIQAC, NRTL, etc.), and regular solution theory, are used to calculate fugacity coefficients, activity coefficients, and the Poynting factor. Note that if an equation of state is used, there is no need to specify a method for calculating non-ideal parameters since they are taken into account in the EoS and are related through thermodynamic correlations.

In commercial simulation, vapour-liquid equilibrium is usually modeled using equations of state. In particular, cubic equations of state are commonly used and, if properly modified, they can be used to model polar as well as non-polar compounds. In this work, the Advanced Peng-Robinson equation of state (APR EoS), by Virtual Materials Group is

used [VMG, 2010], which includes a volume translation correction to better describe liquid densities.

### 2.3.3 Extrapolation of Vapour Pressure

For heavy components, it is a challenge to obtain reliable vapour pressure data because they have high molecular weight and their vapour pressure can be lower than  $10^{-4}$  kPa at low to moderate temperatures. At these pressure values, the uncertainty of direct pressure readings increases since the adsorption-desorption processes and metal perspiration become significant with respect to the pressure reading [Roth, 1990]. To overcome this issue, indirect measurements are performed (Section 2.3). However, these techniques may generate new sources of error when the data are transformed from the indirect measurement to vapour pressure.

An alternative is to extrapolate reliable vapour pressure data points measured above  $10^{-4}$  kPa. In this case, it is recommended for the vapour pressure equation or the equation of state to be correlated using calorimetric data as a constraint, as shown in Equation 2.11 [Růžička and Majer, 1996].

$$\min j$$

$$j = \sum_i \frac{(\ln P_i^{\text{exp}} - \ln P_i^{\text{calc}})^2}{\sigma_{\ln P_v}^2} + K_H \sum_i \frac{(\Delta H_i^{\text{exp}} - \Delta H_i^{\text{calc}})^2}{\sigma_{\Delta H}^2} + K_C \sum_i \frac{(\Delta C_i^{\text{exp}} - \Delta C_i^{\text{calc}})^2}{\sigma_{\Delta C}^2}, \quad [2.11]$$

where,  $i$  is the data point counter,  $\Delta H$  is the enthalpy difference between the gas and the liquid phase,  $\Delta C_p$  is the heat capacity difference between the gas and the liquid phase,  $\sigma$  is the variance of each physical property measurement, and  $K$  is a weight factor which adjust the magnitude of the different experimental data relative to the unit used.

For the method to be useful for extrapolation towards lower temperatures, calorimetric data must be available at temperatures at which vapour pressure of the substance is expected to have high uncertainty (lower than  $10^{-4}$  kPa). Usually, enthalpy of vaporization is not taken into account as a constraint in Equation 2.11 because these data are scarce and are usually not as reliable as heat capacity experimental data [Růžička and Majer, 1996]. The optimization function is then reduced to::

$$\min j = \sum_i \frac{(\ln P_i^{\text{exp}} - \ln P_i^{\text{calc}})^2}{\sigma_{\ln P_v}^2} + K_C \sum_i \frac{(\Delta C_i^{\text{exp}} - \Delta C_i^{\text{calc}})^2}{\sigma_{\Delta C}^2}, \quad [2.12]$$

The vapour pressure is calculated using either an equation of state or a vapour pressure equation. The heat capacity is calculated using the Clapeyron equation (Equation 2.1) and the definition of heat capacity, Equation 2.13

$$dH = C_p dT, \quad [2.13]$$

which leads to

$$\Delta C_i = R \left[ \frac{d}{dT} T^2 \left( \frac{d \ln P_v}{dT} \right) \right], \quad [2.14]$$

Equations 2.12 through 2.14 have been applied extensively [Roháč et al., 1999, 2000; Mokbel et al., 2000; Fulem et al., 2004].

#### ***2.3.4 Vapour Pressure of Biodiesels***

The vapour pressure of biodiesels can be predicted as a molar average of the vapour pressure of its components at high temperatures using Raoult's law, Equation 2.10. Yuan et al. [2002] modeled the vapor pressure of three different biodiesels at temperatures above 250 °C, matching experimental data to within 1% [Allen et al., 1999; Goodrum, 2002].

However, at conditions near the triple point, deviation from the ideal behaviour expressed in Raoult's law may occur probably because the liquid phase becomes less ideal when the molecular interactions forces increase as the molecules become more closely packed near the triple point. One way to account for the non-ideal behaviour in the liquid phase is through the activity coefficient of the individual components, as expressed in Equation 2.9. Contribution methods, such as UNIFAC, have been used to model the activity coefficient of vegetable oil systems [Ceriani and Meirelles, 2004]. However, an equation of state approach is more convenient for commercial simulators.

There is an increasing data base of vapour pressure of biodiesels and of esters from fatty acids in the open literature; however, most of this data is only available at high temperatures. There are fewer caloric data for biodiesel and the correspondent esters;

hence, there is a need for more reliable data, in order to create precise models of biodiesel fuels.

### ***2.3.5 Vapour Pressure of Heavy Oil***

Heavy oils are expected to exhibit liquid-vapour two-phase equilibrium over a wide range of conditions [Shaw and Zou, 2007]. The vapour pressure is expected to be very low, due to the molecular weight of heavy oil fractions; hence, an ideal gas phase can be assumed.

In an ideal vapour phase, Equation 2.10 can be written as Equation 2.15

$$P = \sum_i x_i \gamma_i P_i^{sat}, \quad [2.15]$$

Normally, Equation 2.15 forms part of the flash vaporization algorithm used to calculate vapour pressures of the crude oil [Pedersen et al., 1989; Neau et al., 1993; Daiwei et al., 2006]. Equation 2.15 will be used to examine the main considerations that are taken into account when modeling vapour pressure behaviour in heavy oils. Three major items of importance are: the discretization of the mixture, the liquid phase non-ideal behaviour, and the saturation pressure.

Discretization is required for heavy oils because they have a wide boiling point range; using a single pseudo-component to predict the vapour pressure of a heavy oil may lead to incorrect predictions of phase behaviour. Therefore, a heavy oil must be treated as a mixture of several components or pseudo-components. Generally, five pseudo-

components are considered for heavy oil fraction but the number and the method used to fractionate the oil are not fixed [Whitson-Brule, 2000].

Activity coefficients are also considered in the model due to strong deviations from ideal behaviour in the liquid phase as a consequence of the large number and diversity of components in the heavy oil. The self associative behaviour of asphaltenes as well as asphaltene precipitation, molecule asymmetry and polarity should be considered when using any particular activity coefficient model [Akbarzadeh et al, 2004; McFarland, 2007]. Note, the use of an EoS implies an inherent calculation on the activity coefficient and no activity coefficient method apart from the EoS should be used.

Vapour pressure equations or equations of state (EoS) are used to calculate the vapour pressure of each pseudo-component. The Maxwell-Bonnel correlation is one of the most commonly used vapour pressure equations for conventional oils, especially in the low pressure region [Maxwell and Bonnell, 1957; Gray et al. 1985]. However, it is based on conventional oil data and uses the Watson K-factor as a characteristic of the oil, which, in the case of heavy oils, may not be appropriate. Other methods that are more applicable to heavy oils are the property correlations of Lee-Kesler [1975], and Twu [1984, Twu et al., 1994], and the vapour pressure equation of Ambrose-Walton [1989].

The Peng-Robinson equation of state is the most successful EoS in predicting hydrocarbon-based PVT behaviour including vapour pressure. EoS methods use critical

properties as their parameters; therefore, internally consistent correlations for critical constants of the pseudo-components must be available.

Experimental vapour pressure data of heavy oil and heavy petroleum fractions are needed to tune the models and improve the correlations; however, data are scarce in the open literature. Furthermore, most of the available data are measured at temperatures near the cracking point of the oil [Schwartz et al., 1987; Rodgers et al., 1987]. In order to characterize heavy oil fractions, reliable vapour pressure data are needed at temperatures below 200 °C.

## **2.4 Measurement Methods for Vapour Pressure**

Weir and de Loos [2005] group the numerous existing vapour pressure measurement methods into five categories: static, dynamic, effusion, transpiration, and calorimetric. A brief description of each method is provided below.

### ***2.4.1 Static Methods***

In static methods, the sample is placed in a closed vessel at constant temperature and the pressure is then measured. The static apparatus measures the pressure exerted by the substance directly, providing an advantage over the other techniques in repeatability, and temperature stability. Indirect measurements of vapour pressure have more sources for

error that propagate. This later technique is chosen as the methodology for the high vacuum vapour pressure measurement system (HV-VPMS) used in this thesis.

One of the main disadvantages of direct vapour pressure measurements is the adsorption-desorption process of the vapour molecules with the wall of the apparatus. This phenomenon occurs at any working condition; however, at pressures below approximately  $10^{-4}$  kPa, the adsorption-desorption rates can be significant with respect to the pressure readout, limiting the certainty of the data [Fulem et al., 2003; Monte et al., 2006]. The difficulty of modeling this kind of phenomenon means that it cannot be accounted for to correct the pressure reading; hence, there is an indeterminate error at pressure readings below  $10^{-4}$  kPa.

Other disadvantages of static pressure measurement are the sensitivity of the technique to impurities and dissolved gases in the sample, leak rates, and thermal transpiration (Section 2.4.3). These disadvantages can be mitigated in the construction and design of the apparatus, as well as purification and degassing procedures over the sample.

#### ***2.4.2 Dynamic Methods***

Dynamic methods are characterized by the movement of the sample in the equipment. The most common method is known as ebulliometry and is analogous to the distillation process with a small reflux. The idea is to measure the boiling point of the sample while varying the pressure of the apparatus. The main advantage is that impurities can be detected and accounted for. The disadvantages of this method are the relatively large

amounts of the sample required and the need for substances that can boil at the apparatus working conditions.

### ***2.4.3 Effusion Methods***

Effusion methods determine the vapour pressure of a sample by measuring weight loss through a small orifice, open to a vacuum chamber, by means of diffusion or free evaporation (Knudsen effusion, or Langmuir effusion, respectively). Several modifications of this basic principle are presented in the open literature. They differ somewhat in the measurement principle and in different adaptations to overcome the weaknesses of the original method. The main disadvantage of these techniques is the time that is required for an experiment to be performed.

### ***2.4.4 Transpiration Methods***

The transpiration method involves the measurement of a substance carried about by an inert gas that passes above the sample at a given rate that assures both vapour movement and equilibrium. Chromatographic techniques fall into this category. The uncertainty of the method is determined mainly by the uncertainty of the measurement of the sample quantity. These types of techniques have the advantage that require less time than other techniques and can be applied over a wide variety of conditions. However, incorrect zeroing of the apparatus can easily introduce errors and must be taken into account carefully.

#### ***2.4.5 Calorimetric Methods***

These methods measure the enthalpy of vaporization of the sample and relate it to the vapour pressure by means of the Clapeyron equation (Equation 2.1). The uncertainty of the method depends on the uncertainty of the measurement of the amount of heat required to evaporate the sample and of the amount of sample evaporated.

Two approaches to determine the enthalpy of vaporization can be employed. The first one is a direct measurement of the amount of heat added and the amount of the sample evaporated. The second is indirect and uses the phase behaviour of the sample in coexistence with another well-known substance. The enthalpy of vaporization of the mixture is calculated from the vapour pressure data of the mixture. Given the well known enthalpy of vaporization of the reference substance, the enthalpy of vaporization of the unknown substance is calculated. Note that the enthalpy of solution of the mixture must be also taken into account.

### **2.5 Vacuum Physics**

Systems under high vacuum go through a phenomenon called thermal transpiration that is not seen at normal conditions or even at low to medium vacuum conditions. Thermal transpiration directly affects the uncertainty of the vapour pressure measurements. The topic is reviewed briefly below and the reader is referred to a discussion of vacuum physics by Redhead et al. [1968] for further information.

### 2.5.1 Rarefied Gas Theory

A gas at sub atmospheric conditions (pressures below 100 kPa) is said to be rarefied and can be fairly well described by the ideal gas law:

$$P = \frac{\rho RT}{M}, \quad [2.16]$$

The molecular density and flow of a rarefied gas can be modeled by the ideal gas law and the kinetic theory of gases using the Maxwell-Boltzmann velocity profiles, respectively. The latter is used when calculating the molecular incidence rate,  $\Phi_M$ , that is, the number of molecules striking an element of a surface perpendicular to its direction, Equation 2.17

$$\Phi_M = \frac{\rho_M}{2\sqrt{\pi}} \left[ \frac{2kT}{m_M} \right]^{1/2}, \quad [2.17]$$

where  $\rho_M$  is the molecular density,  $k$  is the Boltzmann constant, and  $m_M$  is the mass per molecule. Another important aspect is the average mean free path of the molecule,  $\lambda$ , defined as the average of the distances traveled by a molecule between successive collisions with another molecule over a certain period of time [Roth, 1990], Equation 2.18

$$\lambda = \frac{1}{\sqrt{2}\pi d_M^2 \rho_M}, \quad [2.18]$$

where  $d_M$  is the average diameter of a molecule. This parameter will determine the characteristic regime in which the gas is flowing.

### ***2.5.2 Gas Flow Rate at Low Pressures***

There are three regimes for rarefied gas flow: viscous flow, molecular flow, and intermediate or Knudsen flow (Figure 2.12). These three types of flow may be distinguished by the molecular density of the gas, the mean free path of the molecules, and the geometry of the system, which can be accounted for by the Knudsen number,  $K_n$  (Equation 2.19) [Green, 1968].

$$K_n = \frac{\lambda}{d_{eq}}, \quad [2.19]$$

Knudsen number values smaller than 1 are representative of the viscous flow regime. As the mean free path increases in the same system the Knudsen number approaches unity, which corresponds to the transition between the viscous and the intermediate regime (Figure 2.13); Knudsen values greater than unity are representative of the molecular regime [Hablanian. 1997; Šetina, 1999].

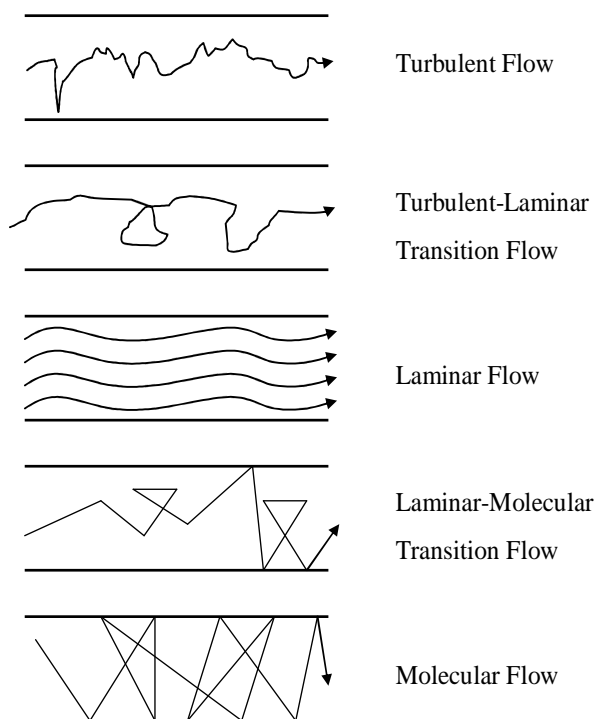


**Figure 2.12** Molecular trajectories in various flow types (Modified from Hablanian, 1997).

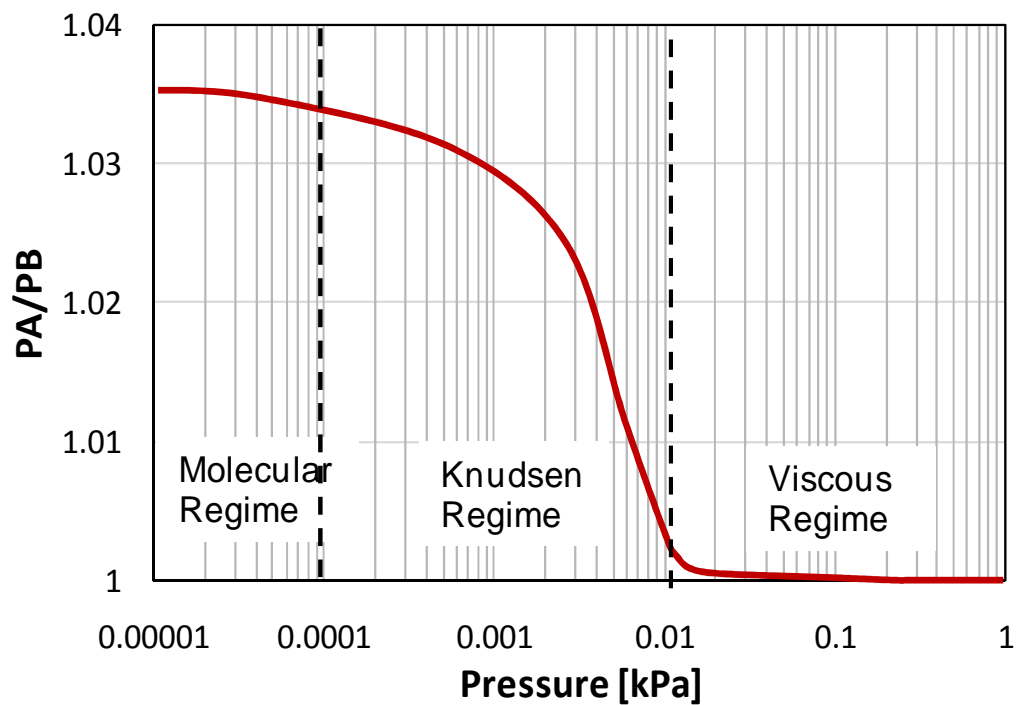


**Figure 2.13** Pressure reading as a function of flow regime (modified from Setina, 1999).

### 2.5.2.1 Viscous Regime

Viscous flow is the type of flow encountered in conventional (i.e. at atmospheric pressure) and low vacuum systems and may exist even at high vacuum conditions depending on the configuration of the system. It is characterized by a bulk movement of the gas and it is principally governed by viscous forces. The Reynolds number,  $Re$ , (Equation 2.20) is used to describe the viscous flow main characteristics.

$$Re = \frac{\rho v d_{eq}}{\mu}, \quad [2.20]$$

where  $v$  is the mean velocity of the fluid through the hydraulic equivalent diameter,  $d_{eq}$  is the equivalent hydraulic diameter, and  $\mu$  is the viscosity of the fluid. High Reynolds numbers occur in turbulent flow where stream lines are rather eddy like. As the Reynolds number decreases the stream lines become straighter until laminar flow is reached. A transition flow is achieved at Reynolds numbers from 3000 to 2000 in isolated systems.

### 2.5.2.2 Molecular Regime

At the conditions encountered in the viscous flow regime, the gas molecular density is relatively high, resulting in bulk gas movement. When the pressure is lowered and the gas becomes more and more rarefied, the gas molecular density decreases and so does the probability of the molecules striking one another before striking the walls of the container. The bulk gas movement diminishes and the gas molecules behave almost independently of each other.

As can be seen in Equation 2.18, as the molecular density decreases the free path increases and can achieve values orders of magnitude greater than the system itself. In that case, gas flow is controlled by the interaction of the gas molecules with the walls of the system and by its thermal velocity. The gas is said to be in the molecular regime [Holland et al., 1974; Roth, 1990]. The concept of pressure under these conditions is difficult to define since the molecules strike the surface randomly in too few numbers for the statistical averaging observed in bulk gas behaviour to occur, Figure 2.12.

#### 2.5.2.3 Knudsen or Intermediate Flow

Knudsen or intermediate flow is the transition flow occurring between molecular and viscous flow. It is analogous to the transition flow occurring between laminar and turbulent flow in the sense that it represents a change in flow stream line behaviour. The analogous Reynolds number is the Knudsen number.

#### ***2.5.3 Thermal Transpiration***

Thermal transpiration is a phenomenon in which, at equilibrium conditions, a pressure gradient is observed between two points that are at different temperatures. This effect occurs at Knudsen numbers greater than one; that is, at intermediate and molecular flow regimes.

In order to interpret the phenomenon, consider two chambers, A and B, connected at different temperatures,  $T_A$  and  $T_B$  (Figure 2.14) at viscous flow and non-equilibrium

conditions. Due to the thermal gradient ( $T_A - T_B$ ), a movement of molecules will occur from A to B, until equilibrium conditions are met. The steady state condition demands that there be no molecular density gradient in the system, which leads to the equality  $P_A = P_B$  [Holland et al., 1974; Roth, 1990].

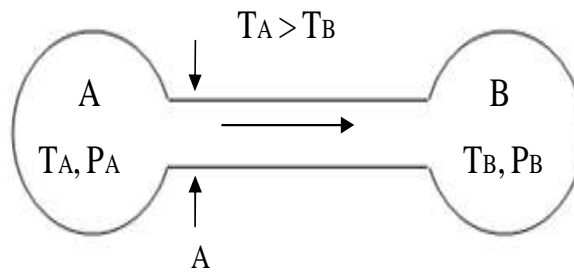


**Figure 2.14** Chamber representation for thermal transpiration phenomenon.

However, when the conditions are such that the gas flow is in the molecular regime, the same steady state condition (equality of molecular density) leads to [Wu, 1968; Holland et al, 1974; Roth, 1990]:

$$\frac{P_A}{P_B} = \sqrt{\frac{T_A}{T_B}} = R_K, \quad [2.21]$$

where  $R_K$  is the Knudsen's value sometimes referred as the “invariant K”. Equation 2.21 is derived from the definition of molecular flow,  $q_M = \Phi A$ , and the ideal gas law. Wu [1968] claimed that  $R_K$  is not invariant when thermal transpiration occurs in anisotropic situations and proposed a modified “invariant K” which accounts for isotropy.

Experimentally, it has been found that the limiting value,  $R_K$ , is slightly different than the square root of the temperature ratio [Šetina, 1999]. This difference is often explained by other phenomena occurring in a typical vacuum system such as gas-surface adsorption-desorption [Siu, 1973]. When the gas is in the Knudsen regime, the pressure ratio of the two chambers lies in between unity and the Knudsen's value (Figure 2.13).

Several correlations have been proposed for predicting the thermal transpiration effect in the transition regime. Note that the pressure ratio is independent of the type of gas in the molecular and viscous regimes. In the transition regime, however, the pressure ratio depends on the mean free path of the gas molecules; therefore, it depends on the type of gas. This fact has been confirmed experimentally [Šetina, 1999].

Thermal transpiration affects pressure measurement as long as there is a difference in temperature between the sample chamber and the pressure transducer; the system must also be on intermediate or molecular regime, which, in turn, depends on the system hydraulic equivalent diameter (configuration and dimensions of the system) and the average pressure (related to the mean free path).

This phenomenon can be mitigated by maintaining the whole measurement system at a constant temperature. However, this is difficult to achieve and the usual practice in vapour pressure measurement is to keep the measurement devices warmer than the sample chamber to avoid condensation in the connecting lines [Fulem et al., 2003].

Hence, thermal transpiration is usually an issue and must be considered as an anomaly of pressure measurement system under high vacuum conditions.

## **2.6 Summary**

The main idea of this chapter was to introduce three main topics that are of primary importance when constructing the new high vacuum apparatus. First, the introduction to heavy oil characterization demonstrated the need for vapour pressure data at high vacuums and showed how the data would be used for phase behaviour modeling. Second, the vapour pressure modelling section provided the means to analyse vapour pressure data obtained from the apparatus. Third, the vacuum physics section examined the experimental and data interpretation issues that can be encountered at high vacuum conditions. These topics are essential in order to develop a robust and reliable apparatus and a comprehensive method to model and predict the data.

## CHAPTER THREE: EXPERIMENTAL METHOD

A major component of the thesis work was to design and construct a high vacuum vapour pressure measurement system (HV-VPMS). The purpose of the HV-VPMS is: 1) to measure vapour pressure of mixtures and pure components at high vacuum conditions; 2) to fractionate homogeneous mixtures by using deep vacuum single flash vaporization at different temperatures. This chapter presents the main features that were taken into account when designing and building the HV-VPMS, including calibration, equipment testing, and vapour pressure measurement. A brief description of liquid heat capacity measurement using a differential scanning calorimeter is also provided.

### 3.1 Experimental Materials

Naphthalene ( $C_{10}H_8$ , CAS No: 91-20-3), n-hexadecane ( $C_{16}H_{34}$ , CAS No: 544-76-3), and n-eicosane ( $C_{20}H_{42}$ , CAS No: 112-95-8) were selected to test the repeatability and reproducibility of the apparatus. Naphthalene has well established vapour pressure and calorimetric data and is recommended as a reference compound for vapour pressure measurements below 1 kPa [Sinke, 1974; Růžička et al. 2005]. Hexadecane and eicosane are petroleum-related hydrocarbons with molecular weight of 224 and 282 g/mol which are values that match the range of the lightest fraction of bitumen and heavy oil; hence,

they are expected to exhibit similar vapour pressures. Pure component samples were purchased from Aldrich Chem., with purity greater than 99.7%; no further purification procedures *a priori* were made. Selected physicochemical properties are listed Table 3.1 Vapour pressure literature data for these substances are analyzed in Section 3.5.

**Table 3.1** Selected physical properties of naphthalene, n-hexadecane, and n-eicosane.

<b>Property</b>	<b>Naphthalene</b>	<b>Hexadecane</b>	<b>Eicosane</b>
Melting point	80.3 °C (353 K)	18 °C (291 K)	37 °C (310 K)
Boiling point	218 °C (491 K)	287 °C (560 K)	343 °C (616 K)
Specific gravity @ 25 °C	1.14	0.773	0.789
Flash point	79-87 °C	135 °C	>113 °C
Auto ignition point	525 °C	201 °C	-

In addition, biodiesel samples were tested to assess the performance of the apparatus in measuring the vapour pressure of heavy complex but well defined mixtures (molecular weight higher than 200 g/mol). Biodiesel samples from seven different sources were analyzed. The samples were provided by Shell Canada, the National Institute of Standards and Technology (NIST), and the Alberta Research Council (ARC). Selected properties are shown in Table 3.2

**Table 3.2** Selected physical properties of biodiesel samples.

<b>Biodiesel Source</b>	<b>Average Molecular Weight (g/mol)</b>	<b>Color</b>	<b>Appearance @ 18 °C</b>
-------------------------	---	--------------	---------------------------

Canola (South Alberta)	293.17	Amber	Liquid
Canola (Saskatchewan)	291.53	Dark Amber	Liquid
Soy (Sunrise, US)	291.77	Leach White	Liquid
Soy (Mountain Gold, US)	291.27	Dark Amber	Liquid
Rapeseed (Europe)	294.56	Amber	Liquid
Palm (Europe)	283.69	Leach transparent	Below cloud point
Coconut (Europe)	218.16	Leach White	Liquid

Finally, a bitumen sample from Western Canada provided by Shell Canada (WC\_B1) was obtained for vapour pressure and deep vacuum fractionation experiments. Physical characteristics of this bitumen sample are presented in Table 3.3

**Table 3.3** Selected physical properties of bitumen sample from the Western Canadian Bitumen (WC\_B1).

Property	Value
Average Molecular Weight	510 g/mol
Average Specific Gravity	1.007
Initial Boiling Point	213 C
Asphaltene Content	17 wt%

### 3.2 Apparatus Design

The HV-VPMS is a static apparatus (Section 2.4). The operating principle of the apparatus is very simple as illustrated in Figure 3.1. A sample is opened to a fixed

volume initially at vacuum and allowed to equilibrate at constant temperature. The pressure is the vapour pressure of the sample at the given temperature. The temperature can be changed to obtain another vapour pressure. Alternatively, the vapour phase can be withdrawn to fractionate the original sample and then the vapour pressure of the residue can be measured. While the principle is straightforward, it is a challenge to construct and operate such an apparatus at the vacuum conditions required for this study. Similar kinds of apparatus have been designed and tested with excellent results for pure components [Fulem et al., 2003; Monte et al., 2006]. No record was found in the open literature for this kind of apparatuses being used for the measurement of vapour pressure or fractionation of complex, heavy mixtures.

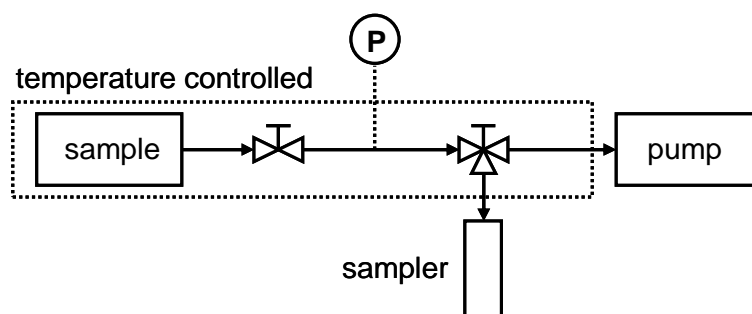


**Figure 3.15** Schematic of a static vapour pressure apparatus.

Figure 3.2 shows a photograph of the HV-VPMS. The system consists of two components: a degassing or sample preparation apparatus (DA) and a vapour pressure measurement apparatus (VPMA). The DA is used to remove dissolved gases and light solvents from the sample; the VPMA is used to measure vapour pressure of sample fractionation. The use of the DA prior to the VPMA ensures that the sample is clean

before it is evaluated, which in turn keeps the VPMA clean. The separation of the degassing and measurement into two apparatuses also accelerates the procedure (measuring one sample's vapour pressure whilst degassing the next sample). A detailed description of the system is provided in Appendix B.



**Figure 3.16** High Vacuum Vapour Pressure Measurement system (HV-VPMS); Vapour Pressure Measurement Apparatus VPMA (above) and Degassing Apparatus DA (below).

### *3.2.1 Apparatus Design Criteria*

The main working variables to be considered in the design are temperature, pressure, and sample size. Although a wide variety of substances can be used in the HV-VPMS,

particular emphasis was placed on heavy oil and bitumen. The following sections describe how the different criteria were taken into account.

### Temperature

In general, the working temperature range of the system is defined by the thermal stability of the substances to be analyzed and by mechanical limitations of the different parts of the apparatus.

From the thermal stability point of view, hydrocarbons and, specifically, heavy oil and bitumen, provide an upper temperature limit, given by the cracking point temperature (approximately 300°C). Above this temperature the analyzed substance is chemically transformed and the measured vapour pressure is no longer valid. From the mechanical point of view, the heating/cooling elements, seals, and electronic devices all have temperature constraints. The relevant temperature ranges of the HV-VPMS are summarized in Table 3.4.

**Table 3.4** Temperature operational range for the HV-VPMS.

<b>System</b>	<b>T-Range</b>	<b>Comment</b>
<u>VPMA</u>		
Lower limit	20 – 25 °C	Ambient temperature, depending on local conditions. No cooling devices in the system
Upper limit operational	200 °C (60 °C)	Maximum value for diaphragm gauge. If the cold cathode gauge is used, the maximum temperature is 60 °C
Upper limit bake out	400 – 600 °C	650 °C is maximum temperature allowed for heat tapes; 400 °C recommended – there must be no electronic devices in place

---

<u>DA</u>		
Lower limit	20 – 25 °C	Ambient temperature, depending on local conditions. No cooling devices in the system
Upper limit operational	150 °C (60 °C)	Maximum value for diaphragm gauge. If the cold cathode gauge is used, the maximum temperature is 60 °C
Upper limit bake out	200 °C	200 °C limit recommended before Viton o-ring seals start deforming – electronic devices must be shut down

---

### Pressure

The pressure range of the system is determined, at its lower limit, by the expected vapour pressure of the heaviest substance to be evaluated at the working temperature; in this case, heavy oil and bitumen. The type of pumping equipment and pressure measurement devices are specified by this range. The upper limit of the apparatus is set to be atmospheric pressure, since no over-pressure system is considered.

The expected vapour pressure of heavy oil and bitumen is calculated from experimental data. However, vapour pressure data for heavy petroleum mixtures are scarce and unreliable. Furthermore, the majority of the data found in the literature are at temperatures near the cracking point. Therefore extrapolation or modeling of the data was required to estimate the design conditions; that is, the vapour pressure of heavy oil at low temperatures (around 50 °C).

In this case, Athabasca residue vapour pressure data [Schwarz et al., 1987] was fitted and extrapolated using the Cox equation (Section 2.2), Figure 3.3. Experimental data for

hexadecane are also provided as a reference, since its molecular weight (and vapour pressure) is similar to the lightest molecule in heavy oils and bitumen samples.

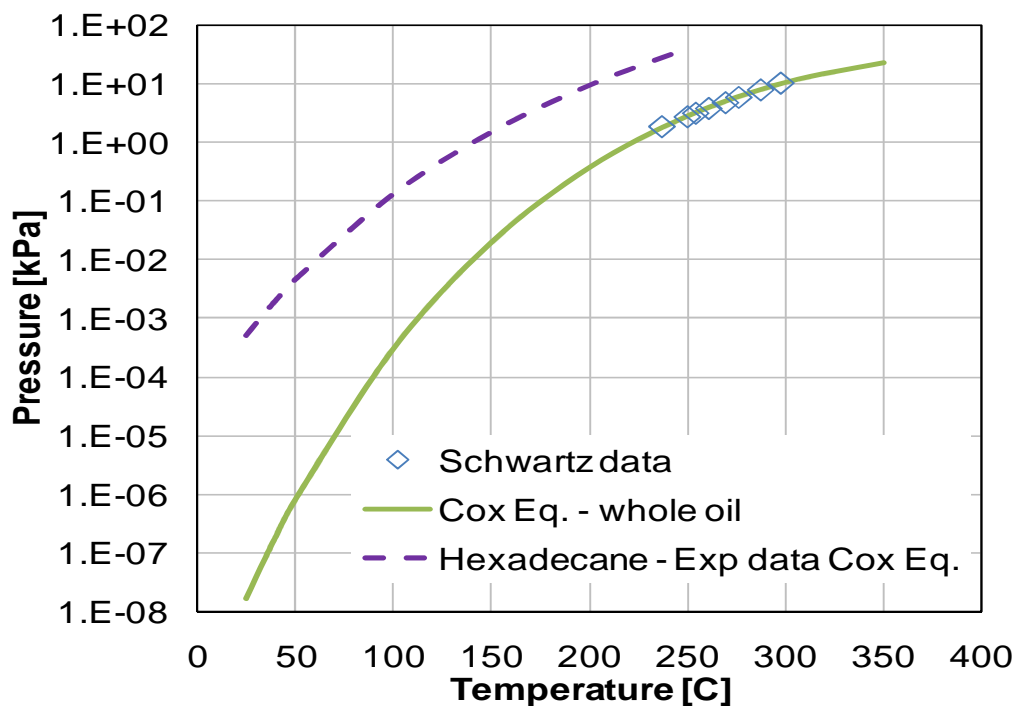


**Figure 3.17** Experimental and modeled vapour pressure data for Athabasca residue and hexadecane.

Figure 3.3 shows that the expected vapour pressure of dead bitumen and bitumen fractions at temperatures below 100°C ranges from approximately  $10^{-1}$  kPa at 100°C down to approximately  $10^{-8}$  kPa at room temperature. The HV-VPMS pumps and pressure transducers were selected for this pressure range.

### Sample Size

The sample size should be small in order to mitigate mass transfer limitations for viscous samples and facilitate equilibrium conditions. On the other hand, enough material should

be allocated in the sample vessel to ensure that it will not evaporate completely at experimental conditions. Sample vessels of approximately 20 mL were used in the design of the HV-VPMS (Appendix B). It was found that this volume is sufficient to obtain an entire vapour pressure curve of a heavy substance (molecular weight higher than 200 g/mol).

### Pipe Diameter

Pipe diameter was determined based on two criteria: thermal transpiration and pump time. The former is mitigated with a larger pipe diameter whereas the latter is minimized with a smaller pipe diameter.

As introduced in Section 2.4, pipe diameter partly determines the flow regime of the vapour at operational conditions which, in turn, determines whether thermal transpiration occurs in the system. The other parameters that determine flow regime are temperature and molecule size. Thermal transpiration occurs when the flow regime is intermediate or molecular; this is characterized by a Knudsen number lower than 1, where the Knudsen number is defined as:

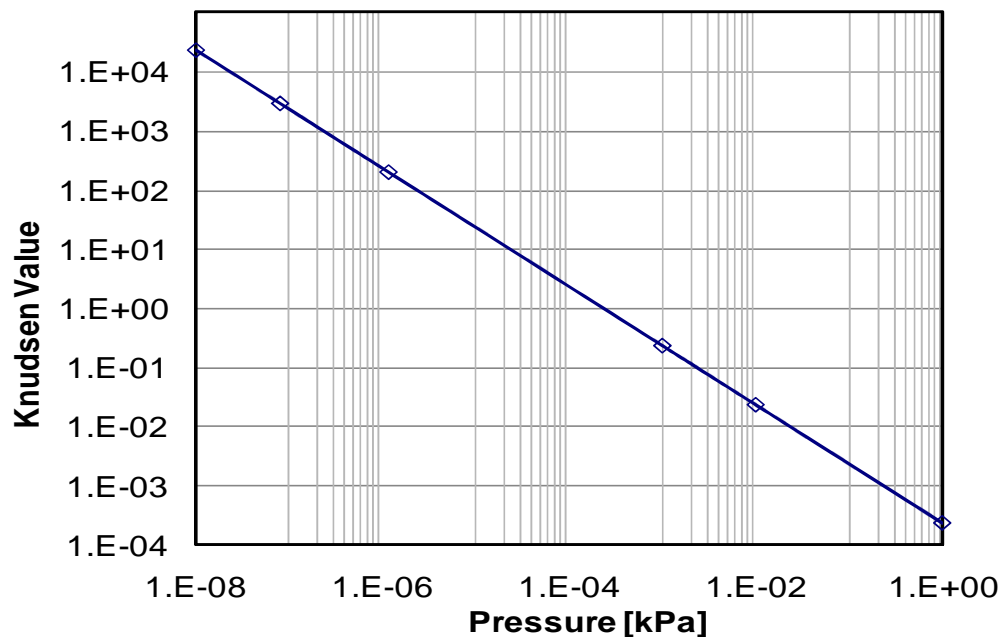
$$K_n = \frac{\lambda}{d_{eq}}, \quad [3.1]$$

Figure 3.4 shows the effect of pressure on the Knudsen number for a hypothetical molecule of 1 nm at 200 °C in a 1 inch inner diameter system. The transition to molecular

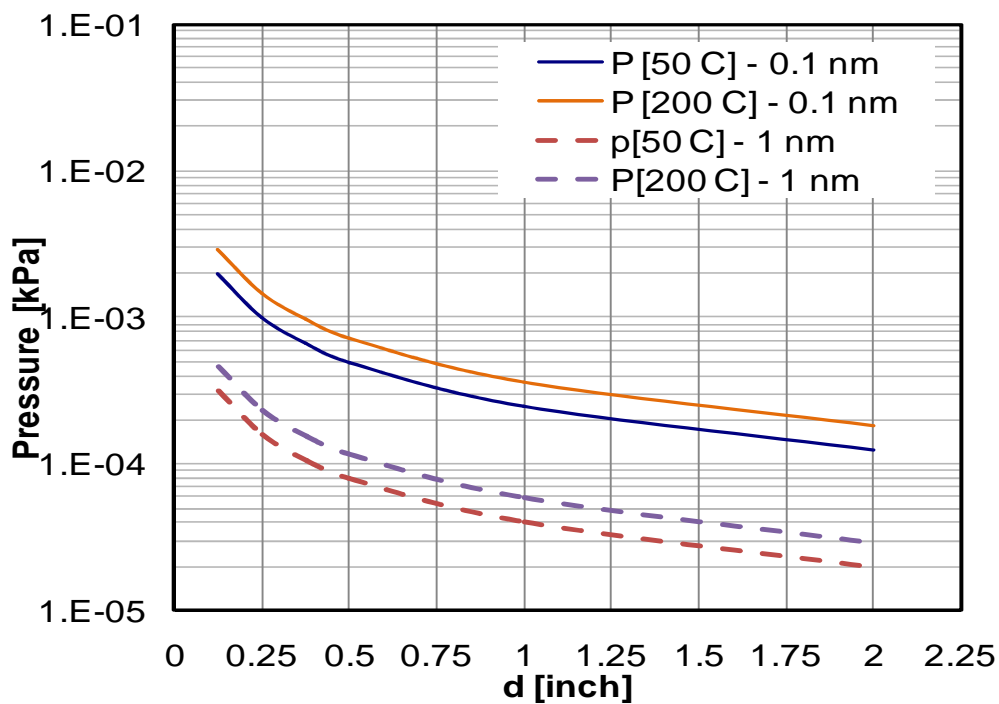
flow for this particular system,  $K_n$  equal to 1, occurs when the pressure decreases below approximately  $7 \cdot 10^{-3}$  kPa (transition pressure).

Figure 3.5 shows the transition pressure as a function of temperature, molecular size, and inner pipe size. Below a pipe size of about 1 inch, the transition pressure starts to increase significantly as the pipe size decreases. Note, the figure encompasses molecular sizes from 0.4 nm (an air molecule) to 1 nm (approximately an asphaltene monomer [Groenzin and Mullins, 2001]). Most of the curves for the 1 nm molecule lay below  $10^{-4}$  kPa, the value at which the uncertainty of direct vapour pressure measurement starts to increase significantly (Chapter 2). The pressure transition curve of a heavy oil or biodiesel fuel is expected to lie between the solid and dotted lines in Figure 3.5 since its molecular size must lie between that of air and an asphaltene monomer.

A pipe diameter of 1 inch was selected to avoid part of the thermal transpiration effect and yet provide an acceptable pump down time (Section 3.3). Caution is necessary at pressures close to  $10^{-4}$  kPa since thermal transpiration corrections to the vapour pressure may be required, Appendix A.



**Figure 3.18** Knudsen number as a function of pressure at 200 °C with an inner diameter of 1 in. and a 1nm molecule.



**Figure 3.19** Transition pressure for thermal transpiration as a function of pipe inner diameter, molecule size, and temperature.

### ***3.2.2 Vapour Pressure Measurement Apparatus***

The VPMA schematic is shown in Figure 3.6. For the sake of simplicity, the explanation of the apparatus is divided into five different systems: Sample Chamber, Pressure Measurement, Temperature Control, Pumping, and Cold Finger. Each system is summarized below and a detailed description is provided in Appendix B. In addition, seals for the fittings are a critical component of any vacuum apparatus and they are discussed as well.

#### Sample Chamber

The sample chamber consists of a sample vessel and a metal valve, Figure 3.7. The sample vessel is a stainless steel (SS) Swagelok full nipple, with a ConFlat (CF) 133 fittings and an approximate volume of 20 mL. The bottom part is sealed with a Swagelok CF133 blank and the upper part is connected to an all metal angle valve with a manual actuator.

#### Pressure Measurement

The pressure in the chamber is measured with an Inficon diaphragm gauge capable of measuring pressures in the 1 to  $10^{-4}$  kPa range. This gauge has an internal heater which sets it at 200 °C for every measurement. This high temperature ensures that the readouts are stable and mitigate possible instabilities and noise from the environment. The gauge is connected directly to a computer to record the pressures on a digital file using LabView 8.6 © [National Instruments, 2008].

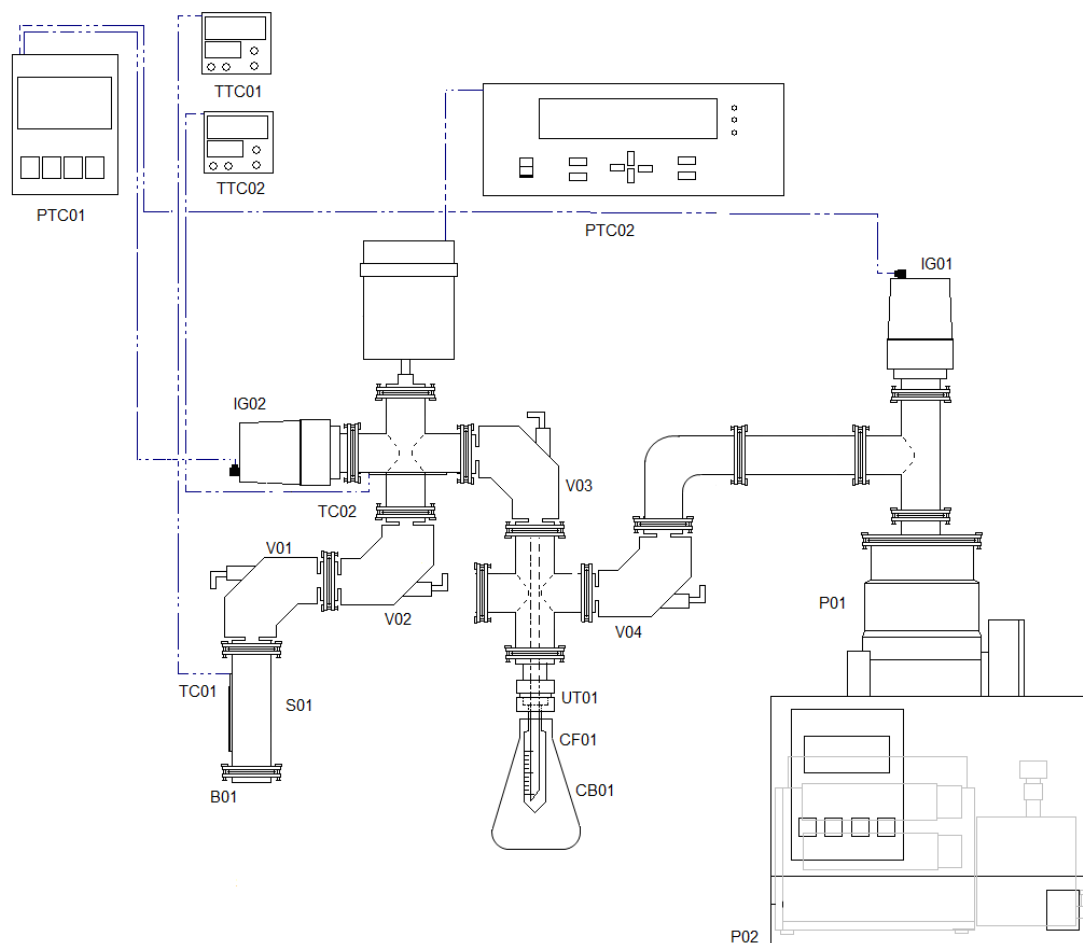


**Figure 3.20** Vapour Pressure Measurement Apparatus (VPMA). S01: sample vessel; V01: all metal angle valve; TC01: J-Type Thermo couple; RTD01: RTD transducer; UT01: Swagelok UltraTorr fitting; CF01: Pyrex Cold Finger; IG01: Combined Pirani-Cold Cathode Ion Pressure Gauge; DG01: Diaphragm Pressure Gauge; PTC01: Pressure Transducer/Read Out; TTC01: Temperature Transducer/Controller; P01: Turbomolecular Pump; P02: Backing Diaphragm Pump.

Due to the short range of applicability of the Inficon gauge, another set of pressure measurements is obtained with a second gauge. This gauge is connected through the free CF port as seen in Figure 3.6. Three options can be used: a combined cold cathode-Pirani gauge from Pfeiffer, a silicone diaphragm gauge from Alter, or no gauge (a blank is used instead).

- The combined Pirani-Cold cathode gauge is capable of measuring pressures in the range of 100 to  $5 \cdot 10^{-7}$  kPa. However, this gauge has not been proved to work with substances other than noble gases and moisturized air and only works at temperatures below 60 °C. Therefore, measurements with this gauge must be treated with caution. This gauge can be connected directly to a computer for pressure readout and record.
- The silicone diaphragm gauge is capable of measuring pressures in the range of 100 to 0.001 kPa and can be used at temperatures up to 300 °C.

Vapour pressure readings are limited on the high end by the resolution of the gauges to be used and on the lower end by gauge resolution, pump suction, and/or adsorption/desorption processes [Roth, 1990]. Figure 3.8 and Table 3.5 show the applicability range of the available pressure gauges.

**Table 3.5** Pressure operational range for the different gauges in the HV-VPMS.

<b>Gauge</b>	<b>P min [kPa]</b>	<b>P max [kPa]</b>
Inficon diaphragm (200 °C)	$5.00 \cdot 10^{-4}$ kPa	$1.48 \cdot 10^{-1}$ kPa
Baratron diaphragm (150 °C)	$5.00 \cdot 10^{-3}$ kPa	$1.04 \cdot 10^0$ kPa
Pfeiffer Cold cathode/Pirani	$9.5 \cdot 10^{-10}$ kPa	$1.01 \cdot 10^3$ kPa
SEN -100 diaphragm	$6.0 \cdot 10^{-3}$ kPa	$1.00 \cdot 10^3$ kPa

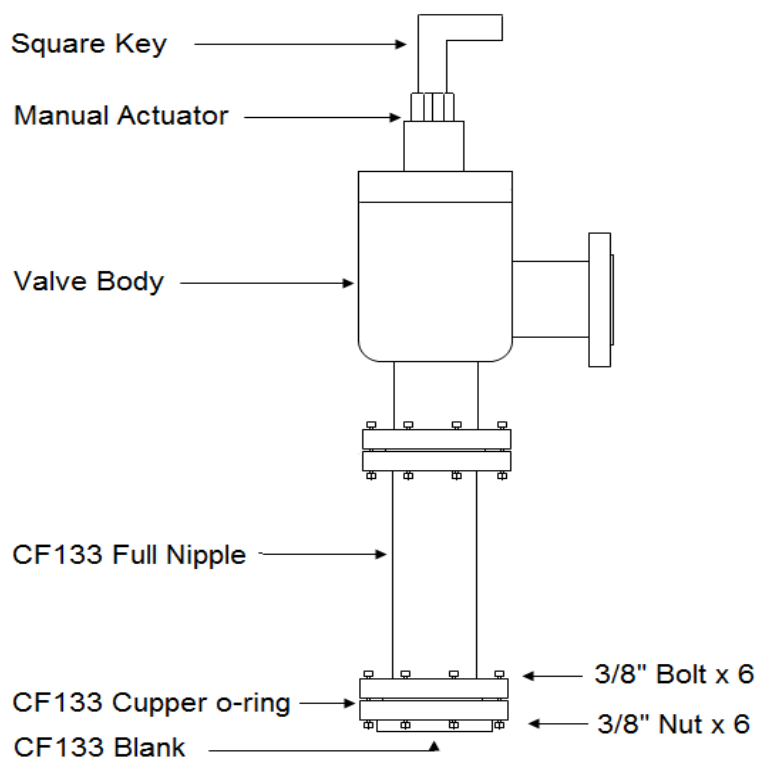


**Figure 3.21** Sample Chamber Schematic.

Table 3.5 shows that the minimum pressure readout is achieved with the Cold cathode gauge at approximately  $9.5 \cdot 10^{-10}$  kPa, which is similar to the limit pump suction when the system has been outgassed. However, at pressures below approximately  $10^{-4}$  kPa, absorption and desorption of the molecules to and from the pipe as well as permeation of atmospheric gas molecules through the pipe lead to indeterminate pressure measurement uncertainties [Roth, 1990; Fulem and Ruzcika, 2009]. Note, these processes occur at any condition; however, their effect on the total pressure readout increases significantly as the pressure is decreased.  $P_{\max}$  in Table 3.5 will determine the high end pressure resolution of the system (depending on the selected gauge) and adsorption/desorption phenomena will determine the lower end as  $10^{-4}$  kPa (for known uncertainty measurements).

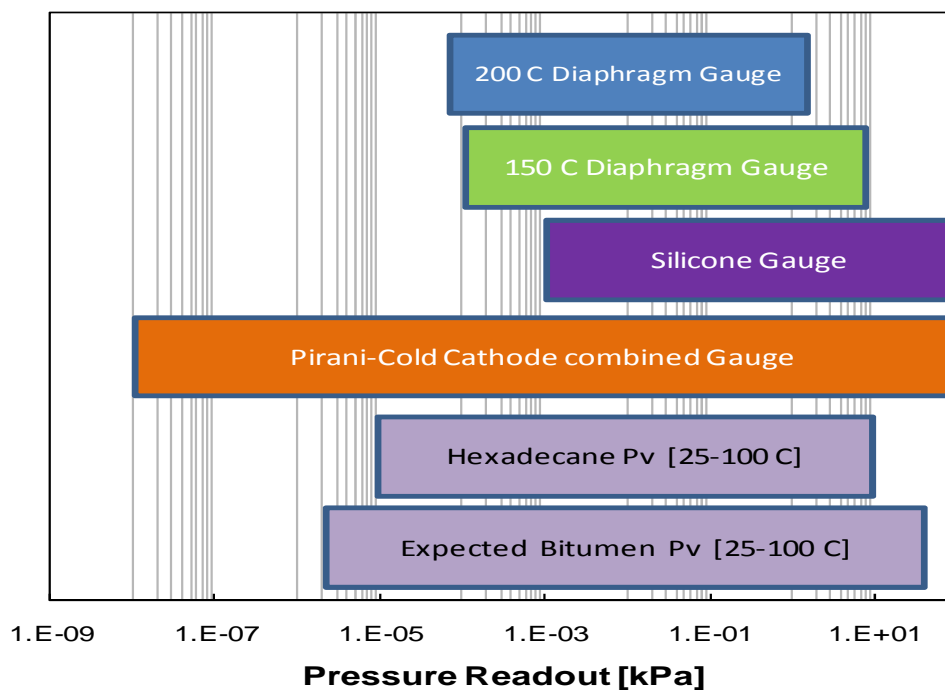


**Figure 3.22** Pressure gauges applicability ranges and literature and expected vapour pressure values for hexadecane and WC\_B1 bitumen, respectively.

### Temperature Measurement and Control

The temperature of the system is read by J-type thermocouples attached to the pipes and vessels using adjustable metal clamps (Appendix B). Values of the temperature are displayed on a Waltflow SD series readout with a resolution of 0.1 °C. The same device contains an auto-tuned PID (Proportional-Integral-Derivative) controller that is used to maintain the temperature of the system at a desired value to within  $\pm 0.1$  °C.

Electric heat tapes wrapped on the apparatus provide the heat to maintain a desired temperature. These heat tapes were selected for reliability, price, and provide small

equipment flexibility and solutions. The maximum working temperature of the tapes is approximately 650 °C. Heating tapes are connected to a fuse box for protection and to the PID controller. Finally, the heat tapes and pipes are insulated using insulation tape made of carbon fiber.

There are two sections of the VPMA that are temperature-controlled. The first one is the sample chamber, set to the desired temperature value at which the vapour pressure is measured. The second section is the pressure measurement system; this section is kept at 200°C to ensure stability of the measurements, facilitate vapour transport, and mitigate possible condensation. See Appendix B for the procedure used to keep the apparatus clean.

### Pumping

In order to generate ultra high vacuum, UHV, (below  $1.10^{-6}$  kPa [Roth, 1990]), the options are a turbomolecular propulsion pump or a cryogenic pump. The former was selected since it does not require a cooling device. In general, prices for the two types of technologies are similar.

The pumping system is comprised of a Pfeiffer pumping station model TSH 071 E capable of reach a final pressure of  $10^{-10}$  kPa at a rate of 60 L/s, nitrogen based. It consists of a turbomolecular pump, a dry diaphragm backing pump, and a display. The pressure at pump suction is measured by a Cold Cathode-Pirani pressure gauge, Figure

3.6. The pump cannot handle liquid and condensates are removed before the suction with the cold finger system. For piping technical details and construction see Appendix B.

#### Cold Finger

For sample collection and pump protection, a modified centrifuge tube with a tee-relieve system was designed and constructed, which is used as a cold finger, Figure 3.9. The vapour exiting the sample vessel enters the cold finger from the top of the cross into the inner tube. Subsequently, the vapour follows a winding path to the bottom of the centrifuge tube. Ideally, the cold finger and the winding path provide enough contact time for the vapour to condense at the bottom of the Pyrex tube and be collected. The cold finger is cooled down by means of an oil bath, which, in turn, can be cooled down by ambient air or dry ice. The non-condensable gas (mainly air) is liberated through the outer section of the tee-relieve system and goes into the pump. For piping technical details and construction see Appendix B.

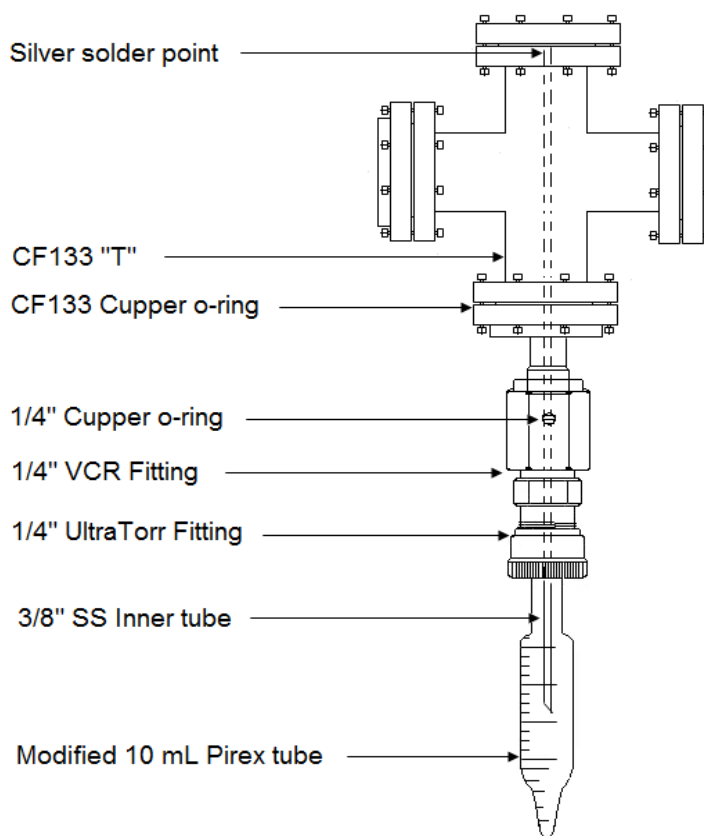


**Figure 3.23** Cold Finger schematic.

### Seals

The seals are the main source of leaks. To minimize these leaks, CF flanges with copper o-ring gaskets were used, capable of holding vacuum down to  $10^{-11}$  kPa. Note that a metal o-ring is only useable once and must be replaced every time the flanges are disconnected.

### ***3.2.3 Degassing Apparatus***

The degassing apparatus is similar to the measurement apparatus, and is shown in Figure 3.10. This apparatus is used to prepare the sample for vapour pressure measurement;

however, it can be used to measure vapour pressures in a similar manner as the VPMA. Specific differences in regards of the VPMA are described below. For technical details and construction see Appendix B.

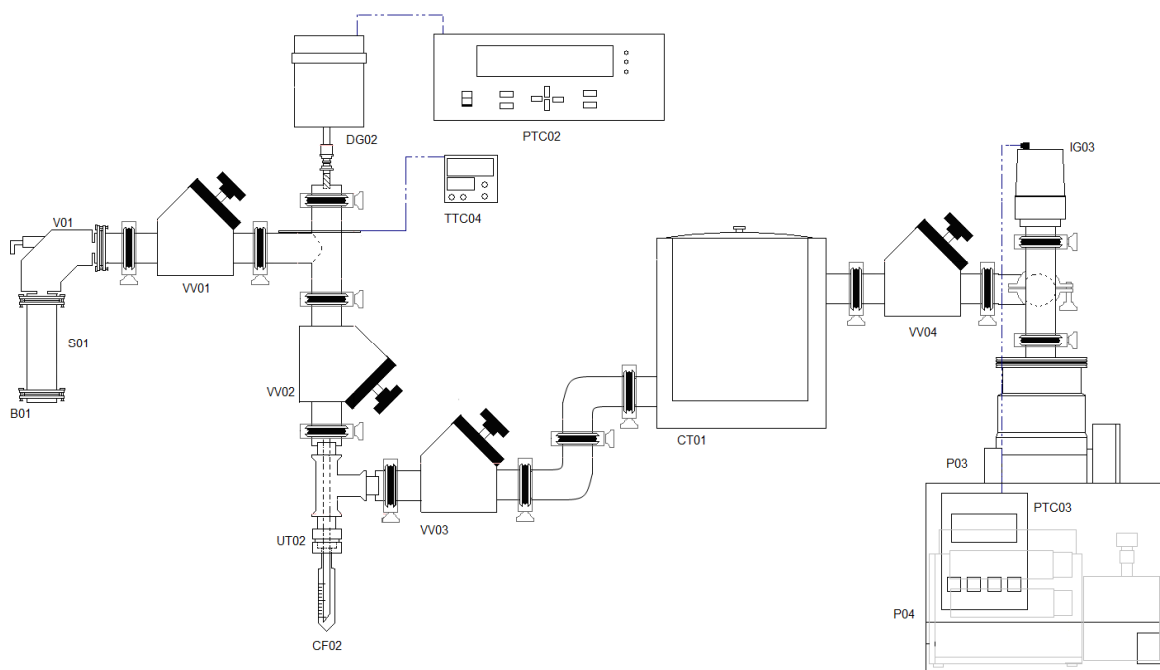


**Figure 3.24** Degassing Apparatus (DA): S01: sample vessel; V06: all metal angle valve; VV01: Viton sealed valve; UT02: UltraTorr fitting; CF02: Pyrex cold finger; CT01: cold trap; IG03: Pirani-Cold Cathode ion gauge; DG02: diaphragm gauge; PTC02: pressure transducer /display for diaphragm gauge; TTC04: temperature transducer/controller; PTC03: pressure display for ion gauge; P03: turbo-molecular pump; P04: diaphragm pump.

### Pressure Measurement

A temperature-controlled MKS Baratron diaphragm gauge is used to measure the pressure in the DA. The steady-measurement temperature is 150°C. This gauge has a

pressure range from 1 kPa to 0.001 kPa. Note that this gauge can be used as the parallel gauge on the VPMA.

### Cold Trap

Using the DA for cleansing and preparing the sample for the VPMA means that the DA handles more volatiles and impurities than the VPMA. These impurities need to be condensed before they reach the pump (otherwise they will condense at the pump and suction will be lost). An 8 L. LACO cold trap with NW25 connections is used as a condenser (CT01, Figure 3.10). Dry ice or water ice can be used to keep the cold trap at temperatures below zero, assuring complete condensation of volatiles. Dry ice is preferred since it does not leave traces to clean.

### Seals

Unlike the VPMA, KF flanges with Viton rubber o-rings were used. Rubber o-rings can hold vacuum down to  $10^{-5}$  kPa and are suitable for elastomeric deformation due to temperature cycles in the equipment, which, in turn, creates leak sources. Since the DA does not operate at high temperatures, the o-rings were considered to be acceptable. Note that the DA and rubber o-rings are a previous prototype of the VPMA and the metal o-rings.

### 3.3 Apparatus Testing and Calibration

Once the apparatus has been assembled, it must be tested for leaks and impurities within the inner pipes. Furthermore, temperature and pressure probes must be tested and calibrated.

#### Hydraulic Testing

The system is tested hydraulically to ensure that the leaks within the pressure and temperature operable ranges have been minimized. Note, it was not possible to completely eliminate leaks at high vacuum. The apparatus is connected to a Varian 797 leak detector with a helium mass spectrometer (Appendix B). Leak tests show that the average leak rates are  $6.5 \cdot 10^{-5}$  atm-cm<sup>3</sup>/s and  $1 \cdot 10^{-4}$  atm-cm<sup>3</sup>/s for the VPMA and DA, respectively. This means, for instance, that a flow of  $6.5 \cdot 10^{-5}$  cm<sup>3</sup>/s of air enters the VPMA at normal atmospheric conditions externally. These results show good sealing in the fittings as compared to other vacuum systems [Roth, 1990].

Next, an out gassing test is performed to determine if the system is clean (Appendix B). In this procedure, the system is baked out at 200 °C for at least 4 days open to pump suction. Subsequently, the system is isolated from pump suction and the pressure rise is measured. A satisfactory outgassing procedure is achieved when the pressure rise is equal to the expected leak rate. This means that the system is clean of impurities and is ready for pressure measurement. Figure 3.11 shows the pressure rise of the VPMA before and after outgassing

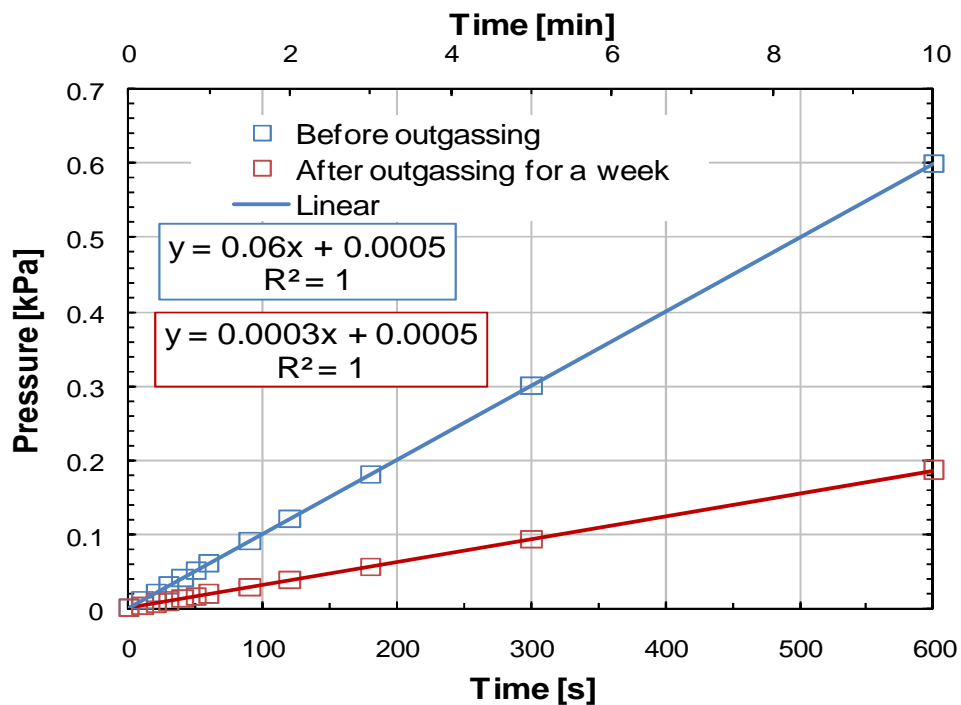


**Figure 3.25:** VPMA pressure rise profile before and after out gassing.

### Pump Down Time (PDT)

The pump down time (PDT) is the pressure profile developed by the system open to pump suction from atmospheric pressure to the ultimate pressure (UP) [Roth, 1990]. It is an important feature of the mechanical performance of the system; however, it does not impinge on vapour pressure measurement except to determine the ultimate (minimum) pressure of the system. Figure 3.12 shows an example of pump down time of the DA and VPMA.

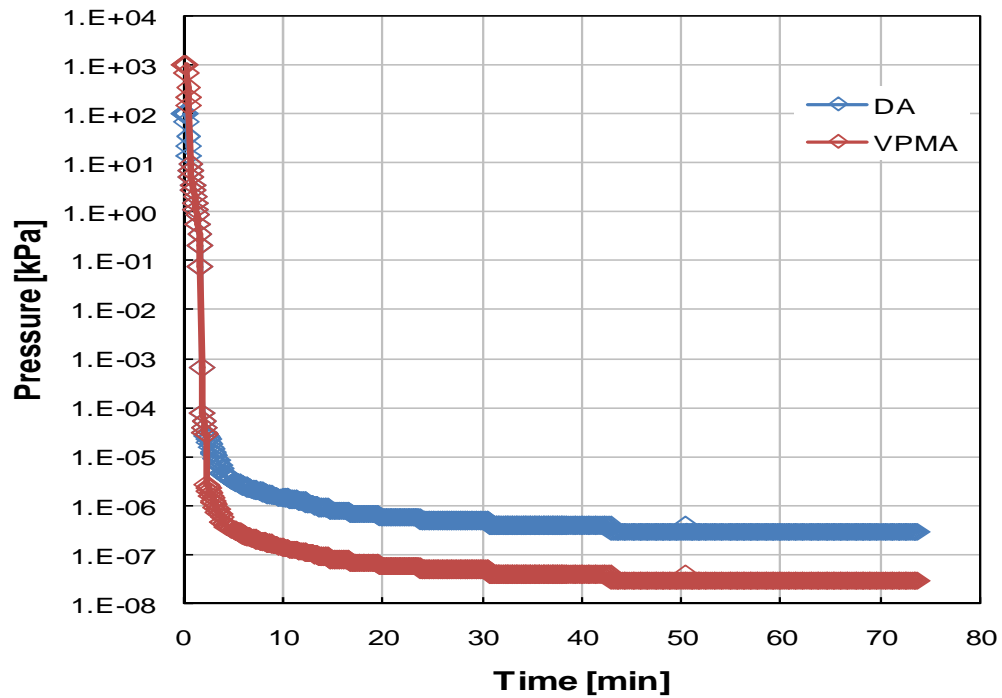


**Figure 3.26** Experimental pump down time of DA and VPMA before out gassing

In general, the pump down time of a vacuum system and its ultimate pressure is determined by a number of factors [Roth, 1990]; Table 3.6 lists these factors for the DA and VPMA systems. The most significant factor determining the pump down time in both systems (DA and VPMA) is the leak rate. By the introduction of metal seals in the VPMA, the pump down time and the ultimate pressures were improved significantly, Figure 3.12.

**Table 3.6** Factors influencing the pump down time and ultimate pressure on a vacuum system.

Factor	Description	DA and VPMA
--------	-------------	-------------

Pump velocity	Determine velocity and capacity of suction – Decrease PDT and UP	Same for both systems
System volume	Determine the amount of gas to be liberated – Increase PDT no change in UP	DA has approx 30% more volume than the VPMA
System conductance	Measure the resistance that the gas has to flow to the pump – Increase PDT no change in UP	Similar for both systems since materials are the same and they both have similar internals (valves, elbows, etc.)
Out gassing rate	Measure of how clean the system is – Increase PDT and UP	Same for both
Permeation rate	Measurement of gas flow through the pipes from atmosphere – Increase PDT and UP	Similar conditions in both systems at the same inner pressure - permeation rate depends on inner pressure
Leak rate	Measurement of gas flow through flange openings from atmosphere – Increase PDT and UP	Higher in DA than VPMA due to different flange configuration

### Thermocouple Calibration

All of the thermocouples were calibrated against a Resistance Temperature Detector (RTD) which had been calibrated against a certified high precision thermometer (HPT - Automatic Systems Laboratories F250 Precision Thermometer Res. 0.025 C). The temperature for the calibrations was controlled with a thermostated bath (FLUKE 6330 Calibration Bath). The calibration chart for the RTD is shown in Figure 3.13 and the calibrated equation for temperature is given by Equation 3.2. A 1:1 calibration ratio was found between the thermocouples and the RTD.

$$T = 0.9945T_{RTD} - 0.1576, \quad [3.2]$$

where  $T$  is the calibrated temperature in °C and  $T_{RTD}$  is the reading of the RTD in °C

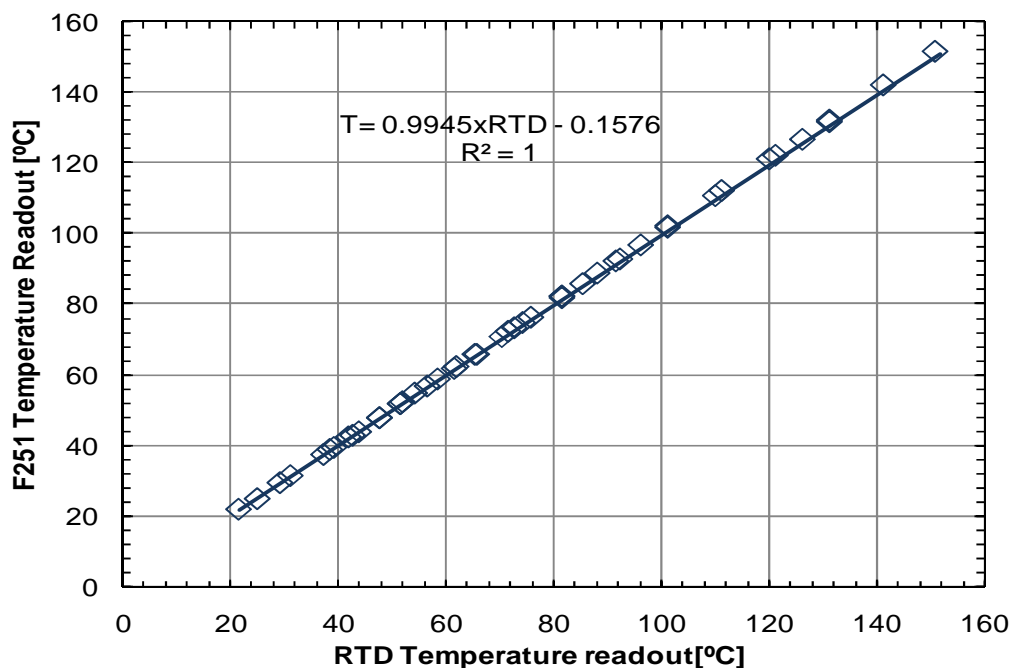


**Figure 3.27** Calibration chart for RTD against F251 HTP.

### Pressure Gauge Calibration

Vapour pressure measurements on the VPMA and DA were taken with temperature controlled diaphragm gauges as shown in Figures 3.6 and 3.10, respectively (also refer to Appendix B) with pressure ranges as specified in Table 3.5. For this type of gauge, a linear calibration is possible at pressures above  $10^{-2}$  kPa. However, below this threshold, a linear calibration is not representative and a logarithmic term may be required [Fulem, 2011].

The first step was to calibrate the diaphragm gauges for the VPMA and DA (DG1 and DG2, respectively) at pressures above  $10^{-2}$  kPa, where the behaviour is expected to be

linear. In this case, the Cold Cathode Pirani gauge (CCP) was calibrated to a reliable low vacuum diaphragm gauge available at the laboratory (GOR). The calibration data are shown in Figure 3.14 and were fitted with the following calibration equation with an AARD of 5.1%.

$$P_{GOR}[kPa] = 0.998P_{CCP}[kPa] + 0.243, \quad [3.3]$$

Subsequently, the diaphragm gauges DG1 and DG2 were calibrated against the CCP and back calculated to calibrated pressures using Equation 3.3. This was necessary because the pressure ranges of the GOR and DG transducers do not overlap. Figure 3.15 shows the calibration plot for DG1; these charts were linearly regressed with an AARD of 8.9%.

$$P_{GOR}[kPa] = 0.015P_{DG1} + 0.316, \quad [3.4]$$

$$P_{GOR}[kPa] = 0.0295P_{DG2} - 0.0027, \quad [3.5]$$

Equations 3.4 and 3.5 are the linear calibration of the diaphragm gauges DG1 and DG2 at pressures above  $10^{-2}$  kPa where  $P_{GOR}$  is replaced with  $P_{meas}$ , the calibrated measured pressure.

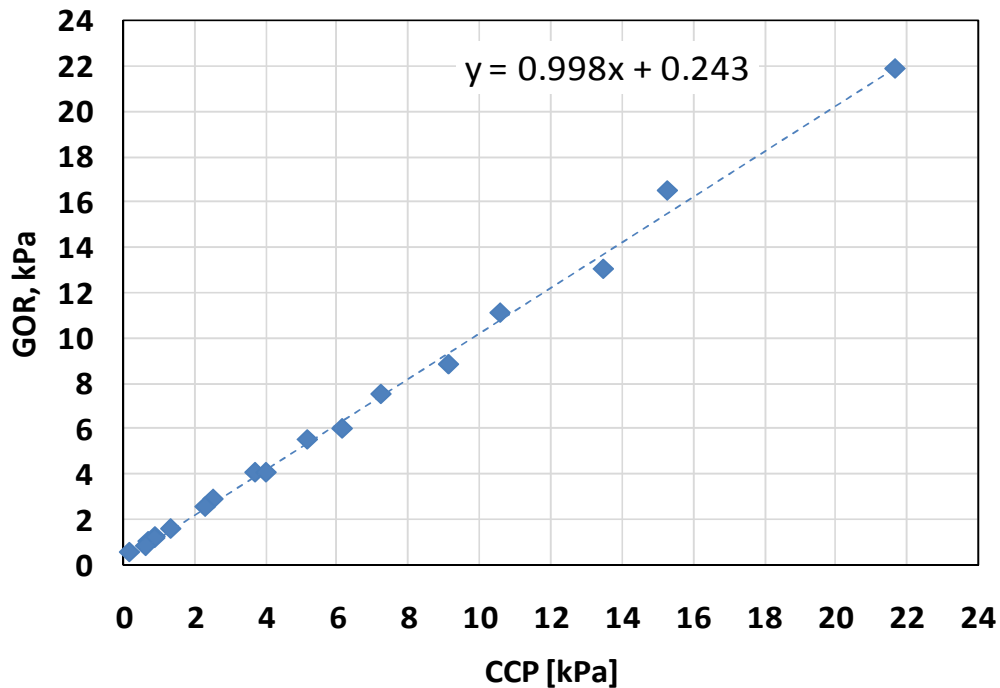


**Figure 3.28** Calibration chart for Cold Cathode- Pirani gauge against GOR diaphragm gauge.

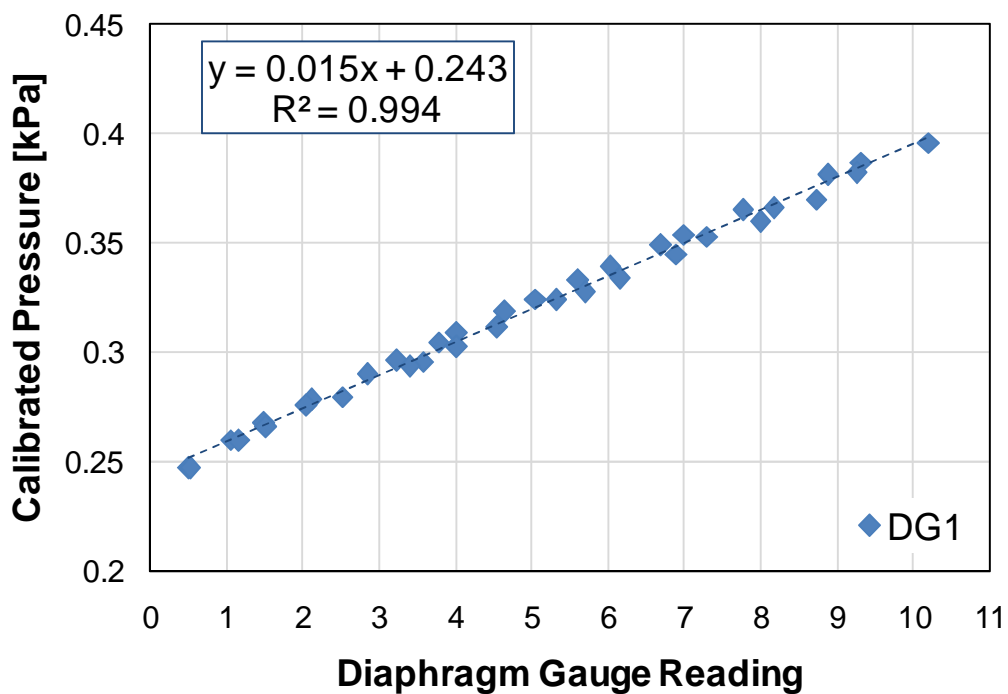


**Figure 3.29** Calibration chart for DG1 diaphragm gauges.

The second step was to determine the calibration curves for pressures below  $10^{-2}$  kPa. In this case, the calibration was performed by comparing the measured vapour pressure of n-icosane with literature data (Section 3.5). Figure 3.16 shows the experimental data (already corrected by Equations 3.4 and 3.5) against literature data regressed with the Cox equation (Table 3.7).

The measured data deviate from the literature data at pressures below  $10^{-2}$  kPa. It is proposed to use a logarithmic expression to correct the pressure reading, accounting for the non-linear behavior of the diaphragm gauge at this pressure range. The calibrated pressure,  $P^*$ , was correlated as

$$P^*[kPa] = P_{DG1} \exp \left[ -22.344 \left( \frac{T_{NL}}{T} - 1 \right) \right], \quad [3.6]$$

$$P^*[kPa] = P_{DG2} \exp \left[ -10.461 \left( \frac{T_{NL}}{T} - 1 \right) \right], \quad [3.7]$$

where  $T_{NL}$  is the temperature, in K, at which the vapour pressure equates to  $10^{-2}$  kPa. The calibrated vapour pressures of eicosane are compared with the extrapolated literature data in Figure 3.17.

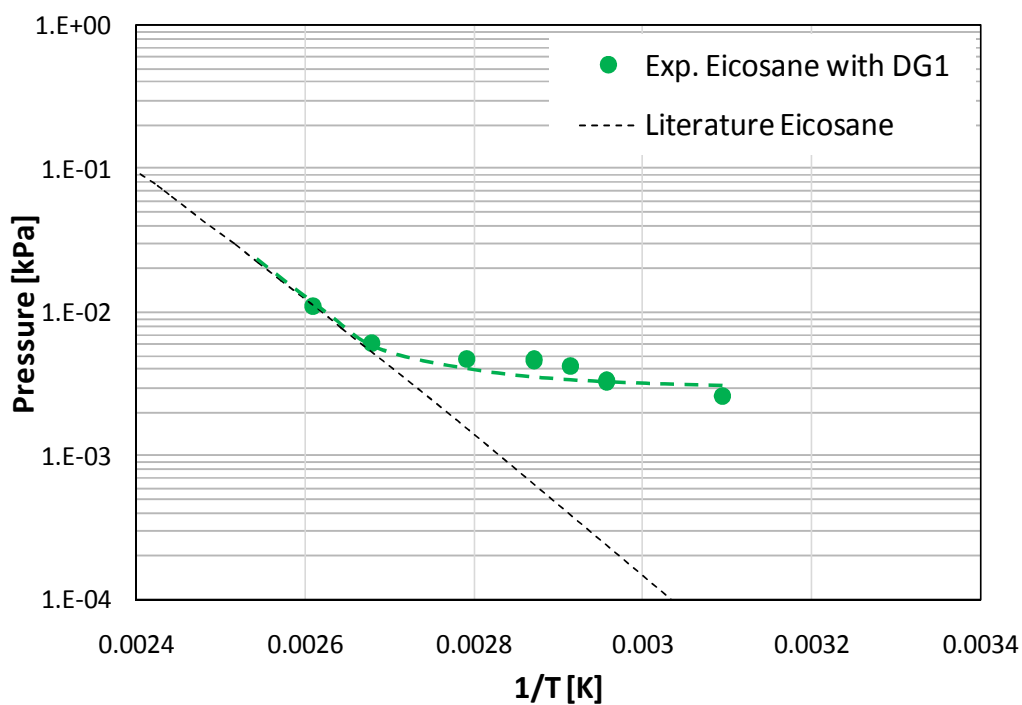


**Figure 3.30** Experimental and literature data for eicosane measured with DG1 – dotted lines show the non-linear tendency of the data and do not represent any particular model.

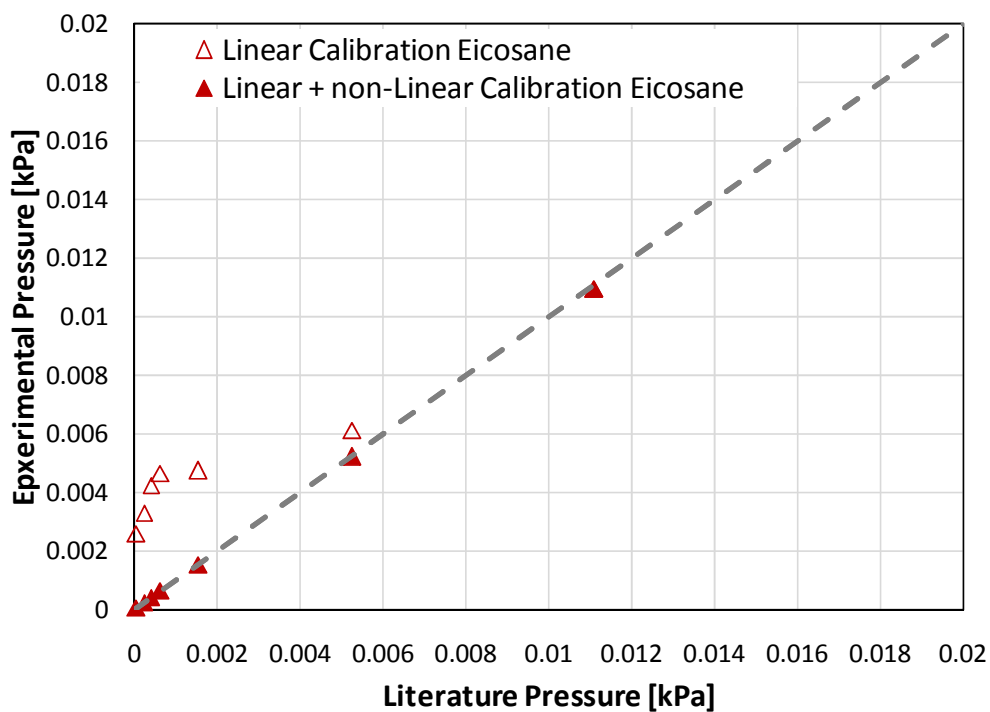


**Figure 3.31** Literature and measured vapour pressure data of eicosane with linear calibration and with linear + non-linear calibration – dotted line represents is at  $45^\circ$ .

### **3.4 Experimental Procedure**

This section introduces the general procedure that is followed for collecting vapour pressure data using the HV-VPMS including degassing and measurement. A short explanation on sample fractionation using the apparatus is also provided. For a detailed description refer to Chapter 8 and Appendix B.

#### ***3.4.1 Degassing***

Samples to be characterized often have light impurities, such as water and light solvents, that affect the vapour pressure measurement since its partial pressure is significant in comparison with the expected vapour pressure of the sample. Some other impurities might be found depending on the source of the sample. Specifically, heavy oil contains traces of light oils, or solvents such as naphtha and toluene, coming from the oil extraction processing. In order to measure vapour pressure correctly, the sample must be degassed.

For the sake of simplicity, Figure 3.18 shows a simplified diagram of the degassing apparatus (DA). The DA is run in cycles to monitor the degassing performance. First, a base line for the system is reached by pumping the system from the Valve V1 onwards with the sample chamber connected. The value of the base line depends on the speed of the pump ( $S_p$ ), the capacitance of the pipe ( $C$ ), the leak rate ( $Q_l$ ), and the out gassing rate ( $Q_o$ ), Table 3.6. Then, Valve V2 is closed and V1 is opened, simultaneously. A jump in

the pressure is recorded, Figure 3.19. This jump depends on the pressure exerted by the sample ( $Q_v$ ) and the leak rate ( $Q_l$ ). Finally, Valve V1 is closed and V2 is opened simultaneously. A drastic change in pressure back to the base line is recorded and a cycle is completed. The degassing of a sample consists of several cycles until at least four to five subsequent cycles repeat. At this point, the sample is sufficiently degassed to be transferred to the VPMA.

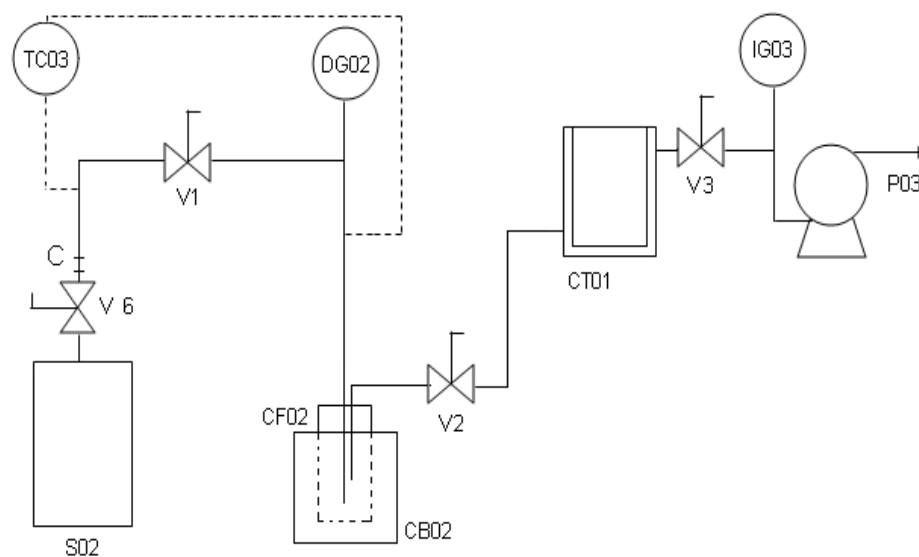


**Figure 3.32** Simplified VPMA schematics

Figure 3.20 shows a complete run of cycles for the degassing of n-hexadecane at 25°C. The data can be divided into three major sections. The first one, labelled “Air”, refers to the degassing of gases trapped on the sample and from the interior of the sample chamber. The second section, labelled “Water + Solvents”, refers to the degassing of water and light solvents or impurities present on the sample and within the walls of the

chamber. The third section, labelled “Steady State Measurement”, is reached when the degassing is finished and a constant vapour pressure is recorded. Note that the three different sections are not always clearly differentiated and some overlap occurs.

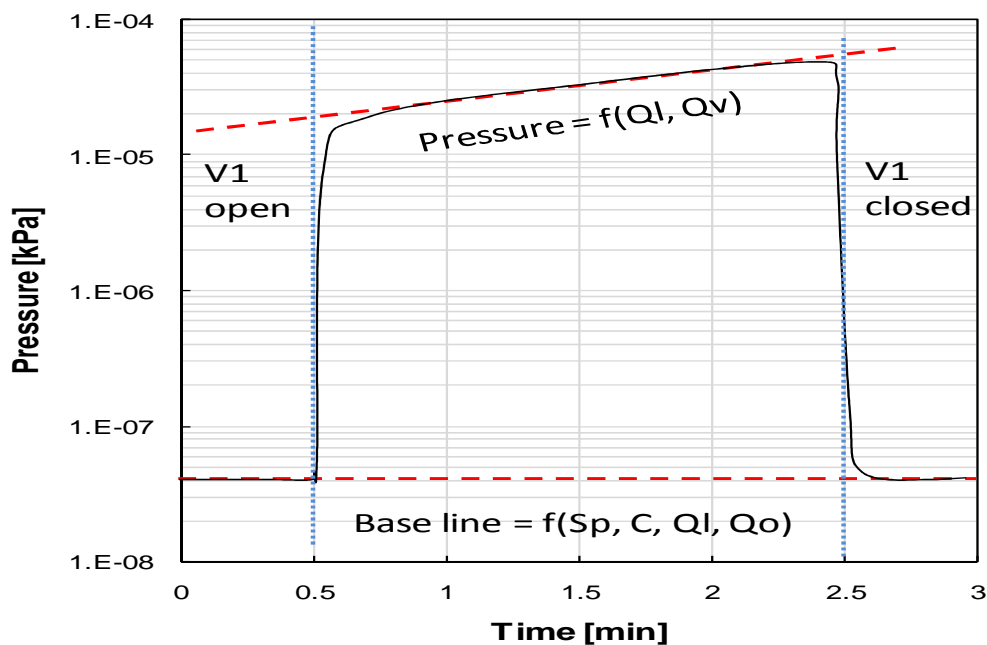


Figure 3.33 A typical degassing cycle.

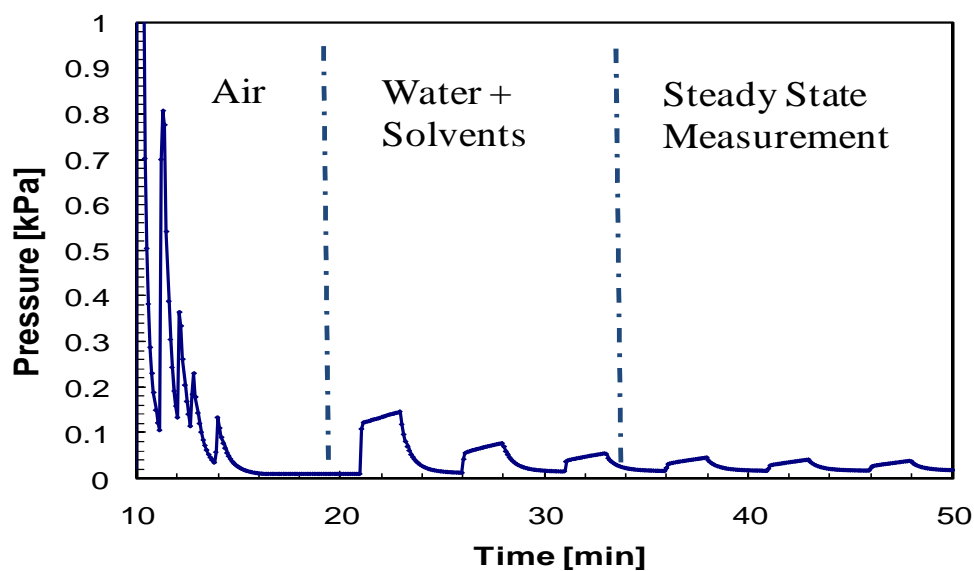
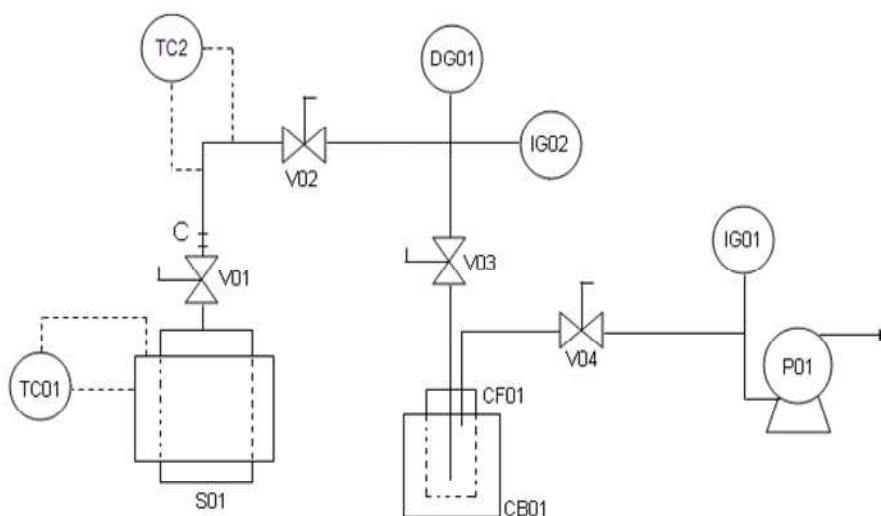


Figure 3.34 Complete cycle of hexadecane degassing at 25°C.

### 3.4.2 Vapour Pressure Measurement

Once the sample and the sample chamber have been degassed, the sample chamber is isolated from the DA by closing V6 in Figure 3.18. The chamber is disconnected and re-connected to the vapour pressure apparatus, as shown in Figure 3.21. The latter must have been already baked out, cleaned, and vacuumed at a pressure lower than whatever base line was used on the degassing apparatus. Subsequently, the vapour pressure apparatus is run in cycles in the same manner as the degassing apparatus. A lower leak rate is expected with the metal gaskets in the VPMA (rather than the rubber gaskets in the DA). A VPMA cycle example is shown in Figure 3.22. The pressure for any given cycle is obtained by extrapolating the pressure trend caused by the leak rate back to the start time of the cycle.



**Figure 3.35** Simplified schematic of the vapour pressure measurement apparatus, VPMA.

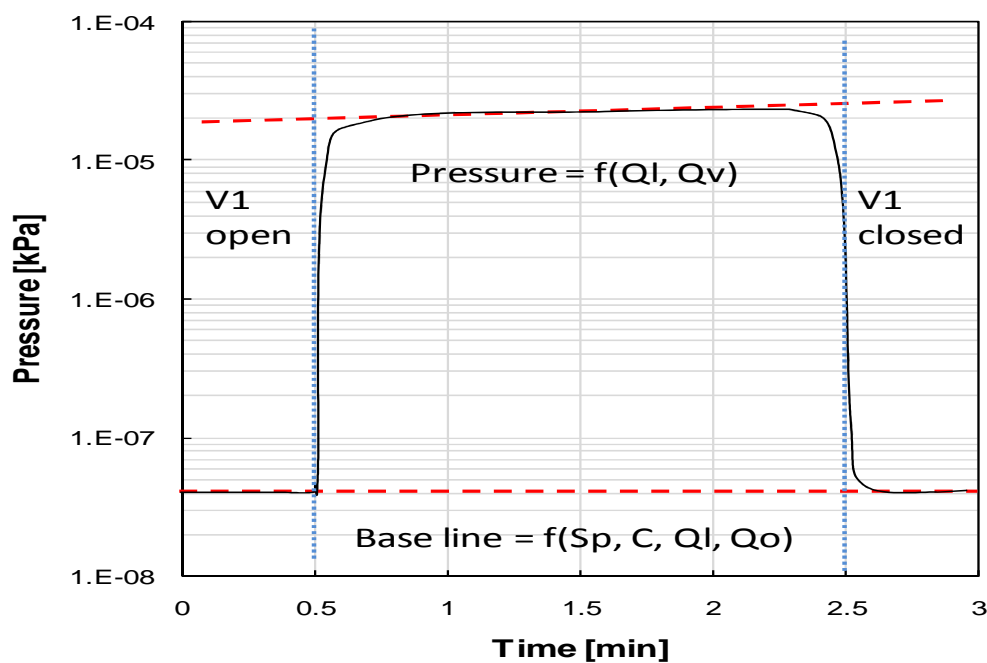


**Figure 3.36** Vapour pressure measurement cycle.

### 3.4.3 Fractionation

It has been proven that both systems, the DA and the VPMA, can be used to systematically fractionate a crude oil; however, the proposed practice is to use the DA for degassing and the VPMA for fractionation. A brief account of the procedure is described as follows (refer to Appendix B for further details).

With V01 closed (Figure 3.21, valve V6 in Figure 3.18), the sample chamber (S01) is set at a given temperature ( $T_0$ ) while the rest of the system is left at a temperature  $30^\circ\text{C}$  above  $T_0$  to avoid condensation in the pipes and facilitate vapour mobility. The cold finger (CF01) must be at a temperature well below  $T_0$  but high enough to ensure that the condensate does not solidify in the inner pipes. At this point, valve V01 is opened and the

sample is left open to pump suction for a given period of time. Figure 3.23 shows the pressure measurements at this early stage of the fractionation process.

As can be seen in Figure 3.23, the pressure in the system tends towards a pseudo-steady state value that is related to the vapour pressure of the substance being fractionated. At this stage, as the sample is left open to pump suction, condensate is collected in the cold finger (CF01, Figure 3.21). When the level of condensate in the cold finger does not change over an interval of at least four hours, it is assumed that the entire sample that can be fractionated at  $T_0$  has been collected.

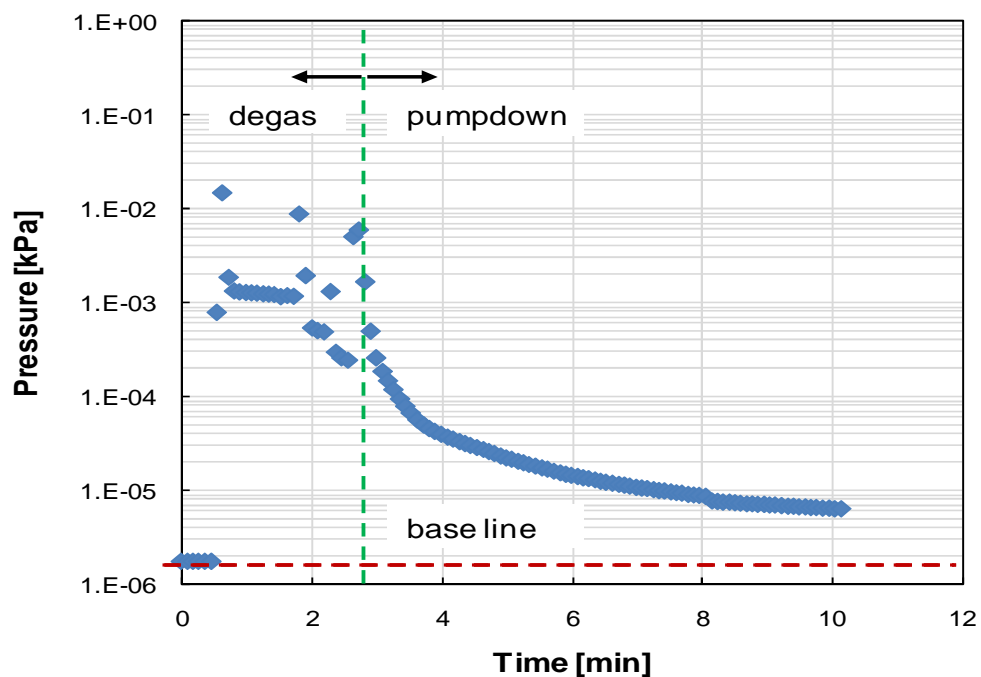


**Figure 3.37** Pump down time for early fractionation stage. Some gas is liberated from the sample even after degassing; however, the amount of time required for the pump down to start is less than three minutes.

If the amount collected is enough for further characterization, then close Valve V01 and leave the system open to pump suction for at least four hours, assuring that no condensate material is left on the inner pipes. In this case, the amount collected is a single temperature fraction of the oil at  $T_0$ . This scenario is optimal for oil fractionation; however, in most cases not enough material is collected at a single temperature.

To collect more material, the temperature is increased from  $T_0$  to  $T_1$  in small increments over time. The amount collected is known as a boiling point range cut. Note that as the temperature range grows broader ( $T_1 - T_0$ ), more components are being collected in the cut. Hence, for oil characterization, it is better to keep the boiling point range as narrow as possible.

Once a given cut is collected, close valve V01 and leave the system open to pump suction for at least four hours to ensure there is no condensate in the inner pipe. Then, turn off the pump and replace the cold finger to continue fractionation of the residue. More details about heavy oil fractionation can be found in Chapter 8 and Appendix B.

### **3.5 Apparatus Testing on Pure Components**

The HV-VPMS apparatus and the pressure gauge calibrations were tested by measuring the vapour pressure of two pure components and comparing with literature data. Naphthalene and n-hexadecane were selected because their vapour pressures matched the

range of interest for heavy oils and biodiesels. Literature data for these pure components were collected from Lemmon's recommended database [Lemmon and Goodwin, 2000].

### ***3.5.1 Assessment of Literature Vapour Pressure Data***

This section focuses on the data assessment for n-hexadecane vapour pressure. The same treatment was performed on naphthalene and n-eicosane (for calibration) literature data.

Hexadecane vapour pressure data were used as recommended by Lemmon and Goodwin [2000]. Data points came from static methods ([Myers and Fenske 1955], [Camin et al. 1954], [Lee et al. 1992], [Morgan and Kobayashi 1994]), distillation ([Francis and Robbins, 1933]), diffusion ([Grenier et al. 1981], [Parks and Moore, 1949]), and ebulliometry ([Mills and Fenton, 1987]). The database account for approximately 190 experimental data points with temperature ranging from 293 to 611 K. The critical properties of n-hexadecane are 722 K and 1410 kPa [Poling et al., 2001].

In order to obtain a consistent dataset, the literature data must be assessed. The Korsten equation can be used for this purpose [Korsten, 2000]

$$\ln P^V = A + \frac{B}{T^{1.3}}, \quad [3.8]$$

The Kornsten equation indicates that a plot of  $\ln(P_V)$  vs.  $T^{-1/3}$  is expected to follow a straight line. Figure 3.24 shows that the dataset consistently follows the expected trend.

However, as pointed by Oonk et al. [1998], this type of methodology can be misleading because systematic errors present on the experimental procedures within different data sets are hidden. Oonk and van Linde [van der Linde et al., 1998; Oonk et al., 1998] suggested a methodology to detect these errors. Their method consists of adding sensitivity to the  $1/T$  coordinate in Figure 3.24, which is achieved by introducing a linear contribution as shown in Equation 3.9:

$$\ln f_P = \ln \left( \frac{P}{P^0} \right) - \beta_0 + \frac{\beta_f}{T}, \quad [3.9]$$

where  $f_P$  is the modified pressure function,  $P^0$  is a reference pressure, and  $\beta_{0,f}$  are adjustable parameters. The  $\beta_{0,f}$  parameters are adjusted so that  $\ln f_P$  is zero when the highest and the lowest values of the vapour pressure data set are evaluated. If  $(P_H, T_H)$  is the highest vapour pressure point in the data set and  $(P_L, T_L)$  is the lowest, then the  $\beta_{0,f}$  parameters are defined as:

$$\beta_0 = \ln \left[ \left( \frac{P_H}{P^0} \right) \left( \frac{P_L}{P_H} \right)^{\frac{T_L}{T_L - T_H}} \right], \quad [3.10]$$

$$\beta_f = \ln \left[ \frac{P_L}{P_H} \right] \left( \frac{1}{T_H} - \frac{1}{T_L} \right)^{-1}, \quad [3.11]$$

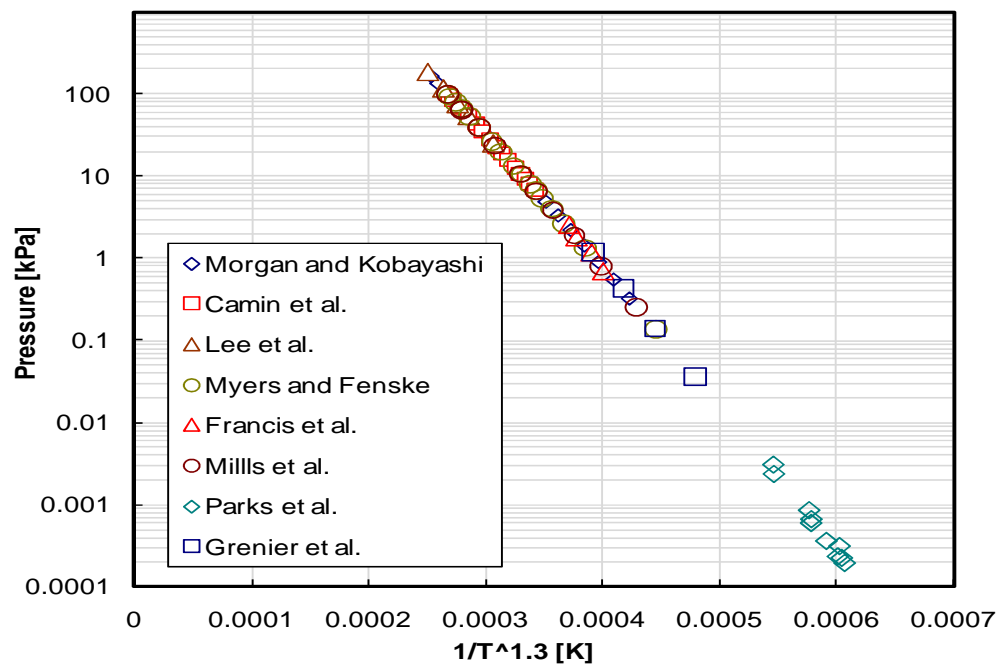


**Figure 3.38** n-Hexadecane literature data plotted with Korsten equation axes.

A consistent set of data must follow a parabola when  $\ln f_P$  is plotted versus  $1/T$ . Figure 3.25 shows the Oonk-van Linde plot for the whole dataset for n-hexadecane. Some of the data points fall outside the parabola indicating that they are not consistent within the dataset. These outlier points were excluded from further analysis. Literature data for naphthalene and n-eicosane was assessed in the same manner.

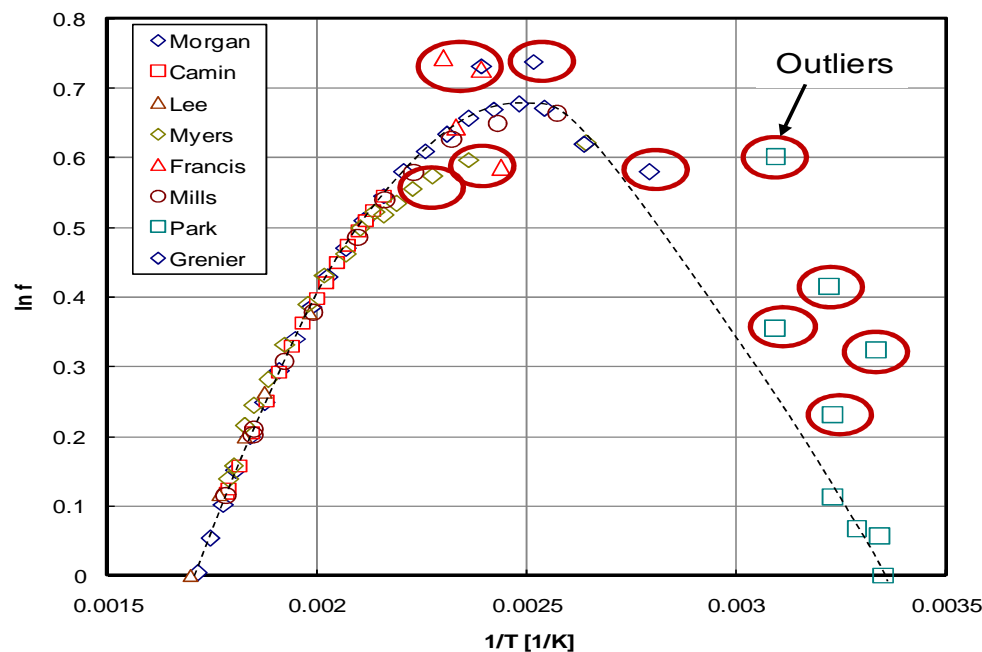


**Figure 3.39** Complete set of n-Hexadecane literature data plotted with the Oonk-van Linde coordinates.

### 3.5.2 Regression of Literature Vapour Pressure Data

Regression of vapour pressure literature data was performed using the Cox equation (Section 2.3) by minimizing the objective function described in Equation 3.12

$$\min(j) = \sum_i [\ln(P^{Calc}_i) - \ln(P^{Exp}_i)]^2 + K_C \sum_i [\Delta C^{Calc}_{P,i} - \Delta C^{Exp}_{P,i}]^2, \quad [3.12]$$

The heat capacity terms were included because, at the temperature range of interest, the vapour pressure data of n-hexadecane and n-eicosane is close to  $10^{-4}$  kPa which is taken as the threshold for known experimental uncertainty. To provide a better regression in the unknown uncertainty region (and close to it), the extrapolation is constrained with heat

capacity data. Results for both regressions are shown in Table 3.7. This regression methodology is further explained in Chapter 4.

**Table 3.7** Cox equation constants for naphthalene and n-hexadecane vapour pressure –  $P_v$  [kPa] =  $P_o \exp[(1-T/T_o) \exp(a_1 + a_2T + a_3T^2)]$ .

Substance	$a_1$	$a_2$	$a_3$	$T_o$ [K]	$P_o$ [Pa]	AARD* [%]
Naphthalene	3.272	$-2.659 \times 10^{-4}$	$-4.347 \times 10^{-9}$	353.7	0.9935	0.01
n-hexadecane	3.024	$-1.831 \times 10^{-3}$	$1.794 \times 10^{-6}$	560.15	101.325	0.43
n-eicosane	3.950	$-1.201 \times 10^{-3}$	$6.861 \times 10^{-7}$	311.16	$1.22 \times 10^{-5}$	5.78

$$* AARD = \frac{1}{n} \sum_{i=1}^n \left| \frac{\ln P_{i,exp} - \ln P_{i,calc}}{P_{i,exp}} \right|$$

### 3.5.3 Vapour Pressure of Naphthalene and Hexadecane

Vapour pressure of naphthalene and n-hexadecane were measured using the VPMA at temperature values ranging from 30 to 140 °C (data can be found in Appendix A). Figure 3.26 shows experimental and literature data from the Cox equations developed in Section 3.5.2. The AARD values are 3 % and 1%, respectively.

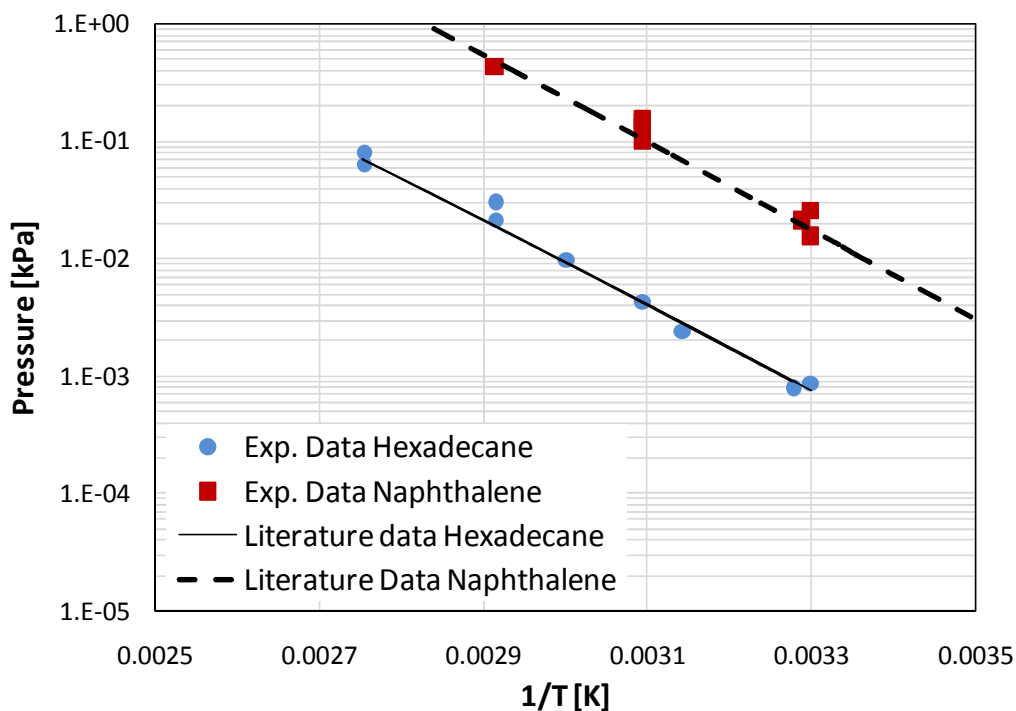


**Figure 3.40** Experimental vapour pressure data for n-hexadecane and naphthalene; literature data shown is regressed with Cox equation, Table 3.7.

### 3.6 Liquid Heat Capacity Experimental Procedure

Liquid heat capacity data are required in the correlation of vapour pressure data, Chapter 2. In this thesis, the liquid heat capacity of biodiesel fuel and heavy oil samples was measured using a differential scanning calorimeter (DSC) TA Q2000 V24.9. These measurements were performed by the Steacie Institute for Molecular Sciences NRC-CNRC in Ottawa, ON. Reported liquid heat capacity data have an average uncertainty of 2%. A brief description of the experimental outcome of a DSC is provided below.

The outcome of a DSC run is a heat flow chart for a given mass of sample (from 1 to 10 mg). This heat flow chart is measured in response of a controlled temperature ramp input

to the system. In this case, a temperature ramp of 5 °C/min was applied. Figure 3.27 shows the heat flow chart and temperature ramp of one of the biodiesel fuels.

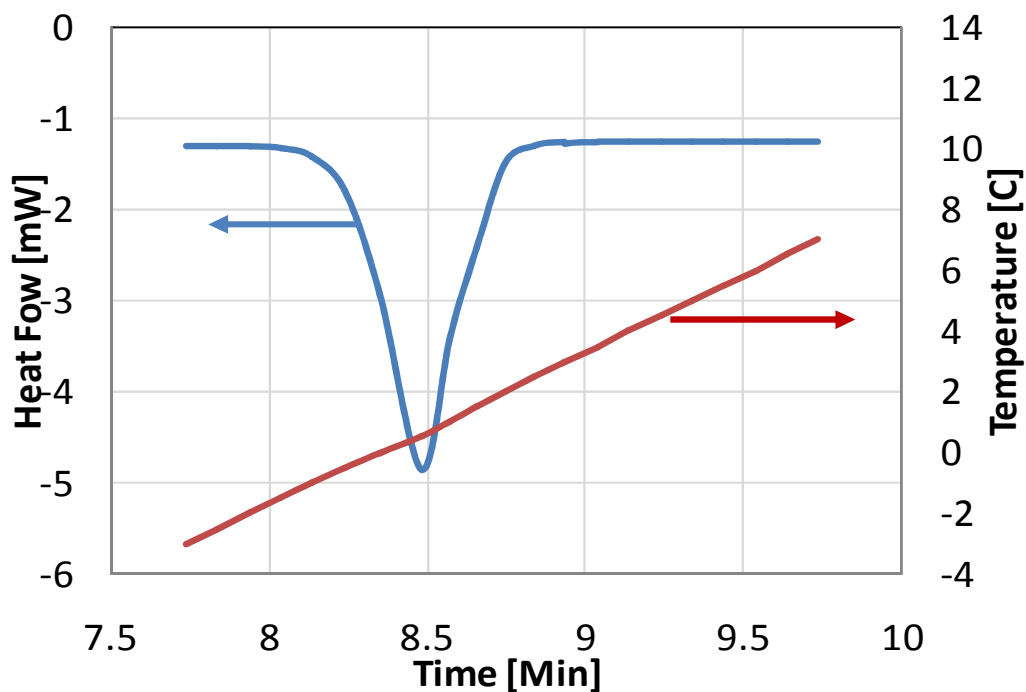


**Figure 3.41** Heat flow and temperature ramp for differential scanner calorimeter assay on a biodiesel fuel sample -4 to 8 °C; sample size of 8.04 mg.

After calibration (Indium was used as a standard), the heat capacity of the substance can be calculated as the ratio of the heat flow and the temperature ramp, Equation 3.12 [Haines, 2002; Weir and de Loos, 2005]:

$$C'_{P,S} = C'_{P,C} \left[ \frac{(d\Delta Q/dt)_3 - (d\Delta Q/dt)_1}{(d\Delta Q/dt)_2 - (d\Delta Q/dt)_1} \right], \quad [3.12]$$

where  $C_{PS}$ ' is the heat capacity of the substance,  $C_{PS}$ ' is the heat capacity of the calibration substance,  $d\Delta Q/dt$  is the slope of the heat flow, and (1), (2), and (3) are three heat flow charts corresponding to the empty equipment, indium, and the substance studied. Figure 3.28 shows the liquid heat capacity of one of the biodiesel samples after Equation 3.12 has been applied.

The heat flow chart, Figure 3.27, can also be used to determine phase transitions [Haines, 2002, Weir and de Loos, 2005]. For instance, Figure 3.29 shows the heat flow chart as a function of temperature. The inflection point in Figure 3.29 is an indication of a phase transition; in this case, for a biodiesel, the inflection point determines the cloud point of the biodiesel (wax precipitation onset) [Knothe and van Gerpen, 2005].

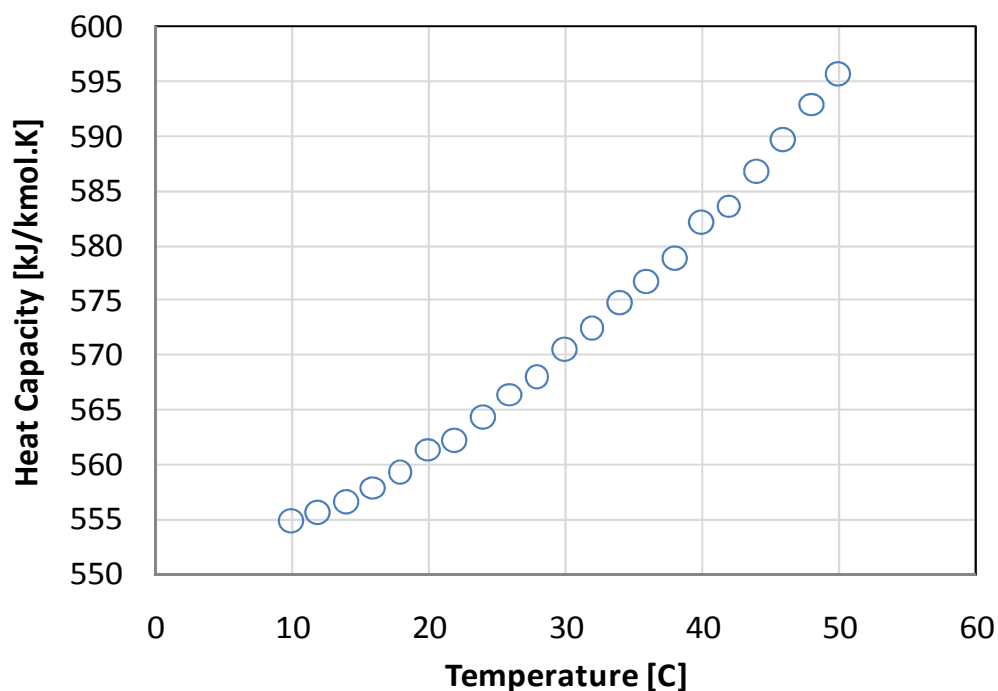


**Figure 3.42** Heat capacity as a function of temperature.

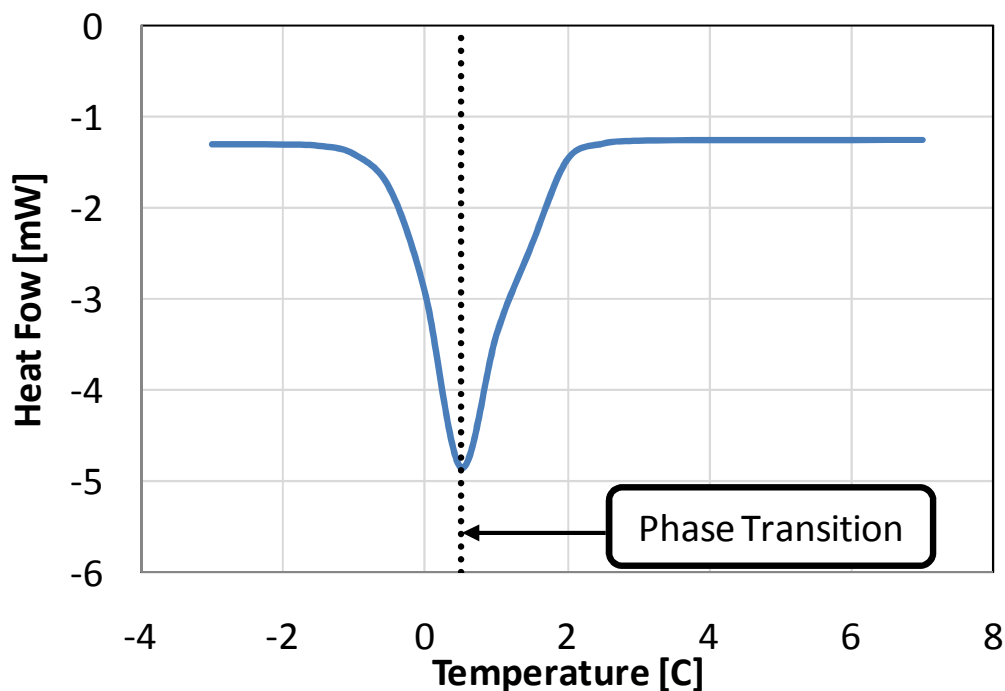


**Figure 3.43** Heat flow as a function of temperature for a biodiesel fuel; sample size is 8.04 mg.

### 3.7 Summary

The development of the new high vacuum vapour pressure measurement system and testing procedures were introduced in this chapter, including the different preliminary criteria for the design, a description of the constituents of the system (complemented by Appendix B), preliminary testing and calibration, procedures for vapour pressure and fractionation of heavy substances, pure component vapour pressure assessment, and measurement of vapour pressure of heavy pure substances.

The final design is a two stage apparatus including a degassing section and a measurement or fractionation section. Among the many variables and challenges

encountered in the design and construction of this system, the following are the most noteworthy.

- The selection of seals that can maintain high vacuum conditions was critical for the performance of the apparatus.
- A non-linear calibration was required for vapour pressure data below  $10^{-2}$  kPa.
- Thermal transpiration must be taken into account at pressures close to  $10^{-3}$  kPa.

## CHAPTER FOUR: CONSTRAINED EXTRAPOLATION OF VAPOR PRESSURE

Chapter 4 introduces a modelling method for vapour pressures at vacuum conditions. Experimental data at pressures below  $10^{-4}$  kPa do not have a well established uncertainty and are not recommended for vapour pressure modelling. Hence, additional calorimetric data are required in order to constrain the model at these low pressure values. A modelling framework for both analytical and equation-of-state approaches is developed that will be used to assess literature data and experimental data obtained with the HV-VPMS in subsequent chapters.

### 4.1 Introduction

For substances with high molecular weights, it is a challenge to obtain reliable vapour pressure data. The vapour pressure of these components can be lower than  $10^{-4}$  kPa at low to moderate temperatures. At these pressure values, the uncertainty of direct pressure readings increases dramatically due to adsorption-desorption and permeation processes inside the measurement apparatus [Roth, 1990; Fulem, 2009]. To overcome this issue, indirect measurements such as effusion or transpiration methods (Chapter 2) are performed [Weir and de Loos, 2005]. However, these indirect techniques may generate new sources of error when the vapour pressure is calculated from the experimental data.

An alternative to indirect measurements is to extrapolate reliable vapour pressure data points measured above  $10^{-4}$  kPa towards lower values. As suggested by Růžička and Majer [1996], heat capacity data can be used to constrain the vapour pressure equation since heat capacity is related to vapour pressure and heat capacity data can be more measured reliably at low temperatures. For example, consider the vapour pressure and liquid heat capacity of methyl oleate (MW = 296 g/g-mol), Figure 4.1.

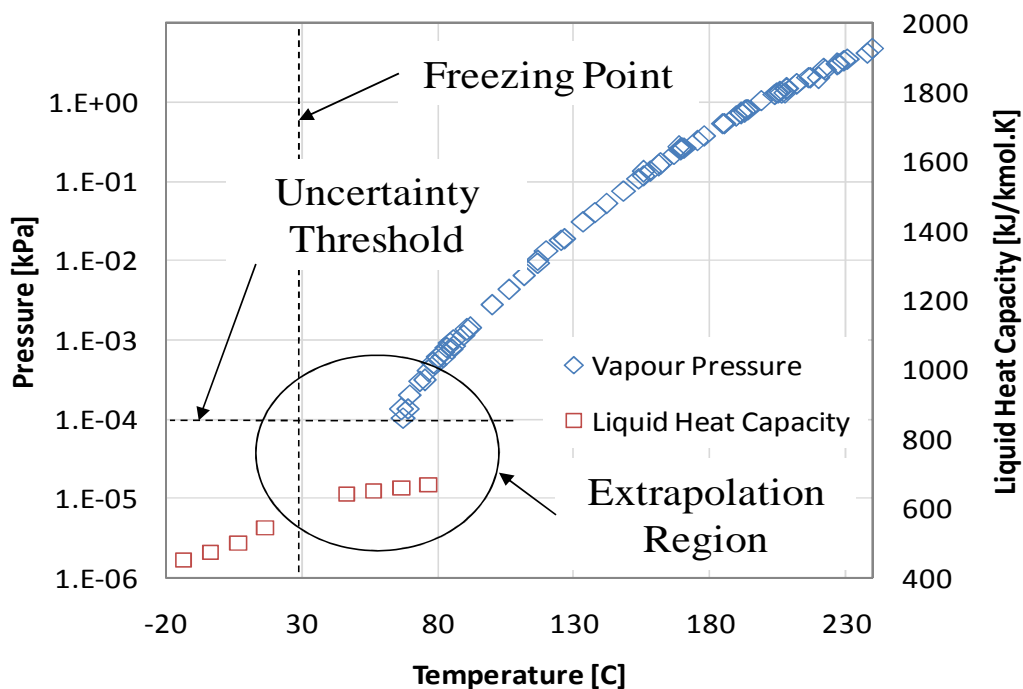


**Figure 4.1** Vapour pressure and heat capacity of methyl oleate; constrained extrapolation of vapour pressure is backed up by liquid heat capacity data above the freezing point.

The experimental vapour pressure data above  $10^{-4}$  kPa (with known uncertainty) can only be obtained at relatively high temperatures (above 67 °C). However, liquid heat capacity data can be easily obtained at lower temperatures where the vapour pressure is expected

to be below the uncertainty threshold. Since these two properties are directly related, the liquid heat capacity can be used to constrain and corroborate an extrapolation of the vapour pressure towards the freezing point of the substance.

The vapour pressure of a component is related to its heat of vaporization through the Clausius-Clapeyron equation [Poling et al. 2001]:

$$\frac{d \ln P_V}{d\left(\frac{1}{T}\right)} = -\frac{\Delta H_V}{R}, \quad [4.1]$$

where  $P_V$  is the vapour pressure,  $T$  is temperature,  $R$  is the universal gas constant, and  $\Delta H_V$  is the enthalpy of vaporization. The enthalpy of vaporization is related to temperature as follows:

$$\frac{\partial(\Delta H_V)}{\partial T} = C_{P,V} - C_{P,L} = \Delta C_P, \quad [4.2]$$

where  $C_{P,V}$  and  $C_{P,L}$  are the heat capacity of the vapour and liquid phases and  $\Delta C_P$  is the difference in the liquid-vapour heat capacities at the phase transition. Equation 4.2 is then substituted into the differential of Equation 4.1 to obtain the relationship between vapour pressure and heat capacity:

$$\Delta C_P = R \left[ \frac{d}{dT} T^2 \left( \frac{d \ln P_V}{dT} \right) \right], \quad [4.3]$$

To constrain a vapour pressure model with heat capacity data, the first step is to identify a vapour pressure model appropriate for the fluid under consideration. Then, the phase transition heat capacity difference is calculated from the model using Equation. 4.3. Finally, the following optimization function is used to tune the vapour pressure model to both vapour pressure and heat capacity data:

$$\min j = \sum_i (\ln P_{V,i}^{\text{Exp}} - \ln P_{V,i}^{\text{Calc}})^2 + K_C \sum_j (\Delta C_{P,j}^{\text{Exp}} - \Delta C_{P,j}^{\text{Calc}})^2, \quad [4.4]$$

where  $i$  stands for the experimental data points and  $K_C$  is a weight factor which scales the heat capacity data to the same magnitude as the natural logarithm of the vapour pressure data. Note that the enthalpy of vaporization can be included into Equation 4.4 if experimental data are available; however, this is usually not the case and Equation 4.4 is generally used [Růžička and Majer 1996].

In this thesis, two approaches are considered for the modelling vapour pressure: 1) analytical, using vapour pressure equations and ideal liquid mixing; 2) equation of state, using the Peng-Robinson equation of state (PR EoS). Each approach is described below.

## 4.2 Analytical Approach

In this approach, the vapour pressure of a mixture is calculated assuming an ideal solution of its constituents as given by Raoult's law:

$$P_{v,\text{Mix}}^{\text{Calc}} = \sum_j x_j P_{v,j}, \quad [4.5]$$

where  $x$  and  $P_v$  are the mole fraction and total ideal vapour pressure of component  $j$ , respectively. To calculate the vapour pressure of the mixture, the composition of the mixture is required as well as a correlation to determine the vapour pressure of the constituents. Růžička and Majer [1996] recommend the Cox equation, among the common vapour pressure equations, to be used when extrapolation is required. This equation has the advantage of not depending on critical properties. In this work, a three degree Cox equation was used [Cox, 1923]:

$$\ln P_V = \ln P_{\text{Ref}} + \left(1 - \frac{T_{\text{Ref}}}{T}\right) \exp(a_{PV,0} + a_{PV,1}T + a_{PV,2}T^2), \quad [4.6]$$

where  $P_{\text{Ref}}$  is a reference pressure at  $T_{\text{Ref}}$ , and  $a_{PV,1-2-3}$  are the correlation constants. The reference state in the Cox equation should be one close to where the extrapolation is intended. For instance, the normal boiling point of the substance may be used when extrapolation at high temperatures is required whereas the normal freezing point may be used if the extrapolation is intended at low pressure values.

For the Cox equation, an equation for calculating the phase transition heat capacity can be obtained, introducing Equation 4.2 into Equation 4.5:

$$\Delta C_P = RT \left[ 2a_{Pv,1} + 4a_{Pv,2}T + (T - T_{Ref}) \left( 2a_{Pv,2} + (a_{Pv,1} + 2a_{Pv,2})^2 \right) \right] \left[ \exp(a_{Pv,0} + a_{Pv,1}T + a_{Pv,2}T^2) \right], \quad [4.7]$$

For an ideal mixture, the phase transition heat capacity of the mixture is given by:

$$\Delta C_{P,mix} = \sum_j x_j \Delta C_{P,j}, \quad [4.8]$$

Usually, liquid heat capacity experimental data are available in the open literature rather than phase transition heat capacity differences. Hence, it is convenient to have an explicit expression for liquid heat capacity from the model; that is:

$$C_{P,L,mix} = C_{P,V,mix} + \Delta C_{P,mix}, \quad [4.9]$$

Since the pressure of the system to be evaluated is low, the vapour phase can be regarded as ideal; hence, the vapour phase heat capacity can be approximated as that of an ideal gas,  $C_P^0$ , and Equation 4.9 becomes:

$$C_{P,L,mix} \approx \sum_i C_{P,i}^0 + \Delta C_{P,mix}, \quad [4.10]$$

Experimental ideal gas heat capacity data for heavy components are scarce; however, reliable predictive methods are available. Most of these methods are based on group contribution methods. Appendix C lists three methods used in this thesis: Joback's method [Poiling et al, 2001], a modified version of the Benson method [Bureš et al., 1981], and the Laštovka -Shaw equation [Laštovka and Shaw, 2008].

The complete set of model equations is then:

$$P_{v,Mix}^{Calc} = \sum_j x_j \exp \left[ \ln P_{Ref,j} + \left( 1 - \frac{T_{Ref,j}}{T} \right) \exp(a_{Pv,0,j} + a_{Pv,1,j}T + a_{Pv,2,j}T^2) \right], [4.11]$$

$$C_{P,L,mix} \approx \sum_i C_{P,i}^0 + RT \left[ 2a_{Pv,1,i} + 4a_{Pv,2,i}T + (T - T_{Ref,i}) \left( 2a_{Pv,2,i} + a_{Pv,1,i} + 2a_{Pv,2,i} \exp(a_{Pv,0,i} + a_{Pv,1,i}T + a_{Pv,2,i}T^2) \right) \right], [4.12]$$

Finally, the Cox parameters in Equations 4.11 and 4.12 are optimized to fit experimental data using Equation 4.5. A value of  $K_C = 1/100$  was used to scale the heat capacity data in kJ/kmol.K to vapour pressure data in kPa.

### 4.3 Equation of State Approach

In the previous section the vapour pressure was modelled using vapour pressure equations. This approach gives correct values for the enthalpy of vaporization and heat

capacity through the Clapeyron equation, if they are correctly fitted. However, a more comprehensive approach is to model vapour pressure using an equation of state which, if correctly fitted, can be used to determine phase equilibria in multi-component mixtures.

#### ***4.3.1 Peng-Robinson Equation of State***

In this work, the Peng-Robinson equation of state [Peng and Robinson, 1976] was selected because it is one of the most successful EoS for non-polar and slightly polar systems. The PR EoS is given by:

$$P = \frac{RT}{v-b} - \frac{a\alpha(\omega, T_R)}{v(v+b)+b(v-b)}, \quad [4.13]$$

where  $v$  is the molar volume,  $b$  is the excluded volume of a molecule,  $T_R$  is the reduced temperature ( $T/T_C$ ),  $T_C$  is the critical temperature,  $\omega$  is the acentric factor,  $a$  is the attractive force parameter and  $\alpha$  is an adjustable parameter to fit the equation of state to the vapour pressure of the substance; that is the saturation pressure or bubble point at a given temperature.

For a pure component, the attractive and repulsive terms are determined through the critical properties of the substance, as:

$$a_i = \frac{0.457265R^2T_{C,i}^2}{P_{C,i}}, \quad [4.14]$$

$$b_i = \frac{0.0777969RT_{C,i}}{P_{C,i}}, \quad [4.15]$$

where  $P_C$  is the critical pressure. In a mixture, the  $a$  and  $b$  parameters are calculated from mixing rules applied to the individual component parameters. In this work, the classic Van der Waals mixing rules are used, given by:

$$b_m = \sum_i x_i b_i, \quad [4.16]$$

$$a_m = \sum_i x_i x_j \sqrt{a_i a_j} (1 - k_{ij}), \quad [4.17]$$

where  $k_{ij}$  stands for the interaction parameters between substance  $i$  and  $j$ . Note that a more sophisticated mixing rule is not considered in this work since the phase behaviour of biodiesels and heavy oil considered in this thesis is expected to be simple; that is, single liquid/vapour phase transitions (Chapter 2). The  $\alpha$ -function for the Peng-Robinson EoS is given by [Wallas, 1985]:

$$\alpha(\omega, T_R) = [1 + f_W(1 - T_R^{0.5})]^2, \quad [4.18]$$

where  $f_W$  is a function of the acentric factor given by:

$$f_W = 0.37464 + 1.54226\omega - 0.26992\omega^2, \quad \omega < 0.5 \quad [4.19a]$$

$$f_W = 0.3796 + 1.485\omega - 0.1644\omega^2 + 0.01667\omega^3, \quad \omega > 0.5 \quad [4.19b]$$

It is useful for calculation purposes to express the equation of state in terms of the compressibility factor,  $Z = PV/RT$ . For the Peng-Robinson EoS, Equation 4.13 is written as [Poiling et al., 2001]:

$$Z^3 - Z^2(1 - B) + Z(A - 2B - 3B^2) - B(A - B - B^2) = 0, \quad [4.20]$$

where  $A$  and  $B$  are defined by:

$$A = \frac{a\alpha(\omega, T_R)P}{(RT)^2}, \quad [4.21]$$

$$B = \frac{bP}{RT}, \quad [4.22]$$

### 4.3.2 Vapour pressure of a pure component

As explained in Chapter 2, the vapour-liquid equilibrium conditions of a pure component can be determined through the equality of the fugacities of the component in each phase [Wallas, 1985]:

$$f^V = f^L, \quad [4.23]$$

where  $f^V$  and  $f^L$  are the fugacities of the vapour and liquid phases, respectively. The fugacity coefficients for each phase are calculated through the Peng-Robinson equation of state as follows:

$$\ln\left(\frac{f^{Phase}}{P}\right) = Z_{Phase} - 1 - \ln(Z_{Phase} - B) - \frac{A}{2.828B} \ln\left(\frac{Z_{Phase} + 2.414B}{Z_{Phase} - 0.414B}\right), \quad [4.24]$$

Usually, Equation 4.24 is solved as follows [Soave, 1986]:

- Assume a value for the vapour pressure
- Calculate the  $A$  and  $B$  parameters from Equations 4.21 and 4.22
- Determine values of  $Z_L$  and  $Z_V$  by solving Equation 4.20 and choosing the lowest and highest roots
- Calculate the fugacities from Equation 4.24
- Modify the vapour pressure if Equation 4.23 is not satisfied

This procedure is iterative since Equation 4.24 is implicit in pressure. As an alternative for pure substances, Soave [1986] proposed the following explicit equation in pressure:

$$\ln\left(\frac{P_R}{T_R}\right) = \sum_{k=1}^4 C_k \left(\frac{\alpha}{T_R-1}\right)^{(k+1)/2} + \sum_{k=5}^{10} C_k \left(\frac{\alpha}{T_R-1}\right)^{k-2}, \quad [4.25]$$

where  $C_k$  is a vector of constants and is tabulated in Table 4.1

**Table 4.8** Constants for the saturation pressure calculation of pure substances using Peng-Robinson Equation of state [Soave, 1986]

<b>k</b>	<b>C<sub>k</sub></b>
1	-3.3466262
2	-9.9145207x10 <sup>-2</sup>
3	1.015969390
4	-1.032780679

5	0.2904927517
6	1.64073501 x10 <sup>-2</sup>
7	-9.67894565 x10 <sup>-3</sup>
8	1.74161549 x10 <sup>-3</sup>
9	-1.56974110 x10 <sup>-4</sup>
10	5.87311295 x10 <sup>-6</sup>

### 4.3.3 Vapour Pressure of mixtures

At equilibrium, the fugacities of each component in each phase are equal:

$$f_i^V = f_i^L, \quad [4.26]$$

However, for mixtures, it is common practice to use equilibrium K-values instead of fugacity values. The K-values are defined, at equilibrium conditions (Equation 4.26), as:

$$K_i = \frac{\phi_i^L}{\phi_i^V} = \frac{f_i^L/x_iP}{f_i^V/y_iP} = \frac{y_i}{x_i}, \quad [4.27]$$

where  $\phi_i^j$  stands for the fugacity coefficient of component  $i$  in phase  $j$ , and  $x_i$  and  $y_i$  stand for the mole fraction of component  $i$  in the liquid and gas phase, respectively. The summation of the gas phase mole fraction equates to unity and Equation 4.27 can be substituted into this summation to obtain:

$$\sum_i y_i = 1 = \sum_i K_i x_i, \quad [4.28]$$

Note that the vapour pressure is a bubble point and, at the bubble point, the composition in the liquid phase,  $x_i$ , is identical to the composition of the feed (mixture). Hence, the values of  $x_i$  are known parameters at this condition. The K-values for each component are calculated from the Peng-Robinson equation of state as follows [Poiling et al., 2001]

$$\ln \Phi_i^j = \frac{b_i}{b_m} (Z^j - 1) - \ln(Z^j - B) - \frac{A}{2\sqrt{2}B} \left( \frac{2\sum_k x_k a_k}{a_m} - \frac{b_i}{b_m} \right) \ln \left( \frac{Z^j + 2.414B}{Z^j - 0.414B} \right), \quad [4.29]$$

where  $i$  stands for the component,  $j$  stands for the phase. Note that the K-values for each component depend on the temperature (a known parameter) and the pressure of the system (the target parameter); since Equation 4.29 is implicit in pressure, solving Equation 4.28 becomes an iterative process. Usually, the vapour pressure of a mixture is calculated through the following procedure [Michelsen, 1982, Soave, 1986]:

- Assume a value for the vapour pressure
- Calculate parameters  $a_m$  and  $b_m$  through Equations 4.15 and 4.16
- Calculate  $A$  and  $B$  parameters through Equations 4.21 and 4.22
- Determine values of  $Z_L$  and  $Z_V$  by solving Equation 4.20 and choosing the lowest and highest roots
- Calculate fugacity coefficients for each component and each phase from Equation 4.29

- Calculate K-values for each component from Equation 4.27
- Modify the vapour pressure if Equation 4.28 is not satisfied

Figure 4.2 shows Equation 4.28 plotted as a function of pressure. Note that, in this case, the function is smooth and, hence, a simple numerical model is sufficient.

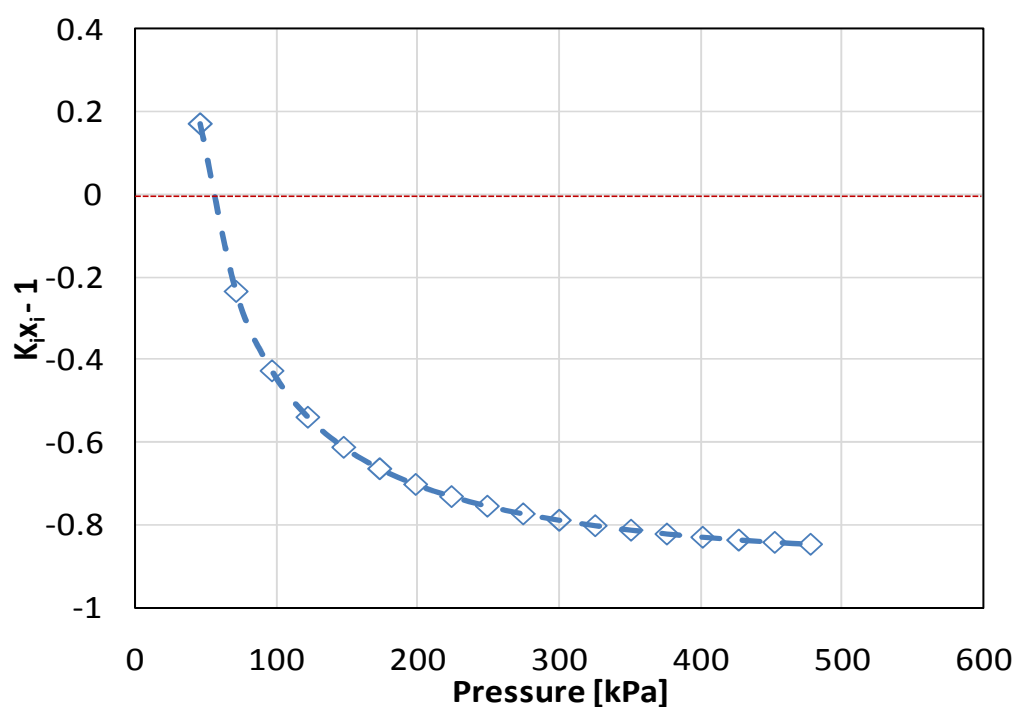


**Figure 4.2** Optimization function for vapour pressure determination.

#### 4.3.4 Heat Capacities and Heat of Vaporization

The enthalpy of vaporization,  $\Delta H_V$ , is defined as [Poiling et al., 2001]

$$\Delta H_V = h_V - h_L, \quad [4.30]$$

where the individual heat capacity contributions,  $h$ , for each phase are calculated as

$$h_j = \frac{1}{\sqrt{8}b} \ln \left[ \frac{2Z_j + B(2 - \sqrt{8})}{2Z_j + B(2 + \sqrt{8})} \right] \left( a\alpha - T \frac{da\alpha}{dT} \right) + RT(Z_j - 1), \quad [4.31]$$

where  $j$  stands for the phase. The phase transition heat capacity can be calculated as:

$$\Delta C_P = C_{P,V} + C_{P,L} \approx C_P^0 + C_{P,L} = C_P^{Res}, \quad [4.32]$$

The heat capacity residue is given by [Poiling et al., 2001]

$$C_P^{Res} = \int_{\infty}^V T \left( \frac{\partial^2 P}{\partial T^2} \right)_V dV - T \frac{\left( \frac{\partial P}{\partial T} \right)_V^2}{\left( \frac{\partial P}{\partial V} \right)_T} - R, \quad [4.33]$$

Using the Peng-Robinson equation of state, Equation 4.33 becomes

$$C_P^{Res} = -T \left[ \frac{1}{b\sqrt{8}} \frac{d^2 a}{dT^2} \log \left( \frac{v+b(1-\sqrt{2})}{v+b(1+\sqrt{2})} \right) + \frac{\left( \frac{R}{v-b} \frac{da}{dT} \frac{1}{(v^2+2bv-b^2)} \right)^2}{\frac{-RT}{(v-b)^2} + \frac{2a(v+b)}{(v^2+2bv-b^2)^2}} \right] - R, \quad [4.34]$$

Note that in order to use Equation 4.32, a model for the ideal gas heat capacity is required. A direct calculation of the ideal heat capacity using the equation of state does not exist and a property correlation methodology is required (Appendix C).

#### ***4.3.5 Adjustment of the Peng-Robinson EoS to Experimental Data***

As with the analytical approach, the equation of state is tuned to fit the experimental data using Equation 4.5. For a pure component, the acentric factor or the function  $f_w$ , Equation 4.19, is adjusted during the optimization. For heavy components, the critical properties and acentric factor must be predicted or adjusted to the vapour pressure data because these components decompose at temperatures below their critical point and therefore experimental values do not exist.

For mixtures, the interaction parameters or mixing rules can be modified. Note, however, that the liquid heat capacity of mixtures is almost insensitive to the interaction parameters since it depends on the second derivative of the attraction parameter in the equation of state. In this case, the heat capacity is not used to constrain the model but rather to verify that the mixture model is accurate for both vapour pressure and heat capacity.

### **4.4 Summary**

A framework was introduced for modeling vapour pressure constrained by liquid heat capacity. The method provides a way determine vapour pressure when experimental data

are not available (above the cracking temperature) or are uncertain (at pressures below  $10^{-4}$  kPa). This modelling framework will be used for biodiesel vapour pressure (Chapters 5 and 6), heavy oil vapour pressure (Chapter 7), and as part of an inter-conversion method to transform measured vapour pressures to atmospheric equivalent boiling points (Chapter 8).

## CHAPTER FIVE: MODELLING THE VAPOR PRESSURE OF FATTY ACID METHYL ESTERS

Chapter five introduces the modelling of the vapour pressure of fatty acid methyl esters (FAMES) which are the main constituents of biodiesel fuels. Modelling FAME vapour pressure is the first step in modelling the vapour pressure of biodiesel fuels. The FAMES model also provides a relatively straightforward application of the vapour pressure method provided in Chapter 4. Both the analytical approach and equation-of-state approaches are examined. In addition, new equations are developed for the liquid and ideal gas heat capacity as well as the vapour pressure of FAMES.

### 5.1 Introduction

Fatty acid methyl esters (FAMES) are produced by the transesterification of fatty acids from vegetable oil and animal fat (Chapter 2) and comprise the main constituents of biodiesel fuels. In common biodiesel fuels, the fatty acid esters range in carbon number from  $C_6$  to  $C_{24}$  (Table 5.1). FAMES can be saturated or unsaturated (with one, two, or three double bonding carbons) [Allen et al., 1999; Goodrum, 2002; Ott and Bruno, 2008].

Since FAMES are the constituents of biodiesels, modelling their vapour pressure is a key step in developing a model for the vapour pressure of these fuels. The vapour pressure of

FAMEs is expected to be very low (below  $10^{-4}$  kPa at room temperature) for components with carbon numbers higher than 14. Hence, it is also important to constrain the vapour pressure model with heat capacity data, as introduced in Chapter 4.

Since data were not available for all FAMEs, the modeling approach was developed in four steps: 1) develop a correlation based on experimental liquid heat capacity data, to estimate the phase transition heat capacities; 2) fit the constrained vapour pressure equation to the available vapour pressure data; 3) develop a vapour pressure correlation for FAMEs for which data are not available; 4) predict the vapour pressure of the FAMEs with no available data. Section 5.2 presents the available data and each step in the model development is discussed in Sections 5.3 to 5.5.

## 5.2 FAMEs Physical Properties

Experimental data of twenty fatty acid methyl esters, ranging in carbon number from 6 to 22, were assessed, Table 5.1. The vapour pressure data set ranges in temperature from 25 to 320 °C whereas liquid heat capacity data ranges from the freezing point to 76 °C.

**Table 5.9** Experimental data for selected FAMEs and temperature range in °C [NIST, 2010].

FAME	Formula	$P_V$			$C_{PL}$		
		Points	$T_{min}$	$T_{max}$	Points	$T_{min}$	$T_{max}$
Methyl hexanoate	C6:0	65	7.55	146.52	-	-	-
Methyl caprylate	C8:0	53	33.69	145.70	12	-	76.85

						33.15	
Methyl caprate	C10:0	70	-	188.20	10	-3.15	76.85
			12.74				
Methyl laurate	C12:0	112	-	226.85	8	6.85	76.85
			11.00				
Methyl myristate	C14:0	90	0.00	237.8	7	25	76.85
Methyl pentadecanoate	C15:0	29	21.85	226.85	5	26.85	76.85
Methyl palmitate	C16:0	110	18.00	321.95	5	36.85	76.85
Methyl heptadecanoate	C17:0	27	21.85	226.85	5	36.85	76.85
Methyl stearate	C18:0	101	21.85	346.95	4	46.85	76.85
Methyl arachidate	C20:0	29	38.00	226.85	3	56.85	76.85
Methyl behenate	C22:0	12	21.85	258.95	-	-	-
Methyl lignocerate	C24:0	-	-	-	-	-	-
Methyl palmitoleate	C16:1	4	26.85	176.85	-	-	-
Methyl heptadecenoate	C17:1	-	-	-	-	-	-
Methyl oleate	C18:1(11)	33	26.85	218.50	-	-	-
Methyl vaccenate	C18:1(9)	-	-	-	-	-	-
Methyl cis-11-eicosenoate	C20:1(11)	-	-	-	-	-	-
Methyl erucate	C22:1	8	26.85	176.85	-	-	-
Methyl linoleate	C18:2	18	26.85	214.95	-	-	-
Methyl linolenate	C18:3	12	26.85	185.7	-	-	-

### 5.3 Phase Transition Heat Capacity

The liquid/vapour phase transition heat capacity is determined as the difference between the heat capacity of the saturated liquid and the saturated vapour, Equation 5.1.

$$\Delta C_{P,FAME} = C_{P,L,FAME} - C_{P,V,FAME} \approx C_{P,L,FAME} - C_{P,FAME}^0, \quad [5.1]$$

where  $C_{PL}$ ,  $C_{PV}$ , and  $C_P^0$  stand for the liquid, vapour, and ideal gas heat capacity. Note that since we are concerned with low vapour pressures, the vapour phase can be regarded

as ideal and  $C_{P,V} \approx C_P^0$  [Růžička and Majer, 1996]. Hence, correlations for the ideal gas and liquid heat capacity are required.

### 5.3.1 Ideal Gas Heat Capacity

No experimental data for the ideal gas heat capacity of FAMES are available in the open literature; hence, a predictive method for this property is required. The model applied in this section is based in part on residual heat capacities calculated with the Peng-Robinson equation of state and is developed in Section 5.6.3. For convenience, the model equations, which are independent of the EOS, are presented here.

#### Saturated FAMES

For saturated FAMES, the ideal gas heat capacity is calculated as follows:

$$C_P^0(0) = a_{CP0} + b_{CP0}T + c_{CP0}T^2, \quad [5.2]$$

where  $a_{CP0}$ ,  $b_{CP0}$ , and  $c_{CP0}$  are calculated as:

$$a_{CP0} = \frac{-2.1079 \times 10^4}{MW - 344.1759} + 230.72 + 0.62516(MW - 344.1759), \quad [5.3]$$

$$b_{CP0} = \frac{125.93}{MW - 344.1759} + 1.4529 + 5.5554 \times 10^{-3}(MW - 344.1759), \quad [5.4]$$

$$c_{CP0} = \frac{-0.19127}{MW - 344.1759} - 8.8626 \times 10^{-4} - 5.9999 \times 10^{-6}(MW - 344.1759), \quad [5.5]$$

### Unsaturated FAMES

For unsaturated FAMES, the ideal gas heat capacity can be calculated, based in its saturated FAME counterpart, using the following expression:

$$\frac{C_P^0(N_{UC})}{C_P^0(0)} = [1 + N_{UC}(-6.1327 \times 10^{-2} + 1.5493 \times 10^{-4}T - 1.842 \times 10^{-7}T^2)], \quad [5.6]$$

where  $N_{UC}$  stands for the number of double bonding in the molecule

### **5.3.2 Liquid Heat Capacity**

#### Saturated FAMES

The liquid heat capacity data of saturated FAMES were regressed to a three degree polynomial, Figure 5.1:

$$C_{PL} = a_{C_{PL-0}} + a_{C_{PL-1}}T + a_{C_{PL-2}}T^2 + a_{C_{PL-3}}T^3, \quad [5.7]$$

where  $C_{PL}$  is the liquid heat capacity in kJ/kmol.K, temperature  $T$  is in Kelvin and  $a_{C_{PL-i}}$  are the adjustable parameters. Values for the constants  $a_{C_{PL}}$  are listed in Table 5.2.

**Table 5.10** Regressed constants for liquid heat capacity for FAMES according to Equation 5.7; temperature in Kelvin.

<b>Formula*</b>	$a_{C_{PL-0}}$	$a_{C_{PL-1}} \times 10^2$	$a_{C_{PL-2}} \times 10^5$	$a_{C_{PL-3}} \times 10^7$	$T_{\min}$	$T_{\max}$	AARD
C8:0	7.29	-4.49	1.49	-1.50	240	350	0.12%
C10:0	-23.36	25.52	-8.09	8.67	270	350	0.34%
C12:0	-23.05	25.76	-8.19	8.83	280	350	0.07%

C14:0	-22.37	26.24	-8.48	9.26	298	350	0.31%
C15:0	-137.38	131.37	-40.43	41.64	300	340	0.04%
C16:0	-22.87	26.07	-8.09	8.56	310	350	0.04%
C17:0	-22.72	26.22	-8.12	8.54	310	350	0.07%
C18:0	-22.81	26.18	-8.04	8.46	320	350	0.03%
C20:0	-21.46	27.14	-8.78	9.64	330	350	-

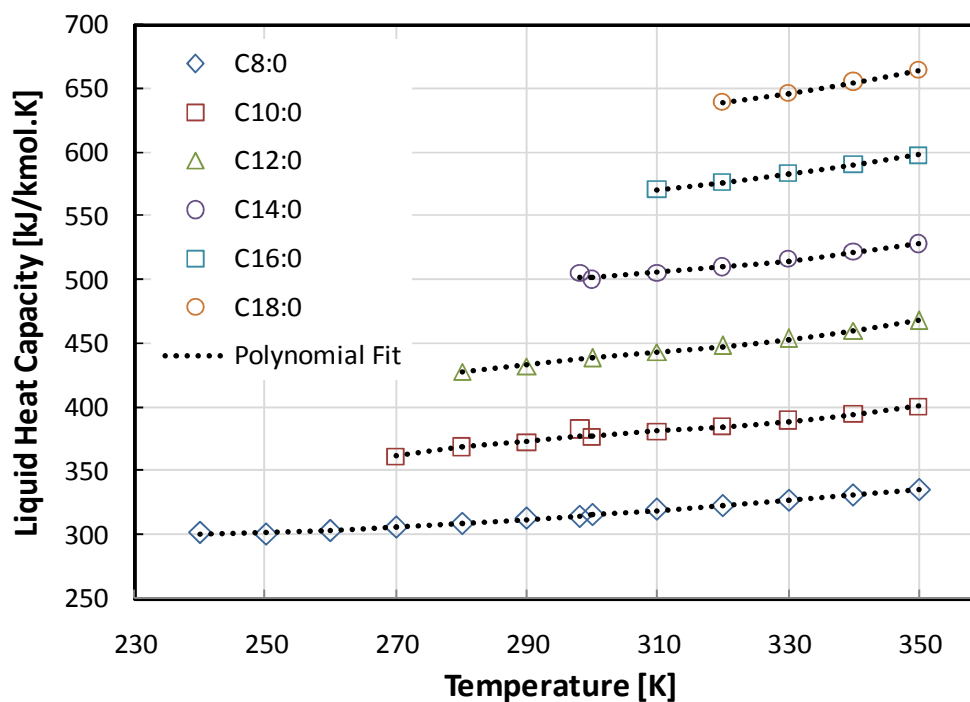


**Figure 5.1** Experimental and regressed liquid heat capacities for selected FAMES.

The Dadgostar-Shaw predictive equation [2011] was applied to determine the liquid heat capacity of the FAMES with no available experimental data:

$$c_{PL} = a_1(\alpha_{Cp}) + a_2(\alpha_{Cp})T + a_3(\alpha_{Cp})T^2, \quad [5.8]$$

where  $\alpha_{Cp}$  is a similarity variable which is related to the elementary composition of a substance as follows:

$$\alpha_{Cp} = \frac{\sum_k \nu_k}{\sum_k \nu_k MW_k}, \quad [5.9]$$

where  $\nu_K$  stands for the stoichiometric number of the molecule  $K$  and  $MW_K$  is the molecular weight. The constants  $\alpha_i$  are given by:

$$a_1(\alpha_{Cp}) = 24.5(-0.3416\alpha + 2.2671\alpha^2), \quad [5.10]$$

$$a_2(\alpha_{Cp}) = -0.1064 \pm 0.3874\alpha^2, \quad [5.11]$$

$$a_3(\alpha_{Cp}) = -9.8231 \times 10^{-5} + 4.182 \times 10^{-4}\alpha^2, \quad [5.12]$$

Equation 5.8 was first applied to calculate the available liquid heat capacity experimental data of the FAMES listed in Table 5.1, with a total AARD of 2.4%. Figure 5.2 shows the experimental data and predicted results for methyl palmitate and Table 5.4 shows specific AARD values for the FAMES. This simple method gives good representative values of FAMES heat capacities. However, to obtain even more precise predictions, a correction factor was introduced as follows:

$$c_{PL} = \left( a_{F1} + a_1(\alpha_{Cp}) \right) + \left( a_{F2} + a_2(\alpha_{Cp}) \right) T + \left( a_{F3} + a_3(\alpha_{Cp}) \right) T^2, \quad [5.13]$$

where  $a_{Fi}$  are the FAMEs correction factors (Table 5.3). The corrected equation, specific to FAMEs, improved the error with a total AARD of 0.7%. Figure 5.2 shows the experimental data and predicted results for methyl palmitate and Table 5.4 lists the AARD for each FAME. The corrected equation was then used to predict the liquid heat capacity of the FAMEs for which data were unavailable (Table 5.1) from their molecular formula.

**Table 5.11** Modified parameters of the Dadgostar-Shaw equation for FAMEs

$a_{F1}$	$a_{F2}$	$a_{F3}$
2.279	$-6.956 \times 10^{-3}$	$9.509 \times 10^{-6}$

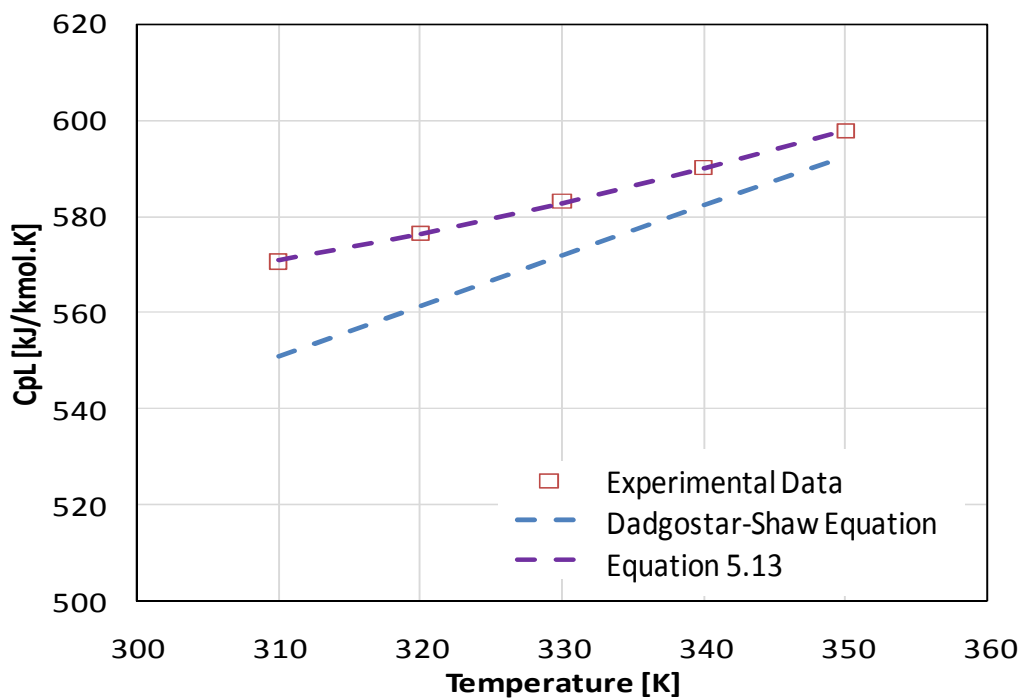


**Figure 5.2** Experimental and predicted liquid heat capacity for methyl palmitate, C16:0. Data from NIST [NIST, 2010].

**Table 5.12** Performance of Dadgostar-Shaw method, Equation 5.8, and Equation 5.13 for known FAMES liquid heat capacity; results of the polynomial regression, Equation 5.7 are shown for comparison.

FAME	Formula	AARD [%]		
		Eq. 5.8	Eq. 5.13	Eq. 5.7
M-Caprylate	C8:0	5.0	0.9	0.1%
M-Caprinate	C10:0	3.1	1.2	0.3%
M-Laurate	C12:0	2.7	0.8	0.1%
M-Myristate	C14:0	2.2	0.7	0.3%
M-Pentadecanoate	C15:0	1.5	1.3	0.0%
M-Palmitate	C16:0	2.0	0.0	0.0%
M-Heptadecanoate	C17:0	1.4	0.8	0.1%
M-Stearate	C18:0	1.8	0.1	0.0%
M-Arachidate	C20:0	2.0	0.7	-

### Unsaturated FAMES

No data were available for the ideal gas heat capacity of the unsaturated FAMES. Hence, it is assumed that the departure function from the corresponding saturated FAME is equal to the same departure function as calculated by Joback's method [Poiling et al., 2001] (Appendix C). The departure function from Joback's method is given by:

$$\frac{c_P^0(N_{UC})}{c_P^0(0)} = \frac{N_{CH_3} \sum_{i=0}^3 a_i T^i + N_{CH_2} \sum_{i=0}^3 b_i T^i + N_{COO} \sum_{i=0}^3 c_i T^i + N_{UC} \sum_{i=0}^3 d_i T^i + \sum_{i=0}^3 e_i T^i}{N_{CH_3} \sum_{i=0}^3 a_i T^i + N_{CH_2} \sum_{i=0}^3 b_i T^i + N_{COO} \sum_{i=0}^3 c_i T^i + \sum_{i=0}^3 e_i T^i}, \quad [5.14]$$

where  $N_{UC}$  is the number of unsaturated bonds (1, 2, or 3),  $N_{CH_3}$ ,  $N_{CH_2}$ , and  $N_{COO}$  are the number of function groups within the molecule, and  $a$ ,  $b$ ,  $c$ ,  $d$ , and  $e$  are standard parameters for the method. Equation 5.14 simplifies to the following expression:

$$\frac{c_p^0(N_{UC})}{c_p^0(0)} = [1 + N_{UC}(-6.1327 \times 10^{-2} + 1.5493 \times 10^{-4}T - 1.842 \times 10^{-7}T^2)] \text{ , [5.15]}$$

#### 5.4 Analytical Vapour Pressure Correlation for FAMES

The vapour pressure of both saturated and unsaturated FAMES was modeled with a three degree Cox equation constrained by heat capacity (Equations 4.11 and 4.12). Note that when there was no liquid heat capacity experimental data, Equation 5.13 or 5.15 were used to predict them. The reference state in the Cox equation should be one close to where the extrapolation is intended and the normal melting point (NMP) of the FAMES was selected. The normal melting points of the different FAMES were collected from the NIST data base [NIST, 2010] and are listed in Table 2.5. However, the vapour pressures of the FAMES at the NMP ( $P_{ref}$ ) were unknown and, therefore, became a fourth adjustable parameter in the Cox equation.

The parameters in the Cox equation were adjusted to the vapour pressure and heat capacities of the FAMES using the constrained optimization (Equation 4.5). Two scenarios were evaluated: Scenario 1: “All-data” is a regression of all the vapour pressure data available with no constraints ( $K_C = 0$  in Equation 4.5); Scenario 2: “Constrained” is a regression of vapour pressure data above  $10^{-4}$  kPa constrained with liquid heat capacity ( $K_C = 1/100$  in Equation 4.5). Table 5.5 shows the regressed coefficients for both scenarios. The AARD of both regression scenarios are shown in Table 5.6. Note that high

deviations in the vapour pressure for the “Constrained” scenario are mainly influenced by experimental values below  $10^{-4}$  kPa.

**Table 5.13** Cox equation parameters for all data and constrained data for FAMEs.

Formula	Scenario 1: All-data				Scenario 2: Constrained			
	$a_{Pv,1}$	$a_{Pv,2} \times 10^3$	$a_{Pv,3} \times 10^6$	$P_{Ref} \times 10^6$	$a_{Pv,1}$	$a_{Pv,2} \times 10^3$	$a_{Pv,3} \times 10^6$	$P_{Ref} \times 10^6$
C6:0	3.673	-1.154	1.058	25.83	3.534	-0.642	0.504	3.63
C8:0	2.973	1.854	-2.574	190.05	3.553	-0.694	0.481	108.04
C10:0	3.763	-1.329	1.074	75.91	3.603	-0.707	0.458	84.67
C12:0	5.053	-6.646	6.907	36.56	3.665	-0.776	0.494	69.24
C14:0	4.892	-5.432	5.252	19.40	3.752	-0.914	0.605	35.73
C15:0	3.970	-1.507	1.123	10.79	3.772	-0.758	0.389	12.35
C16:0	4.496	-3.269	2.685	8.85	3.791	-0.796	0.443	14.55
C17:0	4.121	-1.841	1.388	5.10	3.840	-0.883	0.541	6.454
C18:0	4.612	-3.409	2.740	3.30	3.855	-0.792	0.412	5.64
C20:0	3.987	0.102	-1.532	1.11	3.902	-0.866	0.501	3.02
C22:0	4.094	-0.659	-0.412	0.91	4.059	-1.245	0.716	1.70
C16:1	3.952	0.0834	-0.703	0.000283	4.073	-0.784	0.520	0.000488
C17:1	3.921	0.070	-1.384	0.000129	4.110	-0.669	0.350	0.000216
C18:1(9)	4.242	-0.851	0.255	0.000145	4.288	-1.080	0.527	0.000149
C20:1(11)	4.397	-1.459	1.070	0.000104	4.153	-0.679	0.381	0.000219
C22:1	4.457	-1.541	0.995	0.000193	4.299	-1.087	0.647	0.000323
C18:2	3.982	0.656	-1.324	0.00155 <sup>a</sup>	4.233	-0.855	0.600	0.00419 <sup>a</sup>
C18:3	2.552	6.982	-8.629	0.00352 <sup>a</sup>	4.280	-0.810	0.560	0.000447 <sup>a</sup>

<sup>a</sup> Reference pressure multiplied by  $10^9$

**Table 5.14** Performance of the vapour pressure and heat capacity equations for various FAMEs.

Formula	All-data		Constrained	
	AARD $P_V$ [%]	AARD $\Delta C_P$ [%]	AARD $P_V$ [%]	AARD $\Delta C_P$ [%]
C6:0	5.3	-	5.1	-
C8:0	8.6	162.7	8.6	1.9
C10:0	3.3	47.8	3.5	1.7
C12:0	3.9	283.2	4.1	1.2
C14:0	4.3	246.2	5.1	1.4

C15:0	0.7	52.7	0.6	1.3
C16:0	5.1	201.6	6.9	0.9
C17:0	1.4	77.5	1.8	0.3
C18:0	5.1	216.9	4.9	1.1
C20:0	9.4	129.	10.1	0.2
C22:0	23.3	-	32.8	-
C16:1	6.7	-	26.7	-
C17:1	-	-	-	-
C18:1(9)	3.9	-	4.3	-
C20:1(11)	-	-	-	-
C18:2	9.7	-	9.4	-
C18:3	9.6	-	10.6	-

Figures 5.3 and 5.4 show the results for methyl palmitate and methyl caprylate. Both regressions are similar at vapour pressures above  $10^{-4}$  kPa but they differ slightly at lower pressures (higher deviations were found with heavier FAMES). Note that the majority of experimental values below this threshold were indirect, most of them coming from gas chromatography experiments. On the other hand, liquid heat capacity values calculated with unconstrained data always deviated from literature data and, in some cases, the heat capacity predicted with the unconstrained equation incorrectly decreased with temperature, as shown in Figure 5.4 for methyl caprylate. The constrained regression produced consistent, precise predictions of the heat capacity, Table 5.6. Since heat capacity and vapour pressure are related, the “Constrained” correlation is expected to provide a better prediction of the low vapour pressures than the “All-data” correlation.

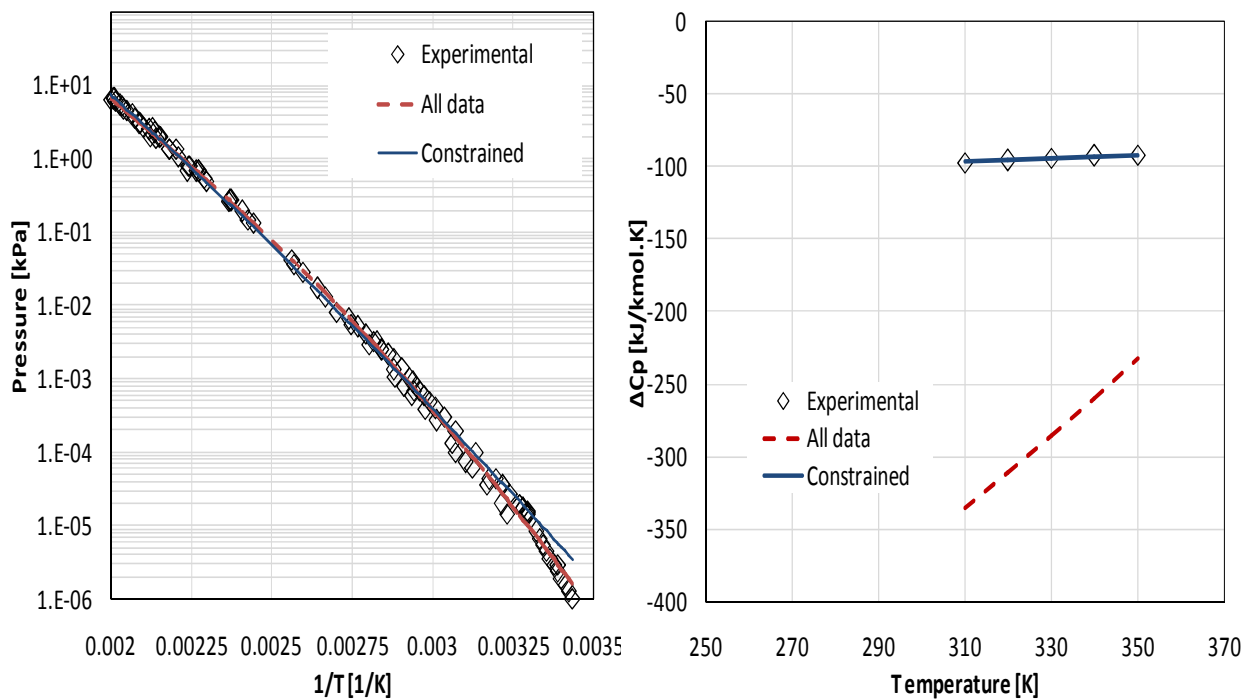


**Figure 5.3** Experimental and regressed vapour pressure of methyl palmitate (Data from NIST [2010]).

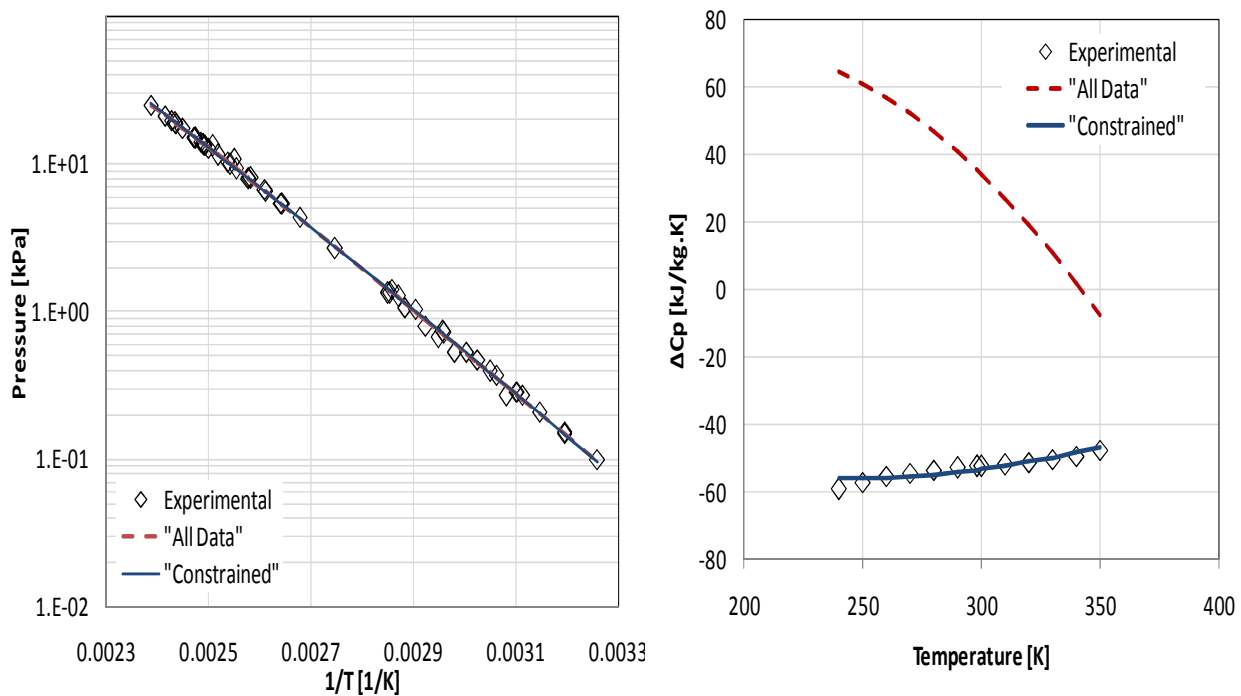


**Figure 5.4** Experimental and regressed vapour pressure of methyl caprylate (Data from NIST [2010]).

The vapour pressure correlations of the FAMES were extrapolated at high temperatures to calculate the normal boiling point. Table 5.7 shows the comparison of these values with experimental data (when available). While the extrapolation of the Cox equation to high temperatures is not expected to be reliable since it was referenced to the normal freezing point, the extrapolated boiling points of most of the FAMES are within 6.3% of the measured values. Note that some of the experimental values for the family of saturated FAMES do not follow a monotonic tendency with the molecular weight of the substance.

**Table 5.15** Experimental and Calculated normal boiling point of different FAMES (Data from NIST [2010]).

<b>FAME</b>	<b>Form.</b>	<b>Exp. NBP</b>	<b>All-data NBP</b>	<b>Constrained NBP</b>
M-Hexanoate	C6:0	423	422.45	421.75
M-Caprylate	C8:0	466.05	471.42	463.44
M-Caprate	C10:0	502.1	502.17	500.19
M-Laurate	C12:0	418.56	519.09	532.01
M-Myristate	C14:0	423.46	550.48	562.64
M-Pentadecanoate	C15:0	440.95	579.28	580.98
M-Palmitate	C16:0	433.70	593.00	590.48
M-Heptadecanoate	C17:0	-	605.25	603.26
M-Stearate	C18:0	444.69	616.39	614.46
M-Arachidate	C20:0	642.10	*	632.66
M-Behenate	C22:0	666.10	*	675.26
M-Palmitoleate	C16:1	-	*	566.95
M-Heptadecenoate	C17:1	-	*	584.68
M-Oleate	C18:1(11)	619.1	658.23	633.85
M-cis-11-Eicosenoate	C20:1(11)	-	599.49	576.44
M-Erucate	C22:1	666.10	632.86	593.38
M-Linoleate	C18:2	619.10	*	585.38
M-Linolenate	C18:3	620.10	*	582.01

\* Vapour pressure equation fails since it develops a maximum value and then starts decreasing

The vapour pressure correlation constrained with liquid heat capacity provides more thermodynamically consistent modelling of the vapour pressure than an unconstrained correlation. For example, the Cox equation parameters from the “Constrained” scenario,  $a_{PV1,2,3}$ , change systematically with the carbon number of saturated FAMES, while those from the “All-data” scenario do not, Figure 5.5. Therefore, the constrained method is recommended for modeling the vapour pressure of FAMES.

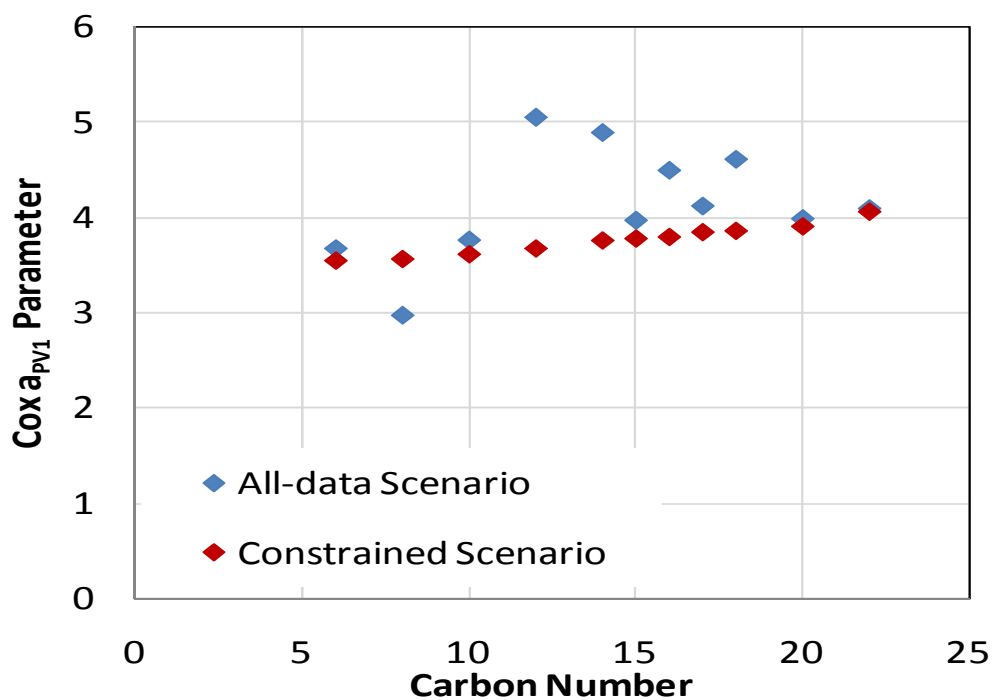


**Figure 5.5a** Cox parameter  $a_{PV1}$  as a function of carbon number for saturated FAMES

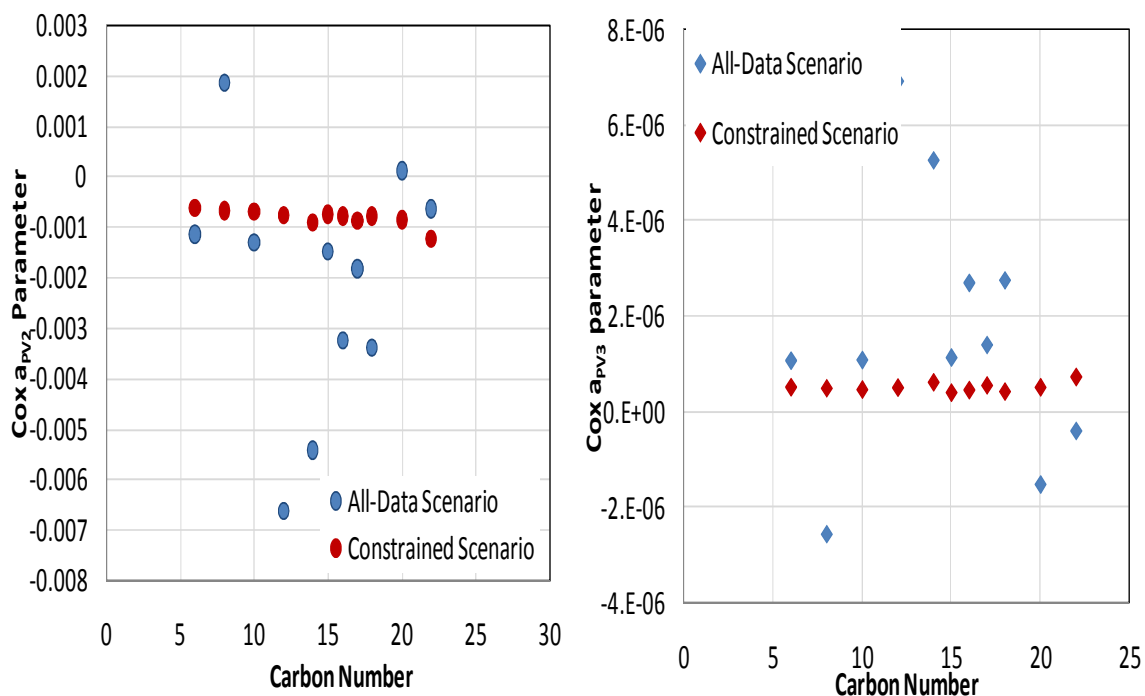


**Figure 5.5b** Cox parameter  $a_{PV2}$  and  $a_{PV3}$  as a function of carbon number for saturated FAMES

### 5.5 Predictive Vapour Pressure Equation for FAMES

The monotonic trends in FAMES properties provided a basis on which to develop a new methodology to predict vapour pressure for FAMES. The proposed predictive equation can be used to determine vapour pressures for FAMES with little or no experimental data, Table 5.1. The method is developed first for saturated FAMES and then extended to unsaturated FAMES.

### 5.5.1 Saturated FAMES Vapour Pressure Equation

The data listed in Table 5.1 were used as the training set for the proposed correlation and experimental data of methyl nonadecanoate (C19:0) [NIST, 2010] was used to test the correlation.

At a given temperature, such as 70°C in Figure 5.6, the vapour pressure of the FAMES decreases exponentially with the carbon number:

$$P(N_C)|_T = a_{CN,0} \exp[a_{CN,1}N_C], \quad [5.16]$$

where  $N_C$  is the carbon number from the fatty acid formula  $N_C:0$ , and  $a_{CN,i}$  are correlation parameters. Each parameter in Equation 5.16 is then regressed versus temperature as follows:

$$a_{CN,0} = 1.908 \exp[0.01715T], \quad [5.17]$$

$$a_{CN,1} = -5.656 + 0.02649T - 4.5417 \times 10^{-5}T^2 + 2.6571 \times 10^{-8}T^3, \quad [5.18]$$

Figure 5.7 shows the regressed parameters. Figure 5.8 (left) shows the experimental data and predictions for the training set. To test Equations 5.16 to 5.18, the vapour pressure of C19:0 was predicted, Figure 5.8 (right). The model predicts the vapour pressure with an AARD of 2.8%.

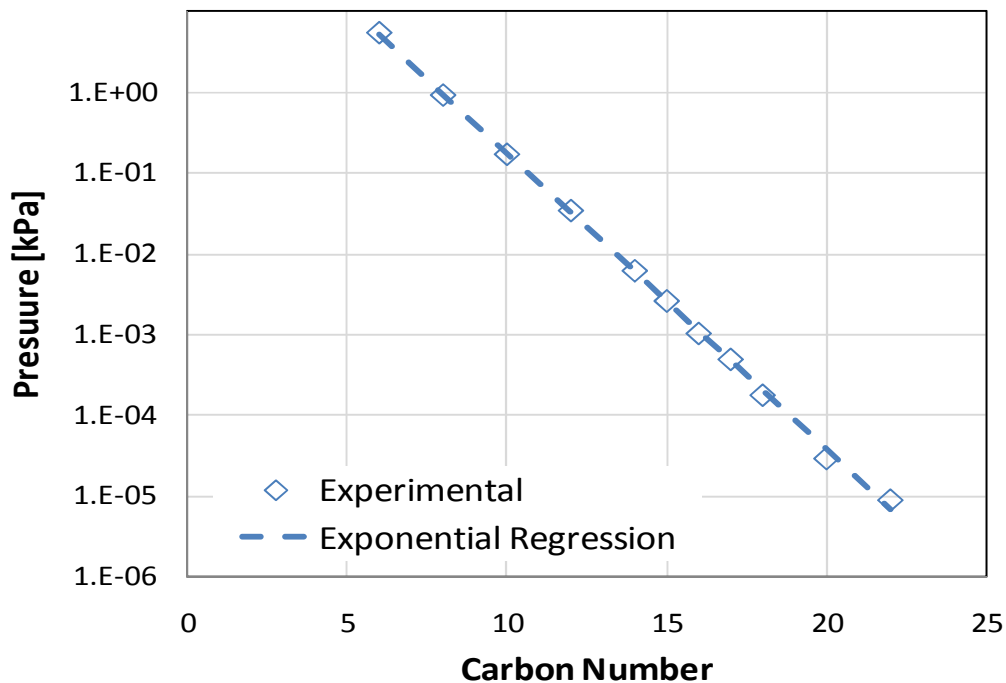


**Figure 5.6** Vapour pressure as a function of carbon number for saturated FAMES at 70 °C.

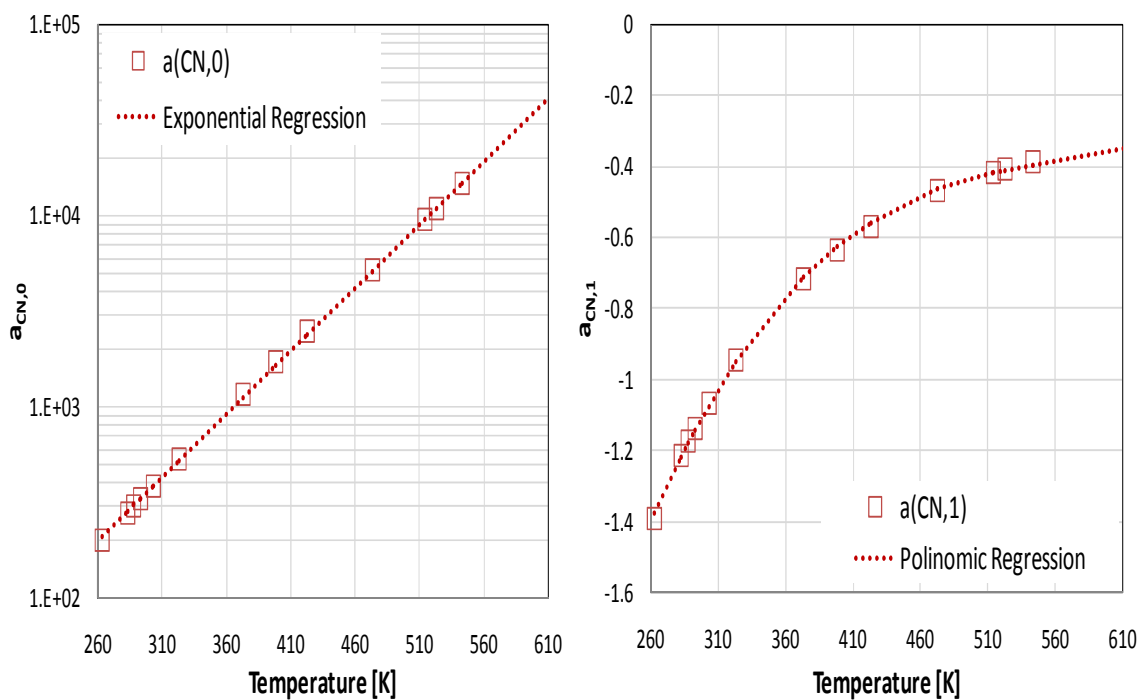


**Figure 7** Parameters  $a_{CN,0}$  and  $a_{CN,1}$  as a function of temperature and fitted with Equations 5.17 and 5.18.

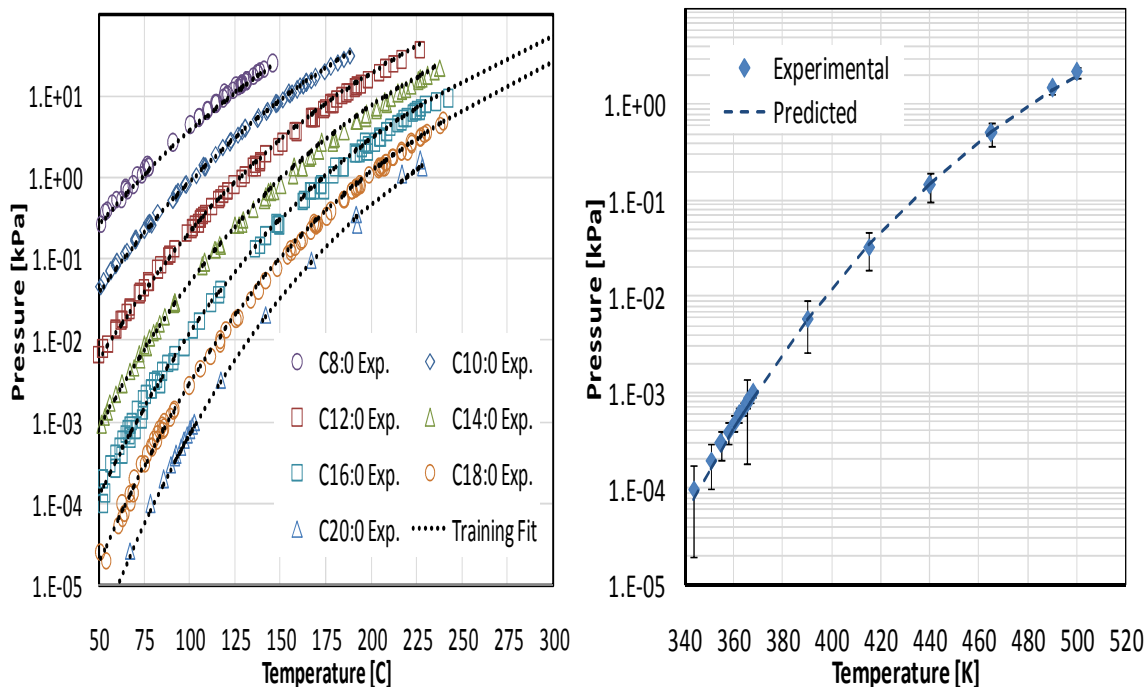


**Figure 5.8** Experimental and predicted values for the training set (left) and the tester, methyl nonadecanoate (right).

### 5.5.2 Unsaturated FAMES Vapour Pressure Equation

For unsaturated FAMES the amount of experimental data is very small which, in turn, limits the scope to develop any method based on this data. Data for C18:0, C18:1, C18:2 and C18:3 were used to develop a preliminary correlation; data for C16:1 was used to corroborate the method. Figure 5.9 (right) shows the experimental data and correlation results (left) for the training set.

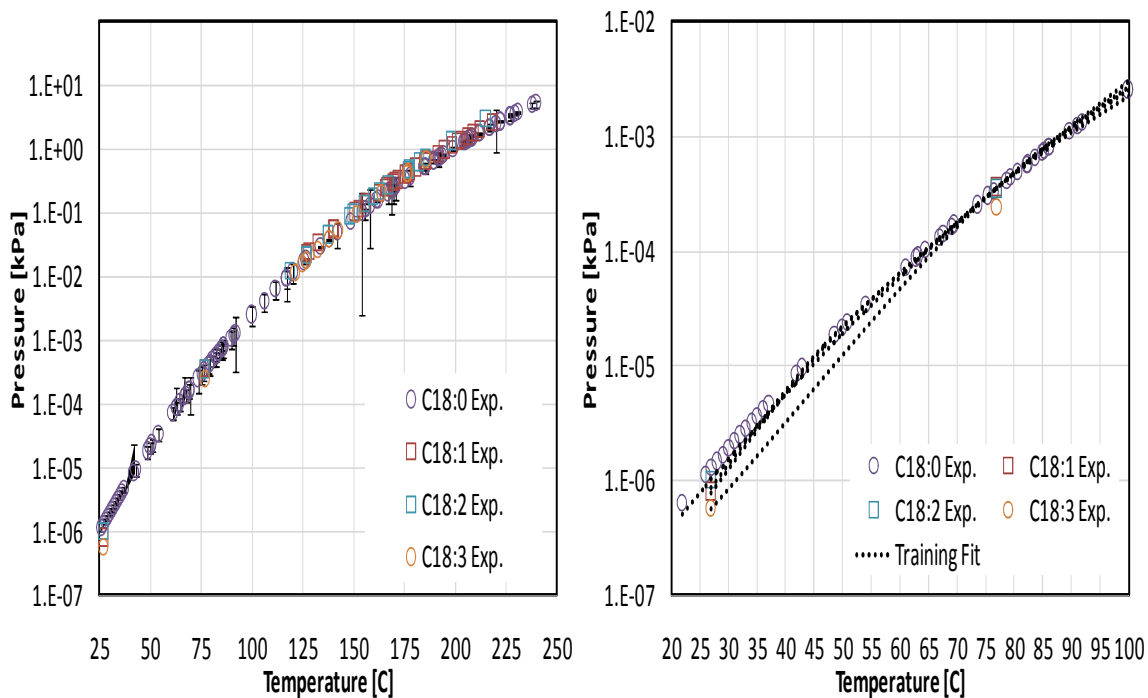


**Figure 5.9** Experimental and correlated vapour pressure data for unsaturated C18 family of FAMES at 30 °C.

At high temperatures, any differences among the vapour pressure of the different FAMES are virtually undistinguishable from the experimental error. However, at low temperatures, the differences become apparent. Therefore, the following departure function is proposed for the unsaturated FAMES at temperatures below 50 °C (323 K).

$$\frac{P_V(N_{UC})_T}{P_V(0)_T} = a_{UC}(N_{UC} + 1) + b_{UC} + \frac{c_{UC}}{N_{UC}+1}, \quad [5.19]$$

where  $N_{UC}$  is the number of unsaturated double bonds and  $a_{UC}$ ,  $b_{UC}$ , and  $c_{UC}$  are correlation parameters. Figure 5.9 shows the departure function, Equation 5.19, at 30°C.

Note that the C18:2 data point was off the trend at all temperatures. There are very few data points and the outlier may arise from experimental error; more data are required to reach a conclusion.

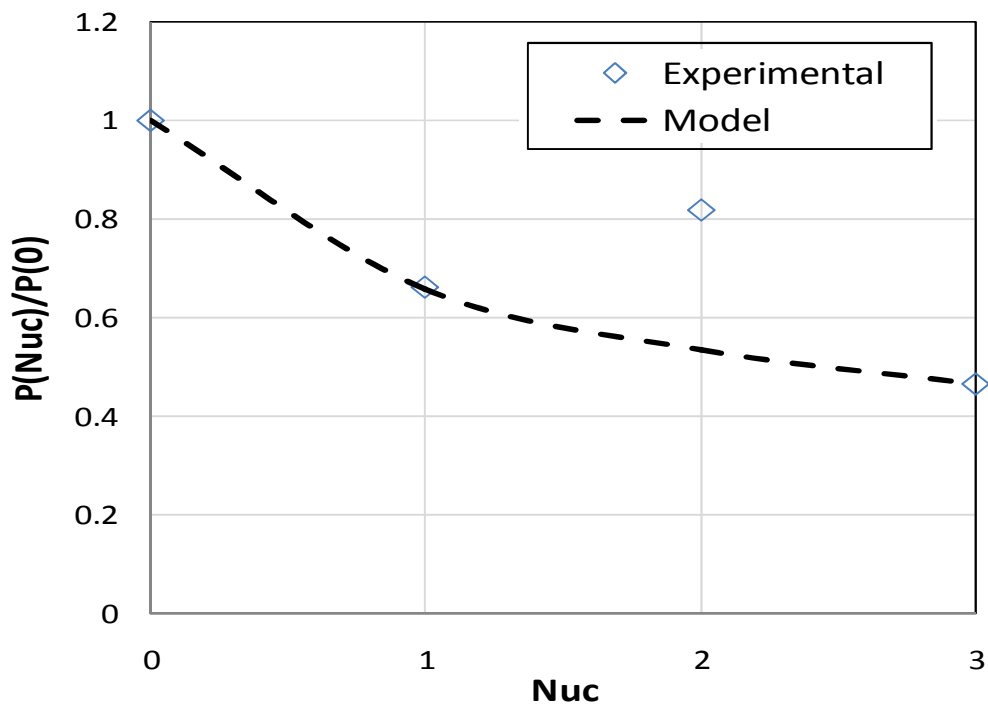


**Figure 5.10** Departure function for unsaturated C18 family of FAMES at 30 °C.

The parameters of Equation 5.19 were regressed as a function of temperature as follows:

$$a_{UC} = 4.62 \times 10^{-5} T^2 - 3.06 \times 10^{-2} T + 5.05, \quad T \leq 323K, \quad a_{UC} = 0 \quad T > 333K \quad [5.20]$$

$$b_{UC} = 3.39 \times 10^{-2} T - 9.93, \quad T \leq 323K, \quad b_{UC} = 1 \quad T > 333K \quad [5.21]$$

$$c_{UC} = -2.97 \times 10^{-2} T + 9.62, \quad T \leq 323.K, \quad c_{UC} = 0 \quad T > 333K \quad [5.22]$$

Note the outlying data point for C18:2 was neglected for the regression. The fit to the training data set is shown in Figure 5.9 (right). To test Equations 5.19 to 5.22, the vapour pressure of C16:1 was predicted, Figure 5.11. The correlation predicts the vapour pressure with an AARD of 2.4%.

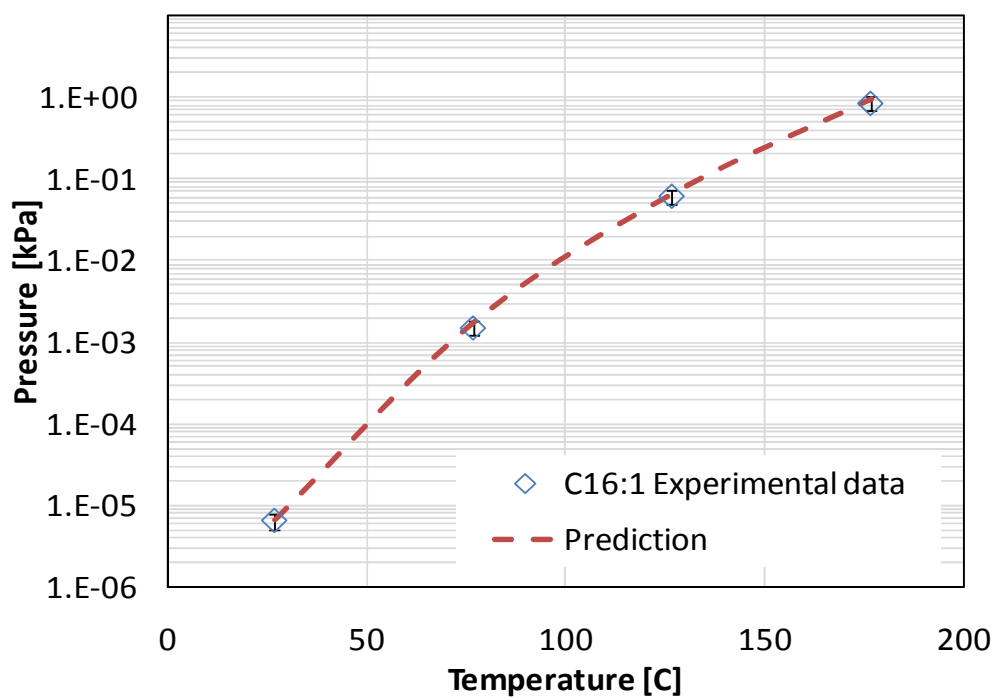


**Figure 5.11** Experimental and predicted values for methyl palmitoleate.

## 5.6 Equation of State Approach for FAMES Vapour Pressure

In the preceding sections, the vapour pressure of FAMES was modelled using analytical vapour pressure equations. This approach provides correct values of the enthalpy of vaporization and heat capacity through the Clapeyron equation, if the correlation parameters are correctly fitted. However, a more comprehensive approach is to model the

FAMEs vapour pressure using an equation of state since an EoS can also be used to calculate phase equilibria in multi-component mixtures (such as biodiesel fuels) if correctly tuned.

As discussed in Chapter 4, an EoS is tuned to fit vapour pressure data by adjusting the function  $f_w$ , Equation 4.19, which depends on the acentric factor. For heavy components, whose critical properties are hypothetical (not measured), the critical properties may also be adjusted. Experimental critical properties for the majority of fatty acid methyl esters do not exist because the hypothetical critical temperature for a FAME is above the cracking temperature; that is, it decomposes below the critical temperature. Therefore, both acentric factor and critical property tuning are considered for the FAMEs.

### ***5.6.1 FAMEs Critical Properties and Acentric Factor***

As recommended by NIST [2010], the hypothetical critical pressure,  $P_c$ , of the FAMEs was estimated using the Wilson-Jasperson and the Ambrose-Walton vapour pressure based methods. The hypothetical critical volume,  $V_c$ , and critical temperature,  $T_c$  were estimated using the Joback group contribution method [Poling et al., 2001]. A group contribution method was considered appropriate because the FAMEs consist of common molecular groups including  $\text{CH}_3$ -,  $-\text{CH}_2$ -,  $-\text{CH}=\text{}$ , and  $\text{COO}$ -, and was also recommended and applied by the NIST TDE Engine [NIST, 2010]. All of the above methods are described in Appendix C and the estimated critical properties are provided in Table 5.8.

Initial estimates for the acentric factor of the FAMES were calculated from the vapour pressure curve (when available), using Pitzer's definition [Poling et al., 2010]:

$$\omega_{Pitzer} = -\log_{10} \left( \frac{P_v}{P_c} \right)_{At T=0.7T_c} - 1, \quad [5.23]$$

where  $\omega_{Pitzer}$  is Pitzer's acentric factor. The estimated acentric factors for the FAMES are provided in Table 5.8.

**Table 5.16** Critical properties and acentric factor of selected FAMES; comparison between contribution method predictions (Calc.) and adjusted values (Adj.) for the Peng-Robinson equation of state.

Formula	Tc [K]			Pc [kPa]			$\omega$		
	Calc.	Adj.	AD [%]	Calc.	Adj.	AD [%]	Calc.	Adj.	AD [%]
C6:0	-	602.793	-	-	2950	-	0.462	0.490	6.1
C8:0	635.6	648	1.9	2064	1984	3.8	0.447	0.509	13.9
C10:0	671.2	683	1.7	1752	1570	10.4	0.511	0.596	16.0
C12:0*	712.165	712.165	0	1755	1507	14.1	0.575	0.696	20.9
C14:0	721	727	1.1	1147	1175	2.4	0.804	0.803	0.1
C15:0	736	736	0	1384	1384	0	0.902	0.873	3.4
C16:0	755	749.8	0.7	1313	1250	4.8	0.853	0.906	6.2
C17:0	760	759.5	0.1	1225	1224	0.1	0.946	0.937	0.9
C18:0	772	772	0	1157	1158	0.1	0.970	0.969	0.1
C20:0	790	788	0.2	1031	1031	0	1.015	1.032	1.7
C22:0	-	804	-	-	985	-	-	1.088	-
C16:1	-	750	-	-	1830	-	1.180	0.977	17.2
C17:1	-	770	-	-	1780	-	-	0.979	-
C18:1(9)	768	777	1.2	1173	1710	45.7	1.125	0.991	11.9
C20:1	-	788	-	-	1650	-	-	1.116	-
C22:1	-	798	-	-	1600	-	-	1.195	-
C18:2	773	783	1.3	1204	3150	161.6	1.466	1.052	28.2
C18:3	774	790	2.1	1127	4850	330.3	3.071	1.105	64.0

a: Joback; b: Ambrose-Walton; c: Wilson-Jasperson

\*Critical temperature measured experimentally

Once the critical properties and acentric factors were estimated, the vapour pressure and enthalpy of vaporization of the FAMES were calculated, as discussed in Chapter 4. Table 5.9 shows deviation values for this approach (Init. Values) and Figure 5.11 shows the results for methyl caprylate, C10:0. The performance of the PR-EoS with initial values is satisfactory (AARD of 36% for vapour pressure and 5.0% for enthalpy of vaporization), except for the unsaturated FAMES (AARD of 350% for vapour pressure). However, the performance of the EoS model can be improved by adjusting the critical properties and acentric factor, as explained in the following section.

**Table 5.17** Performance of the Peng-Robinson EoS for the prediction of vapour pressure and enthalpy of vaporization for various FAMES; comparison of the predictions with initial (Init.) and adjusted (Adj.) critical properties and acentric factor.

Formula	Init. Values		Adj. Values	
	AARD P <sub>v</sub> [%]	AARD ΔH <sub>v</sub> [%]	AARD P <sub>v</sub> [%]	AARD ΔH <sub>v</sub> [%]
C6:0	-	-	5.3	-
C8:0	126.8	6.8	10.8	1.2
C10:0	76.8	8.9	11.6	0.5
C12:0	74.7	9.0	12.5	0.9
C14:0	6.7	1.2	7.5	0.3
C15:0	7.8	3.2	4.1	0.9
C16:0	11.7	2.1	6.4	1.5
C17:0	2.3	-	2.5	-
C18:0	8.9	4.4	4.2	1.3
C20:0	10.7	4.7	11.1	0.7
C22:0	-	-	27.3	-
C16:1	-	-	12.7	-
C17:1	-	-	3.8	-
C18:1(9)	158.6	-	6.5	-

C20:1(11)	-	-	1.5	-
C22:1	-	-	1.4	-
C18:2	235.2	-	10.3	-
C18:3	648.3	-	12.5	-

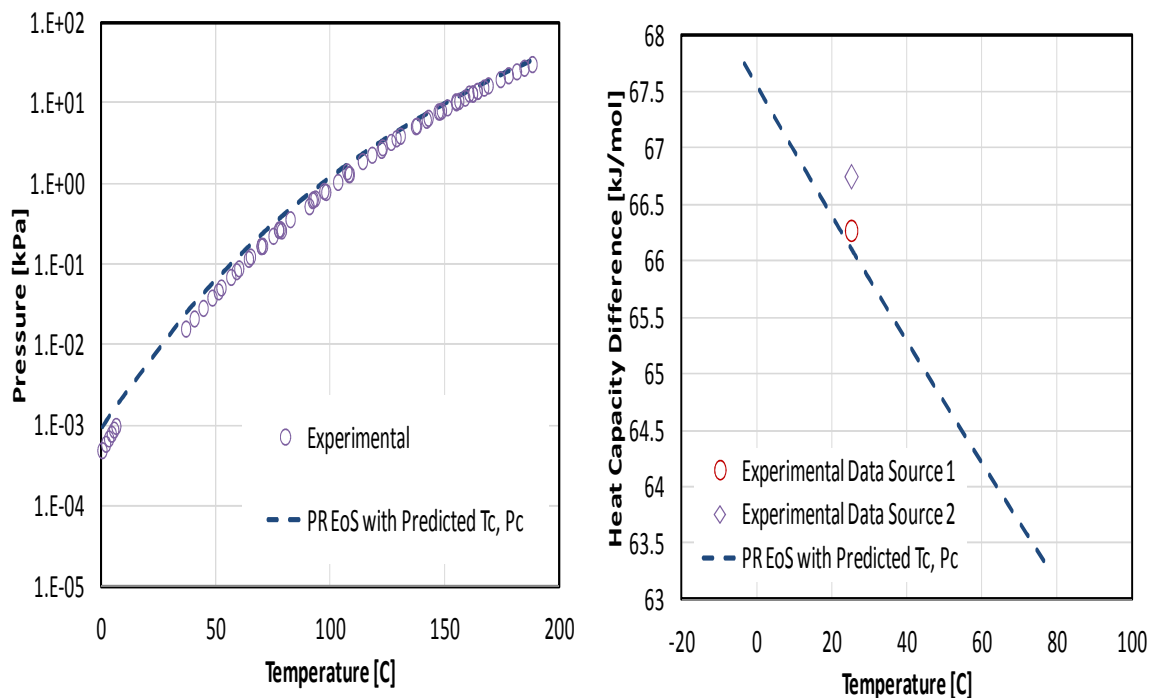


**Figure 5.12** Experimental and predicted vapour pressure and heat of vaporization data for methyl caprate, C10:0 using initial critical properties and acentric factor (Data from two distinct sources [NIST 2010]).

### 5.6.2 Vapour Pressure Calculation and Optimization of Critical Properties and Acentric Factor for FAMES

The critical properties and acentric factor of the FAMES were adjusted to fit the vapour pressure and enthalpy of vaporization (when available) using the Peng-Robinson equation of state, as described in Figure 5.13. Table 5.8 shows the adjusted parameters, Table 5.9 shows the performance of this approach, and Figure 5.14 shows the predicted values for

methyl caprylate as an example. The adjusted values of the critical properties do not differ significantly from the initial estimations, except for the unsaturated FAMEs. However, that these small changes significantly improve the predicted values for the vapour pressure and the enthalpy of vaporization, Table 5.9. The AARD for the vapour pressures of the FAME, including undersaturated FAMES, are all less than 30%.

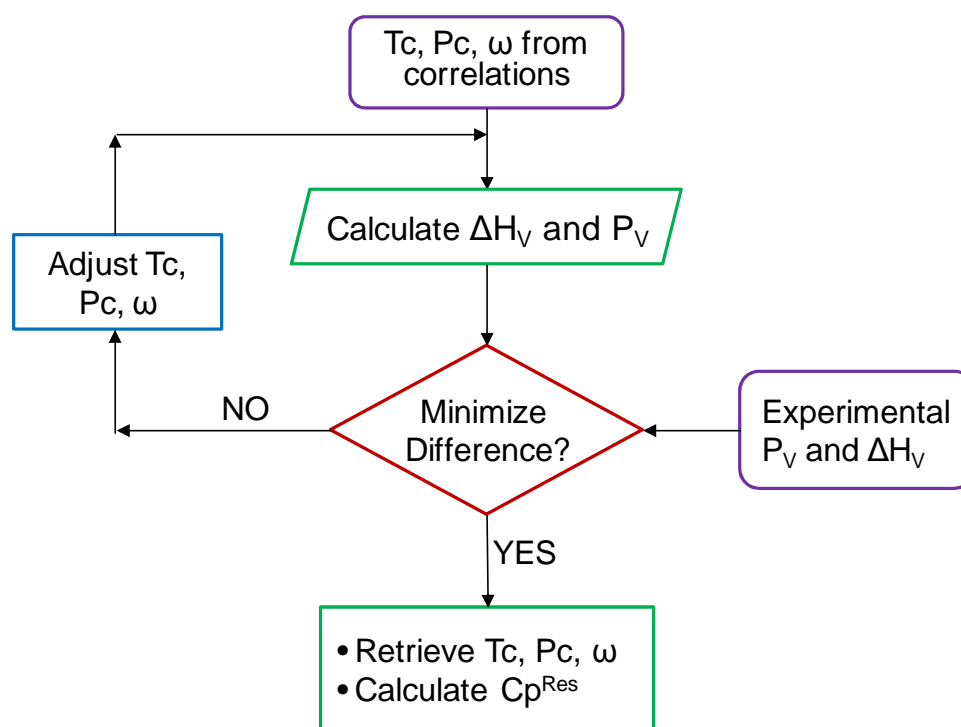


**Figure 5.13** Algorithm to adjust critical properties and acentric factor of FAMEs for the Peng-Robinson equation of state.

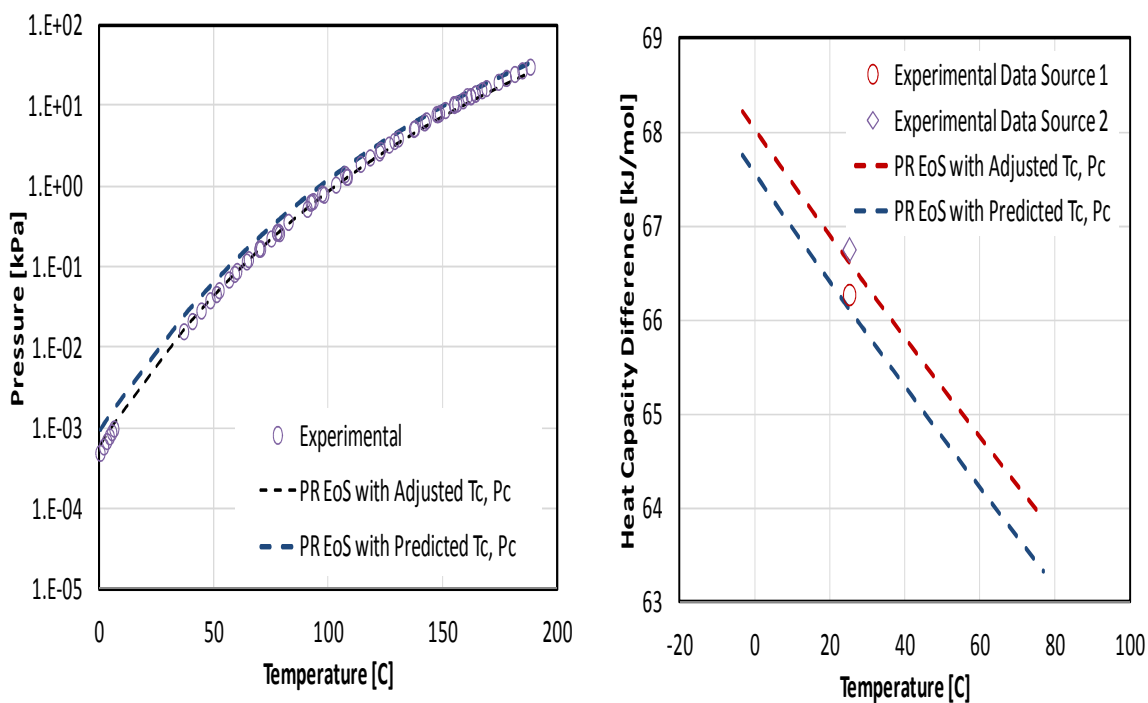


**Figure 5.14** Experimental and predicted vapour pressure and heat of vaporization data for methyl caprate, C10:0 using adjusted critical properties and acentric factor (Data from NIST [2010]).

### 5.6.3 Liquid Heat Capacity Calculation of FAMES

Following the procedure outlined in Figure 5.13, after the critical properties and acentric factor of the FAME were adjusted, the heat capacity residual was calculated from the equation of state. This concept was introduced in Chapter 4. The residual heat capacity and the liquid heat capacity of the substance are correlated as follows:

$$C_P^L = C_P^V + \Delta C_P \approx C_P^0 + \Delta C_P = C_P^0 + C_P^{Res}, \quad [5.24]$$

where  $C_P^{Res}$  is the heat capacity residual or departure function. In order to match the experimental liquid heat capacity data for FAMEs using the Peng-Robinson equation of state, the ideal gas heat capacity,  $C_P^0$ , must be determined. Note that no experimental data for  $C_P^0$  are available and a regression is required, as shown in Figure 5.14.

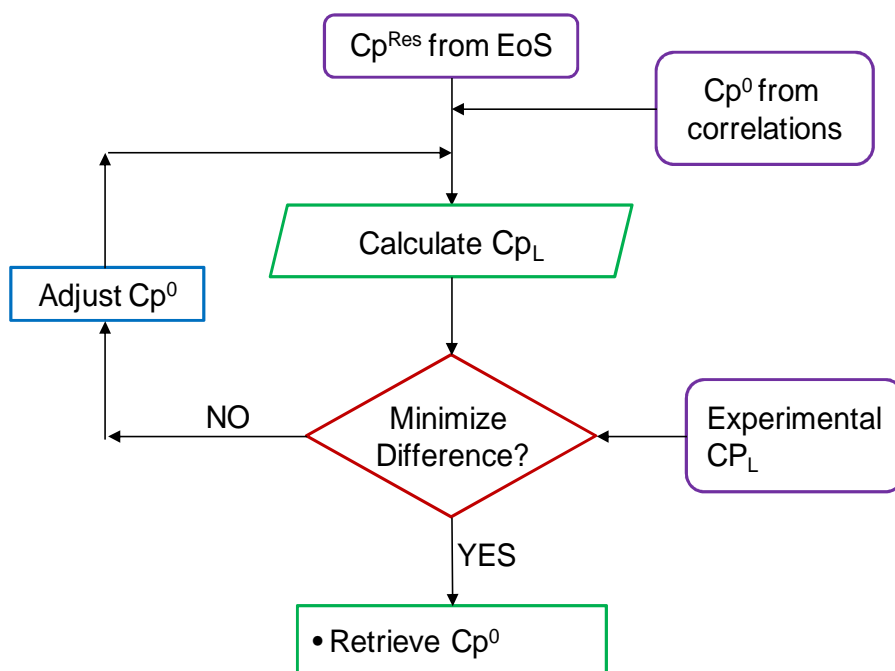


**Figure 5.15** Algorithm to adjust ideal gas heat capacity of FAMEs for the Peng-Robinson equation of state.

The following steps were taken to determine a correlation for  $C_P^0$ : First, for each saturated FAME, the ideal gas heat capacity of the saturated FAMEs with available liquid heat capacity data (Table 5.1) was calculated as follows:

$$C_{P,FAME}^0 = C_{P,L,FAME} - C_{P,FAME}^{Res} , \quad [5.25]$$

Then, the ideal gas heat capacity of this FAME was regressed with a second degree polynomial:

$$C_p^0(T) = a_{cp0} + b_{cp0}T + c_{cp0}T^2, \quad [5.26]$$

As an example, Figure 5.16 shows the calculated and regressed ideal gas heat capacity values for methyl caprylate, C10:0.

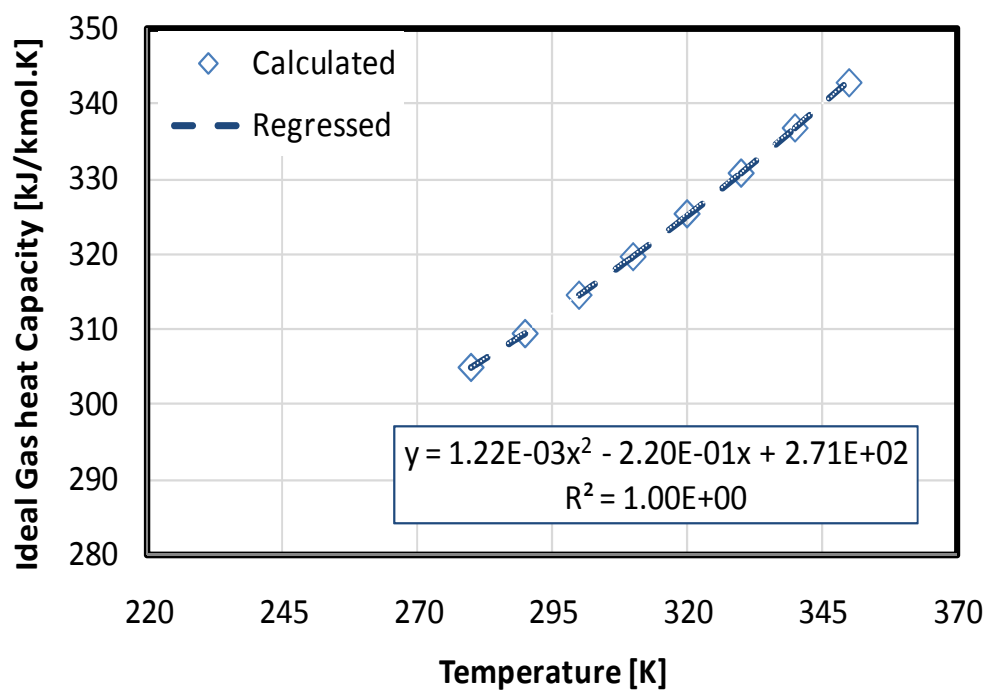


**Figure 5.16** Calculated and regressed ideal gas heat capacity for methyl caprylate, C10:0.

To generalize Equation 5.26 for all saturated FAMES, its parameters were plotted as a function of the molecular weight, Figure 5.17, and fitted as with the following expressions:

$$a_{cp0} = \frac{-2.1079 \times 10^4}{MW - 344.1759} + 230.72 + 0.62516(MW - 344.1759), \quad [5.27]$$

$$b_{cp0} = \frac{125.93}{MW - 344.1759} + 1.4529 + 5.5554 \times 10^{-3}(MW - 344.1759), \quad [5.28]$$

$$c_{cp0} = \frac{-0.19127}{MW - 344.1759} - 8.8626 \times 10^{-4} - 5.9999 \times 10^{-6}(MW - 344.1759), \quad [5.29]$$

Note that in developing Equations 5.27 to 5.29, outliers to the trend were not considered.

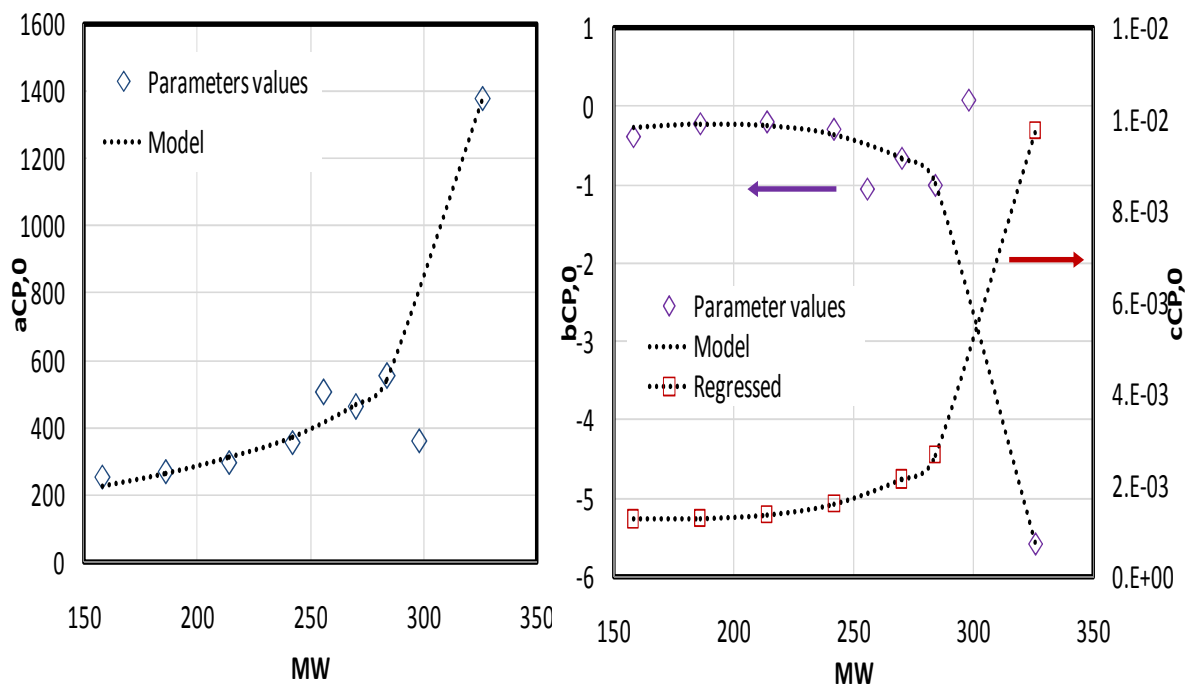


**Figure 5.17** Parameters of Equation 2 as a function of molecular weight.

No data were available for the ideal gas heat capacity of the unsaturated FAMEs, Table 5.1. Hence, it is assumed that the departure function from the corresponding saturated FAME is equal to the same departure function as calculated by Joback's method [Poling et al., 2001] Appendix C. This departure function from Joback's method can be summarized by:

$$\frac{C_P^0(N_{UC})}{C_P^0(0)} = \frac{N_{CH3} \sum_{i=0}^3 a_i T^i + N_{CH2} \sum_{i=0}^3 b_i T^i + N_{COO} \sum_{i=0}^3 c_i T^i + N_{UC} \sum_{i=0}^3 d_i T^i + \sum_{i=0}^3 e_i T^i}{N_{CH3} \sum_{i=0}^3 a_i T^i + N_{CH2} \sum_{i=0}^3 b_i T^i + N_{COO} \sum_{i=0}^3 c_i T^i + \sum_{i=0}^3 e_i T^i}, \quad [5.30]$$

where  $N_{UC}$  is the number of unsaturated bonds (1, 2, or 3),  $N_{CH3}$ ,  $N_{CH2}$ , and  $N_{COO}$  are the number of function groups within the molecule, and  $a$ ,  $b$ ,  $c$ ,  $d$ , and  $e$  are standard parameters for the method. Equation 5.30 can be simplified using the following expression:

$$\frac{C_P^0(N_{UC})}{C_P^0(0)} = [1 + N_{UC}(-6.1327 \times 10^{-2} + 1.5493 \times 10^{-4} T - 1.842 \times 10^{-7} T^2)], \quad [5.31]$$

The generalized ideal gas heat capacity model was compared with two well known predictive methods: the Joback method [Poling et a., 2001] and a modification of the Benson method [Bureš et al., 1981]. These methods can be found in Appendix C. Figure 5.18 shows the performance of the PR EoS with methyl caprate, C10:0, summarized in Table 5.10 for all of the FAMEs considered.

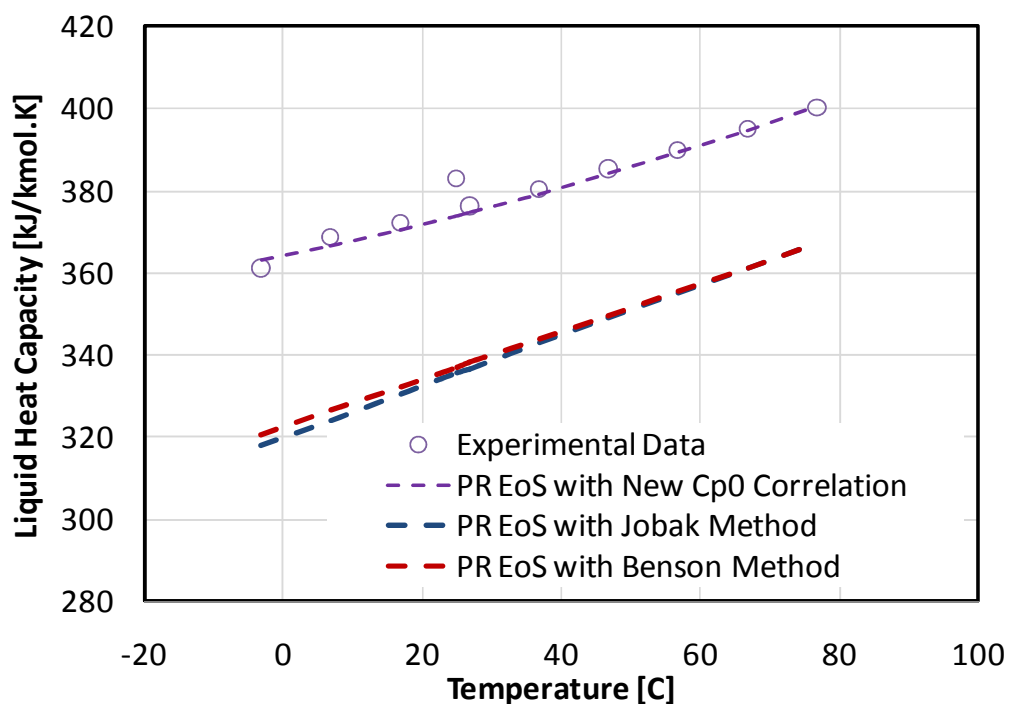


**Figure 5.18** Experimental and predicted liquid heat capacity data for methyl caprate, C10:0 (Data from NIST [2010]).

**Table 5.18** AARD values for the Peng-Robinson EoS for the prediction of liquid heat capacity for various FAMES with three different methods for the ideal gas heat capacity prediction.

Formula	$\Delta C_{PL}$ AARD [%]		
	Equation 4.32	Modified Benson	Joback
C6:0	2.8	9.2	9.4
C8:0	0.6	11.4	11.8
C10:0	0.4	9.9	10.2
C12:0	0.4	8.9	9.1
C14:0	0.2	7.7	7.8
C15:0	0.3	7.1	7.3
C16:0	0.3	6.9	7.0
C17:0	0.3	6.2	6.3
C18:0	0.6	6.8	6.8
C20:0	0.1	7.1	7.1
C22:0	8.1	6.3	6.3
C16:1	3.2	6.1	6.8

C17:1	2.0	5.8	6.2
C18:1(9)	1.1	6.6	7.1
C20:1(11)	3.6	4.6	4.9
C22:1	13.8	12.2	12.4
C18:2	2.6	4.3	3.9
C18:3	1.7	5.3	4.2

## 5.7 Summary

The modelling methodology developed in Chapter 4 was applied in this chapter to assess the vapour pressure of fatty acid methyl esters, main constituents of biodiesel fuels. The proposed methodology was validated. Specific outcomes are summarized below.

1. The importance of constraining vapour pressure models with heat capacity was demonstrated. Although an unconstrained model predicted the vapour pressure accurately, the same model had gross errors in the prediction of heat capacity. In addition, the constrained model parameters followed monotonic trends with the molecular weight of the FAME while the unconstrained parameters did not.
2. New correlations were proposed to predict and/or interpolate experimental vapour pressure, ideal gas heat capacity, and liquid heat capacity of the FAMEs.

It was shown that analytical vapour pressure equations and equations of state generate similar results on vapour pressure and liquid heat capacity calculations. The equation of state approach, although more complex, provides a more comprehensive representation of the fluid than the analytical approach. For example, the equation-of-state characterization is expected to be suitable for a broader range of phase behaviour modeling and will be used for modeling heavy oils.

## CHAPTER SIX: MODELLING BIODIESEL VAPOR PRESSURE AND CALORIMETRIC DATA

In this chapter, biodiesels vapour pressures data are collected and modeled to test the VPMA presented in Chapter 3 and the modeling methodology presented in Chapter 4 on a relatively well defined mixture before proceeding to heavy oil vapour pressures. Biodiesel vapour pressure is of interest in its own right because the volatility of a biodiesel, which is directly related to vapour pressure, is an important factor in the quality control of biodiesel fuels. For instance, vapour pressure is used to calculate the heat of vaporization in order to compare rates of vaporization and injection characteristics with other fuels. Vapour pressures are also used to assess the cold weather properties of these fuels [Goodrum, 2002].

Experimental vapour pressure data of biodiesel fuels are scarce in the open literature with the majority of the data points being measured at temperatures above 200 °C [Goodrum, 1986]; although some work has been developed for lower end vapour pressures [Widergren and Bruno, 2011]. The vapour pressure of biodiesels is expected to be low due to the biodiesel molecular weight (higher than 200 g/mol).

Biodiesel fuels have been modelled using the physical properties of their constituents, fatty acid methyl esters (FAMES), and a mixing rule. For example, Yuan et al. [2005]

modelled the vapour pressure of biodiesel fuels at temperatures above 230 °C assuming Raoult's law with an error better than 1%. However, for the low vapour pressures encountered at lower temperatures, the methodology presented in Chapter 4, which makes use of both calorimetric and vapour pressure data, is required.

In this chapter, the proposed methodology is evaluated on data for seven biodiesel fuel samples from various vegetable sources. The first section of this Chapter deals with the composition, liquid heat capacity, and vapour pressure data collected for these samples. The second section uses the techniques introduced in Chapter 4 and the models developed in Chapter 5 for FAMES to predict and assess the vapour pressure and heat capacity of the biodiesel fuels at temperatures between 50 and 150 °C. Both an analytical method and an equation-of-state approach are evaluated.

## **6.1 Experimental Data of Biodiesels**

Compositional, liquid heat capacity, and vapour pressure data for the biodiesel fuels are required to validate the proposed modeling methodology. Table 6.1 shows a list of the biodiesel fuels assessed in this research as well as the temperature range of the experimental data.

**Table 6.19** Temperature range of vapour pressure and heat capacity data for selected biodiesel fuels.

<b>Biodiesel fuels Source</b>	<b>Code</b>	<b>Vapour Pressure</b>	<b>Liquid Heat Capacity</b>
Canola (South Alberta)	CB-01	60-196 °C	13-55 °C
Canola (Saskatchewan)	I-25	40-100 °C	12-55 °C
Soy (Sunrise, US)	SB100	40-100 °C	14-55 °C
Soy (Mountain Gold, US)	MGB100	30-148 °C	10-55 °C
Rapeseed (Europe)	S102550	40-110 °C	13-55 °C
Palm (Europe)	S090824	35-80 °C	23-55 °C
Coconut (Europe)	S070717	95-125 °C	10-55 °C

### **6.1.1 Composition of Biodiesels**

The components of each of the biodiesel fuels were identified with gas chromatography and mass spectrometry (GC-MS), Table 6.2. These experiments were performed at the National Institute of Standards and Technology (NIST) laboratories in Boulder, CO, with the collaboration of Dr. T. Bruno and Dr. T. Lovestead. Details on the experimental procedure are provided in Appendix A.

To assess the compositional analysis of the biodiesels, a comparison with biodiesels from the open literature was performed. For instance, Figure 6.1 shows the comparison of the two canola biodiesels from Table 6.1 with a canola biodiesel from the literature [Goodrum, 2002]. The profiles of the three fuels are very similar. The small differences in the composition between the biodiesels stem from small differences in the canola source and the production process.

Similar results were found with biodiesel fuels from soy and palm sources (Appendix A); however, rapeseed biodiesel showed an important difference, as seen in Figure 6.2. Wild rapeseed has undergone various genetic modifications to make it ideal for human consumption by stripping off erucic acid (one of those modification led to the development of canola seeds) [Klahorst, 1998, Gunstone et al., 2007]. The rapeseed biodiesel S102550 shown in Figure 6.2 has been stripped of erucic acid, and now resembles more a canola biodiesel than a wild rapeseed biodiesel.

**Table 6.20** Mole fraction percentage of fatty acid methyl esters in different biodiesel fuels.

FAME	CB-01	I-25	S-B100	MG-B100	S102550	S090824	S070717
C6:0	0.00	0.00	0.00	0.00	0.00	0.00	1.01
C8:0	0.00	0.00	0.00	0.00	0.00	0.00	12.56
C10:0	0.00	0.00	0.00	0.00	0.00	0.00	7.74
C12:0	0.00	0.00	0.00	0.00	0.00	0.00	48.32
C14:0	0.00	0.00	0.00	0.60	0.00	1.52	16.59
C15:0	0.00	0.00	0.00	0.00	0.00	0.00	0.00
C16:1	0.00	0.88	0.00	0.54	0.00	0.00	0.00
C16:0	12.74	9.34	11.45	12.51	4.80	45.07	6.71
C17:0	0.00	0.31	0.00	0.00	0.00	0.00	0.00
C18:0	4.11	4.43	3.23	4.89	1.28	3.62	1.54
C18:1 (9)	23.54	57.35	21.29	26.96	59.91	39.49	4.42
C18:1(11)	1.48	2.77	1.48	1.57	3.68	0.00	0.00
C18:2	49.78	15.95	54.88	46.56	19.44	9.84	1.11
C18:3	8.09	7.53	7.39	6.08	9.08	0.19	0.00
C20:0	0.27	0.45	0.27	0.27	1.26	0.34	0.00
C20:1	0.00	1.00	0.00	0.00	0.55	0.00	0.00
<b>MWavg</b>	<b>291.53</b>	<b>293.17</b>	<b>291.77</b>	<b>291.27</b>	<b>294.56</b>	<b>283.69</b>	<b>218.16</b>

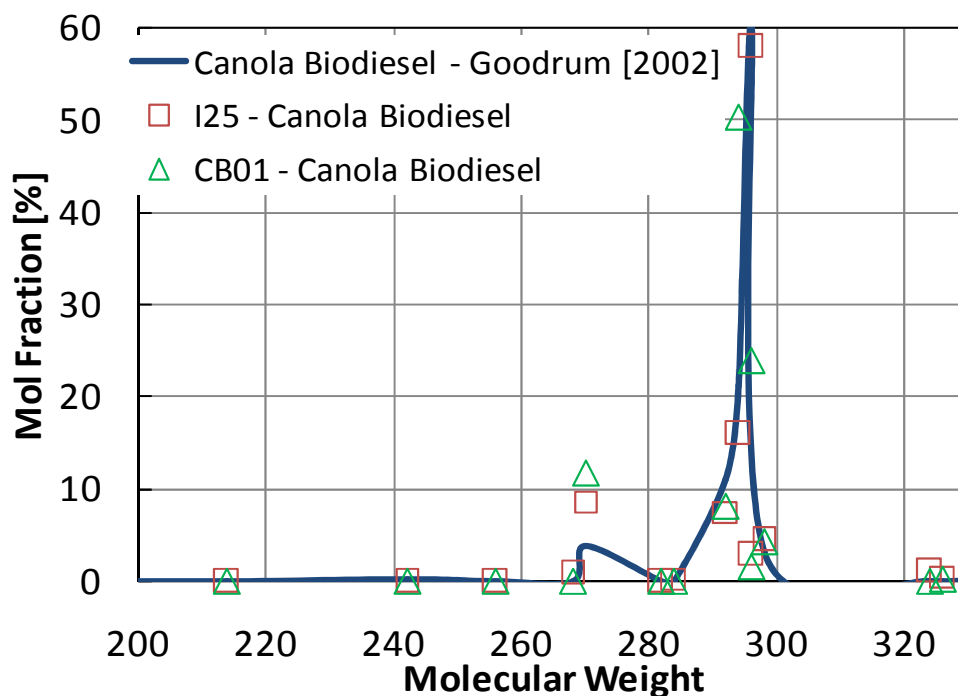


**Figure 6.1** Comparison between measured and literature molecular weight profile for Canola biodiesel. Literature data from Goodrum [2002].

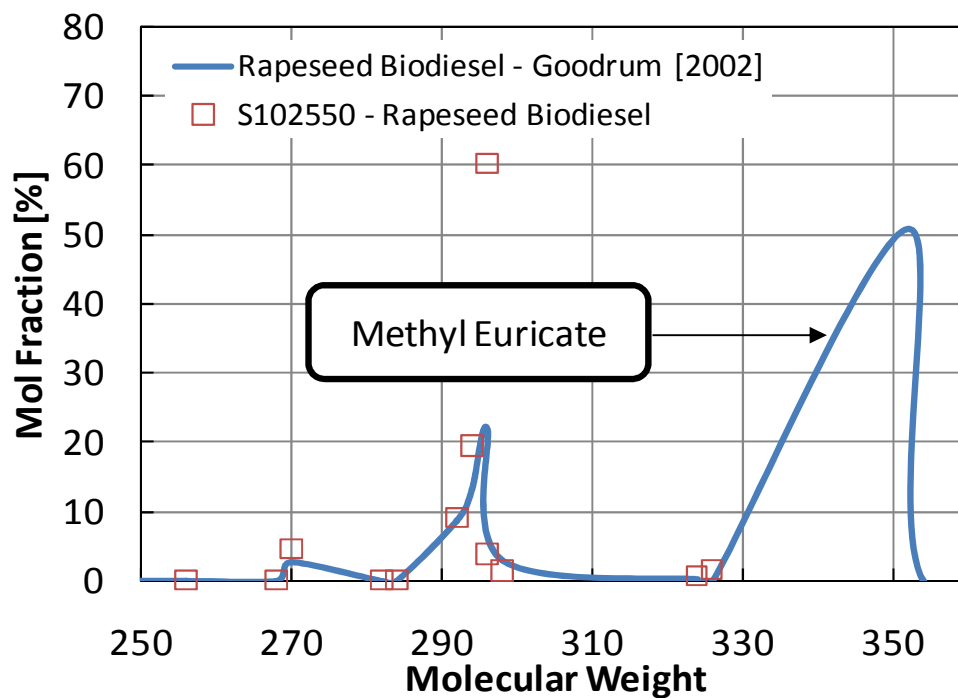


**Figure 6.2** Comparison between measured and literature molecular weight profile for Rapeseed biodiesel. Literature data from Goodrum [2002].

### ***6.1.2 Water Content of Biodiesels***

The solubility of water in biodiesel fuels is very small [Oliveira et al., 2008], typically in the order of 1500 ppm (0.15% wt) [Knothe et al., 2005]. However, it is significantly larger than the solubility of water in petroleum diesel fuels. Biodiesels have a tendency to capture moisture from the surroundings usually during storage. Moisture is a problem for biodiesel application as a fuel since it contributes to corrosion and microbial growth which may plug the filters on an engine [Goodrum and Eitman, 1996, Knothe et al., 2005]. The ASTM D6751 norm limits the water content on biodiesel fuels to 500 ppm (0.05 %wt) [Knothe et al., 2005].

The initial water content of the biodiesels studied in this thesis was measured using a Karl-Fischer titrator Metrohm 787 KF Titrino, with repeatability better than 0.001wt%. The amounts of water in the biodiesels are given in Table 6.3 and are lower than the ASTM D6751 norm. Even this small amount of water would significantly affect the vapour pressure measurements since the volatility of water is hundreds of times higher than that of the biodiesels. The degassing process described in Chapter 3 was found to be sufficient to strip the biodiesel of water since the data were repeatable after different temperature cycles.

To decrease the amount of water in biodiesels during storage, it is recommended to store the samples with an overhead nitrogen cap and molecular sieves. For example, using this

storage option reduced the amount of water in the Sunrise Soy biodiesel, Table 6.1, from 0.038 to 0.004 wt%.

**Table 6.21** Moisture content in studied biodiesels.

<b>Biodiesel Source</b>	<b>Code Name</b>	<b>Water wt%</b>
Canola (South Alberta)	CB-01	0.036
Canola (Saskatchewan)	I-25	0.032
Soy (Sunrise, US)	S-B100	0.038
Soy (Mountain Gold, US)	MG-B100	0.027
Rapeseed (Europe)	S102550	0.029
Palm (Europe)	S090824	0.027
Coconut (Europe)	S170717	0.043

### **6.1.3 Vapour Pressure of Biodiesels**

Vapour pressure data for the biodiesels in Table 6.1 were measured with the VPMA. The degassing apparatus (DA) was used to remove excess air and dissolved water from the samples. The average repeatability is 7.7%. The vapour pressure data are tabulated in Appendix A. As an example, Figure 6.3 shows experimental data for rapeseed biodiesel.

Note that the vapour pressure data set for most of the biodiesels contains points below  $10^{-4}$  kPa, which, as discussed in Chapter 3, may have an unknown uncertainty. These data points were determined from the raw experimental data using the exponential calibration equation that applies for data below  $10^{-2}$  kPa. These data points are listed in Appendix A but were not used for the vapour pressure modeling calculations.

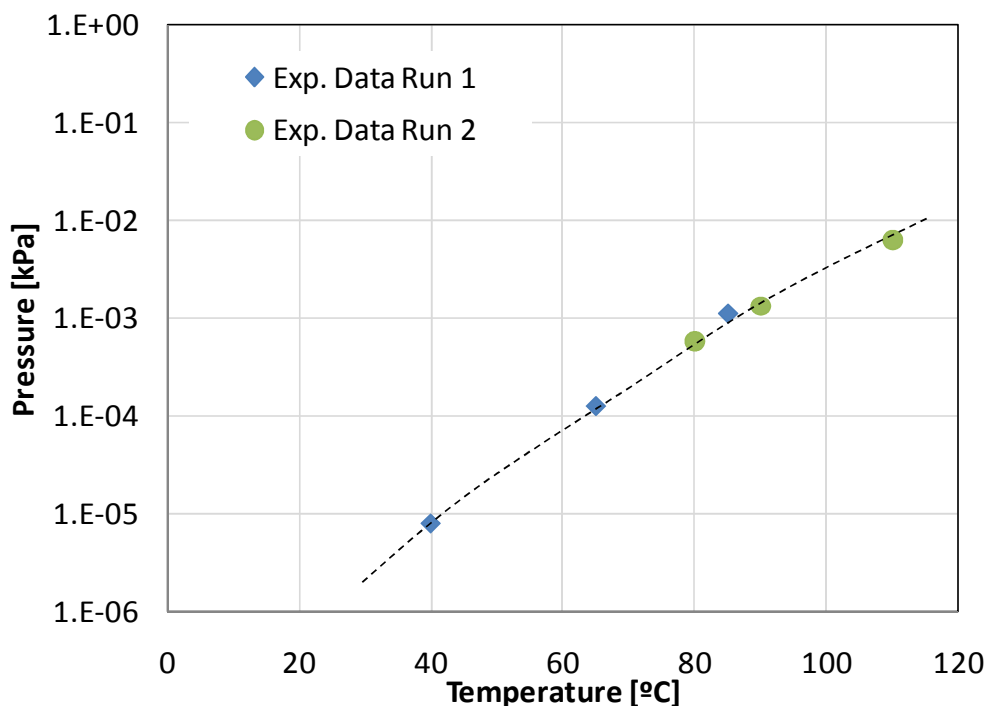


**Figure 6.3** Experimental vapour pressure of rapeseed biodiesel; dotted line is drawn to show the tendency and does not represent any particular model

#### 6.1.4 Liquid Heat Capacity and Cloud Point of Biodiesels

Liquid heat capacity of the biodiesels listed in Table 6.1 was measured using a differential scanning calorimeter, Chapter 3. The dataset, provided in Appendix A, was regressed as a function of temperature to a second order polynomial, as follows:

$$C_{P,L}[\text{kJ}/\text{kmol}\cdot\text{K}] = a_{Cp} + b_{Cp}T[^\circ\text{C}] + c_{Cp}T^2, \quad [6.1]$$

The fitted coefficients,  $a_{Cp}$ ,  $b_{Cp}$ , and  $c_{Cp}$ , are listed in Table 6.4. The average absolute deviation with respect to the measured data is 0.1%.

Table 6.5 lists the cloud points of the different biodiesel samples determined from the calorimeter heat flow, Chapter 3 (Appendix A). Literature data for biodiesels from the same source material is also provided [Knothe et al., 2005]. Biodiesels sharing a common source have similar cloud points because they have a similar composition. Differences with respect to literature data are likely due to differences in composition and saturated/unsaturated FAMES distribution.

**Table 6.22** Polynomial regression coefficients for liquid heat capacity of selected biodiesels.

<b>Biodiesel Source</b>	<b>Code Name</b>	<b>a<sub>CP</sub></b>	<b>b<sub>CP</sub></b>	<b>c<sub>CP</sub></b>	<b>T<sub>min</sub></b>	<b>T<sub>max</sub></b>	<b>AARD</b>
Canola (South Alberta)	CB-01	583.1	1.11	0.010	12	55	0.1%
Canola (Saskatchewan)	I-25	594.8	0.37	0.030	13	55	0.1%
Soy (Sunrise, US)	S-B100	594.4	0.62	0.009	14	55	0.1%
Soy (Mountain Gold, US)	MG-B100	625.3	0.16	0.004	10	55	0.1%
Rapeseed (Europe)	S102550	645.0	0.33	0.015	14	55	0.0%
Palm (Europe)	S090824	564.2	0.62	0.019	24	55	0.2%
Coconut (Europe)	S170717	436.8	0.40	0.004	10	55	0.2%

**Table 6.23** Experimental and literature cloud points (CP) of selected biodiesels (Literature data from Knothe et al., [2005]).

<b>Biodiesel Source</b>	<b>Code Name</b>	<b>CP exp. [°C]</b>	<b>CP lit. [°C]</b>
Canola (South Alberta)	CB-01	0.96	1
Canola (Saskatchewan)	I-25	1.0	1
Soy (Sunrise, US)	S-B100	3.3	0
Soy (Mountain Gold, US)	MG-B100	3.4	0
Rapeseed (Europe)	S102550	0.5	-2*

Palm (Europe)	S090824	17.9	13
Coconut (Europe)	S170717	-6.9	-

\*Wild rapeseed which contain erucic acid, opposite to the sample being assessed, Figure 6.2

## 6.2 Modelling Results of Biodiesel Vapour Pressure and Heat Capacity

### 6.2.1 Analytical Approach

The vapour pressure of the biodiesel fuels assessed in this work was modeled using Raoult's law and the Cox vapour pressure equations correlated for the fatty acid methyl esters (FAMES) in Chapter 5. Liquid heat capacity is modelled using the equations developed in Chapter 5 and assuming an ideal liquid solution:

$$C_{P,L,Biodiesels} = \sum_i x_i C_{P,L,i} , \quad [6.2]$$

where  $i$  stands for the FAMES that comprise the biodiesel. The vapour pressure and liquid heat capacity are predicted using the two scenarios developed in Chapter 5: "All-data" and "Constrained".

Figure 6.4 shows experimental and predicted vapour pressure data for coconut biodiesel S170717 using both scenarios. Figure 6.5 shows the predicted liquid heat capacity for this biodiesel. The vapour pressure data are correctly predicted using both scenarios (AARD of 19 and 10% for the "All-data" and "Constrained" scenarios, respectively). Note that the difference between both scenarios increases as the temperature decreases. This

deviation is an effect of the liquid heat capacity constraint at low temperatures near the freezing point of the FAMES. The liquid heat capacity is well predicted by the “Constrained” scenario model (AARD of 0.4%) but is over predicted by the “All-data” scenario model (AARD of 41%). The “All-data” model also predicts an incorrect trend of liquid heat capacity versus temperature, Figure 6.5. The erroneous behaviour was more severe when the biodiesel contained lighter FAMES (carbon number lower than 14).

Figures 6.6 and 6.7 show the measured and “Constrained” model vapour pressure and heat capacity, respectively, for all of the biodiesel fuels studied. Table 6.6 gives the AARD of both the “All-data” and “Constrained” scenarios. Vapour pressure and liquid heat capacity of biodiesels modeled as an ideal solution (Raoult’s law and Equation 6.1) generated reasonable predictions of experimental data. However, liquid heat capacity predictions of some of the biodiesels are off trend. There may be some non-ideality in the liquid phase that is not accounted for in Equation 6.1, particularly with unsaturated/saturated FAMES interactions.

**Table 6.24** Performance of “All-data” and “Constrained” scenarios in the prediction of biodiesel fuel vapour pressure and liquid heat capacity.

Biodiesel Source	Code	All-data AARD		Constrained AARD	
		P <sub>V</sub>	C <sub>PL</sub>	P <sub>V</sub>	C <sub>PL</sub>
Canola (South Alberta)	CB-01	14.0	7.3	12.4	2.4
Canola (Saskatchewan)	I-25	20.8	3.7	19.3	4.1
Soy (Sunrise, US)	SB100	6.6	7.6	6.6	1.4

Soy (Mountain Gold, US)	MGB100	10.2	4.5	10.4	0.3
Rapeseed (Europe)	S102550	1.3	11.2	1.3	1.3
Palm (Europe)	S090824	1.4	19.7	0.6	2.5
Coconut (Europe)	S070717	9.9	40.9	18.5	0.4
<b>Total</b>	-	<b>9.2</b>	<b>13.5</b>	<b>9.8</b>	<b>1.7</b>

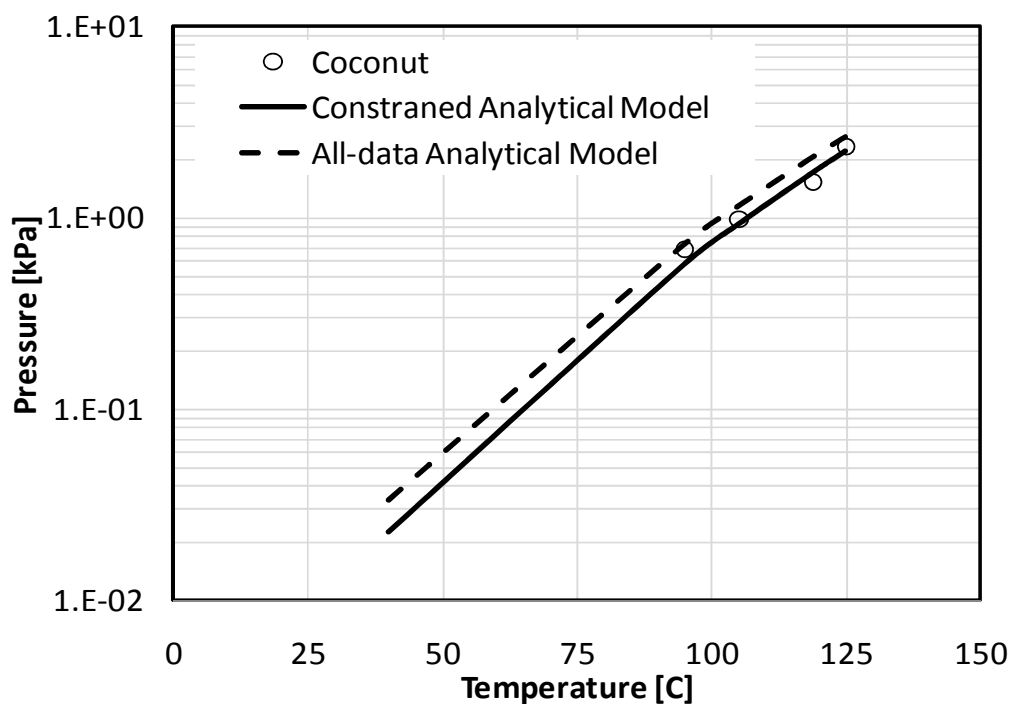


**Figure 6.4** Experimental and predicted vapour pressure of coconut biodiesel S170717 with analytical “All-data” and “Constrained” scenarios.

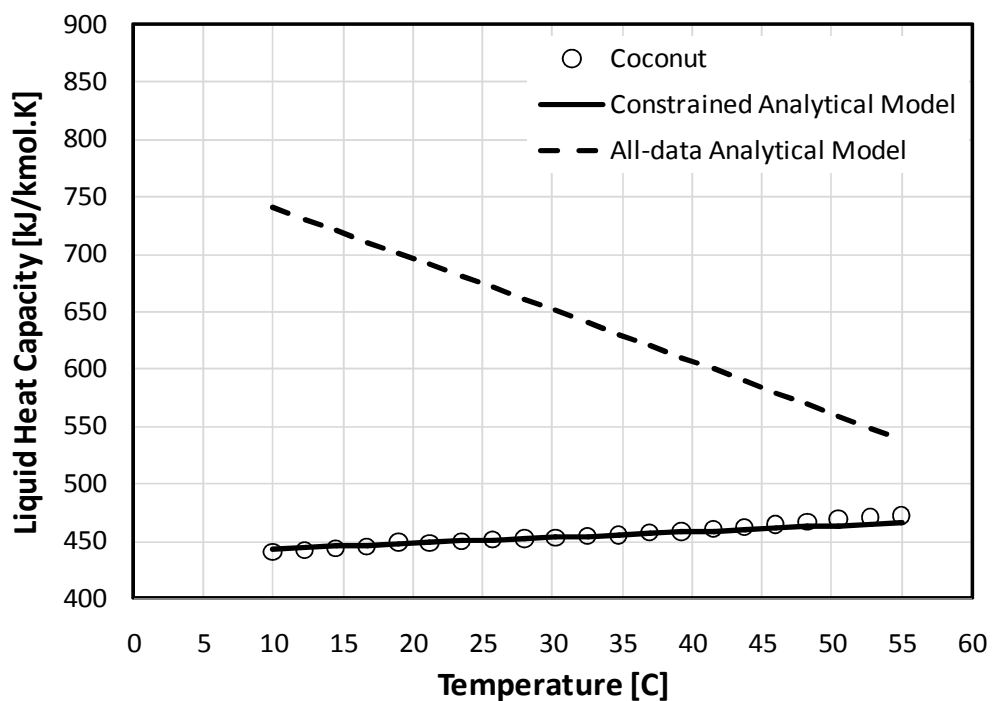


**Figure 6.5** Experimental and predicted liquid heat capacity of coconut biodiesel S170717 with analytical “All-data” and “Constrained” scenarios.

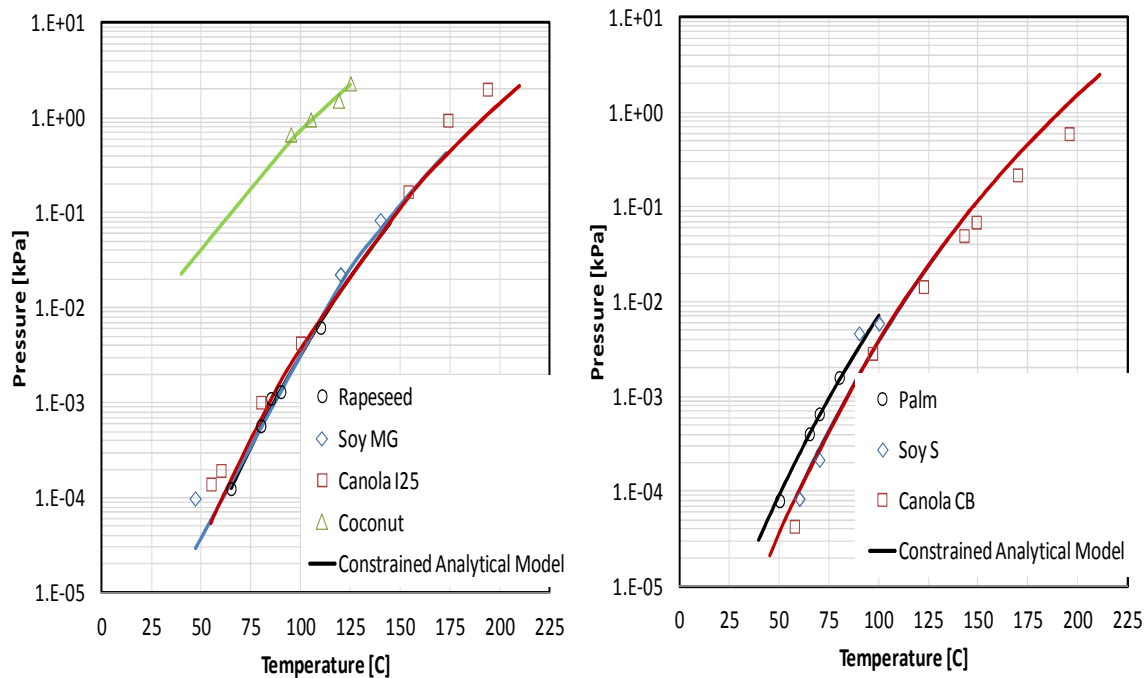


**Figure 6.6** Experimental and predicted vapour pressure of biodiesel fuels listed in Table 6.1 with the analytical “Constrained” scenario.

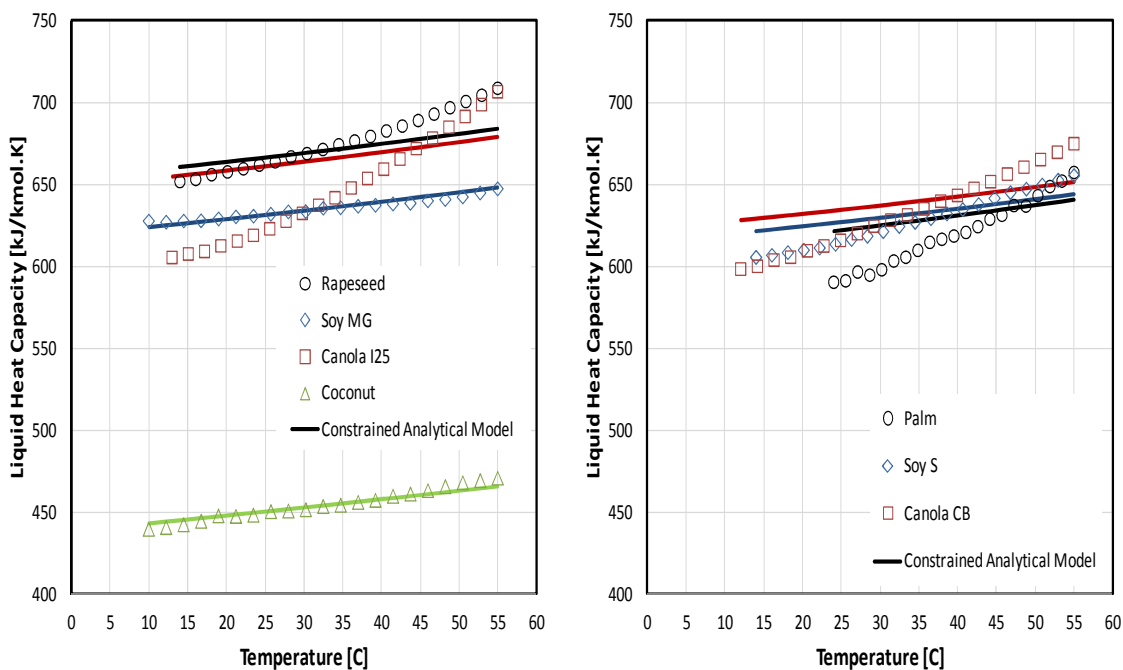


**Figure 6.7** Experimental and predicted liquid heat capacity of biodiesel fuels listed in Table 6.1 with the analytical “Constrained” scenario.

### 6.2.2 Equation of State Approach

The Advanced Peng-Robinson Equation of State (APR-EoS) [Peng and Robinson, 1976; VMG, 2010] was used to simultaneously calculate the vapour pressure and the heat capacity of the biodiesels listed in Table 6.1. Calculations were based on the critical properties and acentric factor for FAMES introduced in Chapter 5. The classic van der Waals mixing rules were used; initially the interaction parameters,  $k_{ij}$ , were set to zero. Figures 6.8 and 6.9 show the measured and modeled vapour pressure and heat capacity, respectively, for all of the biodiesel fuels studied and the AARDs for the model are given in Table 6.7. The average AARD is 12% for vapour pressure and 3% for liquid heat capacity.

**Table 6.25** Performance of APR-EoS prediction of biodiesel fuel vapour pressure and liquid heat capacity.

Biodiesel Source	Code	AARD [%]	
		$P_V$	$C_{PL}$
Canola (South Alberta)	CB-01	21.7	1.9
Canola (Saskatchewan)	I-25	11.7	3.3
Soy (Sunrise, US)	SB100	8.8	1.4
Soy (Mountain Gold, US)	MGB100	15.7	2.7
Rapeseed (Europe)	S102550	9.9	6.6
Palm (Europe)	S090824	4.4	2.0
Coconut (Europe)	S070717	14.5	1.3
<b>Total</b>	-	<b>12.3</b>	<b>2.7</b>

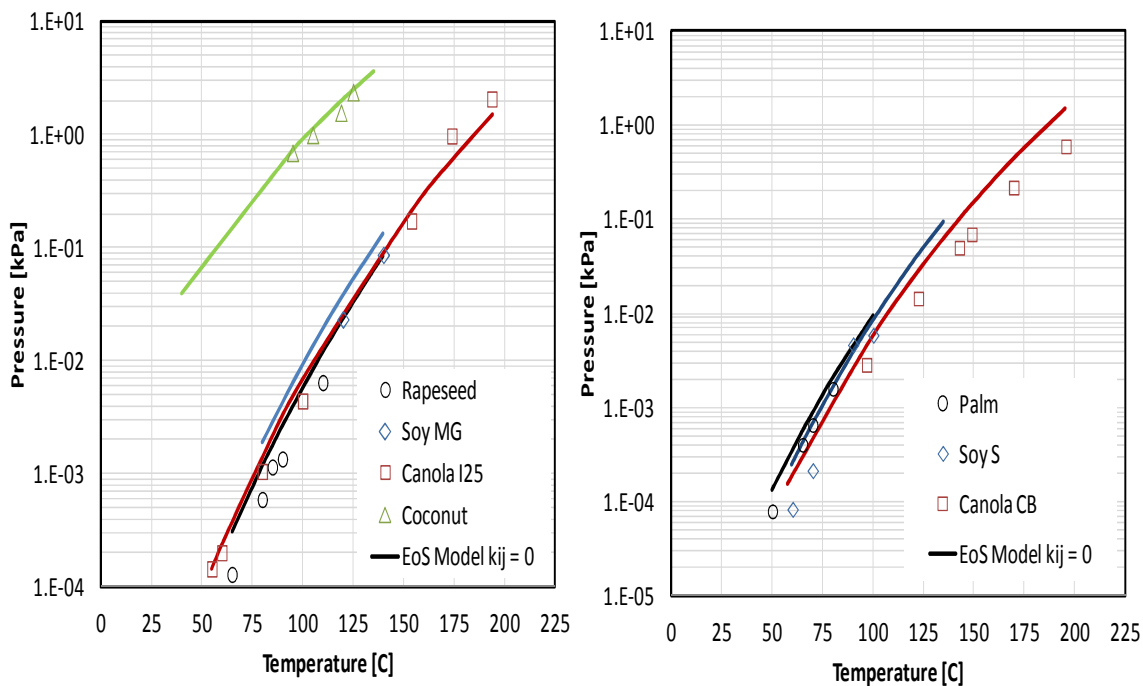


**Figure 6.8** Experimental and predicted vapour pressure of biodiesel fuels listed in Table 6.1 with the Advanced Peng-Robinson equation of state.

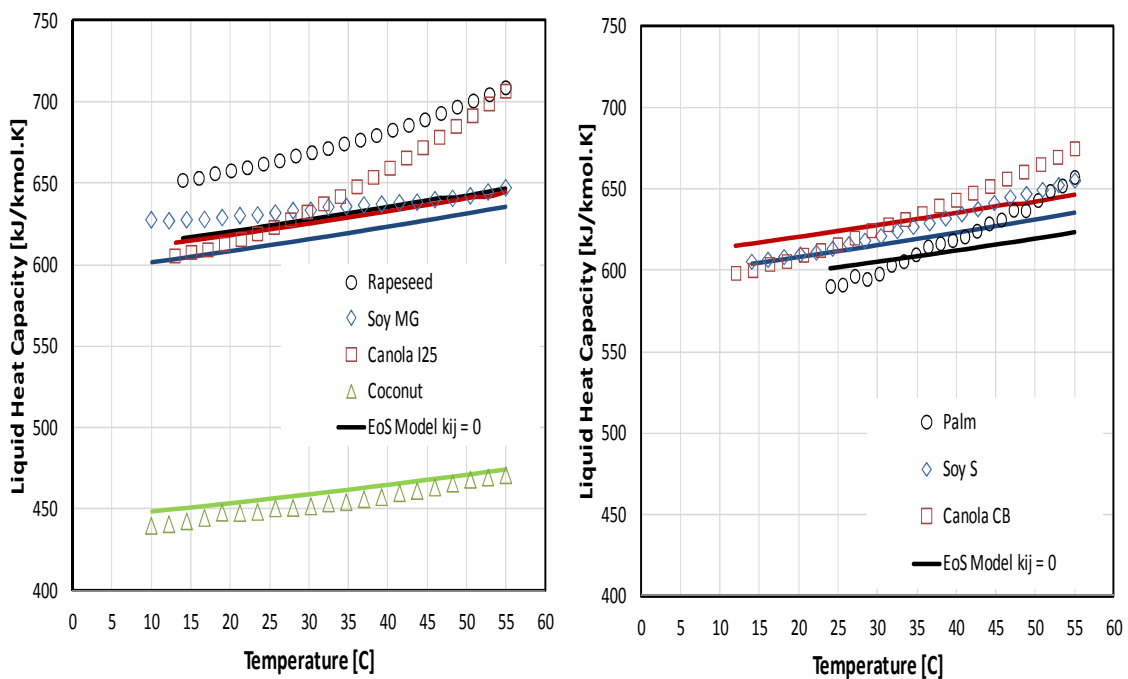


**Figure 6.9** Experimental and predicted liquid heat capacity of biodiesel fuels listed in Table 6.1 with the Advanced Peng-Robinson equation of state.

Note that the differences between predicted and experimental vapour pressure data are positive, meaning that the model is over predicting vapour pressure. The consistent positive deviation suggests that the solution is behaving somewhat non-ideally. Over-predictions in the saturation pressure of substances can be accounted for by decreasing the value of the interaction parameter. In this case, the interaction parameters for all FAME pairs were modelled using the Gao et al. correlation:

$$1 - k_{ij} = \left[ \frac{2\sqrt{T_{Ci}T_{Cj}}}{T_{Ci} + T_{Cj}} \right]^n, \quad [6.3]$$

A decrease in the  $n$ -value in Equation 6.3 decreases the value of  $k_{ij}$ . Figure 6.10 shows the predicted and experimental values for coconut vapour pressure with  $n = 0$  and  $n = -5$ . The AARD was improved by this reduction from 14.5 to 9.5%. Note, however, that the same change in  $n$ -value did not produce any significant difference in the prediction of vapour pressure for the rest of the biodiesels (AARD values remained the same). The difference in sensitivity can be explained in terms of relative volatility (related to the ratio of vapour pressure) of the different FAMEs that comprise the biodiesels. In the case of the coconut biodiesel, as shown in Table 6.2, the composition distribution varies from  $C_6$  up to  $C_{18}$ , which gives a wide range in relative volatility. On the other hand, the majority of the biodiesels range from only  $C_{16}$  to  $C_{18}$  and there is little range in the volatility and therefore little sensitivity to the interaction parameters.

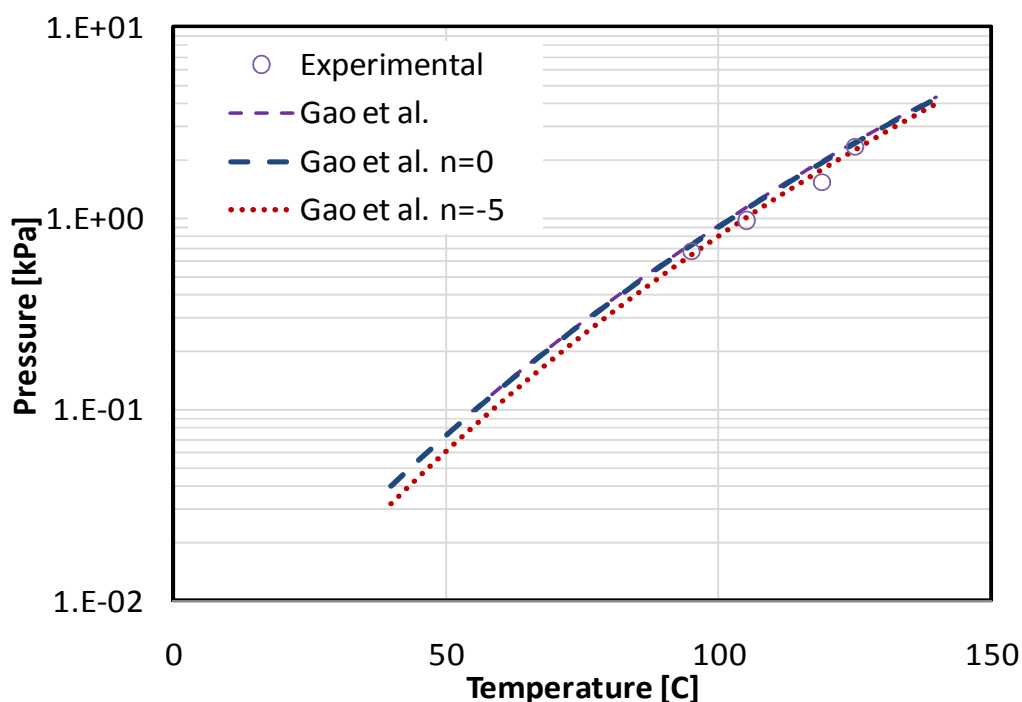


**Figure 6.10** Experimental and predicted vapour pressure of coconut biodiesel with the  $n$  values ranging from  $Z_c$  to  $-5$ .

Liquid heat capacity predictions, in general, were within 3% of the data; however, the predicted trends were slightly off, Figure 6.9. This deviation may be explained by non-idealities in the liquid phase, as noted for the Analytical approach. One way to account for non-ideal solutions in the EoS model is by tuning the interaction parameters. However, it was found that the liquid heat capacity data has low sensitivity to the  $k_{ij}$  values. As discussed in Chapter 4, the liquid heat capacity is calculated using the residual heat capacity by the equation of state; the residual heat capacity depends weakly in the attractive parameter (which contains the interaction parameter) and strongly on the first and second derivative of the attractive parameter (which do not contain the interaction parameter). Figure 6.11 shows the predicted and experimental values for coconut with  $n = 0$  and  $n = -5$ . The AARD value remained the same within 3 significant figures.

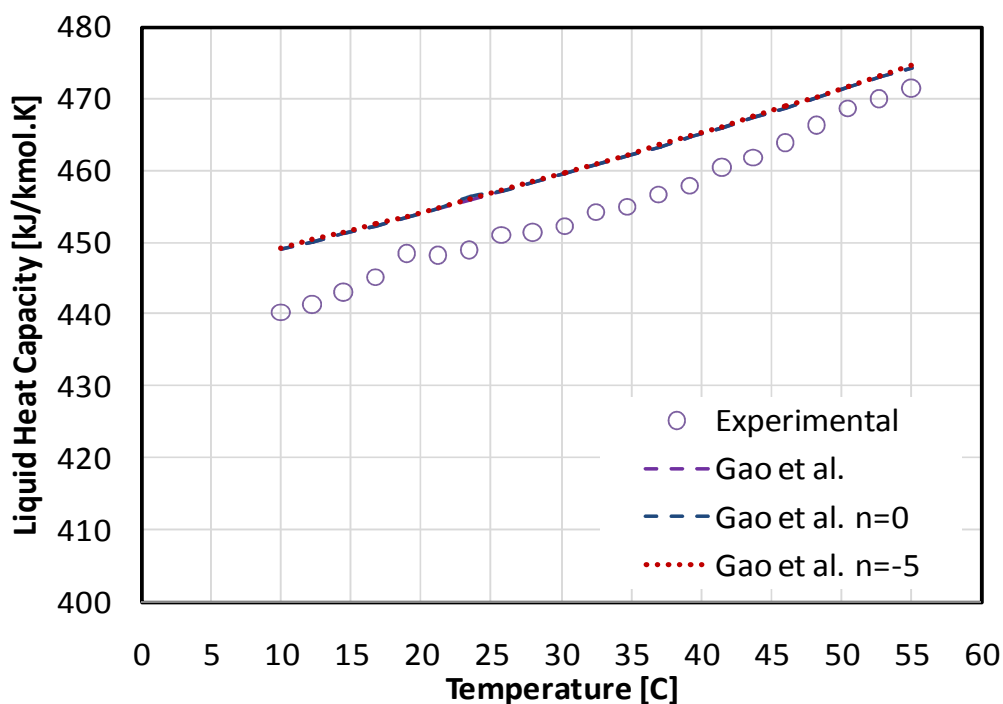


**Figure 6.11** Experimental and predicted liquid heat capacity of coconut biodiesel with the  $n$  values ranging from  $Z_c$  to -5.

One option to account for the apparent non-idealities in the liquid phase of the biodiesels is to use a different approach for the  $k_{ij}$  values; for instance, zero interaction parameters between saturated FAMEs pairs as well as between un-saturated FAMEs pairs and tuned  $k_{ij}$  values between saturated/unsaturated pairs. Another option is to use a different set of mixing rules. However, both the analytical and APR EoS models predict both the vapour pressures and heat capacities with sufficient precision for most practical applications and further refinement is beyond the scope of this thesis. The good agreement (without tuning) between the models and the data provide validation for both the VPMA and the modeling approach.

### 6.3 Summary

Vapour pressure experimental data of complex mixtures (biodiesel fuels) measured with the HV-VPMS were introduced in this chapter. The repeatability of the data was within 8%. The models developed in Chapters 4 and 5 were in good agreement with the data with AARD values better than 12%. The heat capacity constrained models were also in good agreement with liquid heat capacity data with an AARD better than 2%. The importance of constraining vapour pressure models with liquid heat capacity was again demonstrated.

This chapter provided a data validated modelling framework for the vapour pressure and heat capacity of biodiesel fuels, providing the means to better assess and implement this important alternative fuel. The validation of the proposed modeling method is a necessary step towards a reliable experimental and modelling framework for complex ill-defined mixtures, such as heavy oil which is considered in Chapter 7.

## CHAPTER SEVEN: MODELLING HEAVY OIL VAPOUR PRESSURE AND CALORIMETRIC DATA

The phase behaviour of heavy oils and bitumens is typically modeled with an equation of state. Castellanos Diaz et al., [2011] recently develop a characterization methodology for the Advanced Peng Robinson equation-of-state to model vapour-liquid and liquid-liquid equilibria for an Athabasca bitumen mixed with light solvents. The saturation pressures in Castellanos Diaz et al. work were dominated by the light solvents and therefore the ability of the model to predict the vapour pressure of the bitumen was not assessed. Modeling the vapour pressure of the bitumen alone provides another test of the oil characterization, particularly for the lightest part of the fluid.

The vapour pressure of heavy oil is expected to be very low at low to moderate temperatures (20 to 60 °C) due to their high molecular weight. The uncertainty of direct measurements of vapour pressure below approximately  $10^{-4}$  kPa tends to be high, as discussed in Chapters 3 and 4. On the other hand, thermal cracking of the heavy oil fractions limits vapour pressure data to temperatures below 300 °C. Note that the thermal cracking temperature point is, for all practical purposes, independent of the pressure of the system. Hence, the range for which reliable vapour pressure data can be collected for heavy oil fractions is limited and the calorimetric data constrained extrapolation discussed in Chapter 4 is required to determine vapour pressures at the desired conditions.

This chapter presents the proposed oil characterization and equation-of-state based modelling method. The method is applied to a Western Canadian bitumen sample based on its experimental and extrapolated normal boiling point and asphaltene content. Experimental liquid heat capacity and vapour pressure data for this oil are provided and modeled using the methodology presented in Chapter 4.

## **7.1 Experimental Data and Modelling Results for Western Canadian Bitumen**

### ***7.1.1 Vapour Pressure Experimental Data of WC\_B1 Bitumen***

Figure 7.1 shows the vapour pressure of the WC\_B1 bitumen and maltenes measured with the VPMA at a temperature range of 25 to 180 °C. The average repeatability was 6.4%. The vapour pressure data are tabulated in Appendix A. The differences between the vapour pressure of the heavy oil and the maltenes fraction are 5.0% on average, which is close to the average error, 2.9%. This close result was expected since asphaltenes have a high molecular weight and low vapour pressure and therefore contribute a negligible amount of partial pressure to the total pressure of the system.

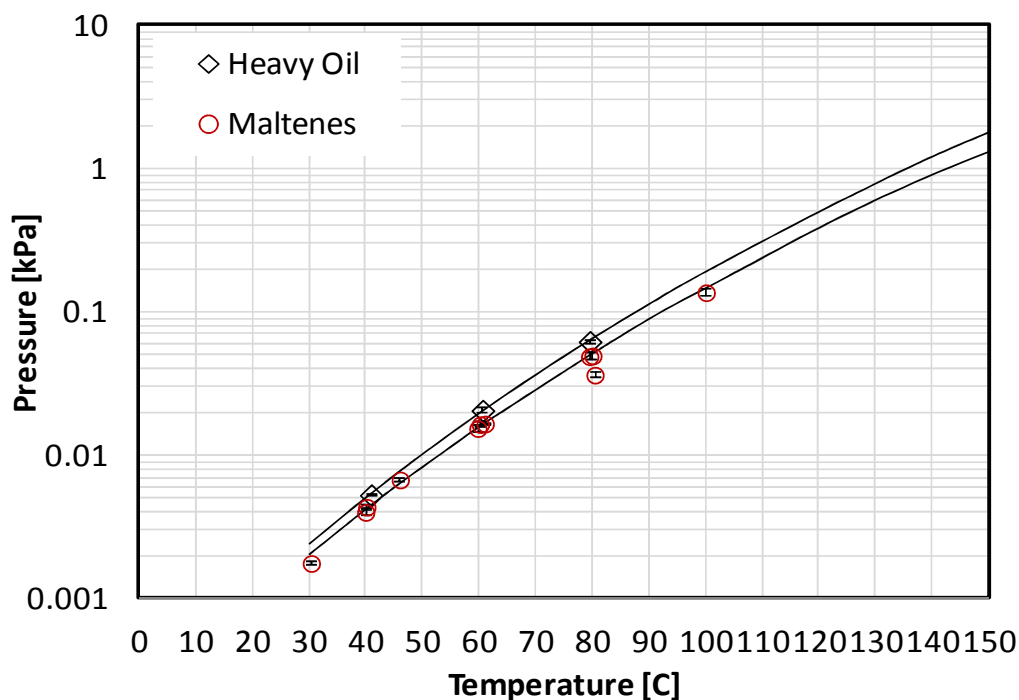


**Figure 7.1** Vapour pressure of WC\_B1 bitumen and maltenes – lines are drawn to show the tendency and do not represent any specific model.

### 7.1.2 Liquid Heat Capacity of Alberta Region Heavy Oil

Figure 7.2 shows the liquid heat capacity of WC\_B1 maltenes as a function of temperature. The data were regressed to a second order polynomial function of temperature [K], Equation 7.1, with an AARD of 0.3%.

$$C_{P,L} = 778.27 - 2.82T + 9.20 \times 10^{-3} T^2, \quad [7.1]$$

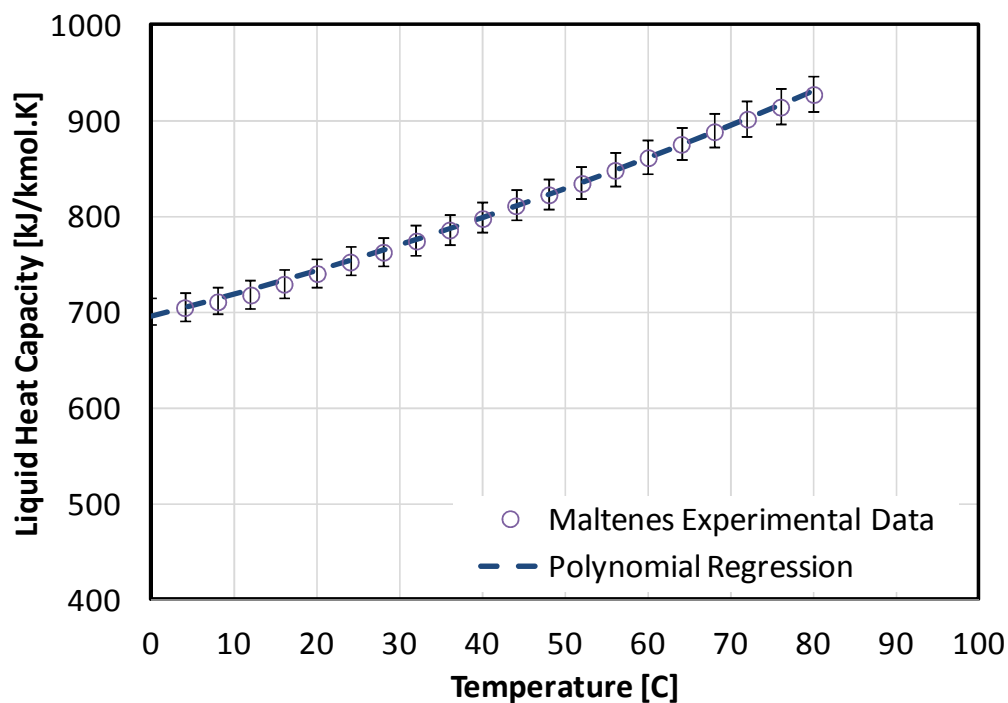


**Figure 7.2** Experimental and regressed liquid heat capacity of WC\_B1 maltenes and fractions.

## 7.2 Modelling Approach for Heavy Oil Vapour Pressure using Equation of State

The modelling of the heavy oil vapour pressure requires a definition of the fluid composition; however, the large amount of components present in a heavy oil sample makes the task of defining every single component virtually impossible. An alternative is to generate narrow-boiling point pseudo-components based on the normal boiling point (NBP) of the heavy oil, as described in Chapter 2. A general characterization introduced by Castellanos Diaz et al. [2011] is described as follows:

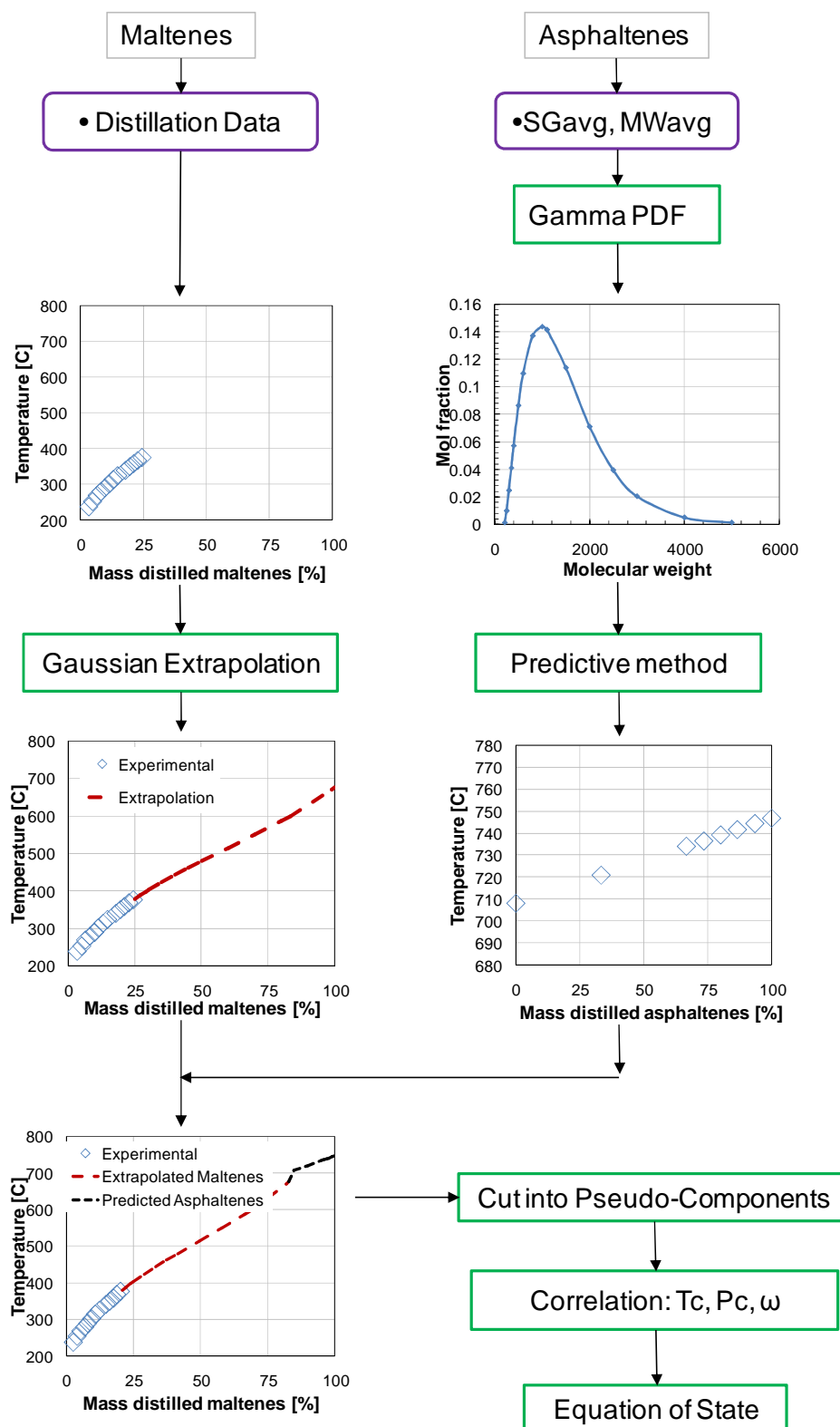
### ***7.2.1 General Characterization of Heavy Oils***

Figure 7.3 shows an algorithm that summarizes a general characterization of heavy oil and bitumen based on the NBP curve [Castellanos Diaz et al. 2011]. The pseudo-components comprising the oil are obtained by dividing the extended NBP curve of the crude oil into boiling cuts. The maltenes and asphaltene fractions are characterized separately as described in Section 2.1.

The normal boiling point of the maltenes fraction as well as the average molecular weight and average specific gravity of the oil are required. The characterization methodology for maltene and asphaltene fractions is outlined below.

#### **7.2.1.1 Maltenes Normal Boiling Point Characterization**

As discussed in Chapter 2, traditional vacuum distillation techniques can provide boiling point data for only 20 to 30 wt% of a heavy oil or bitumen. Since the proposed characterization of the maltenes fraction is based on the NBP curve, an extrapolation of the NBP over the entire boiling range of the maltenes is required.



**Figure 7.3** Algorithm schematics for the modelling of heavy oil and bitumen based on the measured and extrapolated normal boiling point.

Figure 7.4 shows the boiling point data for the WC\_B1 maltenes which are divided into three regions: Light Fraction, Medium Fraction, and Heavy Fraction. The Heavy Fraction is the non-distillable fraction (above approximately 30 wt% distilled of the maltenes). The Light and Medium fractions are distinguished by the shape of their probability distribution as will be discussed later. It is assumed that the normal boiling point profile of the Medium Fraction follows a Standard Normal or Gaussian probability distribution [Huang and Radosz, 1991]. It is further assumed that the Heavy Fraction follows the same distribution as the Medium Fraction.

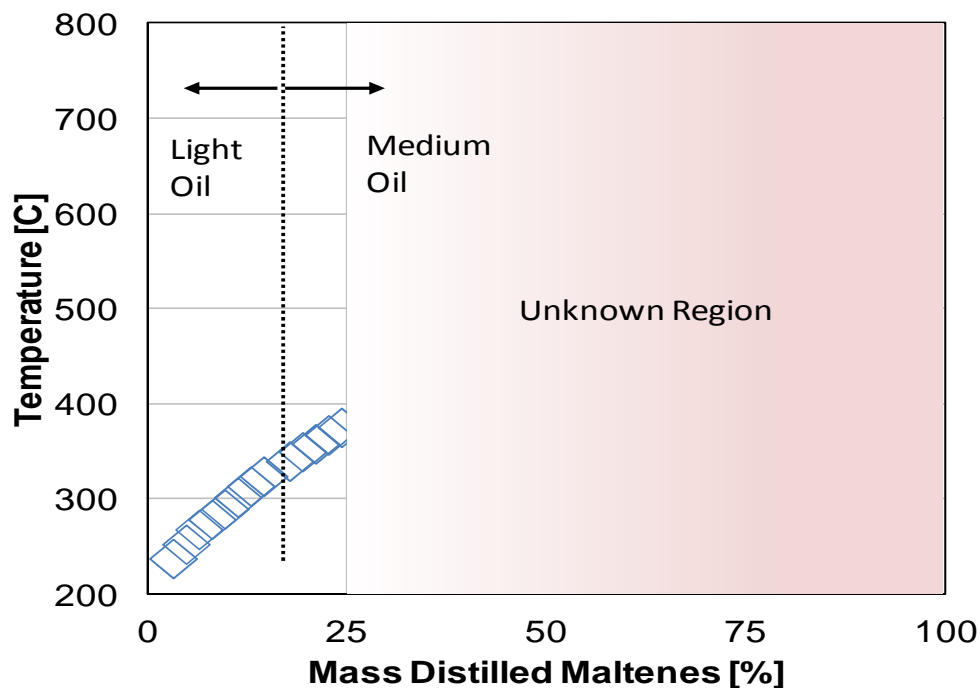


**Figure 7.4** Experimental normal boiling point of WC\_B1 maltenes (Experimental data provided by Sanchez [2011]).

A linear extrapolation of the Gaussian distribution was carried over in a probability plot. The first step in the extrapolation is to transform the heavy oil cumulative mass percentage distilled,  $w$ , into a standard normal distribution given by:

$$w = \int_{-\infty}^Z \frac{1}{\sqrt{2\pi}} \exp\left[-\frac{Z^2}{2}\right] dZ = \frac{1}{2} \left[1 + \operatorname{erf}\left(\frac{Z}{\sqrt{2}}\right)\right], \quad [7.2]$$

where  $w$  is the cumulative mass percentage of bitumen and  $Z$  is the standard normal distribution parameter. Note that the total heavy oil mass percentage is used instead of the maltenes-based mass percentage; otherwise, high peaks on the final boiling point of the maltene fractions are obtained.

Figure 7.5 shows experimental NBP data for WC\_B1 bitumen extrapolated versus the transformed variable  $Z$ . Note that Medium and Light Oil are defined by the point at which the slope of the experimental data in Figure 7.5 changes. The extrapolated  $Z$  values are converted to mass fractions using Equation 7.2 and the resulting extrapolated distillation curve is shown in Figure 7.6.

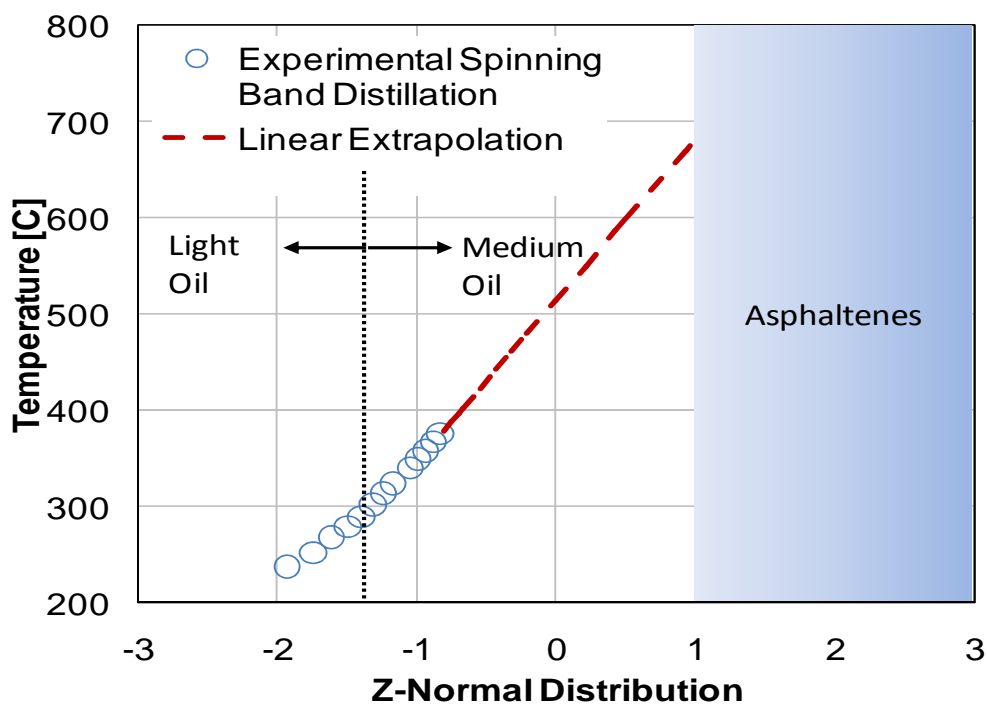


**Figure 7.5** Gaussian extrapolation of the normal boiling point of maltenes based on the Medium region.

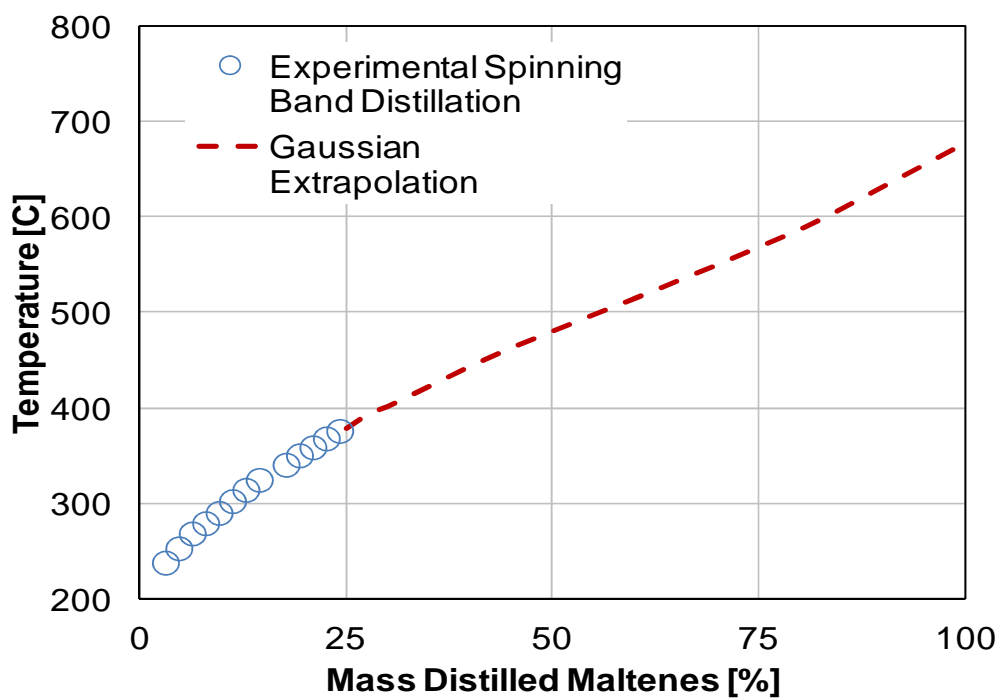


**Figure 7.6** Experimental and extrapolated normal boiling point of WC\_B1 maltenes (Experimental data provided by Sanchez [2011]).

### 7.2.1.2 Asphaltenes Normal Boiling Point Characterization

The normal boiling point of the asphaltenes must be determined indirectly because the expected boiling point of the lightest component in the asphaltene fraction is expected to be higher than its thermal cracking point. One way to evaluate the NBP of asphaltenes is through its molecular weight distribution.

#### Asphaltenes Molecular Weight Distribution

The molecular weight distribution of asphaltenes can be described by the Gamma probability function [Yarranton and Masliyah, 1996], here termed the Gamma Molecular Distribution Function (GMDF):

$$P(MW) = \frac{(MW-\eta)^{\alpha-1}}{\beta\Gamma(\alpha)} \exp\left(-\frac{MW-\eta}{\beta}\right), \quad [7.3]$$

where  $MW$  is the molecular weight,  $P(MW)$  is the probability function of  $MW$ ,  $\beta$  is related to the average molecular weight of the distribution,  $\eta$  is lowest molecular weight in the distribution, and  $\alpha$  is a parameter setting the shape of the distribution.

The GMDF has three adjustable parameters,  $\alpha$ ,  $\beta$ , and  $\eta$ , that are related as follows [Whitson and Brulé, 2000]:

$$\beta = \frac{MW_{Avg} - \eta}{\alpha \Gamma}, \quad [7.4]$$

where  $MW_{AV}$  is the average molecular weight of the sample. If the average molecular weight of the sample is known, only two independent parameters remain ( $\alpha$  and  $\eta$ ). Initially, these parameters are guessed and are then tuned to fit specific physical properties of the oil such as molecular weight and density [Alboudjarewj et al., 2005]. To start the characterization,  $\alpha$  is initially equated to 1 (an exponential distribution) and then  $\eta$  is calculated as follows [Whitson and Brulé, 2000]:

$$\eta = \frac{110}{1 - (1 + 4\alpha^{-0.7})}, \quad [7.5]$$

The values that the parameters  $\alpha$  and  $\eta$  can take are restricted by the computational method. The parameter  $\alpha$  can vary from values near but greater than 0 up to approximately 100 where the gamma function,  $\Gamma$ , becomes a large number. For values of 20 and greater, the distribution resembles a Gaussian distribution and tends to be more pulse-like (the bell becomes thinner). The lowest possible value of  $\eta$  should be around 100 (molecular weight of n- C<sub>7</sub>) whereas the highest possible value should be close to the average molecular weight of the sample. Although in theory the value of  $\eta$  should be close to the molecular weight of an asphaltene monomer, in practical terms, it should be taken as an adjustable parameter rather than a physical property [Whitson and Brule, 2000]. Figure 7.7 shows a schematic of a GMDF:

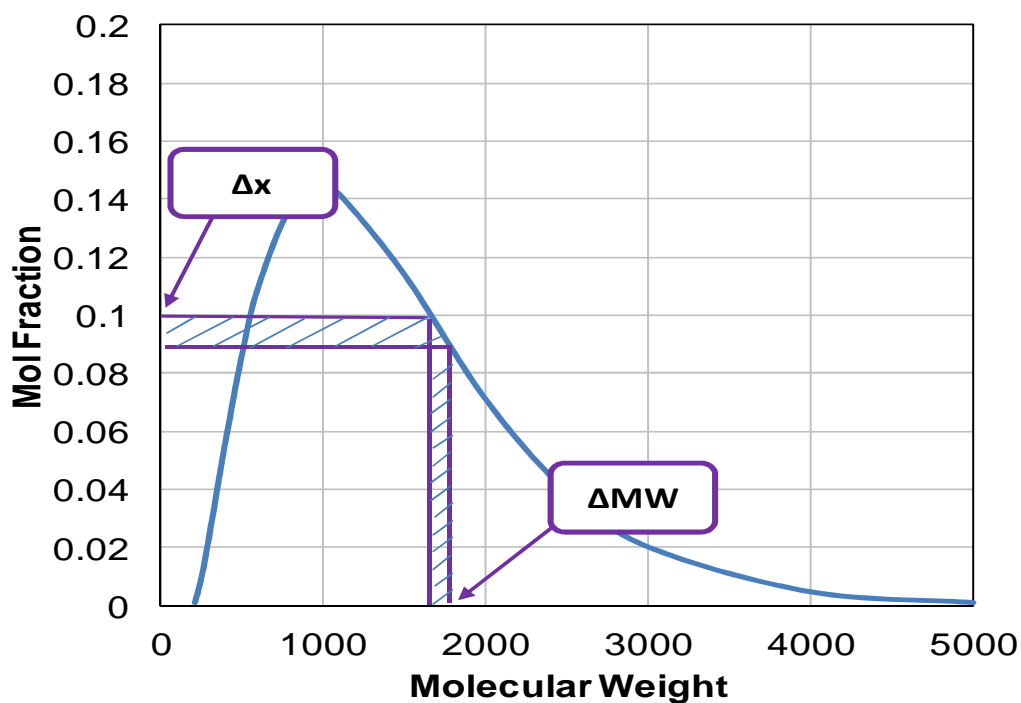


**Figure 7.7** GMDF schematic; compartmentalization of one molecular weight-based pseudo-component is shown.

Once the GMDF has been defined, a first set of asphaltene pseudo-components can be determined by dividing the curve by molecular weight ranges,  $\Delta MW$ , as shown in Figure 7.6. Generally, the width of each division is constant. Each pseudo-component is then characterized by an average molecular weight and its mole fraction,  $\Delta x$ .

#### Determination of the Normal Boiling Point of Asphaltenes

Once the pseudo-components have been defined through the GMDF, it is necessary to determine the specific gravity of each fraction in order to use common property correlations to calculate the normal boiling point. The specific gravity of the asphaltene pseudo-components,  $SG_i$ , can be calculated through Equation 7.6 [Alboudjarewj et al., 2005]

$$SG_i = 670MW_i^{0.0629}, \quad [7.6]$$

Note that the specific gravities of the pseudo-components must be constrained to obtain the correct average specific gravity of the asphaltene fraction. Hence, the specific gravity of each pseudo-component may need to be adjusted (depending on the GMDF chosen). For this purpose, the calculated specific gravity,  $SG_i$ , is multiplied by a proportional parameter,  $k_{SG}$ , to satisfy the following constraint [Whitson and Brulé, 2000]

$$SG_{Avg} = \frac{MW_{Avg}}{\sum_i x_i MW_i}, \quad [7.7]$$

where  $x_i$ : is the pseudo-component mole fraction and  $k_{SG}$ : is the proportional adjustable parameter [Satyro, 2007].

There are several methods that correlate the molecular weight, the specific gravity, and the boiling point for petroleum fractions. Some of these are explicit in boiling point and others are implicit relations that require iterative procedures. The NBP curve of the asphaltenes is obtained by using one of these methods for each pseudo-component. In this case, the Sørense relationship [Sørense, 1989], is used (7.8a for  $70 < MW < 300$  and 7.8b for  $MW > 300$ ):

$$T_b =$$

$$3.76587[\exp(3.7741 \times 10^{-3} MW + 2.98404 SG - 4.25288 \times 10^{-3} MW \cdot SG MW^{0.40167} SG - 1.58262), \quad [7.8a]$$

$$T_b =$$

$$9.3369[\exp(1.6514 \times 10^{-4} MW + 1.4103 SG - 7.5152 \times 10^{-4} MW \cdot SG MW^{0.5369} SG - 0.7276), \quad [7.8b]$$

where  $T_b$  is the normal boiling point in K. Figure 7.8 shows the normal boiling point curve of an asphaltene fraction characterized by  $\alpha=2.5$  and  $\eta=735$ ,  $SG_{avg} = 1.15$ , and  $MW_{avg} = 1800$  g/mol calculated using Equations 7.6 to 7.8.

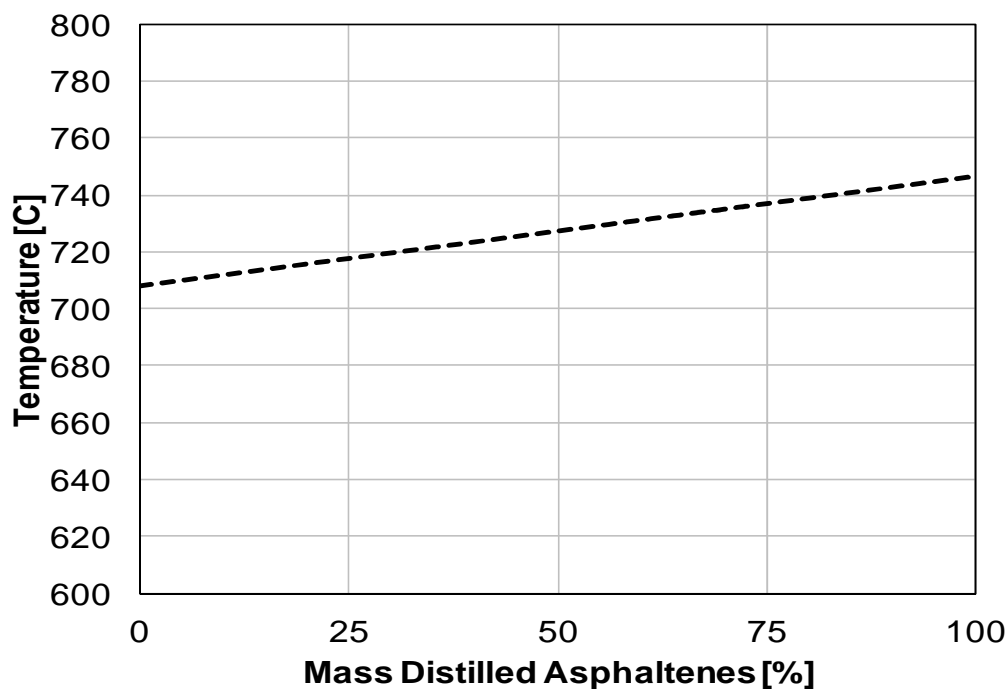


**Figure 7.8** Modelled normal boiling point for asphaltene fraction with  $\alpha=2.5$  and  $\eta=735$ .

### 7.2.1.3 Determination of Heavy Oil Pseudo-Components

Once a normal boiling point curve is provided for the maltenes and asphaltenes fractions, both curves can be combined and normalized to generate a unique NBP curve for the crude oil, Figure 7.9. Note, the constituents of the heavy oil form a continuum and therefore the normal boiling point curve must be continuous. The parameters  $\alpha$  and  $\eta$  were adjusted so that the boiling point of the first asphaltene fraction matched to the boiling point of the final maltene fraction from Gaussian extrapolation.

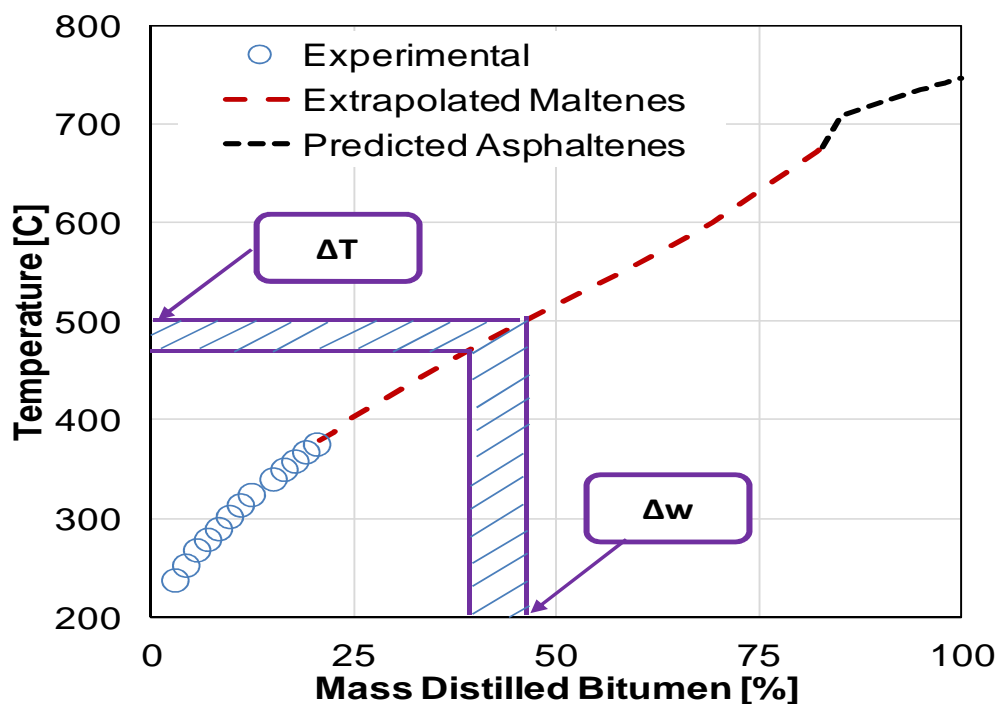


**Figure 7.9** Complete experimental and extrapolation normal boiling point of a bitumen (Experimental data provided by Sanchez [2011]); normal boiling point compartmentalization is also shown.

Boiling point based pseudo-components can be obtained as shown in Figure 7.9. The temperature delta used for the division of the NBP,  $\Delta T$ , can be constant for the entire NBP curve [Satyro, 2007] or can be constant for defined sections of the NBP curve; for instance, a specific temperature delta can be used for the maltenes and another for the asphaltenes [Castellanos Diaz et al., 2011]. In either case, each  $\Delta T$  is associated with a cumulative mass fraction.

Next, the specific gravity and molecular weight values are determined for each pseudo-component. To calculate the specific gravity of the fractions, a cumulative plot of SG for the entire oil is constructed from the Katz-Firoozabadi correlation for maltenes [VMG, 2010] and Equation 7.6 for asphaltenes. Then, the specific gravity of each fraction is calculated as follows:

$$SG_i = \frac{\int_{x_{i-1}}^{x_i} SG \cdot dx}{\Delta x}, \quad [7.9]$$

The molecular weight of each fraction can be then calculated from property correlations such as the Soreide correlation (Equation 7.8).

At this point, the heavy oil pseudo-components are characterized with a mole fraction, normal boiling point, molecular weight, and specific gravity. The next step in the

characterization is to predict the critical properties of the pseudo-components, which are required for modelling using an equation of state. Several authors [Mehrotra and Svrcek, 1985, Castellanos et al., 2011] recommended the Lee-Kesler correlations for the prediction of critical properties of heavy oil and its fractions. This method is described in Appendix C.

### ***7.2.2 Vapour Pressure Calculation***

The vapour pressure of the heavy oil is calculated using the Advanced Peng-Robinson equation of state [VMG, 2010] and classic van der Waals mixing rules, as described in Chapter 4. It is recommended to corroborate the model by calculating the liquid heat capacity of the heavy oil, especially since the vapour pressure of the heavy oils are expected to be below  $10^{-4}$  kPa at moderate temperatures, Chapter 3. As shown in Chapter 4, the ideal gas heat capacity of the substance is required in order to calculate the liquid heat capacity using the equation of state. The Laštovka -Shaw correlation for ideal gas heat capacity was used [Laštovka et al. 2008] (Appendix C).

Finally, interaction parameters between pseudo-component pairs are also required to tune the equation of state model. Castellanos et al. [2011] used the original Gao et al. correlation to calculate the interaction parameters between pseudo-components for heavy oil/solvent phase equilibria modelling. Later in this chapter it will be demonstrated that this assumption remains valid for the liquid-vapour phase equilibrium of bitumen alone.

### 7.3 Modelling the WC\_B1 Sample

The average physical properties of the WC\_B1 bitumen used in this work are provided in Table 7.1. Boiling point data was collected by Sanchez [2011] using spinning band vacuum distillation, Figure 7.10. The maltenes NBP extrapolation was performed using the Gaussian probability distribution, Section 7.2. The asphaltene NBP was predicted using the Gamma distribution function with values of  $\alpha = 2.0$  and  $\eta = 750$ .

The pseudo-components comprising the bitumen were obtained by cutting the normal boiling point using VMGSim 6.0.38 [VMG, 2010]. The maltenes were represented with 10 pseudo-components and the asphaltenes by 5 pseudo-components. Physical properties of the pseudo-components were calculated using the correlations listed in Table 7.2 and are summarized in Table 7.3

The ideal gas heat capacities of the pseudo-components were calculated using the Laštovka-Shaw equation (Appendix C) and then correlated with a three-degree polynomial expression using VMGSim 6.0.38 [VMG, 2011]. Values of the polynomial parameters are shown in Table 7.4

**Table 7.1** Physical properties of WC\_B1 maltenes and asphaltenes

<b>Property</b>	<b>Maltenes</b>	<b>Asphaltenes</b>	<b>Bitumen</b>
Average Molecular Weight	450 g/mol	1800 g/mol	510 g/mol
Average Specific Gravity	1.005	1.105	1.010
Boiling Point Range	207-676 °C	676-750 °C	207-750°C

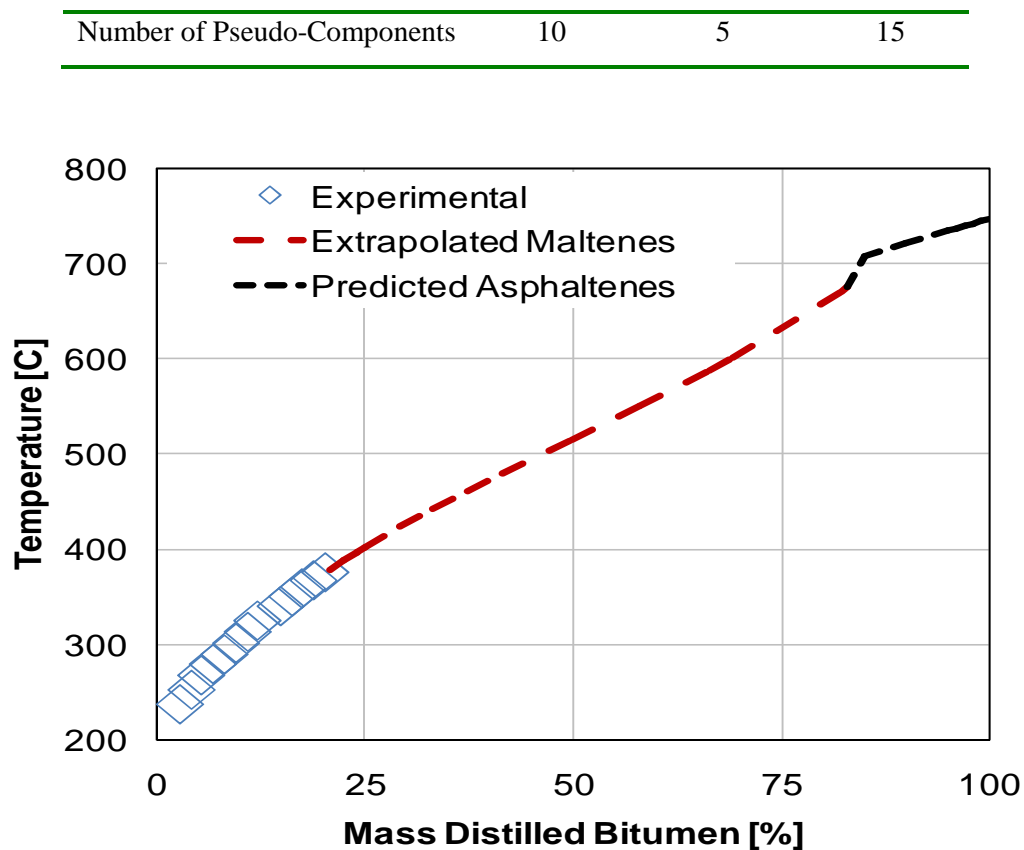


**Figure 7.10** Complete experimental and extrapolated normal boiling point of WC\_B1 bitumen (Data from Sanchez [2011]).

**Table 7.2** Physical property correlations used in WC\_B1 bitumen modelling .

Property	Correlation
Molecular Weight	Lee - Kesler
Maltenes Specific Gravity	Katz - Firoozabadi
Asphaltenes Specific Gravity	Equation 7.6
Critical Temperature	Lee - Kesler
Critical Pressure	Lee - Kesler
Critical Volume	Twu
Acentric Factor	Lee - Kesler - Lee

**Table 7.3** Pseudo-component physical properties of WC\_B1 bitumen.

Pseudo	x	w	SG	Tc [°C]	Pc [kPa]	Vc [kmol/m <sup>3</sup> ]	ω	NBP [°C]
Malt01	0.057	0.023	0.858	418.033	2458.660	0.589	0.502	221.686
Malt02	0.051	0.023	0.872	445.351	2251.800	0.651	0.559	250.093
Malt03	0.062	0.032	0.886	472.495	2059.790	0.718	0.619	279.065
Malt04	0.055	0.031	0.899	498.937	1887.860	0.787	0.681	307.849
Malt05	0.068	0.042	0.911	523.834	1736.870	0.856	0.743	335.506
Malt06	0.063	0.044	0.924	550.165	1596.910	0.929	0.808	364.812
Malt07	0.067	0.051	0.937	575.498	1471.490	1.003	0.874	393.461
Malt08	0.223	0.206	0.965	630.123	1241.660	1.160	1.018	455.687
Malt09	0.188	0.222	0.989	702.193	919.946	1.454	1.270	546.761
Malt10	0.108	0.157	1.007	767.260	673.174	1.777	1.540	634.081
Asph01	0.003	0.005	1.026	766.230	849.228	1.524	1.369	610.916
Asph02	0.012	0.025	1.039	798.680	791.605	1.595	1.437	646.471
Asph03	0.020	0.052	1.054	835.210	746.436	1.658	1.495	684.537
Asph04	0.017	0.061	1.075	876.100	726.730	1.703	1.524	723.110
Asph05	0.006	0.026	1.088	907.000	716.733	1.737	1.536	751.460

**Table 7.4** Parameters for the three-degree regressed polynomial for ideal gas heat capacity calculation of WC\_B1 bitumen pseudo-components.

Pseudo	$C_p^0$ [kJ/kmol.K] = a + bT + cT <sup>2</sup>				
	a	b	c	T <sub>min</sub> [°C]	T <sub>max</sub> [°C]
Malt01	66.14	0.9839	-3.32x10 <sup>-4</sup>	25.000	426.850
Malt02	72.93	1.09	-3.69 x10 <sup>-4</sup>	25.000	426.850
Malt03	79.98	1.22	-4.11 x10 <sup>-4</sup>	25.000	426.850
Malt04	86.97	1.35	-4.57 x10 <sup>-4</sup>	25.000	426.850
Malt05	93.30	1.48	-5.01 x10 <sup>-4</sup>	25.000	426.850
Malt06	99.8	1.63	-5.53 x10 <sup>-4</sup>	25.000	426.850

\Malt07	105.82	1.78	$-6.05 \times 10^{-4}$	25.000	426.850
Malt08	-26.92	2.54	$-1.1 \times 10^{-3}$	25.000	426.850
Malt09	-23.15	3.28	$-1.4 \times 10^{-3}$	25.000	426.850
Malt10	-15.09	4.08	$-1.7 \times 10^{-3}$	25.000	426.850
Asph01	178.67	3.90	$-1.3 \times 10^{-3}$	25.000	426.850
Asph02	198.96	4.67	$-1.6 \times 10^{-3}$	25.000	426.850
Asph03	226.81	5.85	$-2.0 \times 10^{-3}$	25.000	426.850
Asph04	269.82	7.88	$-2.7 \times 10^{-3}$	25.000	426.850
Asph05	296.20	9.47	$-3.3 \times 10^{-3}$	25.000	426.850

#### 7.4 Equation of State Model for Alberta Region Heavy Oil Vapour Pressure

The Advanced Peng-Robinson Equation of State (APR-EoS) [Peng and Robinson, 1976; VMG, 2010] was used to simultaneously calculate the vapour pressure and the heat capacity of the WC\_B1 bitumen and fractions. The classic van der Waals mixing rules were used with adjustable interaction parameters,  $k_{ij}$  determined using the Gao et al. correlation, Equation 7.10

$$1 - k_{ij} = \left[ \frac{2\sqrt{T_{Ci}T_{Cj}}}{T_{Ci} + T_{Cj}} \right]^n, \quad [7.10]$$

Only one parameter,  $n$ , needs to be adjusted for the entire heavy oil. Castellanos Diaz et al. [2011] showed that an  $n$ -value equal to the critical compressibility factor of each pseudo-component pair (the original Gao et al. correlation) suffices to predict the phase

behaviour of heavy oil/solvent mixtures. The validity of this approach will be assessed in the following section.

The vapour pressure curve is calculated using a flash calculation. Figure 7.11 shows the experimental and predicted data for the WC\_B1 bitumen oil and for its maltene fraction. The average AARD was 17%. The liquid heat capacity of the heavy oil was calculated using Equation 7.12:

$$C_P^L \approx \sum_i x_i C_{P,i}^0 - C_P^{Res}, \quad [7.12]$$

where  $C_P^{Res}$  is the heat capacity residual calculated through the equation of state. The ideal gas heat capacity of each pseudo-component,  $C_{P,i}^0$ , was calculated using the polynomial equation listed in Table 7.4. Figure 7.12 shows the experimental and predicted liquid heat capacity of the heavy oil maltenes with an AARD of 3.5%. The predicted trend does not exactly follow the experimental data, mainly due to the predicted ideal gas heat capacity.

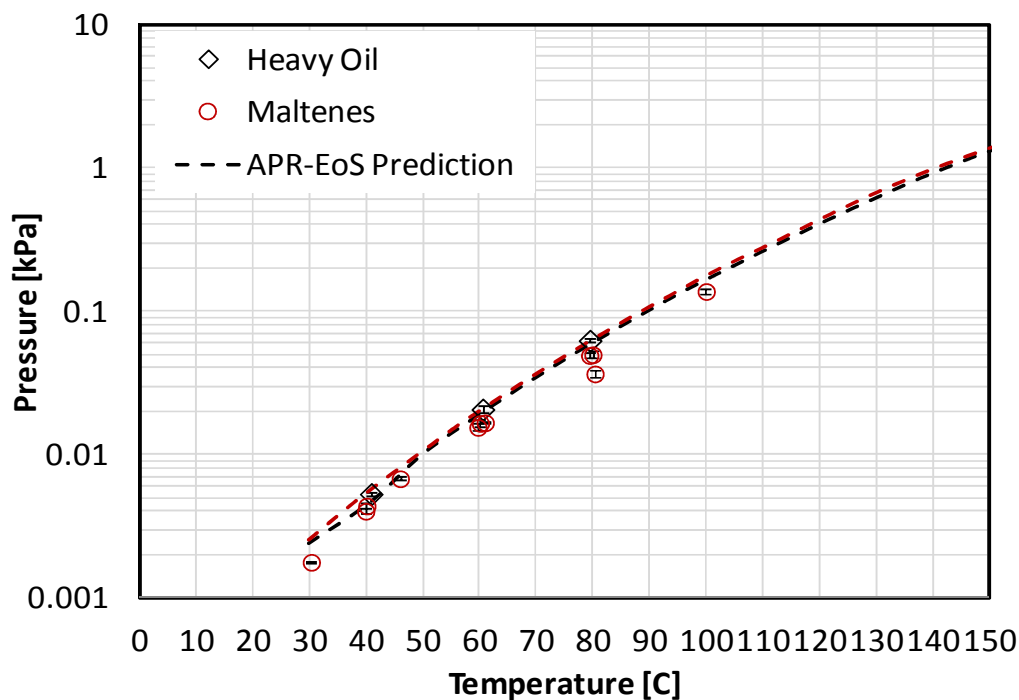


**Figure 7.11** Experimental and predicted vapour pressure of WC\_B1 bitumen and maltene fraction using the APR-EoS.

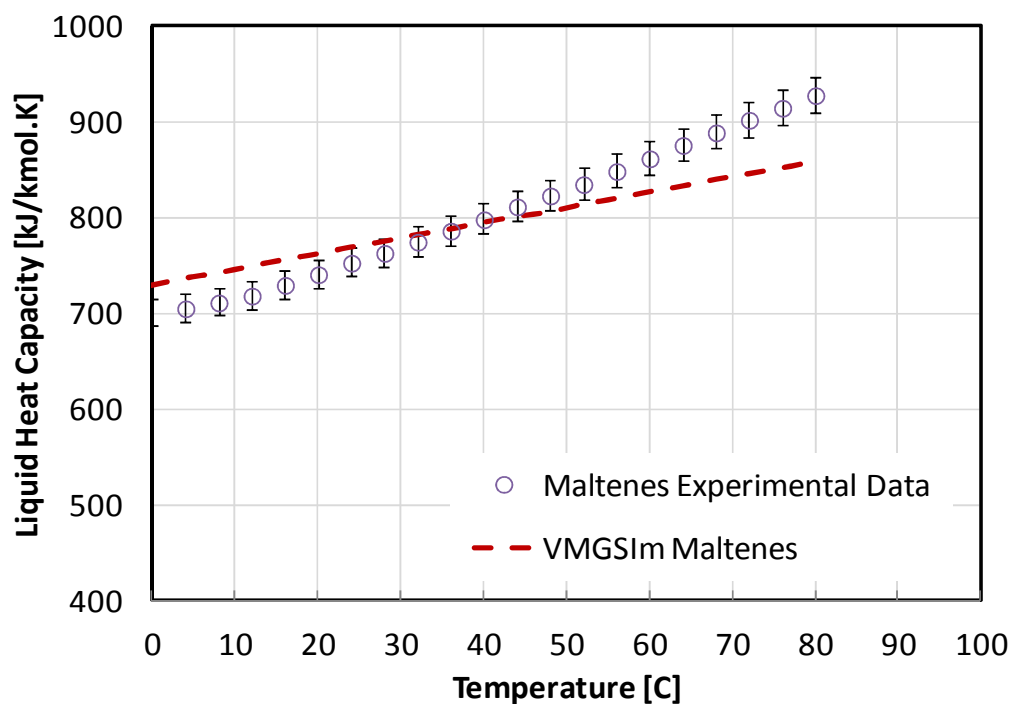


**Figure 7.12** Experimental and predicted liquid heat capacity of WC\_B1 bitumen and maltene fraction using the APR-EoS and the Lastovka-Shaw correlation.

In addition, a sensitivity analysis of the vapour pressure and liquid heat capacity predictions with respect to the interaction parameters was performed. The  $n$ -value was varied from 2 to -1 and the vapour pressure of the maltene fraction calculated, Figure 7.13. The best predictions were obtained with an  $n = 0$  (ideal solution), with an AARD of 15%. The model results suggest that the lightest components of the heavy oil maltenes (which vapour pressure predominate) behave like an ideal solution. However, the difference between the ideal case and the default of  $n$  set to the critical compressibility was small.

With respect to the heat capacity, it was found that the difference between two scenarios (i.e.,  $n=0$  and  $n=2$ ) for a given data point is always lower than 0.4%, less than the average error of the measurement (2%). This sensitivity is low because the calculation of the residual heat capacity by the equation of state depends weakly in the attractive parameter (which contains the interaction parameter) and strongly on the first and second derivative of the attractive parameter (which do not contain the interaction parameter).

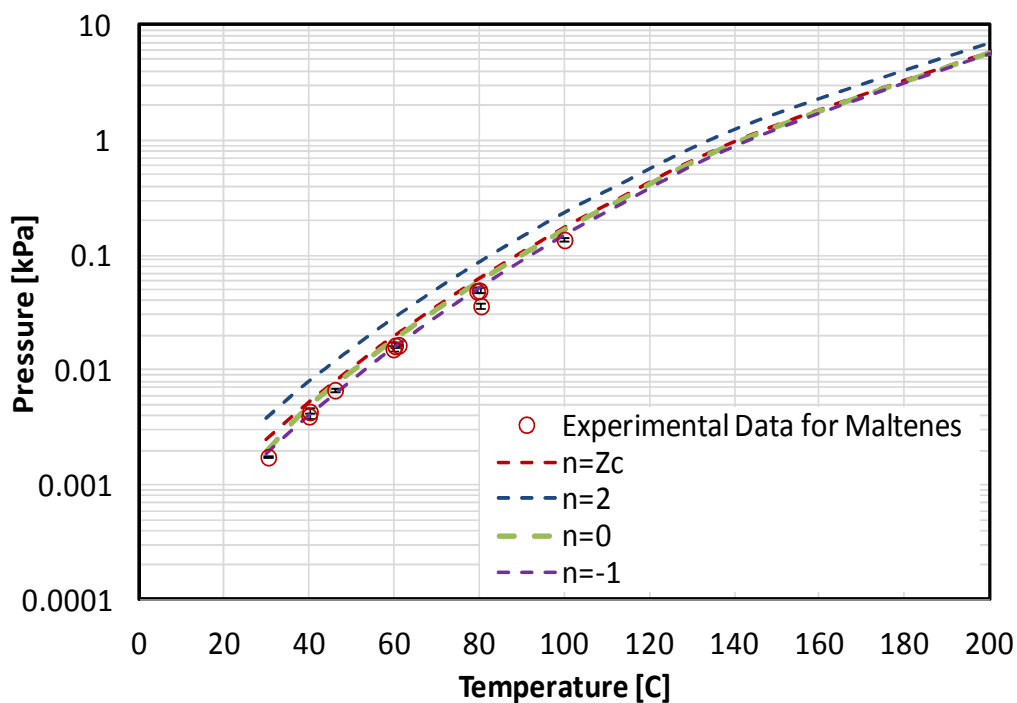


**Figure 7.13** Experimental and predicted vapour pressure values for WC\_B1 maltene fraction at different  $n$ -values for the Gao et al. interaction parameter correlation.

### 7.5 Summary

Experimental vapour pressure data for a Western Canadian bitumen and maltene fraction were presented in this chapter as well as liquid heat capacity data. It was shown that the HV-VPMS produces experimental vapour pressure data of complex heavy mixtures with a repeatability within 2.9%, which corroborates the findings in Chapter 6.

A systematic characterization technique was introduced based on the experimental and extrapolated normal boiling point of the bitumen. It was shown that this characterization coupled with the APR EoS is capable of predicting vapour pressure and liquid heat capacity within 12%. It was concluded that, in order to predict precise values of the

vapour pressure, the interaction parameters between bitumen pseudo-components in the lightest end of the normal boiling point curve should be between the critical compressibility of the pair (around 0.27) and zero.

It was also shown that the equation of state model should account for both vapour pressure and liquid heat capacity in order to be robust and comprehensive. In this chapter, the focus was on low to moderate temperatures at which low vapour pressure is expected. The simultaneous prediction of vapour pressure and heat capacity at high temperatures (below the cracking point) is recommended for a better extrapolation of vapour pressures towards the normal boiling point of the bitumen or fractions.

Although it was proved that the characterization methodology introduced in this chapter predicts bitumen vapour pressure and heat capacity within 12%, the experimental and modelling results are partially biased towards the lightest components in the normal boiling point in two ways: first, the vapour pressure data are dominated by this light fraction and second, the model is based on distillation experimental data that include only this light fraction. The modelling technique developed in this chapter will be applied in Chapter 8 to develop experimental means to extrapolate the normal boiling point of bitumens; therefore, accounting for the characterization of the mid boiling range of the bitumen.

## CHAPTER EIGHT: HEAVY OIL DEEP VACUUM RACTIONATION

As discussed in Chapter 2, distillation is a common method to provide data for crude oil characterization. In the case of conventional crude oils, up to 90-95 wt% of the oil is distillable and sufficient data and property correlations are available to provide a comprehensive characterization. However, in the case of heavy oils and bitumens, only about 20 to 30 wt% can be distilled through commercial vacuum distillation assays [Castellanos-Diaz et al., 2011].

To extend the range of the fractionation, high vacuum conditions are necessary. Figure 8.1 shows hypothetical distillation curves (boiling point curves) of heavy oil at three different pressure conditions: atmospheric, vacuum, and high vacuum. All of the distillation curves stop at the cracking temperature (approximately 300 °C) since beyond this point the substance is chemically transformed and the distillation data no longer relate to the original fluid composition. With this limitation, atmospheric distillation methods, such as ASTM D86, TBP, and ASTM D2887 [Riazi, 2005], can fractionate approximately 9-10% of a heavy oil or bitumen. If the pressure of the system is reduced, the boiling points of the oil constituents are reduced as well and a greater amount of sample can be fractionated before it reaches the cracking temperature. For example, commercial vacuum distillation assays such as ASTM D1160 and the Spinning Band Distillation technique (SBD), which operate at pressures close to 0.13 kPa (1 mmHg) [Riazi, 2005], can fractionate 20 to 30 % in mass of a heavy oil or bitumen. Following the

same logic, a greater amount of heavy oil or bitumen can be fractionated at an even deeper vacuum, Figure 8.1.

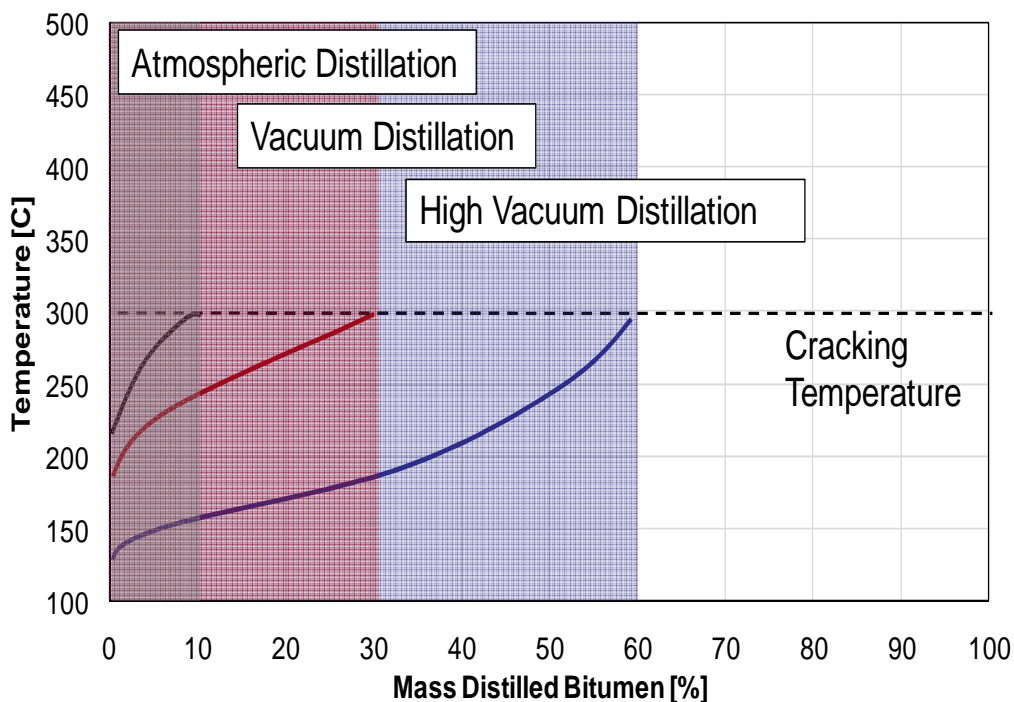


**Figure 8.1** Schematics of distillation performance on a heavy oil or bitumen at different operating pressures.

This chapter introduces a methodology to generate cuts of heavy oil and bitumen samples using deep vacuum fractionation at temperatures ranging from 100 to 300 °C and pressures below  $10^{-2}$  kPa. The high vacuum vapour pressure measurement system (HV-VPMS) presented Chapter 3 is used to perform the fractionation. A Western Canadian bitumen sample (WC\_B1) was fractionated to prove the concept and to develop a preliminary fractionation procedure. An inter-conversion method to obtain atmospheric equivalent boiling points from the data is also introduced. Preliminary property

measurements of the bitumen fractions are presented and briefly discussed. The objective is to prove the concept and establish preliminary procedures. Standardization and detailed characterization are beyond the scope of this thesis.

### **8.1 Preliminary Fractionation Test**

Figure 8.2 shows a simplified schematic of the vapour pressure apparatus (VPMA) that is used for the fractionation process; the degassing apparatus (DA), also part of the HV-VPMS, is used to clean and prepare the sample before fractionation, and is not shown in this chapter (see Chapter 3). To fractionate a sample using the VPMA, the sample temperature is raised to the initial condition at  $T_1$ . From this point, the sample is left open to pump suction by leaving all the connecting valves open. The upper VPMA section is left at a temperature 20 to 30 °C higher than  $T_1$  to facilitate vapour transportation and avoid condensation in the inner pipe. The fraction is collected by condensation in the cold finger which would be replaced when the fractionation at  $T_1$  stops. A more detailed description of the fractionation process is introduced in later in this chapter.

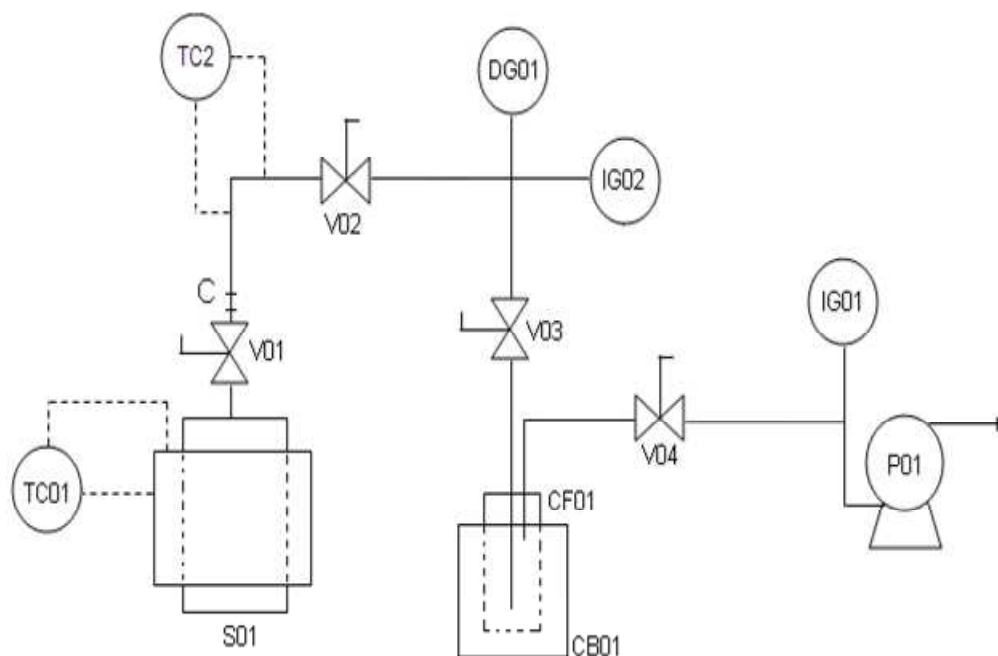


**Figure 8.2** Simplified schematics of the vapour pressure measurement apparatus (VPMA).

Note that the proposed fractionation methodology is analogous to a batch distillation at high vacuum conditions with no reflux and one theoretical stage. Commercial distillation techniques differ in the fact that they are run at higher pressures, they may have partial or total reflux and they may contain more than one theoretical stage [Riazi, 2005].

As a preliminary test, a maltene sample from the WC\_B1 bitumen was fractionated using the HV-VPMS apparatus. In separate experiments, two maltene samples were left open to pump suction at temperatures of 150 and 180 °C, respectively. A 12 wt% fraction and a 25 wt% fraction of the maltenes were obtained from the first and second experiment,

respectively. Note that some mass losses were measured equating to  $\pm 3\%$ , mainly due to vapour from the sample bypassing the cold finger as well as some condensation spots within the inner walls of the apparatus (particularly in the valves bellows). Figure 8.3 is a photograph of the obtained fractions and residue.

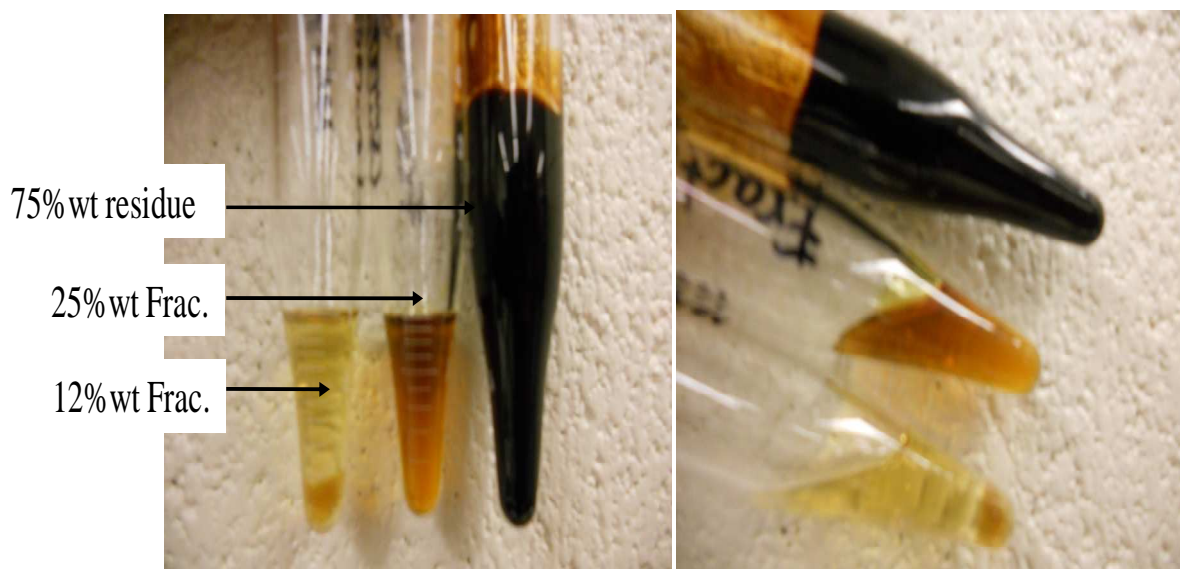


**Figure 8.3** WC\_B1 maltene fractions and residue obtained through deep vacuum fractionation.

The preliminary fractionation demonstrated that approximately 25 w% of the maltene sample was distillable at temperatures below 200°C. This performance matches what most commercial vacuum distillation techniques provide (approximately 25 – 35 wt% maltenes distillation). However, by increasing the temperature of the system from 200 to 300 °C, a deeper fractionation can be achieved.

## 8.2 High Vacuum Fractionation of Heavy Oil

After the preliminary fractionation test, a methodology was developed to systematically fractionate heavy oils at temperatures in the range of 20 to 300 °C using high vacuum conditions. The initial fractionation temperature (150°C) was determined. Then fractions were collected at five different temperatures between 150 and 290°C, Figure 8.4. Note that 68 wt% of the maltenes were fractionated equivalent to 56 wt% of the bitumen. Two key operational issues are the identification of the initial fractionation temperature and the collection of a complete cut at each temperature. They are discussed below.

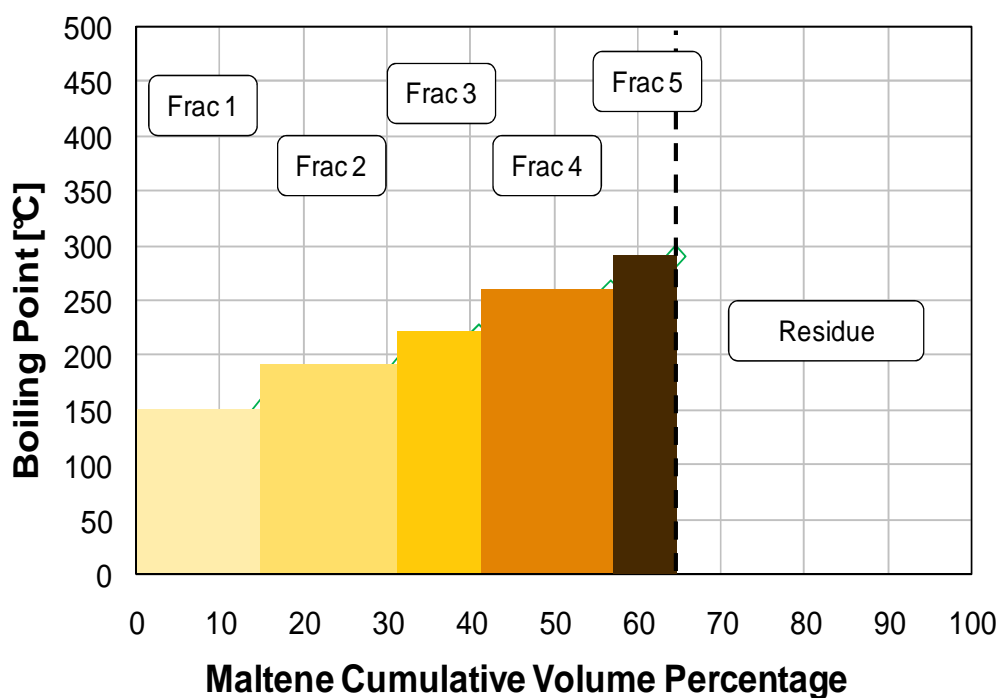


Figure 8.4 Boiling point cuts for WC\_B1 maltenes.

### ***8.2.1 Identifying Initial Temperature of Fractionation***

The initial temperature of fractionation is the temperature at which a detectable amount of condensate is observed in the cold finger. To determine this initial condition, the sample was heated gradually and the cold finger was observed; the pressure of the system was also recorded.

In this case, the maltene sample was heated from 60 to 115 °C through step changes of 15 °C every 10 minutes. During this period, no signs of condensation were observed in the cold finger. Figure 8.5 shows that each temperature step generates an increment in the pressure baseline (pseudo-steady state pressure) mainly due to the increment of the vapour pressure of the substance. Note that the pressure increments were also subject to some variations due to oscillations in the temperature control.

Since no signs of condensation were observed at temperatures between 60 and 115 °C, the heating process was continued with the same temperature step increments. The first sign of condensation was a pressure spike observed when a condensing droplet blocks the capillary tip, Figure 8.6. The pressure peak ends when the oil droplet breaks/detaches and the pressure returns to its pseudo-steady state value. The first pressure peak occurred at 130°C, Figure 8.7, but no measurable condensate was detected. Continuous condensation was not observed until 150°C and therefore the initial fractionation temperature was considered to be 150°C. Note that the initial fractionation temperature may change depending on the kind of heavy oil or bitumen assessed. Hence, a stepwise temperature

heating procedure from atmospheric temperature until condensation is observed is recommended.

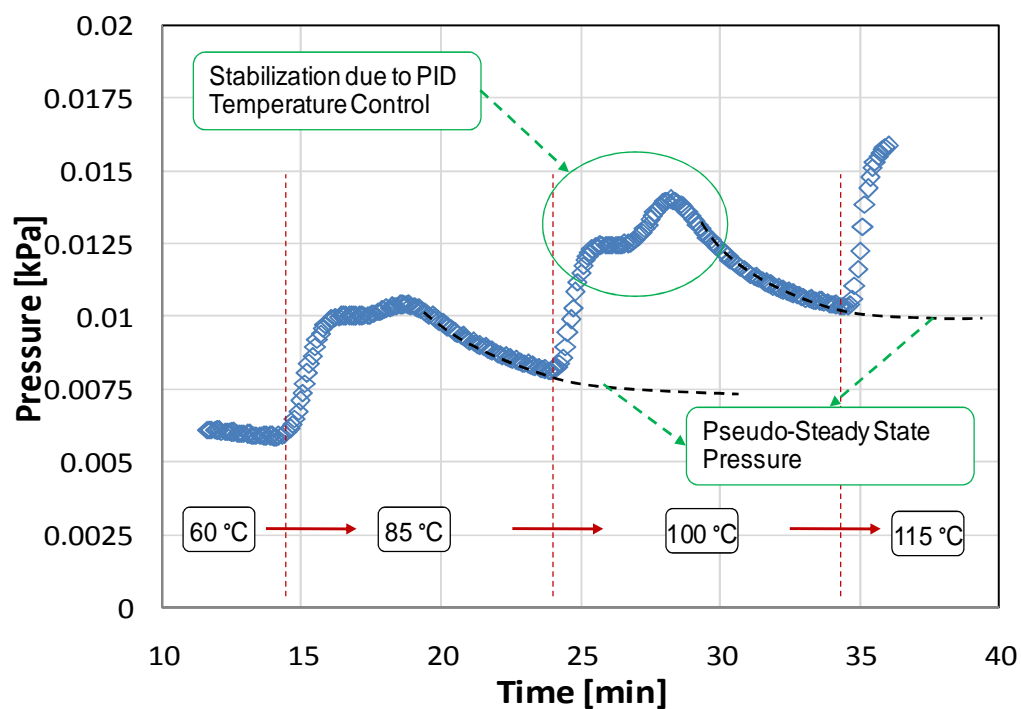


**Figure 8.5** Pressure profile for the fractionation of WC\_B1 maltenes at temperatures from 60 °C to 115°C.

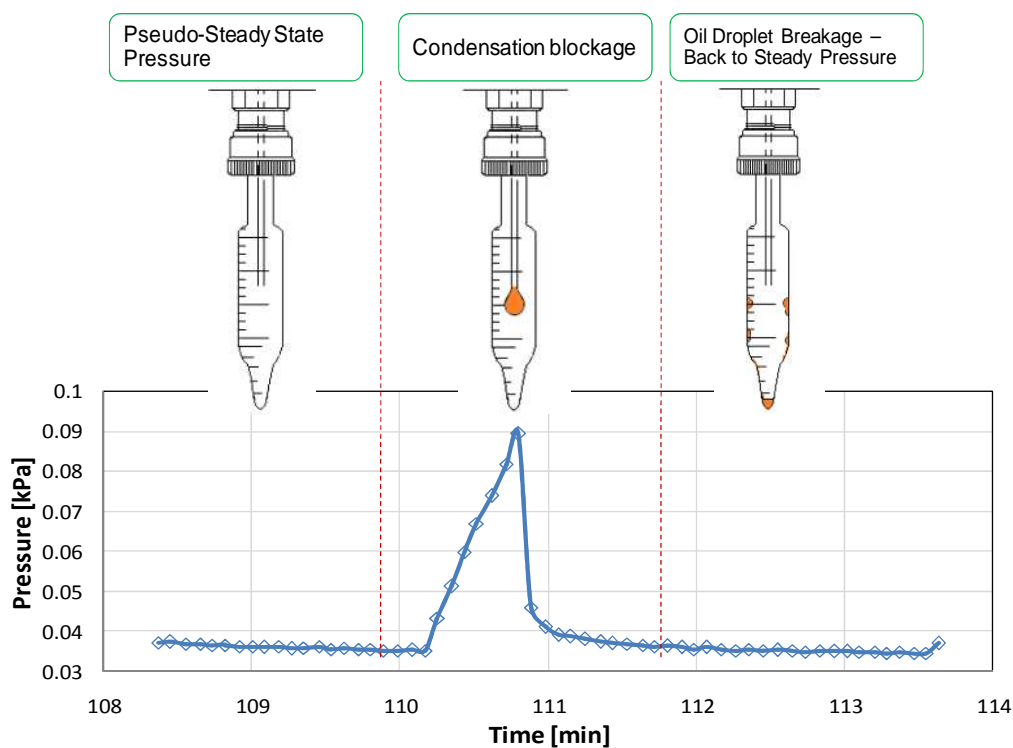


**Figure 8.6** Condensation blockage in the form of oil droplet formation and its pressure profile at 150 °C.

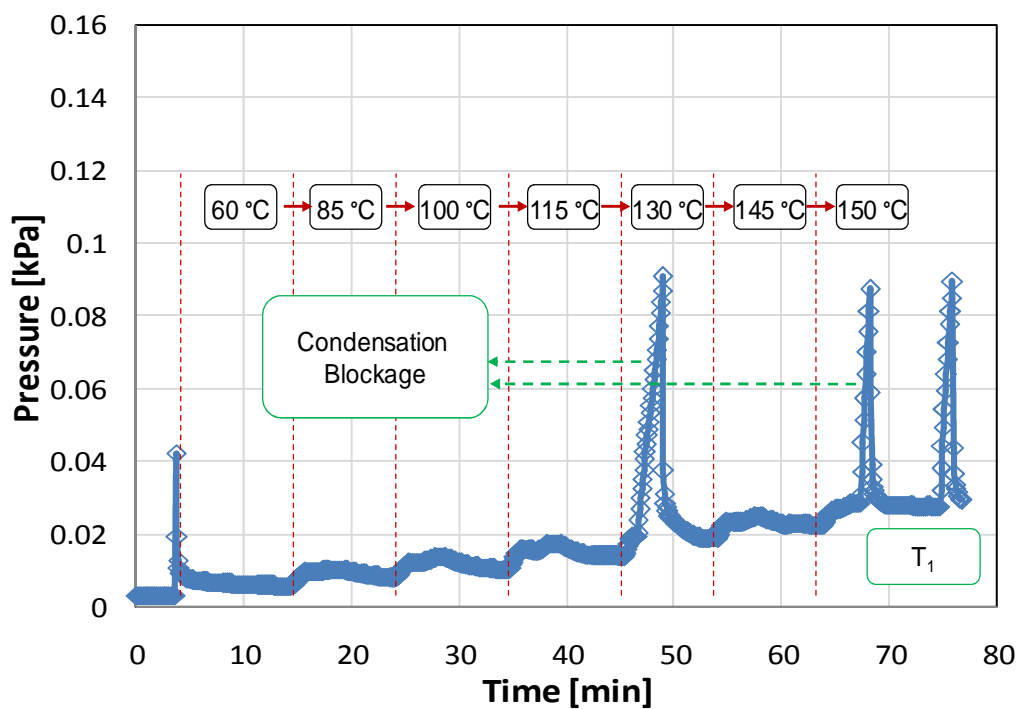


**Figure 8.7** Pressure profile for the fractionation procedure on WC\_B1 maltenes at a temperature range of 60°C to 150 °C.

### ***8.2.2 Collection of Heavy Oil and Bitumen Fractions***

In collecting the first cut at the initial fractionation temperature (150°C in this case), oil droplets formed and detached systematically. Figure 8.8 shows a pressure profile of the fractionation process at 150 °C. Note that the peak height for almost all of the peaks is the same, close to 0.09 kPa. This recurrence is expected since the forces acting on the drop formation, such as vapour pressure, surface tension, and pump suction, remained almost constant through the fractionation. Some differences in the forces acting on the droplet formation do occur and may lead to different (irregular) peak heights. Note that the condensation blockage may delay the collection of sample and, hence, the fractionation process, since it takes time to form the oil droplet. This process is magnified with denser cuts due to an increment in the oil viscosity. It may be possible to mitigate the droplet formation and avoid the pressure spikes by using a slanted capillary tip.

The disappearance of the pressure spikes may be an indicator that a given cut has been completely collected. However, in general, the pressure profile is not useful for determining or predicting when a cut will be completely collected. A better indicator is the volume of the cut collected as a function of time. Figure 8.9 shows the volume profiles of five maltene cuts. The volume profiles approach an asymptote towards the depletion point of the fraction,  $V_F$ .

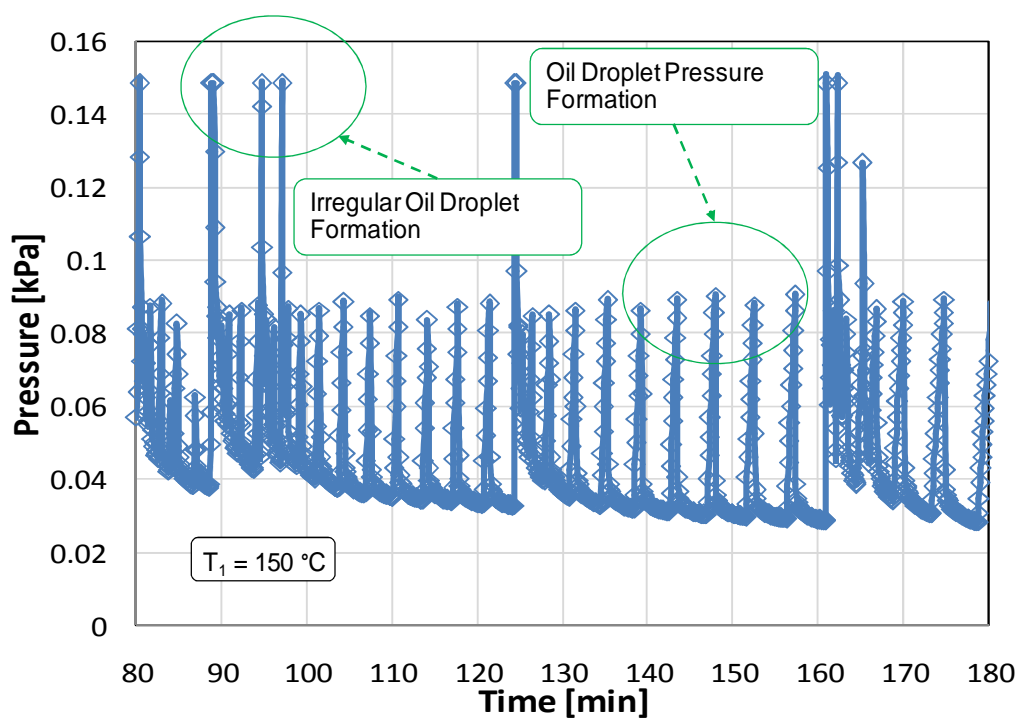


**Figure 8.8** Pressure profile for the fractionation of WC\_B1 maltenes at 150 °C.

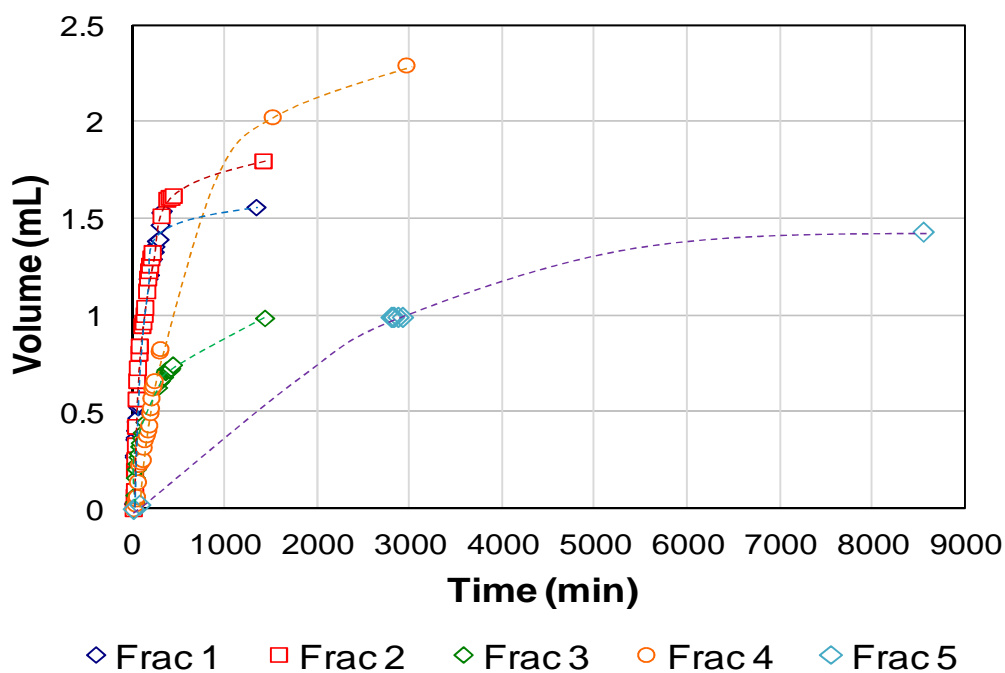


**Figure 8.9** Volume profiles for five WC\_B1 maltene cuts – lines are drawn to show the tendency and do not represent any particular model.

Since the final volumes of each fraction are different, it is convenient to use relative volumes, Equation 8.1

$$V_{Rel} = \frac{V(t)}{V_F}, \quad [8.1]$$

where  $V_{Rel}$  is the relative cumulative volume,  $V(t)$  is the cumulative volume as a function of time, and  $V_F$  is the total volume of the fraction. The relative volume profiles were modeled using two approaches given in Equations 8.2 and 8.3, respectively:

$$V_{Rel} = 1 - \exp[-at], \quad [8.2]$$

$$V_{Rel} = \exp\left[\frac{1}{bt+c}\right], \quad [8.3]$$

In addition to the fitting parameters  $a$ ,  $b$ , and  $c$ , the final volume of each fraction is unknown and becomes a second (or third) fitting parameter. Figures 8.10 and 8.11 show the experimental and fitted relative volume profiles as described by Equations 8.2 and 8.3, respectively. Table 8.1 provides the fitted parameters and deviation values for each approach. Figures 8.10 and 8.11 show that, although, in average, the deviation of the model from the data is lower with Equation 8.2 (total AARD of 10% versus 14%), the shape of the volume profiles is better described by Equation 8.3.

Parameters  $a$ ,  $b$ , and  $c$  can be regressed as a function of the distilled temperature, as follows.

$$a = -2.79x10^{-2} + 1.53x10^{-4}T - 2.02x10^{-7}T^2, \quad [8.4]$$

$$b = -7.97x10^{-2} + 4.60x10^{-4}T - 6.40x10^{-7}T^2, \quad [8.5]$$

$$c = -1.77x10^{-1} + 2.14x10^{-3}T - 8.18x10^{-6}T^2, \quad [8.6]$$

Note that the AARD is slightly increased for the model described by Equation 8.3, from 14 to 17%.

**Table 8.5** Parameter values and absolute and relative deviation values (AAD and AARD) of Equation 8.2 and 8.3 describing the volume profiles of different WC\_B1 maltene fractions.

	Equation 8.2				Equation 8.3				
	a	V <sub>F</sub> [mL]	AARD	AAD [mL]	a	b	V <sub>F</sub> [mL]	AARD	AAD [mL]
Frac 1	-0.0094	1.54	9%	0.04	-0.025	-0.040	1.62	18%	0.08
Frac 2	-0.0060	1.80	18%	0.13	-0.0155	-0.066	1.88	17%	0.13
Frac 3	-0.0039	0.99	16%	0.05	-0.0100	-0.100	1.06	17%	0.06
Frac 4	-0.0016	2.30	6%	0.03	-0.0026	-0.175	2.61	9%	0.05
Frac 5	-0.0004	1.43	2%	0.01	-0.0005	-0.243	1.78	8%	0.01

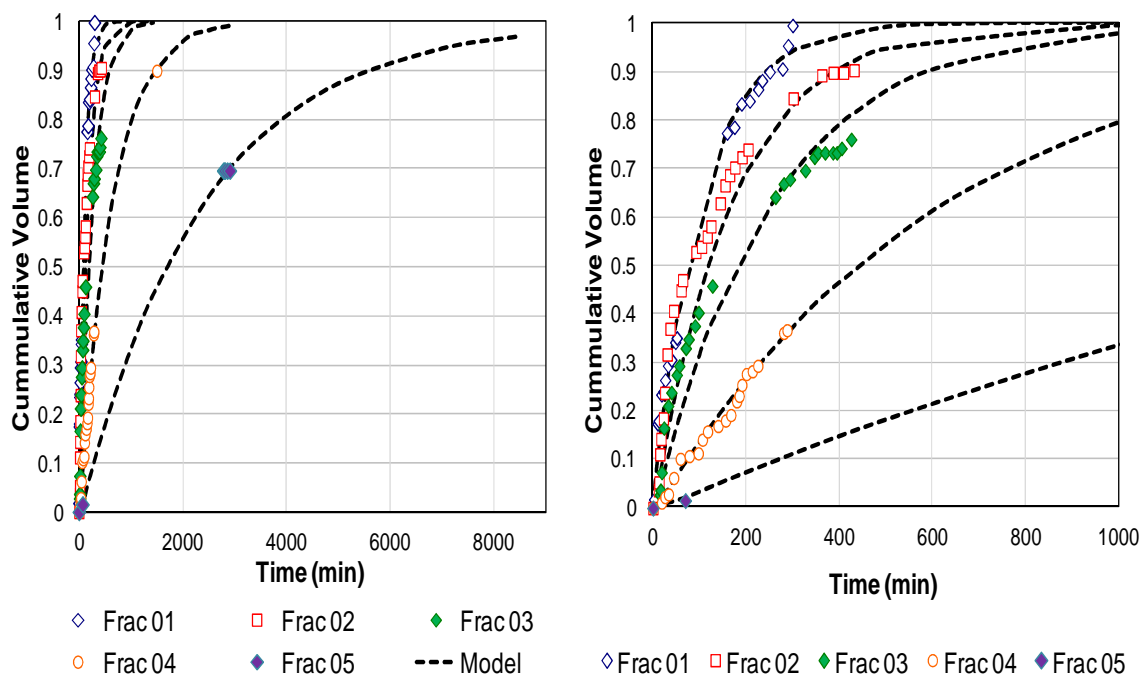


**Figure 8.10** Cumulative volume profiles for five WC\_B1 maltene cuts – Experimental data and fitted model using Equation 8.2.

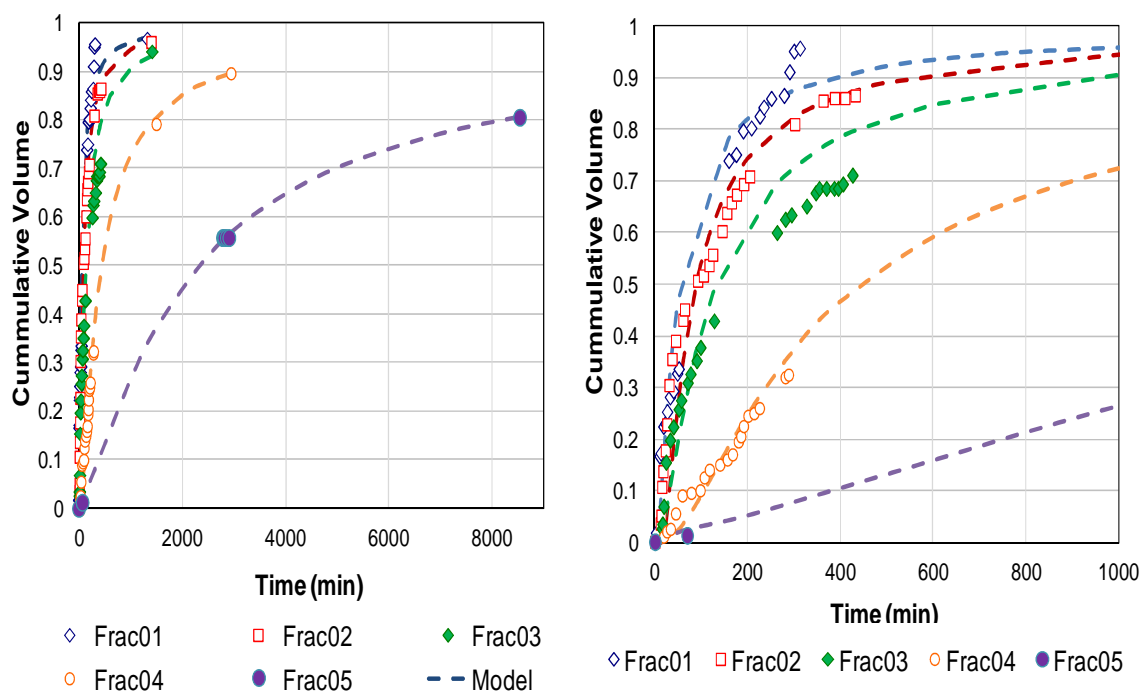


**Figure 8.11** Cumulative volume profiles for five WC\_B1 maltene cuts – Experimental data and fitted model using Equation 8.3.

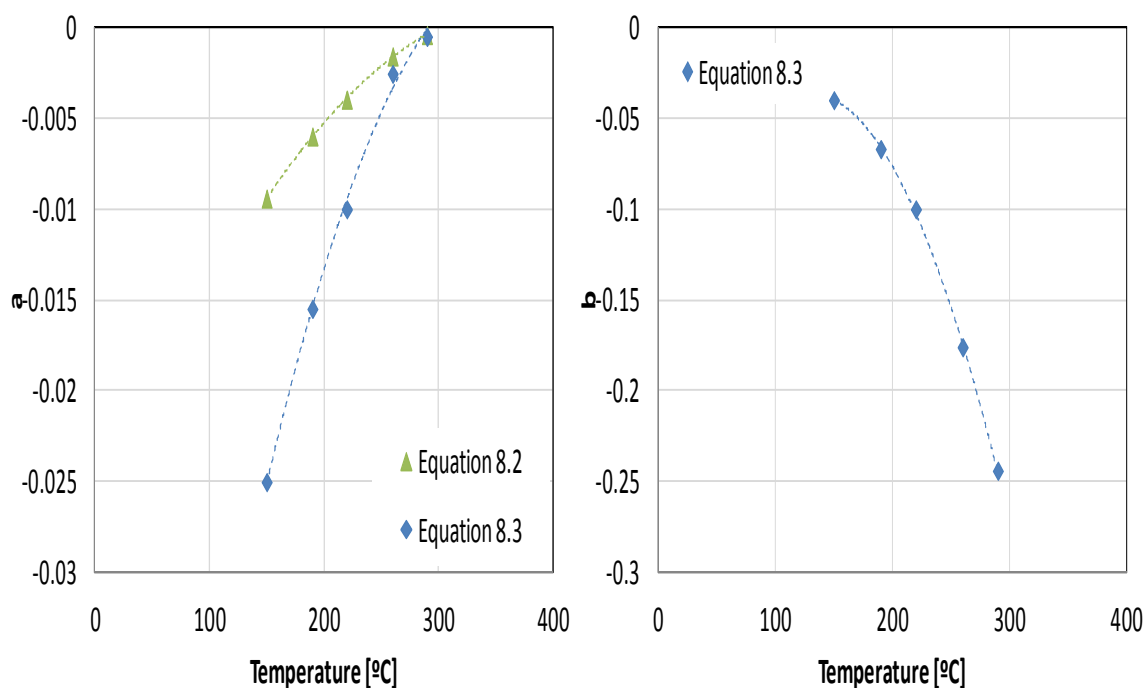


**Figure 8.12** Values of  $t_{95}$  for five fractions from WC\_B1 maltenes – predictions using Equation 8.2 and 8.3.

Note that as the fractions become denser the condensation process becomes significantly slower. Both Equation 8.2 and 8.3 predict that the time at which 95% of the fraction has been collected ( $t_{95}$ ) increases as a double exponential function of temperature, Figure 8.13. However, there is a factor of approximately five between the  $t_{95}$  predicted by Equations 8.2 and 8.3 at any given temperature. In order to determine which scenario better describes the fraction collection dynamics, it is recommended to perform experiments in which the volume profile of each fraction is measured at times longer than 4 to 5 days. Then, the appropriate equation can be used to estimate the required fractionation time at any temperature for similar samples.

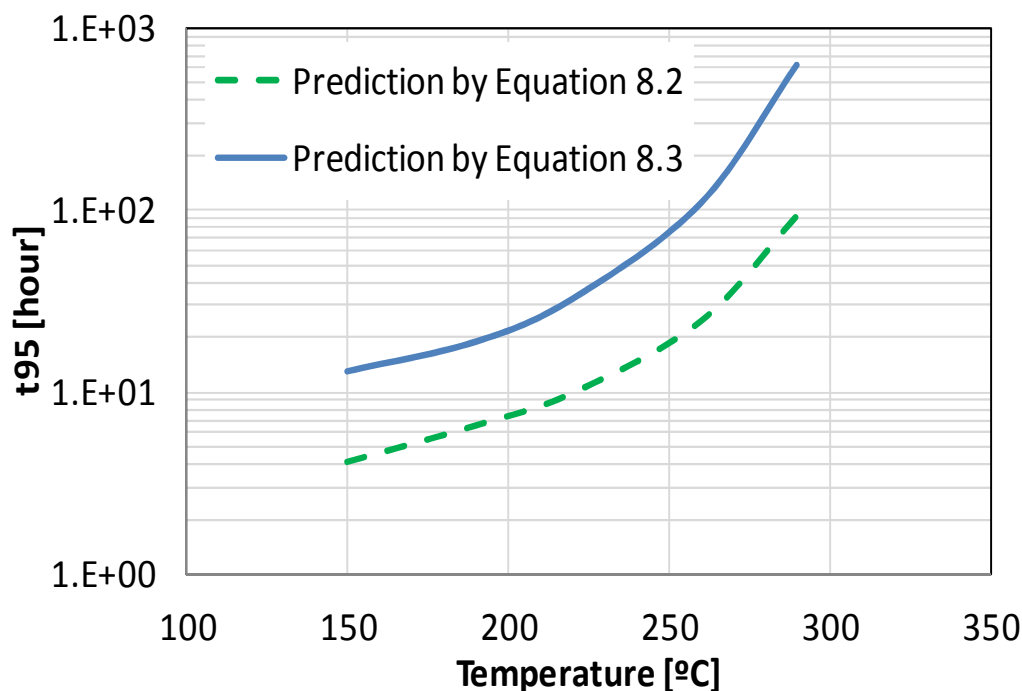


**Figure 8.13** Predicted values of  $t_{95}$  for five fractions from WC\_B1 maltenes – predictions using Equation 8.2 and 8.3.

### 8.3 Inter-conversion of Reduced-Pressure Boiling Point Curves

The characterization of crude oils based on distillation assays requires the boiling points of fractions at atmospheric pressure (normal boiling points). When a distillation assay is run at sub-atmospheric conditions, it is necessary to transform/inter-convert the data into normal boiling points. Several different techniques have been developed for inter-conversion of vacuum distillation assays, most of them based on a particular vapour pressure equation. An equation of state model can also be used for the inter-conversion. However, the most direct way to transform reduced-pressure distillation curves is to measure the vapour pressure of each boiling fraction, correlate the vapour pressure and extrapolate it towards atmospheric pressure. All three approaches are discussed below.

### 8.3.1 Maxwell-Bonnell Inter Conversion Method

When vapour pressure data for each fraction are not available, common inter-conversion methods may be applied to the deep vacuum fractions. One of the most common methods is shown by Riazi [2005] and is based in the Maxwell-Bonnell pressure curves [Maxwell and Bonnell, 1957]. This method is described by Equations 8.7 to 8.11:

$$T_b = T'_b + 1.3889F(K_W - 12) \log_{10} \frac{P_m}{760}, \quad [8.7]$$

$$T'_b = \frac{748.1QT_m}{1+T(0.3861Q-0.00051606)}, \quad [8.8]$$

$$Q = \frac{6.761560-0.987672 \log_{10} P_m}{3000.538-43 \log_{10} P_m}, \quad [8.9]$$

$$F = -3.2985 + 0.009T_b, \quad [8.10]$$

$$K_W = \frac{(1.8T_b)^{1/3}}{SG}, \quad [8.11]$$

where  $T_b$  stands for the normal boiling point in K,  $T_m$  is the measured temperature in K,  $P_m$  is the measured pressure in mmHg, and  $K_W$  stands for the UOP Watson factor. The calculation of normal boiling point through the Maxwell-Bonnell methodology is iterative and depends on the fractionation temperature, the fraction specific gravity, and the pressure of the system.

For this work, the specific gravity and temperature are known whereas the operating pressure is unknown. To determine the operating pressure for this method, an iterative procedure was applied taking into account the first two high vacuum boiling points (HVBPs). Note that these two points should inter-convert to SBD experimental data,

Figure 8.14. Figure 8.15 shows inter-converted values for these first two points using the Maxwell-Bonnell (MB) equations and Figure 8.16 shows the correlated operating pressures as a function of mass distilled.

From this point on, there is no experimental data with which to verify the inter-conversion of the HVBPs. Hence, it is assumed that the pressure profile shown in Figure 8.15 follows a power law, described by Equation 8.12 and shown in Figure 8.16.

$$P_m = 16.567w_c^{-1.185}, \quad [8.12]$$

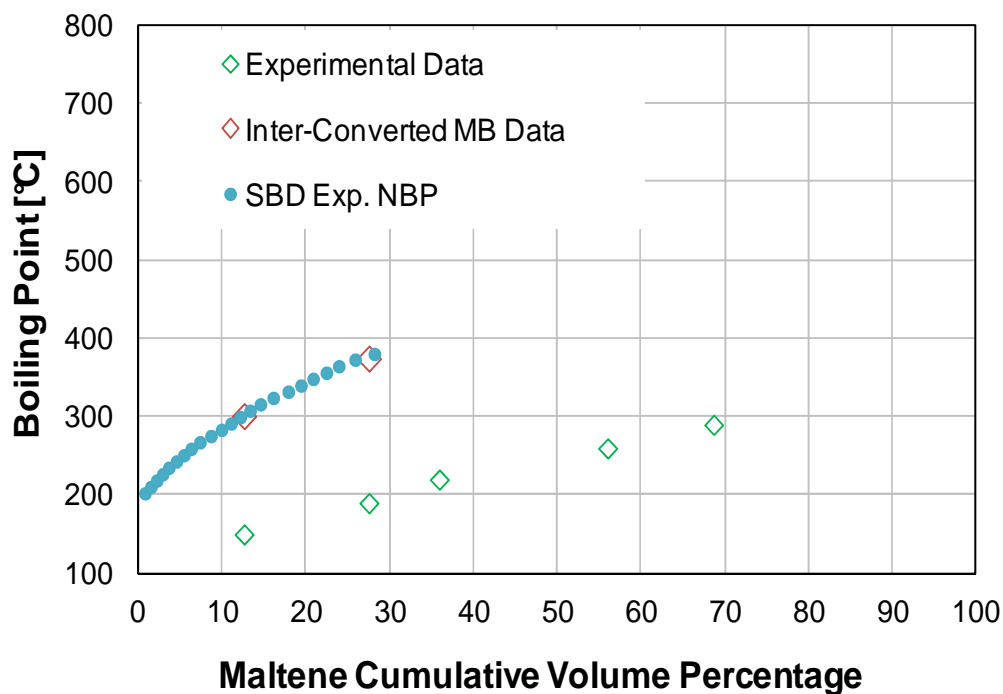


**Figure 8.14** Boiling point profiles for WC\_B1 maltenes \_ Inter-converted values of high vacuum boiling points in the SBD experimental data region.

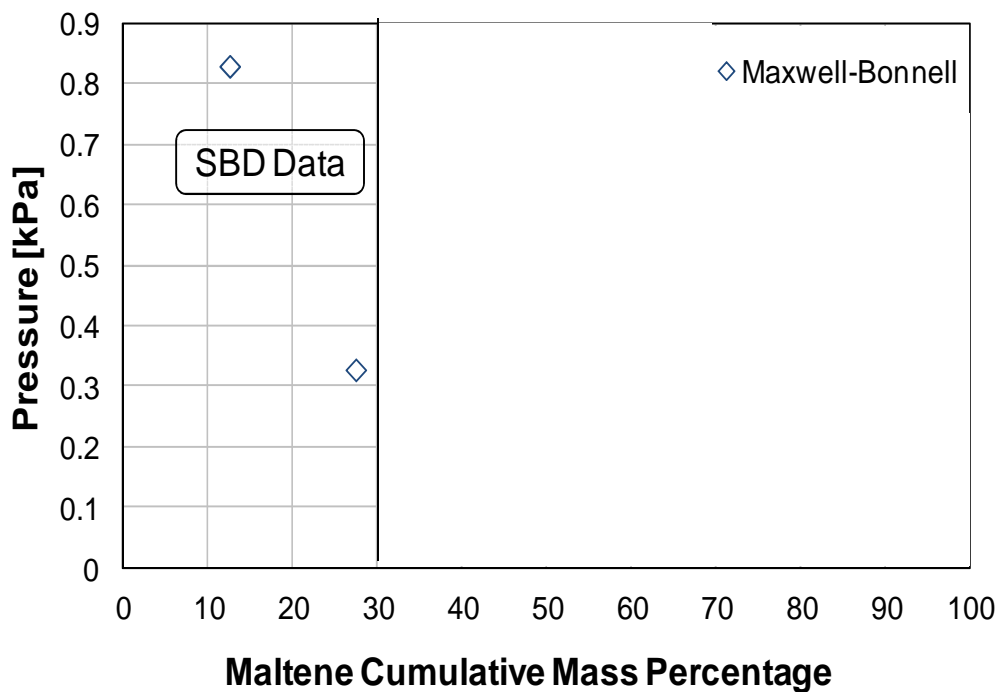


**Figure 8.15** Correlated operating pressures for the first two high vacuum boiling points using the Maxwell-Bonnell equations.

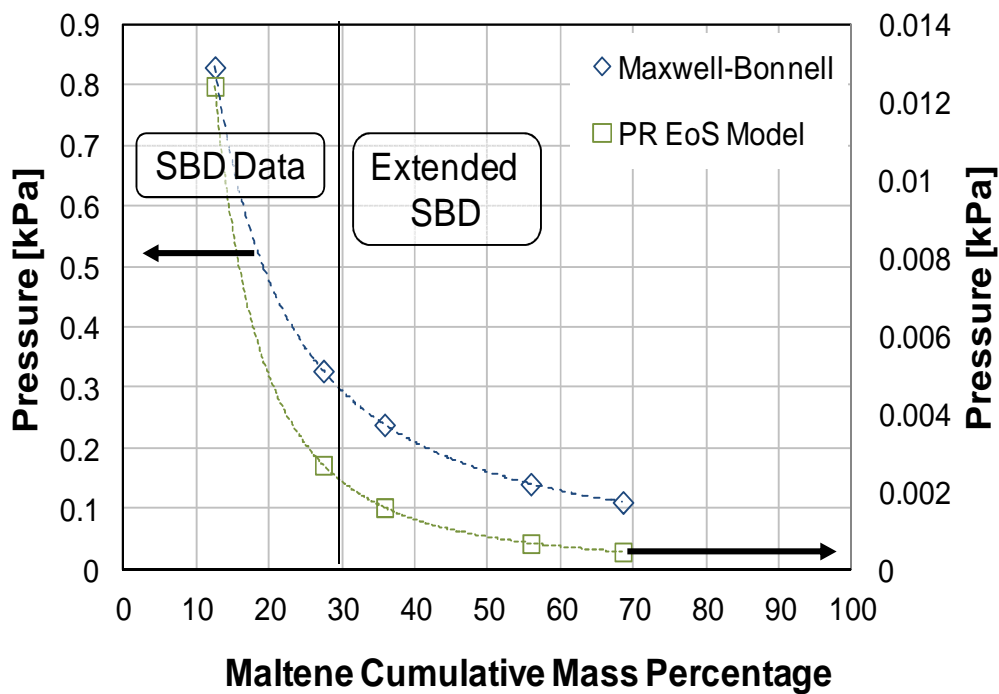


**Figure 8.16** Boiling point profiles for WC\_B1 maltenes – volume based.

Inter-converted HVBPs using the Maxwell-Bonnell method and the operating pressures given by Equation 8.12 are shown in Figure 8.17. The method provides normal boiling points that follow the Gaussian extrapolation of SBD experimental data. Note, however, that the operating pressures for this method range from 0.9 to 0.1 kPa which are extremely high in comparison to the observed HV-VPMS conditions (see Figure 8.6 and 8.7). Hence, while the method may correctly inter-convert the HVBPs, it does not correctly represent the physical conditions found in the apparatus.

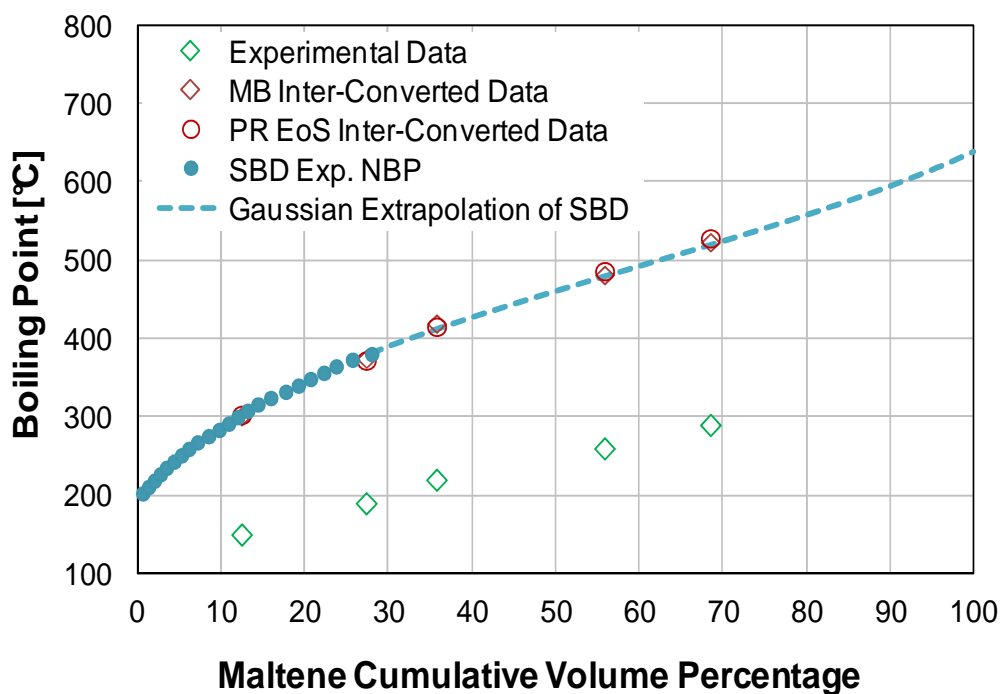


**Figure 8.17** Boiling point profiles for WC\_B1 maltenes – mass based.

### 8.3.2 Equation-of-State Based Inter Conversion Method

An alternative to inter-convert boiling point curves is to predict the vapour pressure of the fraction at atmospheric conditions using an equation of state. First, the heavy oil or bitumen was characterized with critical properties and acentric factors, as introduced in Chapter 7. Then, the deep vacuum fractionation cuts were determined through a flash calculation, as shown in Figure 8.18. Specifications of the flash drum temperature and pressure are required. These properties determine the amount of vacuum cut obtained. Finally, the vapour pressure of the deep vacuum cut was calculated at atmospheric pressure.

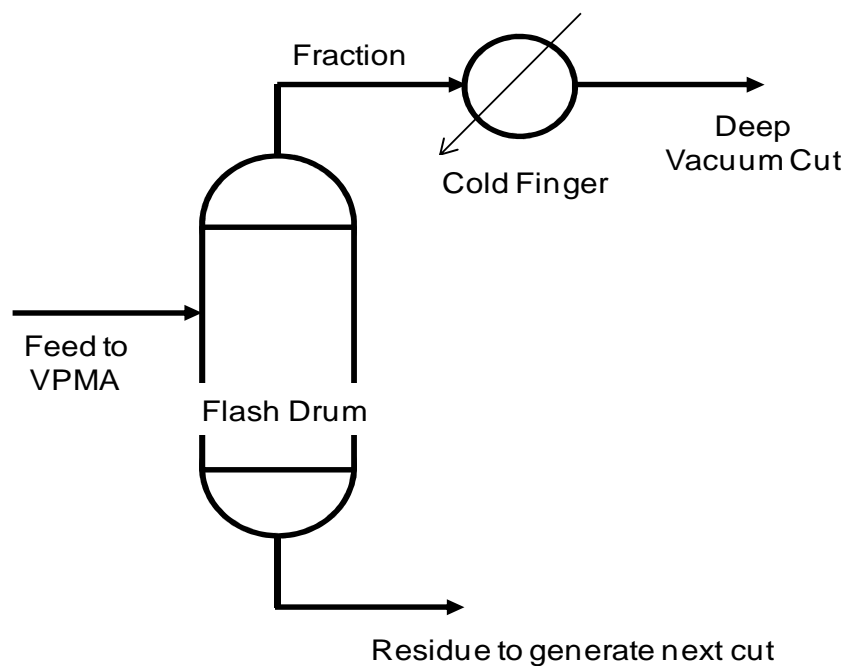


**Figure 8.18** Flash schematics for simulated production of deep vacuum cuts.

Figure 8.30 shows regressed-operating pressures that inter-convert HVBPs into NBPs for the experimental and extrapolated regions of the SBD. The operating pressures were correlated as follows:

$$P_m = 1.745w_c^{-1.957}, \quad [8.13]$$

The performance of the APR-EoS method is equivalent to that of the Maxwell-Bonnel method (within 1%). However, the operating pressure values are much more consistent with observations in the HV-VPMS (in the range of  $10^{-2}$  to  $10^{-4}$  kPa). However, in order to corroborate operating pressure values for the APR-EoS method, the vapour pressure of the different fractions must be measured and extrapolated towards the normal boiling point. As described in Chapter 4, correlation of the vapour pressure constrained with heat capacity would provide a robust methodology of extrapolation.

### ***8.3.3 Inter-Conversion Based on Measured Vapour Pressures***

Since vapour pressures of the five fractions were not yet measured, the feasibility of this inter-conversion approach was tested on the maltene residue fractions obtained in the preliminary fractionation tests (Section 8.1). These residues correspond to the remaining 88% wt and 75% wt of the maltenes. The vapour pressure was measured using the HV-VPMS as described in Chapter 3 and Appendix B.

Figure 8.19 shows the vapour pressure of the residues in a temperature range of 25 to 180°C. The average absolute deviation for all vapour pressure measurements is 2.9%,

with an average repeatability of 6.4%. The vapour pressure data are tabulated in Appendix A. Figure 8.4 also shows the measured vapour pressure of the bitumen and the whole maltenes.

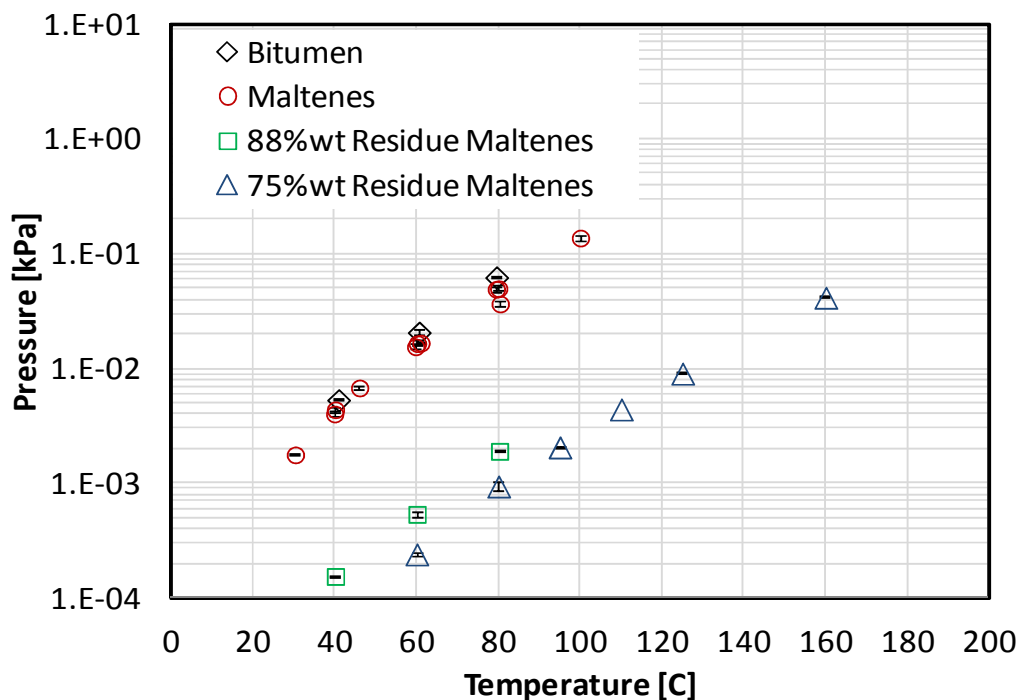


**Figure 8.19** Vapour pressure of WC\_B1 bitumen and fractions.

The vapour pressure data of the WC\_B1 bitumen fractions can be predicted using an equation-of-state model. The accuracy of the prediction made by the EoS model is an indication of the consistency of the characterization of the oil with independent experimental data. If sufficiently accurate, the model can be used to extrapolate the vapour pressure data to atmospheric conditions.

In this case, the composition of the WC\_B1 bitumen was determined from the extended normal boiling point curve in Chapter 7. However, the composition of the 88%wt and

75%wt maltene cuts remains unknown. To determine the compositions of the maltene cuts, a flash calculation was performed in VMGSim 6.0.38 [VMG, 2010]. In the flash calculation, a given flow of maltenes (i.e. F=1 kg/h in Figure 8.18) was fed into a separator at a temperature equal to the experimental fractionation temperature (150 °C and 180 °C for the 88%wt residue and 75%wt residues, respectively). The pressure inside the separator vessel was varied until the target amount of residue was obtained (i.e. L/F = 0.88 and 0.75 for the two residues, respectively). The calculated composition of the simulated residues and the WC\_B1 bitumen and maltenes is listed in Table 8.2:

**Table 8.6** Simulated composition of WC-B1 and fractions.

Pseudo	Mole Fraction			
	Heavy Oil	Maltenes	88%wt Malt.	75%wt Malt.
			Residue	Residue
Malt01	0.050	0.061	0.002	0.000
Malt02	0.044	0.054	0.005	0.000
Malt03	0.055	0.066	0.017	0.001
Malt04	0.048	0.058	0.035	0.004
Malt05	0.060	0.072	0.069	0.012
Malt06	0.056	0.067	0.079	0.029
Malt07	0.059	0.071	0.089	0.065
Malt08	0.197	0.237	0.302	0.373
Malt09	0.166	0.200	0.255	0.327
Malt10	0.095	0.115	0.147	0.188
Asph01	0.009	0.000	0.000	0.000
Asph02	0.035	0.000	0.000	0.000
Asph03	0.058	0.000	0.000	0.000
Asph04	0.050	0.000	0.000	0.000
Asph05	0.018	0.000	0.000	0.000

Once the composition of the WC\_B1 bitumen fractions was determined, the vapour pressure curve was calculated. Figure 8.20 shows the experimental and predicted data for the heavy oil and fractions. The model predicted the data for the maltenes accurately (AARD of 2.3%) but did not predict the residues data as accurately (AARD = 18%). One possible explanation for this miscalculation relates to the uncertainty of the amount of distillate/residue produced. The uncertainty of the fractionation amount is approximately 3%. If the residue amounts are modified from 88 and 75 wt% to 85 and 78 wt% (3.4 and 3.8% difference, respectively), the AARD in the predictions improved from 10% to 1.7%, Figure 8.21.

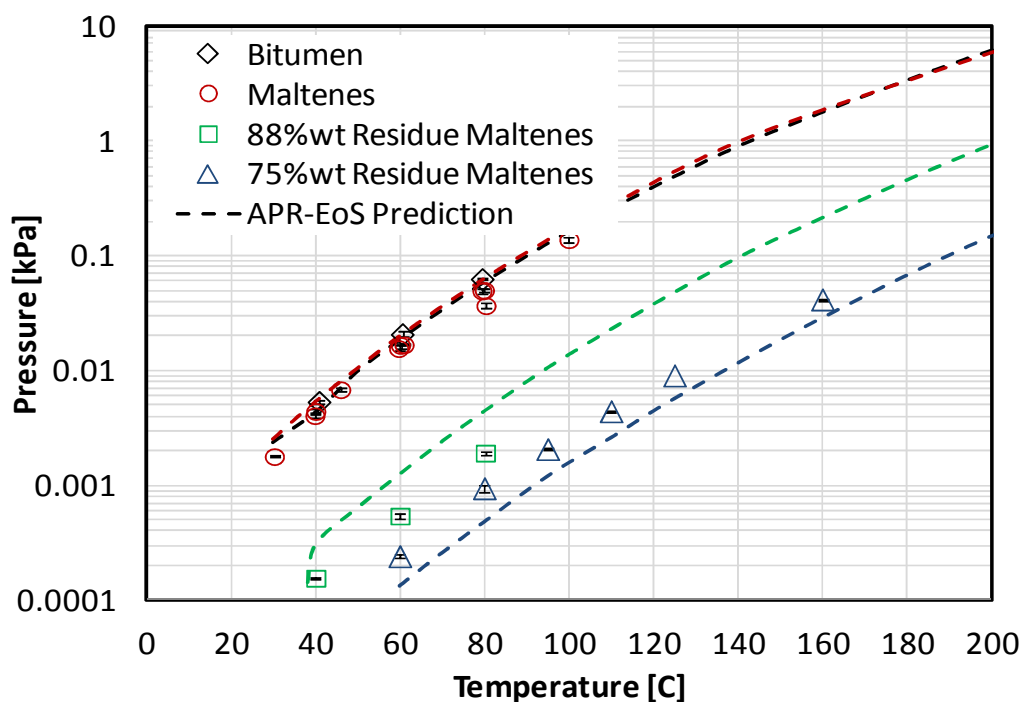


**Figure 8.20** Experimental and predicted vapour pressure of WC\_B1 bitumen and fractions using the APR-EoS – original compositions.

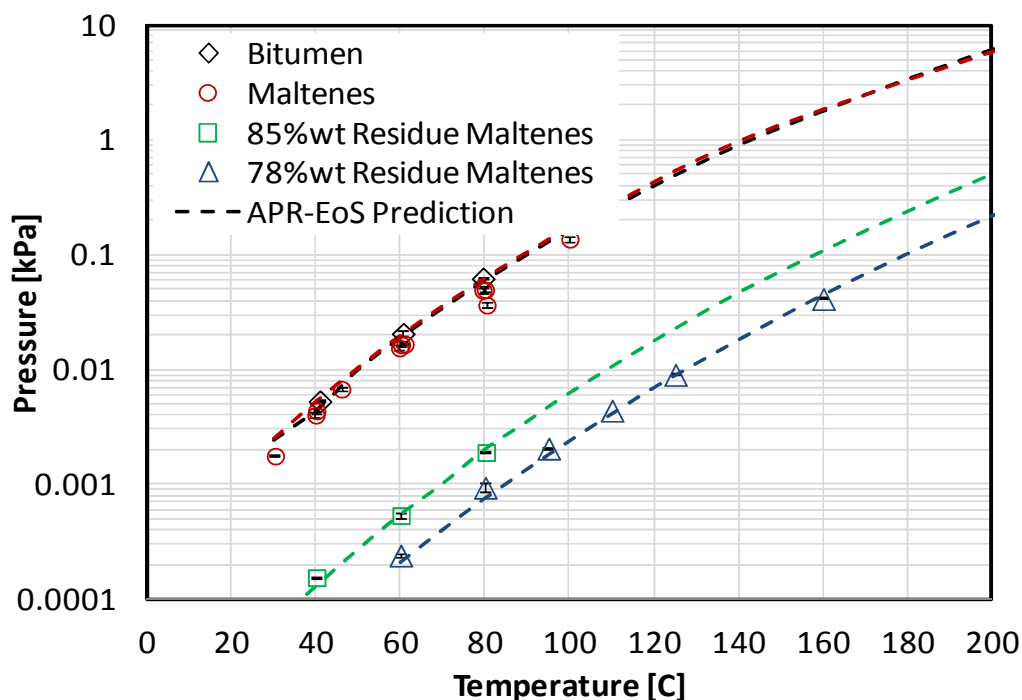


**Figure 8.21** Experimental and predicted vapour pressure of WC\_B1 bitumen and fractions using the APR-EoS – compositions have been relaxed to within experimental error.

These preliminary tests indicate that a tuned equation of state can be used to extrapolate the vapour pressure of the cuts to estimate the atmospheric boiling points. For example, Figure 8.22 shows the extrapolated average boiling point for the maltenes and the two fractions studied (330.2, 427.6, and 454.4 °C, respectively) as shaded regions. The extrapolated boiling points of the cuts are in qualitative agreement with the trend of the spinning band distillation data. However, the cuts are too broad to make a definite, quantitative conclusion. Future work will focus on collecting more cuts and vapour pressures to reduce the uncertainty in the cut volumes and confirm or adjust the equation-of-state tuning.

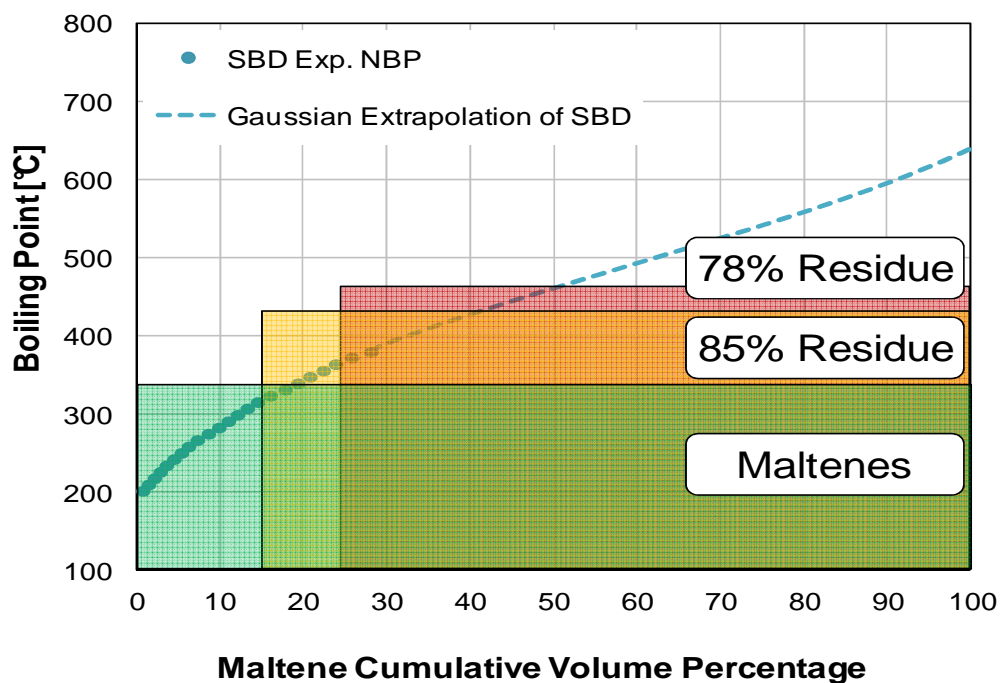


**Figure 8.22** Experimental and extrapolated normal boiling point of WC\_B1 maltenes – a representation of the extrapolated NBP of three cuts is also shown.

### 8.3.4 Comparison to Other Distillation Techniques

Figure 8.23 compares the deep vacuum boiling point curve obtained in this work with normal boiling point experimental data of the WC\_B1 maltenes determined by spinning band distillation (SBD) technique and extrapolated using Gaussian distribution as introduced in Chapter 7. In addition, Simulated Distillation experimental data of the heavy oil is shown [Sanchez, 2011].

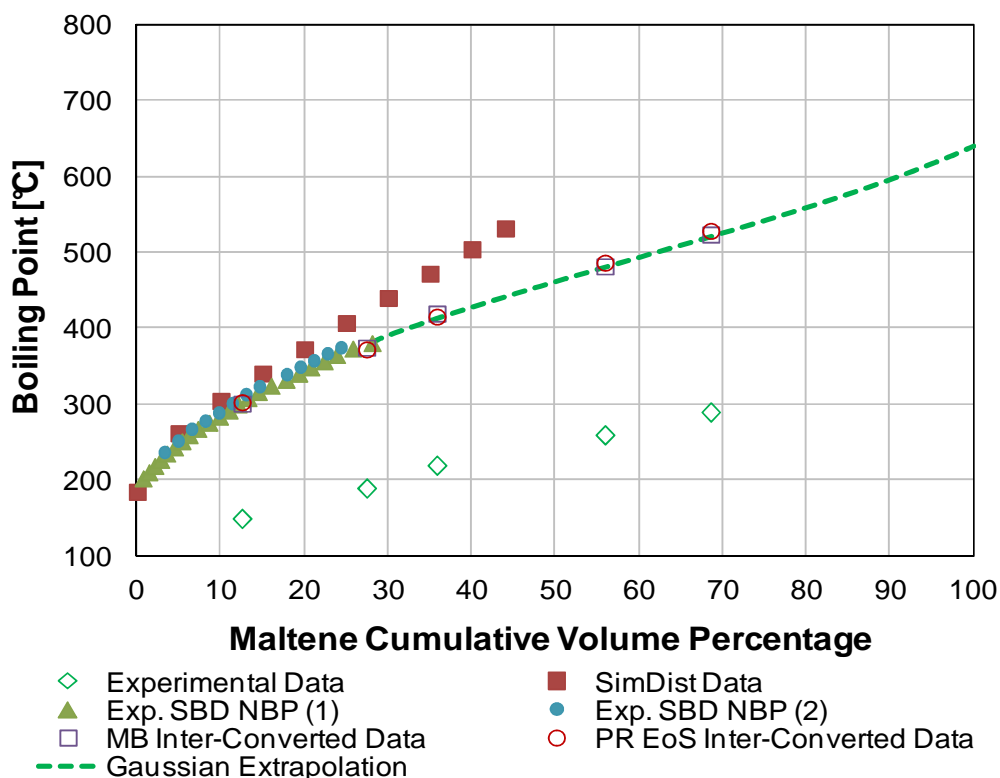


**Figure 8.23** Boiling point profiles for WC\_B1 maltenes – mass based – Experimental data was provided by Sanchez [2011].

The deep vacuum fractionation generated maltenes fractions up to approximately 70 wt% of the maltenes (60 wt% of the bitumen). The mass distilled surpasses the spinning band distillation (29 wt% of the maltenes) and the Extended SimDist (45 wt% of the maltenes). Figure 8.23 shows that the Extended SimDist data deviates from experimental NBP data at above 25% mass distilled and may not be reliable. Recall that the Extended SimDist retention data are converted to boiling points using correlations that are themselves extrapolations. The data provided by the methodology developed in this chapter could be utilized to improve the SimDist calibration curves to up to 60 wt% distilled.

### 8.4 Fractionation Results

Figure 8.24 shows a photograph of the five fractions collected from the WC\_B1 maltenes in this work. Note that the colour of the fractions changes from light amber to dark greenish brown, ending in a pitch black for the residue as the fractions become denser. In addition, the viscosity of the fractions was observed to increase from the first to the last cut. These changes in physical properties are a confirmation of a meaningful fractionation. The volume, boiling range, and density of these fractions are listed in Table 8.3.



**Figure 8.24** Photograph of five the different fractions and residue of WC\_B1 maltenes deep vacuum fractionation.

**Table 8.7** WC\_B1 maltene fractions obtained using the HV-VPMS.

<b>Fraction</b>	<b>V<sub>Frac</sub> [mL]</b>	<b>V<sub>Frac</sub> [mL]*</b>	<b>Mass [g]</b>	<b>Top [°C]</b>	<b>ρ [g/mL]</b>	<b>Time Collected</b>
Frac 1	1.69	1.56	1.46	150	0.9357	22.11 h
Frac 2	1.90	1.80	1.72	190	0.9506	23.39 h
Frac 3	1.10	0.93	0.97	220	0.9707	23.67 h
Frac 4	1.80	2.34	2.32	260	0.9912	49.15 h
Frac 5	1.30	1.44	1.46	290	1.0164	48.52 h
Residue	-	-	3.62	>290	1.0401	-

\* V<sub>Frac</sub>\* stands for the volume of the fraction corrected from mass fraction and density

\*\* Density measured with an AntonPaar densitometer

#### **8.4.1 Reproducibility of Fractionation Data**

A similar procedure as described in this section was followed by Sanchez [2011] to fractionate the same maltenes with the HV-VPMS. Figure 8.25 compares the two data sets as well as the data for the preliminary fractionation procedure, Section 8.1. The reproducibility of the fractionation obtained at independent procedures is 4.8 wt% (16%). Although the two fractionation procedures were slightly different, the reproducibility of the methodology is promising. More experimental data obtained with a standard procedure is required to draw definite conclusions.

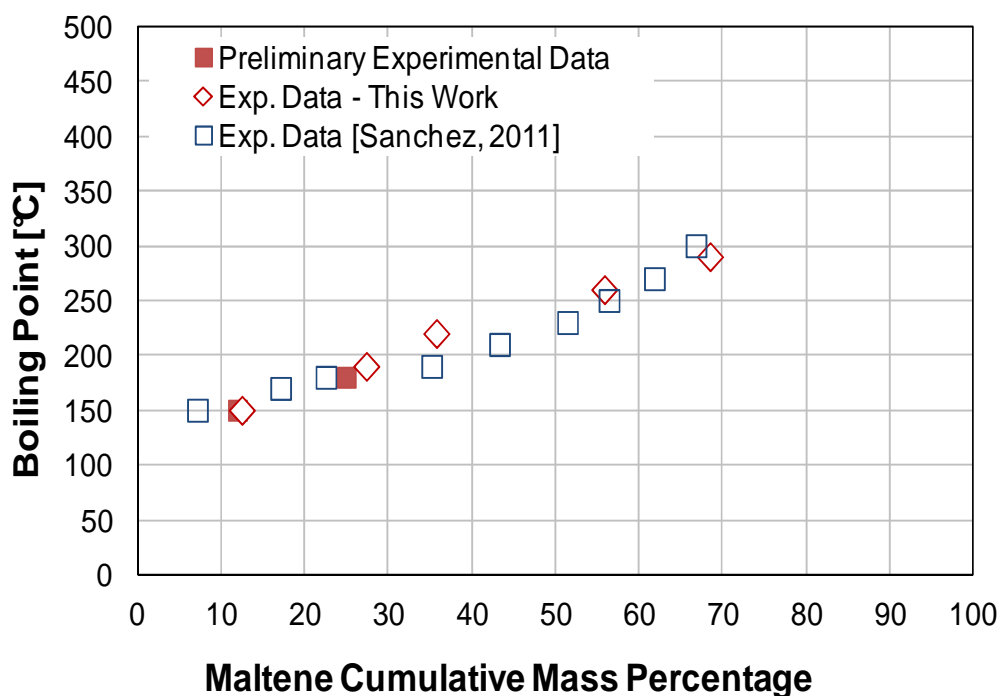


**Figure 8.25** Boiling point profiles for WC\_B1 maltenes – mass based; supplementary data provided by Sanchez [2011]

#### 8.4.2 Density Profiles

The density of the fractions was measured using an Anton Paar DMA4500 density meter. Since the amount of sample is limited and sometimes too viscous to inject into the density meter, the samples were diluted with toluene to a series of different concentrations. The density of the samples was calculated from the mixture densities assuming a density mixing rule. Two mixing rules were evaluated: 1) no excess volume of mixing,

$$\rho_{Mix} = \left[ \frac{w_F}{\rho_F} + \frac{w_T}{\rho_T} \right]^{-1}, \quad [8.14]$$

2) a non-zero excess volume of mixing,

$$\rho_{Mix} = \left[ \frac{w_F}{\rho_F} + \frac{w_T}{\rho_T} - w_F w_T \left( \frac{1}{\rho_F} + \frac{1}{\rho_T} \right) \beta_{12} \right]^{-1}, \quad [8.15]$$

where  $w_i$  is the mass fraction of the fraction ( $F$ ) or the solvent toluene ( $T$ ), and  $\beta_{12}$  is the fitted interaction parameter between the fraction and toluene.

Figure 8.26 shows the density profile of the maltene residue (after high vacuum distillation) at different toluene concentrations. Table 8.4 provides the calculated fraction density and the AARD for each mixing rule. The lightest fractions appear to form nearly ideal mixtures with toluene. However, the values of  $\beta_{12}$  become larger (more non-ideal) for the denser fractions. Note that data for Frac05 was only available at very low concentrations where the distinction between ideal and non-ideal behaviour was too small to detect. The value of  $\beta_{12}$  for Frac05 in Table 8.4 was interpolated. Finally, the average density of the heavy oil maltenes assuming an ideal mixture, as:

$$SG_{Avg} = \frac{1}{\sum \frac{w_i}{SG_i}}, \quad [8.16]$$

A value of 0.9933 g/mL was calculated, which is in reasonably good agreement with the measured value, 0.9871 g/mL (0.63% error), Table 8.4. Note that a non-ideal mixing rule would give a lower density in better agreement with the measured value.

**Table 8.8** Extrapolated values of density for the different WC\_B1 maltene fractions using ideal and non-ideal density models – data provided by Sanchez [2011].

Fraction	Cum. wt%	Ideal Model		Non-Ideal Model		
		SG	AARD	$\beta_{12}$	SG	AARD
Frac 1	6.26	0.9339	0.0013%	0.00013	0.9337	0.0015%
Frac 2	19.98	0.9520	0.0020%	0.00167	0.9506	0.0018%
Frac 3	31.61	0.9823	0.0003%	0.00500	0.9707	0.0016%
Frac 4	45.85	0.9986	0.0061%	0.00873	0.9912	0.0009%
Frac 5	62.22	1.0185	0.0007%	0.01005*	1.0164*	0.0162%*
Residue	84.27	1.0552	0.0127%	0.01071	1.0401	0.0046%
Maltenes	100	0.9871	0.0024%	-	0.9871	0.0024%

\* Interpolated

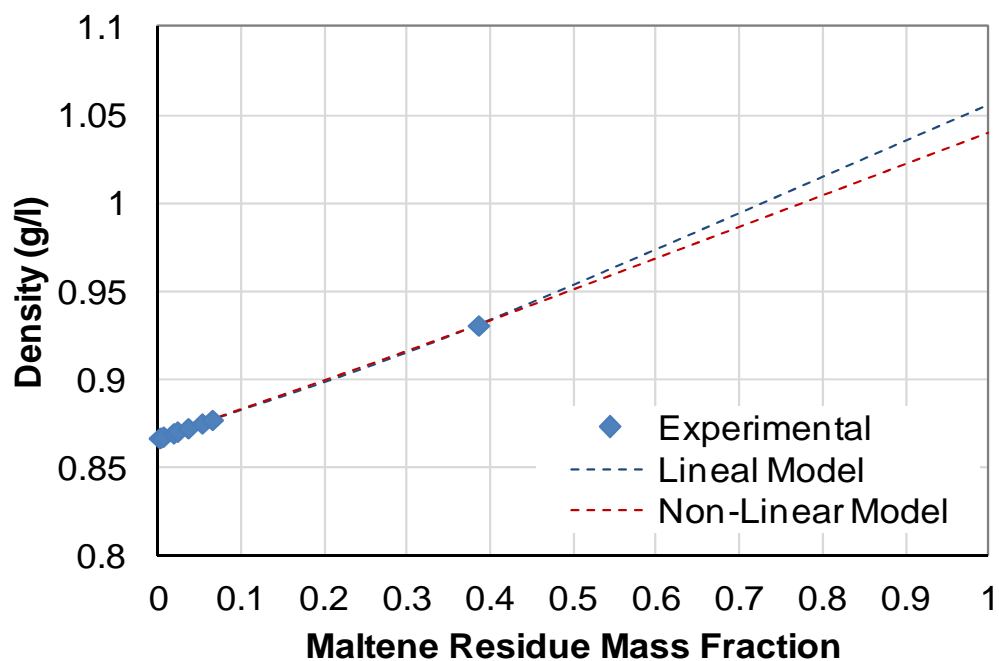


**Figure 8.26** Density profile of WC\_B1 maltene residue (after high vacuum distillation) at different concentrations with toluene – data provided by Sanchez [2011].

Figure 8.27 shows the extrapolated density values for the maltenes as a function of cumulative mass distilled. The cumulative density profile shown in Figure 8.27 was regressed as follows with an AARD of 0.2%:

$$SG_{Frac} = 0.919 + 0.143w_c^{0.880}, \quad [8.17]$$

where  $w_c$  stands for the cumulative mass distilled. The measured density data was also compared with predictions made with the Søreide equation [Søreide, 1989]:

$$SG_{Frac} = 0.2855C_S(MW_{Frac} - 66)^{0.13}, \quad [8.18]$$

where  $C_S$  is an adjustable parameter. Equation 8.18 was applied to the bitumen model described in Section 4.2.3 with an adjusted  $C_S$  parameter of 0.322 which is within the range of 0.3 to 0.4 recommended by Whitson and Brulé [2000]. Figure 8.27 shows that the Søreide equation fits the data accurately, with an AARD of 0.50%. The Søreide equation with the model developed in Chapter 7 provides an accurate representation of the density of the fractions.

Finally, a comparison between the density profiles measured in this work and that of the cuts obtained by Sanchez (Figure 8.25 [Sanchez, 2011]) was performed, Figure 8.27. The average relative difference between the two profiles is 1.0%. Although the procedure to obtain the cuts in this work and that of Sanchez differ slightly, the proximity of the

boiling point profile and the density profiles is an indication that the fractions collected by the HV-VPMS are repeatable.

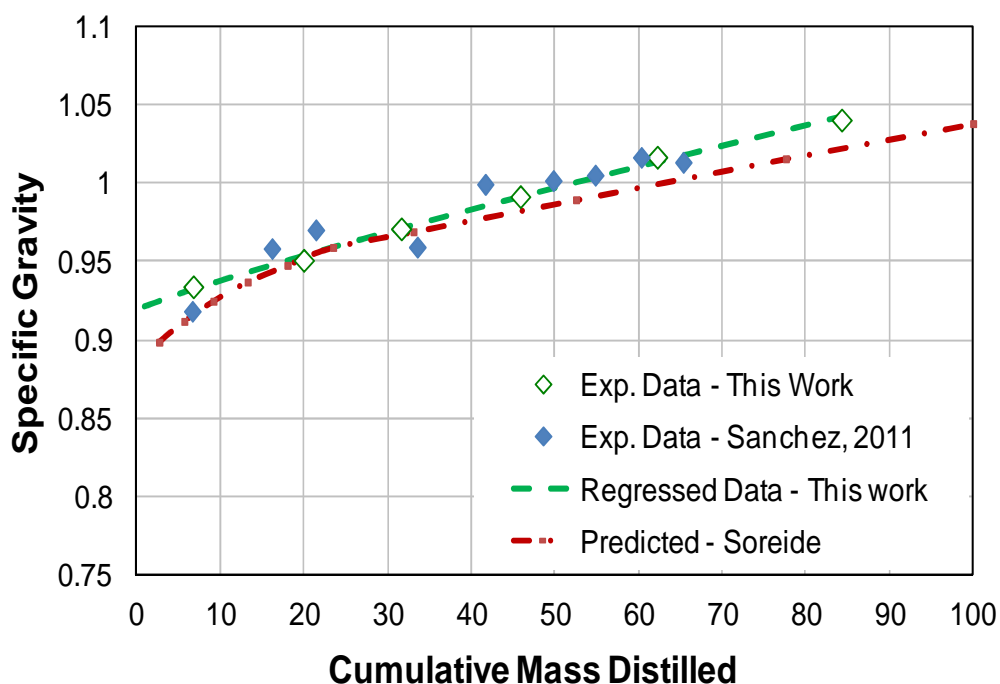


**Figure 8.27** Measured and predicted density of WC\_B1 maltenes fractions as a function of cumulative mass distilled.

### 8.5 Recommended Design Improvements

The preliminary testing identified some areas where the apparatus design could be improved. In particular, the current methodology is time consuming, mainly due to the high viscosity of the heavy oil residues. However, the assessment of mass transfer limitations within the apparatus may lead to shorter experimental times and an improvement in overall methodology. Some of the mass transfer limitations are illustrated in Figure 8.28 and are described below.

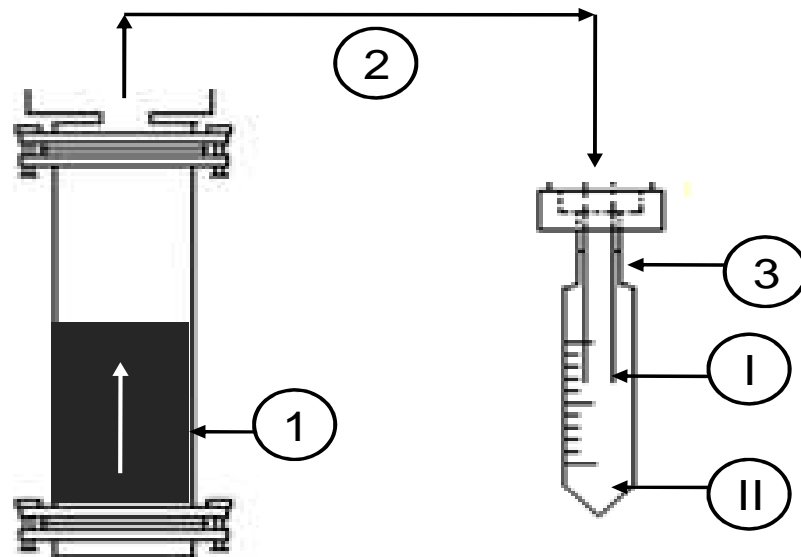


**Figure 8.28** Schematics of sample vessel and cold finger and possible mass transfer limitations involved in deep vacuum fractionation: 1) Liquid phase viscosity and diffusivity; 2) Gas phase mobility; 3) Cold finger condensed fraction mobility; I) Condensation point; II) Condensed fraction volume measurement.

#### Liquid Phase Viscosity and Diffusivity:

Two main processes occur in the liquid phase when a fraction is being depleted from the main sample: a) molecules must diffuse towards the liquid-vapour interface, and b) the molecules must evaporate from the interface. Diffusion of the fractions becomes more difficult and slower as the residue becomes more viscous when the lighter ends are removed. Hence, depletion times increase as the fractions become denser (from 14 hours for the first cut to about 3 days for the final cut).

This phenomenon is already partially mitigated in two ways: 1) the samples were de-asphalted before the experiments which reduced the viscosity of the sample, and 2) as the residue becomes heavier, the operational temperature is increased, therefore decreasing the viscosity of the sample. Recommended improvements are to provide more surface area for evaporation (wider sample vessels) and straighter paths from the evaporation surface to the cold finger to avoid condensation spots.

#### Gas Phase Mobility:

As the residue molecular weight increases, the gas movement becomes slower and more random. This effect is related to the Knudsen parameter,  $K_n$ , Chapter 2. A large molecule is characterized by a small mean free path,  $\lambda$ , as follows:

$$\lambda = \frac{1}{\sqrt{2}\pi d_M^2 \rho_M}, \quad [8.19]$$

With a constant pipe equivalent diameter,  $d_{eq}$ , the Knudsen parameter,  $K_n = \lambda/d_{eq}$ , becomes smaller, which is characteristic of a molecular flow regime. As introduced in Section 2.5.2, this regime is described by the rarefied gas theory of gases as being virtually random and usually slower than a viscous flow regime [Roth, 1990]. Further assessment of average particle size and gas viscosity of the fractions is required to determine the extent of this mass transfer limitation to the experiment.

#### 3. Condensed Fraction Mobility:

The condensation of cuts in the cold finger involves: droplet formation, droplet breakage, and oil accumulation at the base of the cold finger from the oil that is splashed in the drop detachment. The velocity of the accumulation depends strongly on the oil viscosity and the temperature of the cold finger inner wall. With heavier fractions, this process becomes very slow even when the bath temperature is increased significantly. This phenomenon can be mitigated by tapering the tip of the inner tube in the cold finger, as illustrated in Figure 8.29.

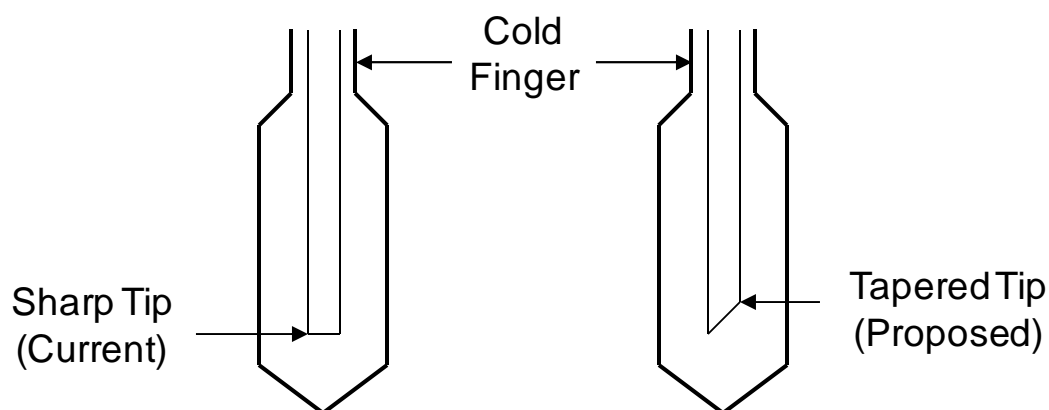


**Figure 8.29** Cold finger tip – Current (right) and Tapered (left).

## 8.6 Summary

The fractionation methodology introduced in this chapter provided the means to characterize approximately 60 wt% of a heavy oil or bitumen sample based on distillation. The amount fractionated significantly surpasses the performance of conventional vacuum distillation techniques; hence, this new method can provide a more

comprehensive assay of heavy oil and bitumen as well as the data to which corroborate or modify physical property correlations.

Preliminary testing indicated that repeatable data can be collected that are consistent with Gaussian extrapolations of the boiling points and existing correlations for properties such as density. The feasibility of an inter-conversion method based on an equation-of-state model was demonstrated. It remains to standardize the methodology and test it on heavy oils and bitumen with different physical properties.

## CHAPTER NINE: CONCLUSIONS AND RECOMMENDATIONS

### 9.1 Dissertation Contributions and Conclusions

The main outcomes of this research project were: 1) the design and construction of a new high vacuum apparatus capable of measuring reliable vapour pressure data and generating consistent heavy oil and bitumen fractions, 2) the development of a new methodology to characterize heavy oil and bitumen phase behaviour based in the collected data. The following conclusions were drawn in reaching these outcomes:

#### *9.1.1 High Vacuum – Vapour Pressure Measurement System*

A high vacuum apparatus was designed and constructed based on temperature and pressure criteria relevant for the measurement of vapour pressure of bitumen and fractions. Several challenges were encountered in the development of this apparatus because the application of this technology to bitumen characterization is new with no record found in the open literature. The main challenges were sustaining high vacuum conditions with minimum leak rate, cleaning, pressure transducer calibrations, and versatility. These issues were successfully overcome by alternatives such as metal seals, long baking periods and degassing techniques, calibrations with heavy hydrocarbons including logarithmic calibration charts, and the invention of novel components, such as the cold finger, to make the apparatus useful for vapour pressure measurement and bitumen fractionation.

The new apparatus was also successfully applied to: 1) the measurement of vapour pressure of well known pure substances, biodisels, and heavy oil and 2) the fractionation of up to 55 wt% of a bitumen. Vapour pressure data were repeatable to within 5%. The fractionation proves the versatility and promising use of this apparatus since it distilled double what is achievable with commercial vacuum distillation techniques. The property trends observed from several fractionations were consistent.

### ***9.1.2 Vapour Pressure Experimental Data***

Vapour pressures of three pure substances, seven biodiesel fuels from different vegetable sources, bitumen from Western Canada, and three fractions from the bitumen were measured with the HV-VPMS at temperatures from 30 to 180 °C. The first set of data was used to calibrate and test the apparatus whereas the rest of the data was used to characterize and corroborate modelling techniques for biodiesels and bitumens.

The vapour pressure data set presented in this work is a novel contribution since experimental data for biodiesels and bitumens is extremely scarce and is only available at temperatures above 230 °C and near the cracking point. These data were used to complement the open literature data set and to extend modelling and property correlation techniques over a wider temperature range.

Vapour pressure experimental data was supplemented with a variety of other experimental data, including liquid heat capacity data, water content and composition of

biodiesels, and distillation curves and density profiles for bitumen and fractions. Experimental data of these key physical properties are also scarce in the open literature.

### ***9.1.3 Vapour Pressure Extrapolation Technique***

Extrapolation of vapour pressure constrained to match heat capacity data was applied in this work. Although this technique has been used for modelling the vapour pressure of pure components, no record of the application of this technique for complex, heavy mixtures was found. Hence, its use in the modelling of the vapour pressure of biodiesels and bitumens is a novel contribution.

The technique was used to predict the vapour pressure and liquid heat capacity, simultaneously, to within 12% and 3%, respectively, of the data. It was shown that modelling of vapour pressure with no constraint can generate gross errors (as high as 200%) in the liquid heat capacity prediction. The method generates similar predictions using analytical vapour pressure equations and cubic equations of state.

Extrapolation of vapour pressure of fatty acid methyl esters was also assessed on data from the open literature. New property correlations for the ideal gas heat capacity, liquid heat capacity, and vapour pressure of these esters were proposed.

Finally, the application of this technique to develop a consistent and reliable inter-conversion method for low pressure boiling point fractions into normal boiling point for bitumens was demonstrated.

#### ***9.1.4 Heavy Oil and Bitumen Characterization Method***

A novel method to characterize heavy oil and bitumen was presented. In this method, pseudo-components are assigned for heavy oil or bitumen based on extrapolated measured normal boiling point curves. The characterization is then input into the Advanced Peng-Robinson equation of state to predict phase behaviour. The method was separately tested on previously collected data for Athabasca bitumen (Castellanos Diaz et al. [2011]) where it was shown to fit and predict the phase behaviour of bitumen and solvent mixtures. In this thesis, the method was applied to WC\_B1 bitumen where it successfully predicted vapour pressure and liquid heat capacity data.

It can be concluded that the interaction between bitumen pseudo-components, especially in the lightest region of the normal boiling point curve, can be modelled using the APR EoS and interaction parameters from the original Gao et al. correlation [1992]. Most of the data considered were vapour-liquid equilibrium data which is dominated by the lighter components. However, there is some evidence that the middle range of the distillation curve is also accurately represented including correct predictions of liquid-liquid equilibrium [Castellanos Diaz et al., 2011], the simultaneous prediction of asphaltene precipitation onset and saturation pressures [Castellanos Diaz et al. 2011; Agrawal et al. 2011], and the inter-conversion of low pressure extended boiling points developed in this thesis.

### ***9.1.5 Fractionation of Heavy Oil and Bitumen***

A Western Canadian bitumen sample was fractionated using the HV-VPMS. Five discrete fractions were obtained at temperature ranging from 150 to 290 °C, accounting for 56 wt% of the bitumen. These results were repeatable to within 8%. The performance of the deep vacuum fractionation surpasses that of any commercial distillation technique, almost doubling the amount fractionated. The fractionation provided, reproducible physical fractions that can be further studied. Having samples of the fractions provides the opportunity to corroborate and/or develop physical property correlations for significantly larger fraction of a bitumen.

The direct result of the deep vacuum fractionation is a low pressure boiling point curve which must be transformed into its more convenient normal boiling point curve form. The heavy oil and bitumen characterization methodology developed in this work was used to develop a preliminary inter-conversion technique that reproduced conventional distillation data of the bitumen to within 1%. This inter-conversion technique was used to convert the remainder of the boiling curve, extending the normal boiling point to 56 wt% of the bitumen. The extended normal boiling point followed the Gaussian extrapolation of the conventional distillation data. It remains to corroborate this technique with vapour pressure data for each bitumen cut.

## **9.2 Recommendations**

The success of this research opens a wide variety of research possibilities for the improved characterization of heavy oil and bitumen. Given the novelty of the techniques

introduced in this work, especially that of the new high vacuum apparatus, there is also room for improvement. The following topics of research and improvement are recommended:

1. Increase the size of the sample vessel on the Vapour Pressure Measurement for the fractionation process. Two objectives can be achieved with this improvement: first, the amount of a particular fraction is larger, hence providing enough material for more characterization assays; second, narrower boiling point cuts can be obtained.
2. Use pressure transducers DG1 and DG2 on the VPMA simultaneously to decrease the uncertainty of the vapour pressure data.
3. Modify the cold finger inner tube tip with a tapered tip to minimize condensation blockage and enhance fractionation dynamics.
4. Measure vapour pressure curves of different heavy oil and bitumen cuts and residues to provide definite corroboration of the proposed inter-conversion techniques. The vapour pressure curves can be modeled and extrapolated to the normal boiling point.
5. Measure the liquid heat capacity of different heavy oil and bitumen cuts at low and high temperatures. The low end of the temperature range is set by the liquid-solid transition of the sample whereas the high end of the temperature range is set by either the cracking temperature or the limitations of the calorimeter. These data points can serve to constrain extrapolation of vapour pressure curves towards the normal boiling point.

6. Fractionate heavy oil and bitumen with narrower boiling point cuts. In this work, about 20 to 30 °C cuts were generated. Fractions with narrower cuts can provide better resolution of the normal boiling point curve.
7. Record heavy oil and bitumen fractions volume profiles with time intervals of at least 4 to 5 days per cut. This procedure would be a little tedious but would provide enough data to determine a proper model for the fractionation dynamics. The fractionation time for different cuts can be used to determine suitable times for subsequent bitumen analyses
8. Develop a mass transfer analysis for the fractionation process in the high vacuum apparatus to provide insight on: the dynamics of the apparatus, the viscosity of liquid and gas bitumen fractions, diffusivity, and pipe capacitance. The exact model may be extremely complicated but with appropriate assumptions it may be possible to generate a simpler yet reliable model. Note that the gas phase is ideal, which simplifies the mathematics significantly. Thermal transpiration should be accounted for as well.
9. Construct a model for the prediction of bitumen viscosity from its pseudo-components. The data required to test such a model is the viscosity profiles with temperature of the different cuts
10. Modify Simdist calibration curves to better account for the chemistry distribution of the heavy oil and bitumen. Currently, extended SimDist remains unreliable beyond 20 to 30 wt% distilled. This commonly used technique can be improved by providing new calibration curves based on the extended low pressure boiling point curve generated in this work

Measure the composition of each cut from several heavy oils and bitumen using techniques such as gas chromatography or mass spectrometry. Compare the cut compositions with the same cuts from an independent experiment (spinning band distillation). Compare the cuts to the same cuts from a bitumen with different properties. The data can be used to confirm that the cuts produced by the high vacuum apparatus are repeatable and consistent. The same procedure can be performed with different physical properties as well.

## References

- Agrawal, P., Schoeggl, F. F., Satyro, M. A., and Yarranton, H. W., Case Study: Modelling the Phase Behaviour of Solvent Diluted Bitumen, *Canadian Unconventional Resources Conference*, Calgary, Canada, November, **2011**
- Akbarzadeh, K.; Ayatollahi, S.; Moshfeghian, M.; Alboudwarei, H.; and Yarranton, H Estimation of SARA Fraction Properties with the SRK EoS, *J. Can. Pet. Tech.* **43 (9)**, **2004**, 31-39
- Alazard, N.; and Montadert, L. Oil resources for the Next century: What's Ahead?, *Nonrenewable Resources*, 2 (3), **1993**, 197-206
- Alboudwarej, H.; Akbarzadeh, K.; Svrcek, W. Y.; and Yarranton, H. W. A Generalized Regular Solution Model for Asphaltene Precipitation from n-Alkane Diluted Heavy Oils and Bitumens. *Fluid Phase Equilibria*, 232, **2005**, 159-170
- Allen, C. A. W.; Watts, K. C.; Ackman, R. G.; and Peg, M. J. Predicting the Viscosity of Biodiesel Fuels from Their Fatty Acid Ester Composition, *Fuel*, 78, **1999**, 1319-1326
- Altget, K. H., and Boduszynski, M., in: Composition and Analysis of Heavy Petroleum Fractions, Ed. Dekker, New York, **1994**
- Ambrose, D.; and Walton, J. Vapor Pressures up to Their Critical Temperatures of Normal Alkanes and 1-Alkanols, *Pure and Applied Chemistry*, **61 (8)**, **1989**, 1395-1403
- AOSTRA. The Thermodynamic and Transport Properties of Bitumen and Heavy Oils, *Alberta Oil Sands Technology & Research Authority*, Canada, **1984**

AEUB, "Alberta Energy Reserves 2005 and Supply/Demand Outlook for 2006-2015", ST98-2006, Alberta Energy and Utilities Board, Calgary, **2006**

Badamchi-Zadeh, A.; Yarranton, H. W.; Svrcek, W. Y.; and Maini, B. B. Phase Behaviour and Physical Measurements for VAPEX solvents: Part I. Propane and Athabasca Bitumen. *J. Can. Petr. Tech.*, 48, **2009a**, 54-61

Badamchi-Zadeh, A.; Yarranton, H. W.; Maini, B. B. and Satyro, M. A. Phase Behaviour and Physical Measurements for VAPEX solvents: Part II. Propane, Carbon Dioxide and Athabasca Bitumen *J. Can. Petr. Tech.*, 48, **2009b**, 57-65

Batistella, C. B.; Sbaite, P.; Wolf Maciel, M. R.; Maciel Filho, R.; Winter, A.; Gomes, A.; Medina, L.; and Kunert, R. Heavy Petroleum Fractions Characterization: A New Approach Through Molecular Distillation, *Second Mercosur Congress on Chemical Engineering and Fourth Mercosur Congress on Process Systems Engineering*, **2005**, 1-10

Bestougeff, M; Burollet, P. F.; and Byramjee, R. J. Heavy Crude Oils and Their Classification, *UNITAR, Coal Age Mining Information Services*, McGraw-Hill, **1984**

Bureš, M.; Majer, V.; and Záborský, M. Modification of Benson Method for Estimation of Ideal-Gas Heat Capacities, *Chem. Eng. Sci.*, 36, **1981**, 529-537

Butler, R. M., Thermal Recovery of Oil and Bitumen, Prentice Hall, New Jersey, **1991**

Camin, D. L.; Forziati, A. F.; and Rossini, F. D. Physical Properties of n-Hexadecane, n-Decylcyclopentane, n-Decylcyclohexane, 1-Hexadecene, and n-Decylbenzene, *J. Phy. Chem.* 58, 440-442, **1954**

Castellanos-Diaz, O.; Modaresghazani, J.; M. A. Satyro; and H. W. Yarranton; Modeling the Phase Behavior of Heavy Oil and Solvent Mixtures; *Fluid Phase Equilibria*, 304, **2011**, 74-85

Ceriani, R.; and Meirelles, A. Predicting Vapor-Liquid Equilibria of Fatty Systems, *Fluid Phase Equilibria*, 215, **2004**, 227-236

Conceição, M. M., Roberlúcia, A. C., Silva, F. C., Bezerra, A. F., Fernandes Jr., V. J., and Souza, A. G. Thermoanalytical Characterization of Castor Oil Biodiesel, *Renewable & Sustainable Energy Reviews*, 11, **2007**, 964-975

Cox, E. R. Pressure-Temperature Chart for Hydrocarbon Vapors, *Ind. Eng. Chem.*, 15, **1923**, 592-593

Dadgostar, N.; and Shaw, J. A Predictive Correlation for the Constant-Pressure Specific Heat Capacity of Pure and Ill-Defined Liquid Hydrocarbons, *Fluid Phase Equilibria*, Paper in Press, **2011**

Daiwei, G.; Jinsen, G.; and Chunming X. The Application of UNIFAC Group-Contribution Model in Vapor-Liquid Equilibrium of Heavy Oil, *Pet. Sci. Tech.*, **24**, **2006**, 423-430

Dzida, M., and Prusakiewicz, P. The Effect of Temperature and pressure on the Physicochemical Properties of Petroleum Diesel Oil and Biodiesel Fuel, *Fuel*, 87, **2008**, 1941-1948

Enzer, H.; Dupree, W.; and Miller, S. Energy Perspectives, *U.S. Dept. of the Interior*, Washington, U.S.A., **1975**

Francis, A. W., and Robbins, G. W., *J. Am. Chem. Soc.*, 55, **1933**, 4339

Fulem, M.; Růžička, K.; Růžička, V.; Hulicius, E.; Šimeček, T.; Melichar, K.; Pangrác, J.; Rushworth, S. A.; and Smith, L. M. Vapour Pressure of Metal Organic Precursors, *J. Crystal Growth*, 248, **2003**, 99-107

Fulem, M.; Růžička, K.; Růžička, V.; Šimeček, T.; Hulicius, E.; and Pangrác, J. Vapour Pressure and Heat Capacities of Metal Organic Precursors,  $Y(thd)_3$  and  $Zr(thd)_4$ , *J. Crystal Growth*, 264, 192-200, **2004**

Fulem, M.; Becerra, M.; Anwarul Hasan, M. D.; Zhao, B.; and Shaw, J.M. Phase Behaviour of Maya Crude Oil Based on Calorimetry and Rheometry, *Fluid Phase Equilibria*, 272, **2008**, 32-41

Fulem, M. and Růžička, V.; Private Conversation, Institute of Chemical Technology, Prague, **2009**

Fulem, M., Private Communication, University of Calgary, Calgary, **2011**

Gao, G.; Dadiron, J. L.; Saint-Guirons, H.; Xans, P.; and Montel, F. A Simple Correlation to Evaluate Binary Interaction Parameters of the Peng-Robinson Equation of State: Binary Light Hydrocarbon Systems. *Fluid Phase Equilibria*, **1992**, 74-85

Goodrum, J. W., and Eiteman, M. A. Physical Properties of Low Molecular Weight Triglycerides for the Development of Bio-Diesel Fuel Models, *Bioresource Technology*, 56, **1996**, 55-60

Goodrum, J. W. Volatility and Boiling Points of Biodiesel from vegetable Oils and Tallow, *Biomass and Bioenergy*, 22, **2002**, 205-211

Gray, J. A.; Holder, G. D.; Brady, C. J.; Cunningham, J. R.; Freeman, J. R.; and Wilson, G. M. Thermophysical Properties of Coal Liquids. 3. Vapor Pressure and Heat of Vaporization of Narrow Boiling Coal Liquid Fractions, *Ind. Eng. Chem. Process Des. Dev.*, 24 (1), 97-107, **1985**

Gray Jr. R. D.; Heidman, J. L.; Springer, R. D.; and Tsonopoulos, C. Characterization and Property Prediction for Heavy Petroleum and Synthetic Liquids, *Fluid Phase Equilibria*, 53, **1989**, 355-376

Green, D. L.; Hopson, J. L.; and Li, J. Running Out of and Into Oil: Analyzing Global Oil Depletion and Transition through 2050, Oak Ridge National Laboratory Report for the U. S. Department of Energy, **2003**

Green, G. The Design and Construction of Small Vacuum Systems, Chapman and Hall Ltd, London, **1968**

Grenier-loustalot, M. F., Potin-Gautier, M., and Grenier, P., Applications Analytiques de la Mesure des Tension de Vapeur par Saturation d'un Gaz Inerte Cas des Alcanes Normaux et des Polyethyleneglycols, *Analytical Letters*, 14(A16), **1981**, 1335-1349

Groenzin, H., and Mullins, O. C., Molecular Size and Structure of Asphaltenes, *Petroleum Science and Technology*, 19(1-2), **2001**, *Asphaltene Chemistry and Solids Deposition*

Gunstone, F. D., Harwood, J. L., and Dijkstra A. J., The Lipid Handbook, 3<sup>rd</sup> ed., CRC, Boca Raton, **2007**

Hablanian, M. H. High-Vacuum Technology: A Practical Guide, 2<sup>nd</sup> Edition, Marcel Dekker, Inc., New York, **1997**

Haines, P. J., Principles of Thermal Analysis and Calorimetry, RSC Paperbacks, **2002**

Hedrick, B. W.; Seibert, K. D.; and Crewe, C. A New Approach to Heavy Oil and Bitumen Upgrading, UOP LLC, **2006**

Holland, L.; Steckelmacher, W.; and Yarwood, J. Vacuum Manual, E & F. N. SPON, London, **1974**

Huang, S. H.; and Radosz, M. Phase Behavior of Reservoir Fluids III: Molecular Lumping and Characterization. *Fluid Phase Equilibria*, 66, **1991a**, 1-21

Huang, S. H.; and Radosz, M. Phase Behavior of Reservoir Fluids IV: Molecular Weight Distributions for thermodynamic Modeling. *Fluid Phase Equilibria*, 66, **1991b**, 23-40

Jahangini, M.; Jacobsen, R. T.; Stewart, R. B.; and McCarty, R. D. A Thermodynamic Property Formulation for Ethylene from the Freezing Line to 450 K at Pressures to 260 MPa, *Int. J. Thermodynamics*, **7(3)**, **1986**

Janisch, A. Oil Sands and Heavy Oil: Can They Ease the Energy Shortage?, *paper presented at the 1<sup>st</sup> UNITAR International Conference on heavy Crude and Tar Sands*, Edmonton, Canada, **1979**

Jiang, Q., Recovery of Heavy Oil Using Vapex Process; PhD. Thesis, University of Calgary, AB, Canada, **1997**

Kinghorn, R. R. An Introduction to the Physics and Chemistry of Petroleum, John Wiley & Sons, Norwich, **1983**

Khayan, M. Proposed Classification and Definitions of Heavy Crude Oils and Tar Sands, *UNITAR, Coal Age Mining Information Services*, McGraw-Hill, **1984**

Klahorst, S. Dreaming of the Perfect Fat, *Food Product Design - Perspectives*, **1998**

Korsten, H., Internally Consistent Prediction of Vapor Pressure and Related Properties, *Ind. Eng. Chem. Res*, 39, **2000**, 813-820

Knothe, G., and van Gerpen, J., *The Biodiesel Handbook*, AOCS Publishing, **2005**

Laštovka, V., Fulem, M., Becerra, M., and Shaw, J., A Similarity Variable for Estimating the Heat Capacity of Solid Organic Compounds Part II. Application: Heat Capacity Calculation for Ill-Defined Organic Solids, *Fluid Phase Equilibria*, 268(12), **2008**

Lee, B. I.; and Kesler M. G. A Generalized Thermodynamic Correlation Based on Three-Parameter Corresponding States, *AIChE J.*, **22**, **1975**, 510-527

Lee, C.; Dempsey, D. M.; Mohamed, R. S.; and Holder, G. Vapor-Liquid Equilibria in the Systems of n-Decane/Tetralin, n-Hexadecane/Tetralin, n-Decane/1-Methylnaphthalene, and 1-Methylnaphthalene/Tetralin, *J. Chem. Eng. Data*, 37, 163-165, **1992**

Leelavanichkul, P.; Deo, M. D.; and Hanson, F. V. Crude Oil Characterization and Regular Solution Approach to Thermodynamic Modeling of Solid Precipitation at Low Pressure, *Pet. Sci. Tech.* 22 (7-8), **2004**, 973-990

Lemmon, E. W.; and Goodwin, A. R. H. Critical Properties and Vapor Pressure Equation for Alkanes  $C_nH_{2n+2}$ : Normal Alkanes with  $n \leq 36$  and Isomers for  $n=4$  through  $n=9$ , *J. Phys. Chem. Ref. Data*, 29 (1), 1-39, **2000**

Maxwell, J.B.; and Bonnell, L.S. Derivation and Precision of a New Vapor Pressure Correlation for Petroleum Hydrocarbons, *Ind. Eng. Chem.* **49(7)**, **1957**, 1187-1196

McFarland A. Evaluation of New co-Volume Mixing Rules for the Peng Robinson Equation of State, MSc. Thesis, University of Alberta, Canada, **2007**

Merdrignac, L.; and Espinat, D. Physicochemical Characterization of Petroleum Fractions: the State of the Art, *Oil & Gas Sci. Tech.-Rev. IFP*, 62 (1), **2007**, 7-32

Mehrotra, A. K.; Sarkar, M.; and Svrcek, W. Y., Bitumen Density and Gas Solubility Predictions Using the Peng-Robinson Equation of State, *AOSTRA Journal of Research*, 1 (4), **1985**, 216-229

Michelsen, M. L. The Isothermal Flash Problem. Part I. Stability, *Fluid Phase Equilibria*, 9, **1982a**, 1-19

Michelsen, M. L. The Isothermal Flash Problem. Part II. Phase Split Calculation, *Fluid Phase Equilibria*, 9, **1982b**, 21-40

Mills, P. L., and Fenton, R. L., Vapor Pressures, Liquid Densities, Liquid Heat Capacities, and Ideal Gas Thermodynamic Properties for 3-Methylhexanal and 3,4-Dimethylpentanal, *J. Chem. Eng. Data*, 32, **1987**, 266-273

Mokbel, I.; Růžička, K.; Majer, V.; Růžička, V.; Ribeiro, M.; Jose, J.; Záborský, M. Vapor Pressures and Thermal Data for Three High-Boiling Compounds of Petroleum Interest: 1-Phenyldodecane, (5 $\alpha$ )-cholestane, Adamantane, *Fluid Phase Equilibria*, 169, **2000**, 191-207

Monte, J. S. M.; Santos, L. M.; Fulem, M.; Fonzeca, J. M.; and Sousa, C. New Static Apparatus and Vapor Pressure of Reference Materials: Naphthalene, Benzoic Acid, Benzophenone, and Ferrocene, *J. Chem. Eng. Data*, 51, 757-766, **2006**

Morgan, D. L.; and Kobayashi, R. Direct Vapor Pressure Measurements of Ten n-Alkanes in the C<sub>10</sub>-C<sub>28</sub> Range, *Fluid Phase Equilibria*, 97, 211-242, **1994**

Myers, H. S.; and Fenske, M. R. Measurement and Correlation of Vapor Pressure Data for High Boiling Hydrocarbons, *Ind. Eng. Chem.*, 47 (8), 1652-1658, **1955**

National Institute of Standards and Technology, NIST. ThermoData Engine (TDE) Version 5.0, Pure compounds, Equations of state, Binary mixtures, and Chemical Reactions. NIST Standard reference Database #103b. Thermophysical Research Center. USA. **2010**

National Instruments, LabView 8.6, User Manual, National Instruments Corporation, Texas, **2008**

Narvaez, P. C., Rincon S. M., Castaneda, L. Z. and Sanchez, F. J. Determination of Some Physical and Transport Properties of Palm Oil and of its Methyl Esters, *Latin American Applied Research*, 38, **2008**, 1-6

Neau, E.; and Jaubert, J. Characterization of Heavy Oils, *Ind. Eng. Chem. Res.*, **32**, **1993**, 1196-1203

Oliveira, M. B., Varanda, F. R., Marrucho, L. M., Queimada, A. J., and Coutinho, J. A. P., Prediction of Water Solubility in Biodiesel with the CPA Equation of State, *Ind. Eng. Chem. Res.* 47, **2008**

Oonk, H.A., van der Linde, P. R., Huinink, J, and Blok, J. G., Representation and Assessment of Vapor Pressure Data; a Novel Approach Applied to Crystalline 1-bromo-4-chlorobenzene, 1-chloro-4-iodobenzene, and 1-bromo-4-iodobenzene, *J. Chem. Thermodynamic*, 30, **1998**, 897-907

Ott, L.; and Bruno, T. Variability of Biodiesel Fuel and Comparison to Petroleum-Derived Diesel Fuel: Application of a Composition and Enthalpy Explicit Distillation Curve Method, *Energy & Fuel*, 22, **2008**, 2861-2868

Parks, G. S., and Moore, G. E., Vapor Pressure and Other Thermodynamic Data for n-Hexadecane and n-Dodecylcyclohexane near Room Temperature, *J. Che. Phys.*, 17 (11), **1949**, 1151-1153

Pedersen, K.S.; Fredenslund, A.; and Thomassen, P. Properties of Oils and Natural Gases. Gulf Publishing Company. USA. **1989**

Pedersen, K. S.; Thomassen, P; and Fredenslundm, A. Characterization of Gas Condensate Mixtures: C+7 Fractio Characterization. Chorn, L. G.; and Mansoori, G. A.; Taylor and Francis, New York, **1989**

Peng, D. Y., and Robinson, D. B. A New Two-Constant Equation of State, *Ind. Eng. Chem. Fund.*, 15(1), **1976**, 59-64

Poling, B. E., Prausnitz, J. M., and O'Connell, J. P., The Properties of Gases and Liquids, 5<sup>th</sup> edition, McGraw-Hill, **2001**

Read, J.; and Whiteoak, D. The Shell Bitumen Handbook, 5<sup>th</sup> Edition, Shell Bitumen, Thomas Telford Publishing, **2003**

Redhead, P. A.; Hobson, J. P.; and Kornelsen, E. V. The Physical Basis of Ultra-high Vacuum, Barnes and Noble, New York, **1968**

Riazi, M. R. Characterization and Properties of Petroleum Fractions, 1<sup>st</sup> Edition, *ASTM international*, U.S.A. **2005**

Rodgers, P.; Creagh, L.; Prange, M.; and Prausnitz, J. M. Molecular Weight Distributions for Heavy Oil Fossil Fuels from Gel Permeation Chromatography and Characterization Data, *Ind. Eng. Chem. Res.*, **26**, **1987**, 2312-2318

Roháč, V.; Růžička, V.; Růžička, K.; Poledníček, M.; Aim, K.; Jose, J.; and Zábanský, M. Recommended Vapour and Sublimation Pressures and Related Thermal Data for Chlorobenzenes, *Fluid Phase Equilibria*, **157**, **1999**, 121-142

Roháč, V.; Čenský, M.; Zala, D.; Růžička, V.; Růžička, K.; Sporka, K.; and Aim, K. Vapor Pressure and Liquid Heat Capacity of Perhydroacenaphthylene and Perhydrophenanthrene, *J. Chem. Eng. Data*, **45**, **2000**, 1205-1210

Roth, A. Vacuum Technology, 3<sup>rd</sup> edition, North-Holland, Netherlands, **1990**

Růžička, K.; and Majer, V. Simple and Controlled Extrapolation of Vapor Pressures toward the Triple Point, *AIChE J.*, **42** (6), 1723-1740, **1996**

Růžička, K.; Fulem, M.; Růžička, V. Recommended Vapor Pressure of Solid Naphthalene, *J. Chem. Eng. Data*, **50**, 1956-1970, **2005**

Sanchez, C.; Private Communication, University of Calgary, Calgary, **2011**

Satyro M. A.; Private Communication, Virtual Materials Group, Calgary, **2007**

Schwarz, B. J.; Wilhelm, J. A.; and Prausnitz, J. M. Vapor Pressures and Saturated-Liquid Densities of Heavy Fossil-Fuel Fractions, *Ind. Eng. Chem. Res.* **26**, **1987**, 2353-2360

Šetina J. New Approach to Corrections for Thermal Transpiration Effects in Capacitance Diaphragm Gauges, *Metrologia*, **36**, **1999**, 623-626

Shaw, J. M.; and Zou, X. Chapter 19: Phase Behavior of Heavy Oils. In: Asphaltenes, Heavy Oils, and Petroleomics, Edited by: Mullins, O.C.; Sheu, E. Y.; Hammami, A.; and Marshall, A. G., Springer, USA, **2007**

Sinke, G. C., A Method for Measurement of Vapour Pressures of Organic Compounds Below 0.1 Torr. Naphthalene as a Reference Substance, *J. Chm. Thermodyn.* **6**, **1974**

Siu, M. Equations for Thermal Transpiration, *J. Vac. Sci. Technol*, **10** (2), **1973**, 368-372

Smith, D. F.; Rahimi, P.; Teclemariam, A.; Rodgers, R. P.; Marshall, A. G. Characterization of Athabasca Bitumen Heavy Vacuum Gas Oil Distillation Cuts by Negative/Positive Electrospray Ionization and Automated Liquid Injection Field Desorption Ionization Fourier Transform Ion Cyclotron Resonance Mass Spectrometry, *Energy & Fuels*, **22**, **2008**, 3118-3125

Smith, J.M.; Van Ness, H. C.; and Abbot, M. M. Introduction to Chemical Engineering Thermodynamics, *McGraw-Hill Companies, Inc.* U.S.A., **1996**

Soave, G. Direct Calculation of Pure-Compound Vapour Pressures through Cubic Equations of State, *Fluid Phase Equilibria*, **31**, **1986**, 203-207

Søreide I. Improved Phase Behavior Predictions of Petroleum Reservoir Fluids from a Cubic Equation of State, PhD Thesis, the Norwegian Institute of Technology and Applied Geophysics, Norway, **1989**

Speight, J. G. The Chemistry and Technology of Petroleum, 3<sup>rd</sup> Ed., Marcel Dekker, Inc., New York, **1999**

Twu, C. H. An Internally Consistent Correlation for Predicting the Critical Properties and Molecular Weights of Petroleum and Coal-Tar Liquids, *Fluid Phase Equilibria*, **16**, **1984**, 137-150

Twu, C. H.; Coon, J. E.; and Cunningham, J. R. A Generalized Vapor Pressure Equation for Heavy Hydrocarbons, *Fluid Phase Equilibria*, **96**, **1994**, 19-31

van der Linde, Blok, J. G., and Oonk, H.A., Naphthalene as a reference Substance for Vapor Pressure measurements Looked Upon from an Unconventional Point of View, *J. Chem. Thermodynamics*, **30**, **1998**, 909-917

Van Nes, K.; and van Western, H. A., Aspects of the Constitution of Mineral Oils, Elsevier New York, **1951**

Vetere, A. The Riedel Equation, *Ind. Eng. Chem. Res.*, **30**, **1991**, 2487-2492

Virtual Materials Group Inc VMG. VMGSim Version 5.0.5, VMGSim User's Manual. Calgary Alberta, **2010**

Wagner, W. New Vapour Pressure Measurements for Argon and Nitrogen and a New Method for Establishing Rational Vapour Pressure Equations, *Cryogenics*, **1973**, 470-482

Wallas, S. M. Phase Equilibria in Chemical Engineering, *Butterworth Publishers*, U.S.A., **1985**

Waring, W. Form of a Wide-Range Vapor Pressure Equation, *Ind. Eng. Chem.*, **1954**, 762-763

Weir, R. D., and de Loos, Th. W. Measurement of the Thermodynamic Properties of Multiple Phases, IUPAC, Physical Chemistry Division, Commission on Thermodynamics, Elsevier, The Netherlands, **2005**

Whitson, C. H. Characterizing Hydrocarbon Plus Fractions, *Trans. AIChE*, 275, **1983**

Whitson, C. H., and Brulé, M. R. Phase Behavior. Monograph Volume 20, Henry L. Doherty Series, Society of Petroleum Engineers Inc, USA, **2000**

Widegren, J. A., and Bruno, T. J., Vapor Pressure Measurements on Saturated Biodiesel Fuel Esters by the Concatenated Gas Saturation Method, *Fuel*, 90(5), **2011**

Wiley-Interscience. Wiley Critical Content, Petroleum Technology, Volume 1, *John Wiley & Sons, Inc*, U.S.A., **2007**

Wu, Y. Theory of Thermal Transpiration in a Knudsen Gas, *J. Chem. Physics*, 48 (2), **1968**, 889-894

Yarranton, H. W., and Masliyah, J. H. Molar Mass Distribution and Solubility Modeling of Asphaltenes, *AIChE J.*, 42(12), **1996**, 3533-3543

Yuan, W., Hansen, A. C.; Zhang, Q. Vapor Pressure and Normal Boiling Point Predictions for Pure Methyl Esters and Biodiesel Fuels, *Fuel*, 84, **2005**, 943-950

## **APPENDIX A: EXPERIMENTAL DATA**

The following Appendix complements experimental data collected for the development and corroboration of vapour pressure modeling of pure components, biodiesels and heavy oils which is not shown in the body of the thesis work.

Experimental heat capacity of biodiesels and heavy oil was collected in the National Research Council (NRC) molecular sciences laboratories in Ottawa, ON. Biodiesel composition was collected at the National Institute of Standards and Technology (NIST) laboratories in Boulder, CO. Distillation curves for Western Canadian bitumen were collected at the Asphaltene and Emulsion Research (AER) group at the University of Calgary. Finally, vapour pressure data was collected using the HV-VPMS.

**TABLE OF CONTENTS**

- A1. Pure Component Vapour Pressure Experimental Data
  - A1.1 Hexadecane
  - A1.2 Eicosane
  - A1.3 Naphthalene
- A2. Biodiesels
  - A2.2 Biodiesel Composition
    - A2.2.1 Experimental Methodology
    - A2.2.2 Experimental Results
  - A2.3 Biodiesel Vapour Pressure
  - A2.4 Biodiesel Heat Capacity
- A3. Piece River Heavy Oil
  - A3.1 Distillation and SimDist
  - A3.2 Vapour Pressure
  - A3.3 Heat Capacity

### A1. Pure Component Vapour Pressure Experimental Data

Experimental vapour pressure data of pure components collected in this work using the HV-VPMS is shown in this section. The data shown consist of the raw data, the calibrated data, the thermal transpiration factor (Chapter 4), and the uncertainty. Experimental vapour pressure is then determined as shown in Equation A1.

$$P_{Experimental} = P_{Raw} C_F C_T \quad [A1]$$

where CF is the calibration factor (Section 3.4), and CT is the thermal transpiration factor (Section 2.5)

Note that in order to know whether the thermal transpiration factor is applied or not (if it is in the molecular flow regime, Section 2.5), the molecule size is required. A rough approximation of the molecule size is given by the volume parameter b in the Advanced Peng-Robinson equation of state (Chapter 4). Then, the molecule radii can be calculated, assuming a spherical molecule, as

$$r_m = \left( \frac{3b}{4\pi N_A} \right)^{1/3} \quad [A2]$$

This value and the transition pressure (Section 2.5) are also listed in the tables below:

### A1.1 Hexadecane

**Table A.1** Experimental Vapour Pressure of Hexadecane

T [°C]	T <sub>uncer</sub> [°C]	P <sub>Raw</sub> [kPa]	r <sub>Mol</sub> [nm]	P <sub>Tran</sub>	C <sub>T</sub>	P <sub>Corr</sub> [kPa]	Uncer. [%]
25.1	0.1	1.71x10 <sup>-3</sup>	0.60	5 x10 <sup>-5</sup>	1	6.82x10 <sup>-4</sup>	4.1
25.2	0.1	1.24x10 <sup>-3</sup>	0.60	5 x10 <sup>-5</sup>	1	5.01x10 <sup>-4</sup>	3.5
30.1	0.1	5.61x10 <sup>-3</sup>	0.60	5 x10 <sup>-5</sup>	1	8.96 x10 <sup>-4</sup>	2.5
30.6	0.1	1.61x10 <sup>-3</sup>	0.60	5 x10 <sup>-5</sup>	1	7.91x10 <sup>-4</sup>	2.5
32.1	0.1	4.24 x10 <sup>-3</sup>	0.60	5 x10 <sup>-5</sup>	1	7.94 x10 <sup>-4</sup>	1.8
34.2	0.1	2.01 x10 <sup>-3</sup>	0.60	5 x10 <sup>-5</sup>	1	1.13x10 <sup>-3</sup>	1.7
35.8	0.1	2.06x10 <sup>-3</sup>	0.60	5 x10 <sup>-5</sup>	1	1.23x10 <sup>-3</sup>	3.5
38.7	0.1	2.31x10 <sup>-3</sup>	0.60	5 x10 <sup>-5</sup>	1	1.52x10 <sup>-3</sup>	2.5
44.5	0.1	3.16x10 <sup>-3</sup>	0.60	5 x10 <sup>-5</sup>	1	2.53x10 <sup>-3</sup>	1.2
45.1	0.1	4.93 x10 <sup>-3</sup>	0.60	5 x10 <sup>-5</sup>	1	2.46 x10 <sup>-3</sup>	2.4
46.3	0.1	3.98x10 <sup>-3</sup>	0.60	5 x10 <sup>-5</sup>	1	3.39x10 <sup>-3</sup>	0.3
49.9	0.1	4.63x10 <sup>-3</sup>	0.60	5 x10 <sup>-5</sup>	1	4.45x10 <sup>-3</sup>	1.3
50.1	0.1	6.14 x10 <sup>-3</sup>	0.60	5 x10 <sup>-5</sup>	1	4.38 x10 <sup>-3</sup>	0.5
56.9	0.1	6.78x10 <sup>-3</sup>	0.60	5 x10 <sup>-5</sup>	1	6.78x10 <sup>-3</sup>	6.2
59.5	0.1	8.66x10 <sup>-3</sup>	0.60	5 x10 <sup>-5</sup>	1	8.66x10 <sup>-3</sup>	2.2
60.1	0.1	7.01 x10 <sup>-3</sup>	0.60	6 x10 <sup>-5</sup>	1	9.87 x10 <sup>-3</sup>	1.4
70.1	0.1	3.01 x10 <sup>-2</sup>	0.60	6 x10 <sup>-5</sup>	1	3.01 x10 <sup>-2</sup>	3.5
70.1	0.1	2.19 x10 <sup>-2</sup>	0.60	6 x10 <sup>-5</sup>	1	2.19 x10 <sup>-2</sup>	11.5
79.3	0.1	2.73x10 <sup>-2</sup>	0.60	6 x10 <sup>-5</sup>	1	2.73x10 <sup>-2</sup>	2.4
89.9	0.1	6.99x10 <sup>-2</sup>	0.60	6 x10 <sup>-5</sup>	1	6.99x10 <sup>-2</sup>	4.3
89.9	0.1	8.22 x10 <sup>-2</sup>	0.60	6 x10 <sup>-5</sup>	1	8.22 x10 <sup>-2</sup>	6.0
90.1	0.1	6.42 x10 <sup>-2</sup>	0.60	6 x10 <sup>-5</sup>	1	6.42 x10 <sup>-2</sup>	3.3

### A1.1 Eicosane

**Table A.2** Experimental Vapour Pressure of Eicosane

T [°C]	T <sub>uncer</sub> [°C]	P <sub>Raw</sub> [kPa]	r <sub>Mol</sub> [nm]	P <sub>Tran</sub>	C <sub>T</sub>	P <sub>Corr</sub> [kPa]	Uncer. [%]
50.0	0.1	2.59x10 <sup>-3</sup>	0.7	4x10 <sup>-5</sup>	1	4.88x10 <sup>-5</sup>	0.2
65.0	0.1	3.31x10 <sup>-3</sup>	0.7	4x10 <sup>-5</sup>	1	2.12x10 <sup>-4</sup>	1.6
69.9	0.1	4.24x10 <sup>-3</sup>	0.7	4x10 <sup>-5</sup>	1	3.99x10 <sup>-4</sup>	0.1
75.0	0.1	4.64x10 <sup>-3</sup>	0.7	4x10 <sup>-5</sup>	1	6.35x10 <sup>-4</sup>	0.1
84.9	0.1	4.75x10 <sup>-3</sup>	0.7	4x10 <sup>-5</sup>	1	1.51x10 <sup>-3</sup>	0.4
100.1	0.1	6.13x10 <sup>-3</sup>	0.7	5x10 <sup>-5</sup>	1	5.21x10 <sup>-3</sup>	0.2
109.7	0.1	1.10x10 <sup>-2</sup>	0.7	5x10 <sup>-5</sup>	1	1.10x10 <sup>-2</sup>	0.3

### A1.2 Naphthalene

**Table A.3** Experimental Vapour Pressure of Naphthalene

<b>T [°C]</b>	<b>T<sub>uncer</sub>[°C]</b>	<b>P<sub>Raw</sub> [kPa]</b>	<b>r<sub>Mol</sub> [nm]</b>	<b>P<sub>Tran</sub></b>	<b>C<sub>T</sub></b>	<b>P<sub>Corr</sub> [kPa]</b>	<b>Uncer. [%]</b>
29.9	0.1	2.01x10 <sup>-0</sup>	0.4	1x10 <sup>-4</sup>	1	2.54x10 <sup>-2</sup>	9.0
30.1	0.1	1.35x10 <sup>-0</sup>	0.4	1x10 <sup>-4</sup>	1	1.55x10 <sup>-2</sup>	3.2
31.2	0.1	1.72x10 <sup>-0</sup>	0.4	1x10 <sup>-4</sup>	1	2.11x10 <sup>-2</sup>	2.1
50.2	0.1	9.01x10 <sup>-0</sup>	0.4	1x10 <sup>-4</sup>	1	1.30x10 <sup>-1</sup>	14.1
50.0	0.1	6.88x10 <sup>-0</sup>	0.4	1x10 <sup>-4</sup>	1	9.85x10 <sup>-2</sup>	10.2
50.1	0.1	9.80x10 <sup>-0</sup>	0.4	1x10 <sup>-4</sup>	1	1.42x10 <sup>-1</sup>	2.1
50.1	0.1	1.04x10 <sup>+1</sup>	0.4	1x10 <sup>-4</sup>	1	1.52x10 <sup>-1</sup>	2.1
70.0	0.1	2.87x10 <sup>+1</sup>	0.4	1x10 <sup>-4</sup>	1	4.26x10 <sup>-1</sup>	17.9

## A2. Biodiesels

Experimental data on biodiesels comprises composition and physical properties, including liquid heat capacity, cloud points, and vapour pressure.

### A2.2 Biodiesel Composition

The information presented below is an extract of a report obtained from the National Institute of Standards and Technology laboratories in Boulder, Colorado, Thermophysical Properties Division, with the permission and collaboration of Dr. Tomas Bruno and Dr. Tara M. Lovestead.

#### A2.2.1 Experimental Methodology

The components of each of the samples were identified with gas chromatography and mass spectrometry (GC-MS) with a 30 m capillary column with a 0.15 µm coating of the stationary phase, 50 % cyanopropyl-50 % dimethyl polysiloxane. This stationary phase has proven to be optimal for the analysis of biodiesel fuel samples.

The samples were prepared in *n*-hexane and injected with an autosampler into a split/splitless injector set with a 100 to 1 split ratio. The injector was operated at a temperature of 325.0 °C and a constant head pressure of 10 psig. A temperature program of 80 °C for 2 minutes followed by temperature ramping at 8 °C per minute to 220 °C and a hold at 220 °C for 5 minutes was used. Mass spectra were collected for each peak from 33 to 750 relative molecular mass (RMM) units. Spectral peaks were interpreted with guidance from the NIST/EPA/NIH Mass Spectral Database [1995], The American Oil Chemists' Society's The Lipid Library [2001], and the CRC Handbook of Fundamental Spectroscopic Correlation Charts [2005]

Once the compounds in each sample were identified, the biodiesel fuel samples were analyzed with GC and flame ionization detection (GC-FID) with external standards to determine the compounds. Aliquots (3 µL) from crimp-sealed vials of each sample were injected with an automatic sampler. High-purity nitrogen was used as the carrier and makeup gas. The split/splitless injection inlet was maintained at 325.0 °C. The column and temperature program were identical to that of the GC-MS analysis. The FID was maintained at 275.0 °C.

#### *A2.2.2 Experimental Results*

Figures A-1 to A-4 shows the comparison of the experimental data with open literature data of biodiesels with a common generic source. For results on the molecular weight distributions of the biodiesels considered in this work refer to Chapter 6

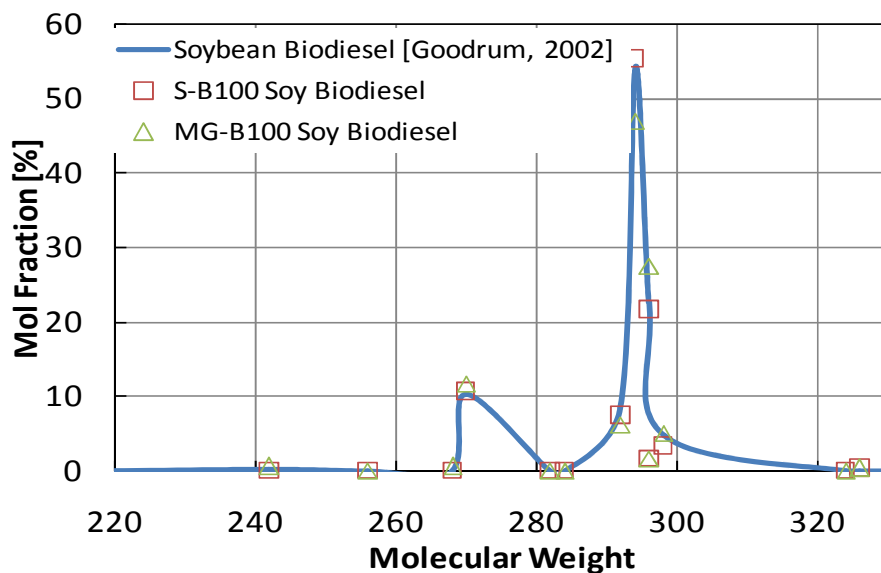


**Figure A.1** Comparison between open literature and experimental molecular weight distributions for soybean biodiesels

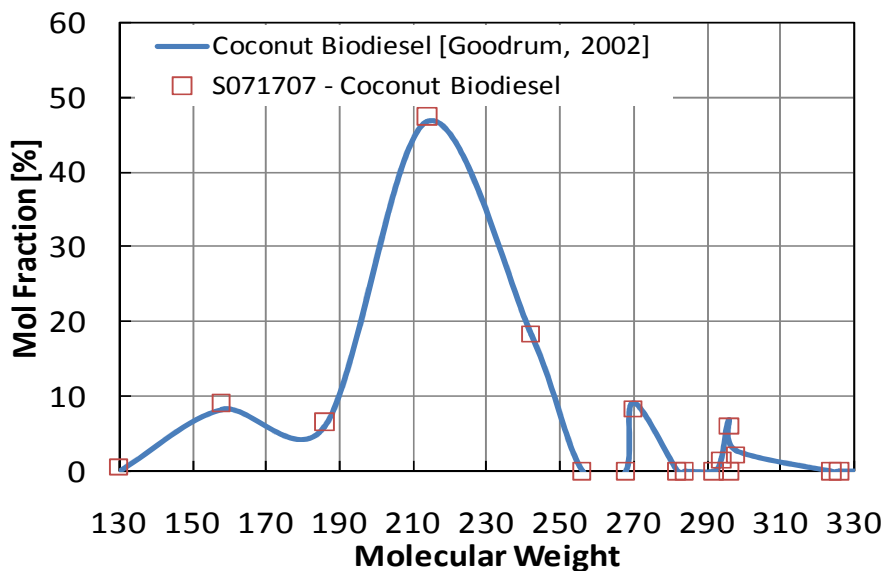


**Figure A.2** Comparison between open literature and experimental molecular weight distributions for coconut biodiesels

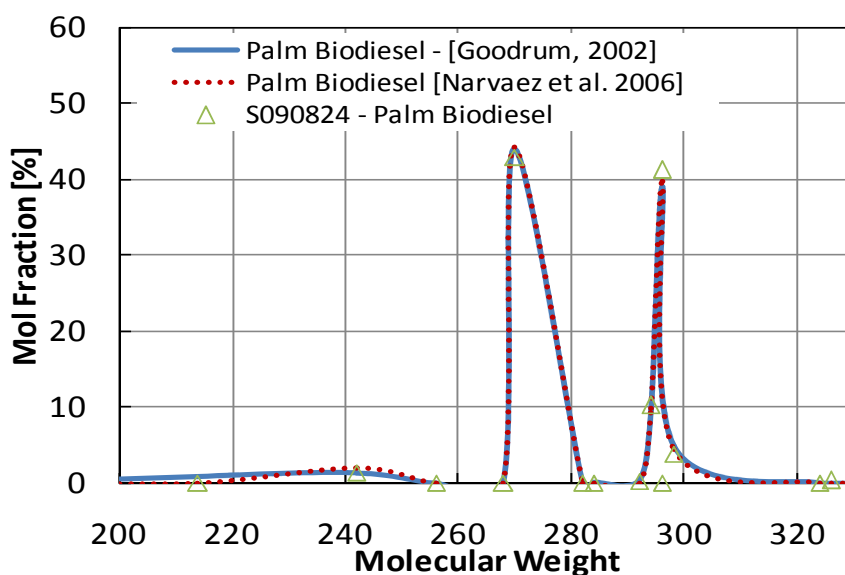


**Figure A.3** Comparison between open literature and experimental molecular weight distributions for palm biodiesels

### A2.3 Biodiesel Vapour Pressure

**Table A.4** Experimental Vapour Pressure of Palm Oil Biodiesel

T [°C]	T <sub>uncer</sub> [°C]	P <sub>Raw</sub> [kPa]	r <sub>Mol</sub> [nm]	P <sub>Tran</sub>	C <sub>T</sub>	P <sub>Corr</sub> [kPa]	Uncer. [%]
35.0	0.1	0.46	0.6	5x10 <sup>-5</sup>	1	1.53x10 <sup>-5</sup>	0.3
40.1	0.1	0.45	0.6	5x10 <sup>-5</sup>	1	2.21x10 <sup>-5</sup>	1.7
50.1	0.1	0.52	0.6	5x10 <sup>-5</sup>	1	8.21x10 <sup>-5</sup>	0.3
65.0	0.1	0.63	0.6	6x10 <sup>-5</sup>	1	4.09x10 <sup>-4</sup>	0.5
69.9	0.1	0.67	0.6	6x10 <sup>-5</sup>	1	6.64x10 <sup>-4</sup>	0.5
80.0	0.1	0.73	0.6	6x10 <sup>-5</sup>	1	1.16x10 <sup>-3</sup>	0.3

**Table A.5** Experimental Vapour Pressure of Rapeseed Oil Biodiesel

T [°C]	T <sub>uncer</sub> [°C]	P <sub>Raw</sub> [kPa]	r <sub>Mol</sub> [nm]	P <sub>Tran</sub>	C <sub>T</sub>	P <sub>Corr</sub> [kPa]	Uncer. [%]
40.0	0.1	0.46	0.5	8x10 <sup>-5</sup>	0.8	7.95x10 <sup>-6</sup>	2.1
65.0	0.1	0.55	0.5	8x10 <sup>-5</sup>	1	1.27x10 <sup>-4</sup>	1.2
80.1	0.1	0.67	0.5	9x10 <sup>-5</sup>	1	5.85x10 <sup>-4</sup>	0.1
84.9	0.1	0.81	0.5	9x10 <sup>-5</sup>	1	1.13x10 <sup>-3</sup>	3.3
90.0	0.1	0.73	0.5	9x10 <sup>-5</sup>	1	1.34x10 <sup>-3</sup>	0.6
109.8	0.1	0.89	0.5	9x10 <sup>-5</sup>	1	6.33x10 <sup>-3</sup>	1.8

**Table A.6** Experimental Vapour Pressure of Canola I25 Oil Biodiesel

<b>T [°C]</b>	<b>T<sub>uncer</sub>[°C]</b>	<b>P<sub>Raw</sub> [kPa]</b>	<b>r<sub>Mol</sub> [nm]</b>	<b>P<sub>Tran</sub></b>	<b>C<sub>T</sub></b>	<b>P<sub>Corr</sub> [kPa]</b>	<b>Uncer. [%]</b>
40.0	0.1	0.66	0.5	$8 \times 10^{-5}$	0.8	$2.26 \times 10^{-5}$	4.1
55.0	0.1	0.81	0.5	$8 \times 10^{-5}$	1	$1.43 \times 10^{-4}$	0.5
60.1	0.1	0.77	0.5	$8 \times 10^{-5}$	1	$1.98 \times 10^{-4}$	0.6
80.0	0.1	0.88	0.5	$9 \times 10^{-5}$	1	$1.04 \times 10^{-3}$	0.1
100.2	0.1	0.94	0.5	$9 \times 10^{-5}$	1	$4.35 \times 10^{-3}$	0.1

**Table A.7** Experimental Vapour Pressure of Canola CB Oil Biodiesel

<b>T [°C]</b>	<b>T<sub>uncer</sub>[°C]</b>	<b>P<sub>Raw</sub> [kPa]</b>	<b>r<sub>Mol</sub> [nm]</b>	<b>P<sub>Tran</sub></b>	<b>C<sub>T</sub></b>	<b>P<sub>Corr</sub> [kPa]</b>	<b>Uncer. [%]</b>
96.7	0.1	0.83	0.5	$9 \times 10^{-5}$	1	$2.88 \times 10^{-3}$	0.4
122.3	0.1	1.29	0.5	$1 \times 10^{-4}$	1	$1.46 \times 10^{-2}$	4.0
142.7	0.1	3.68	0.5	$1 \times 10^{-4}$	1	$5.05 \times 10^{-2}$	5.9
148.8	0.1	5.67	0.5	$1 \times 10^{-4}$	1	$8.03 \times 10^{-2}$	2.4
169.6	0.1	22.12	0.5	$1 \times 10^{-4}$	1	$3.27 \times 10^{-1}$	16.8
195.5	0.1	53.25	0.5	$1 \times 10^{-4}$	1	$7.94 \times 10^{-1}$	50.1

**Table A.8** Experimental Vapour Pressure of Soy S-B100 Oil Biodiesel

<b>T [°C]</b>	<b>T<sub>uncer</sub>[°C]</b>	<b>P<sub>Raw</sub> [kPa]</b>	<b>r<sub>Mol</sub> [nm]</b>	<b>P<sub>Tran</sub></b>	<b>C<sub>T</sub></b>	<b>P<sub>Corr</sub> [kPa]</b>	<b>Uncer. [%]</b>
39.9	0.1	0.41	0.5	$8 \times 10^{-5}$	0.8	$1.07 \times 10^{-5}$	5.0
59.8	0.1	0.46	0.5	$8 \times 10^{-5}$	0.8	$8.44 \times 10^{-5}$	1.0
70.1	0.1	0.52	0.5	$8 \times 10^{-5}$	1	$2.18 \times 10^{-4}$	1.6
90.0	0.1	1.46	0.5	$9 \times 10^{-5}$	1	$4.70 \times 10^{-3}$	12.8
100.0	0.1	1.08	0.5	$9 \times 10^{-5}$	1	$5.95 \times 10^{-3}$	0.7

**Table A.9** Experimental Vapour Pressure of Soy MG-B100 Oil Biodiesel

<b>T [°C]</b>	<b>T<sub>uncer</sub>[°C]</b>	<b>P<sub>Raw</sub> [kPa]</b>	<b>r<sub>Mol</sub> [nm]</b>	<b>P<sub>Tran</sub></b>	<b>C<sub>T</sub></b>	<b>P<sub>Corr</sub> [kPa]</b>	<b>Uncer. [%]</b>
29.9	0.1	0.6	0.5	$8 \times 10^{-5}$	0.8	$1.35 \times 10^{-5}$	5.2
47.0	0.1	0.9	0.5	$8 \times 10^{-5}$	1	$1.00 \times 10^{-4}$	7.6
119.8	0.1	1.84	0.5	$9 \times 10^{-5}$	1	$2.29 \times 10^{-2}$	0.1
140.1	0.1	6.00	0.5	$1 \times 10^{-4}$	1	$8.52 \times 10^{-2}$	0.1

**Table A.10** Experimental Vapour Pressure of Coconut Oil Biodiesel

T [°C]	T <sub>uncer</sub> [°C]	P <sub>Raw</sub> [kPa]	r <sub>Mol</sub> [nm]	P <sub>Tran</sub>	C <sub>T</sub>	P <sub>Corr</sub> [kPa]	Uncer. [%]
50.0	0.1	5.18	0.6	8x10 <sup>-5</sup>	1	7.29x10 <sup>-2</sup>	17.7
50.1	0.1	5.50	0.6	9x10 <sup>-5</sup>	1	7.77x10 <sup>-2</sup>	12.3
70.1	0.1	20.25	0.6	9x10 <sup>-5</sup>	1	2.99x10 <sup>-1</sup>	26.0
95.0	0.1	45.78	0.6	8x10 <sup>-5</sup>	1	6.82x10 <sup>-1</sup>	2.4
105.0	0.1	65.65	0.6	9x10 <sup>-5</sup>	1	9.80x10 <sup>-1</sup>	5.2
119.1	0.1	102.98	0.6	9x10 <sup>-5</sup>	1	1.54x10 <sup>0</sup>	10.9
124.8	0.1	156.32	0.6	9x10 <sup>-5</sup>	1	2.34x10 <sup>0</sup>	9.8

### A2.3 Biodiesel Heat Capacity

Figure A.5 shows the heat flows from the differential scanner calorimeter as a function of temperature of different biodiesels samples. The cloud point of the different biodiesels is also shown (Section 5.2). Tables A.12 to A.20 show experimental liquid heat capacity data for the eight (8) biodiesels studied.

**Table A.11** Liquid heat capacity of Canola CB-01 biodiesel

T[°C]	C <sub>p</sub> [kJ/kmol.K]	T[°C]	C <sub>p</sub> [kJ/kmol.K]	T[°C]	C <sub>p</sub> [kJ/kmol.K]
11.99	598.90	27.04	620.50	42.09	648.16
14.14	600.61	29.19	625.06	44.24	652.19
16.29	604.40	31.34	628.75	46.39	656.81
18.44	606.16	33.49	631.93	48.53	661.03
20.59	610.05	35.64	635.63	50.69	665.69
22.74	612.95	37.79	640.29	52.83	670.17
24.89	616.44	39.94	643.84	54.99	675.33

**Table A.12** Liquid heat capacity of Canola I25 biodiesel

T[°C]	C <sub>p</sub> [kJ/kmol.K]	T[°C]	C <sub>p</sub> [kJ/kmol.K]	T[°C]	C <sub>p</sub> [kJ/kmol.K]
12.98	605.95	27.70	628.05	42.40	666.02
15.08	608.08	29.80	632.87	44.50	672.37

17.18	609.66	31.90	637.85	46.60	678.72
19.28	613.05	34.00	642.36	48.70	685.47
21.40	615.94	36.10	648.39	50.80	691.96
23.48	619.47	38.20	654.15	52.90	699.19
25.58	623.41	40.30	659.82	54.99	707.05

**Table A.13** Liquid heat capacity of Soy MG-B100 biodiesel

T[°C]	Cp [kJ/kmol.K]	T[°C]	Cp [kJ/kmol.K]	T[°C]	Cp [kJ/kmol.K]
9.99	628.13	25.74	632.32	41.49	638.58
12.24	627.44	27.99	633.77	43.74	638.98
14.49	628.16	30.24	633.94	45.99	640.45
16.74	628.32	32.49	635.97	48.24	641.29
18.99	629.45	34.74	636.29	50.49	642.83
21.24	630.70	36.99	637.16	52.74	645.27
23.49	631.11	39.24	637.78	54.99	647.81

**Table A.14** Liquid heat capacity of Soy S-B100 biodiesel

T[°C]	Cp [kJ/kmol.K]	T[°C]	Cp [kJ/kmol.K]	T[°C]	Cp [kJ/kmol.K]
13.99	606.03	28.35	618.91	42.70	638.26
16.03	607.27	30.38	621.69	44.75	642.03
18.08	608.90	32.45	624.82	46.80	645.51
20.14	610.41	34.50	627.36	48.85	647.65
22.18	611.71	36.55	629.62	50.90	650.12
24.23	613.96	38.60	632.53	52.95	653.06
26.30	616.83	40.65	635.14	55.00	655.90

**Table A.15** Liquid heat capacity of Rapeseed biodiesel S090824

T[°C]	Cp [kJ/kmol.K]	T[°C]	Cp [kJ/kmol.K]	T[°C]	Cp [kJ/kmol.K]
13.99	652.27	28.35	667.27	42.70	686.10
16.03	653.56	30.38	669.29	44.75	689.47

18.08	656.44	32.45	671.83	46.80	693.38
20.14	658.16	34.50	674.66	48.85	697.27
22.18	660.03	36.55	676.99	50.90	701.04
24.23	662.29	38.60	679.80	52.95	704.87
26.30	664.27	40.65	683.12	55.00	709.13

**Table A.16** Liquid heat capacity of Palm biodiesel S102550

T[°C]	Cp [kJ/kmol.K]	T[°C]	Cp [kJ/kmol.K]	T[°C]	Cp [kJ/kmol.K]
23.99	590.86	34.84	610.28	45.70	631.69
25.54	591.72	36.39	615.18	47.24	637.60
27.09	597.10	37.95	617.06	48.78	637.30
28.64	595.18	39.50	619.03	50.33	643.63
30.19	598.47	41.05	621.24	51.89	649.20
31.74	603.81	42.59	624.77	53.43	652.55
33.30	606.09	44.13	629.30	54.99	657.79

**Table A.17** Liquid heat capacity of Coconut biodiesel S102550

T[°C]	Cp [kJ/kmol.K]	T[°C]	Cp [kJ/kmol.K]	T[°C]	Cp [kJ/kmol.K]
9.99	440.27	25.75	450.98	41.50	460.33
12.23	441.27	28.00	451.31	43.75	461.64
14.48	442.99	30.24	452.17	46.00	463.75
16.75	445.09	32.49	454.09	48.25	466.21
18.98	448.36	34.75	454.86	50.50	468.56
21.23	448.11	37.00	456.58	52.75	469.89
23.49	448.83	39.23	457.84	55.00	471.36

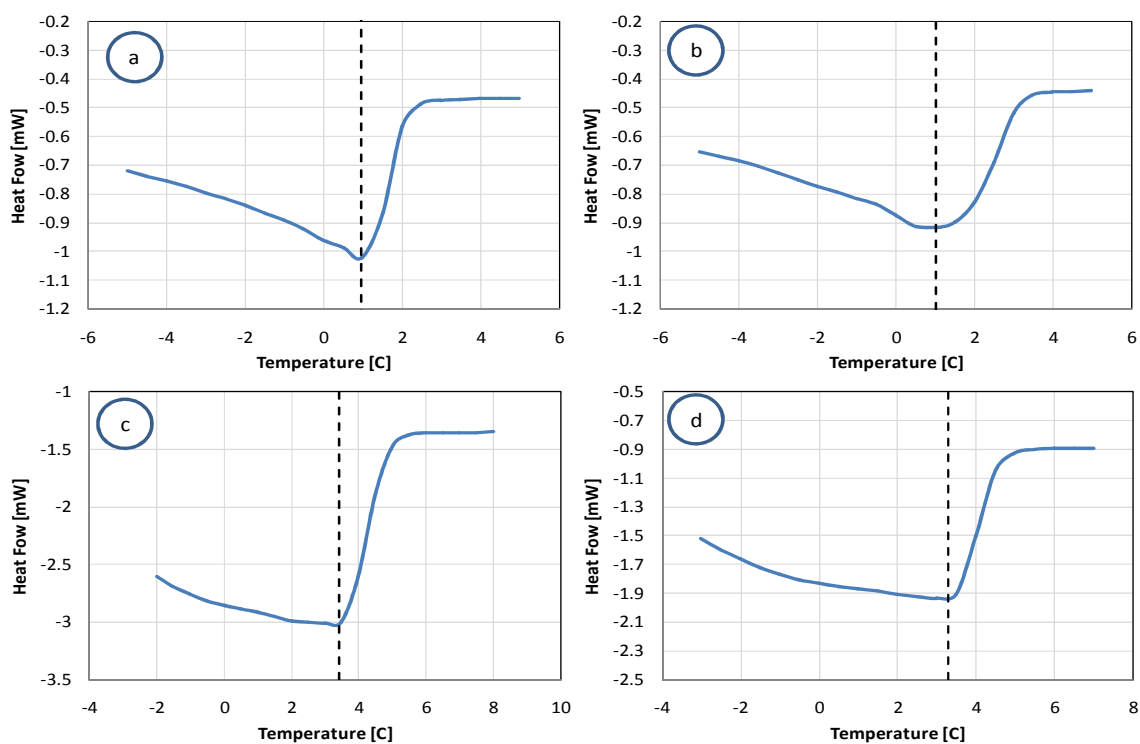


**Figure A.4a** Heat flow for different biodiesels: a) CB01 Canola, b) I25 Canola, c) MG-B100 Soy, d) S-B100 Soy

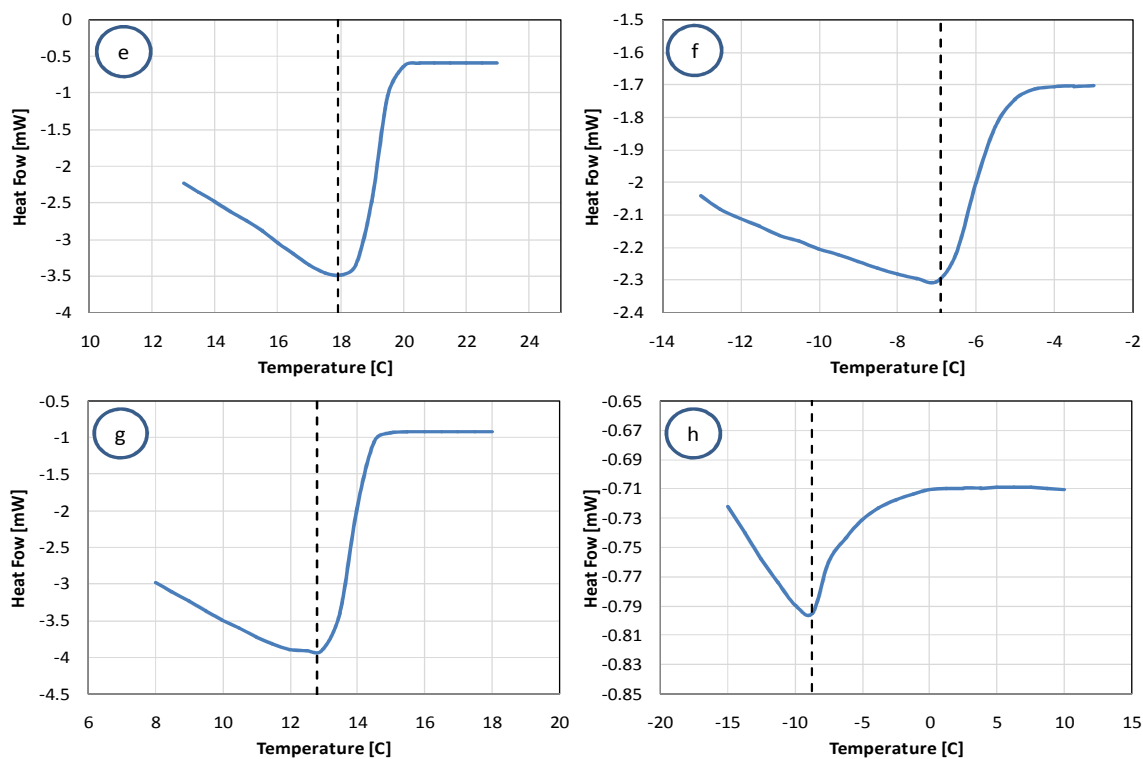


**Figure A.5b** Heat flow for different biodiesels: e) S080824 Palm, f) S071707 Coconut, g) Sylfat9014 Tallow, h) I26 Tallow

### A3. Western Canadian Bitumen

Western Canadian bitumen experimental data comprises high vacuum distillation, vapour pressure of heavy oil and fractions, and liquid heat capacity of Peace River maltenes. The distillation data section is complemented with two Spinning Band Distillation experiments (data provided by Sanchez [2011] and Simulated Distillation data [Mehrotra et al., 2005])

#### A3.1 Distillation and SimDist

**Table A.18** Experimental High Vacuum Distillation Data for WC-B1 Maltenes

<b>T</b> [°C]	<b>Distilled</b> Bitumen wt%	<b>Distilled</b> Maltenes wt%	<b>T</b> [°C]	<b>Distilled</b> Bitumen wt%	<b>Distilled</b> Maltenes wt%
150	9.9	12.0	220	29.7	35.8
150	10.4	12.5	260	46.4	55.9
180	20.7	25.0	290	56.9	68.5
190	22.7	27.4			

**Table A.19** Experimental SBD Data for WC-B1 Maltenes  
[Data provided by Sanchez [2011]]

<b>T</b> [°C]	<b>Distilled</b> Bitumen wt%	<b>Distilled</b> Maltenes wt%	<b>T</b> [°C]	<b>Distilled</b> Bitumen wt%	<b>Distilled</b> Maltenes wt%
202.6	0.6	0.7	300.0	10.0	12.1
210.8	1.2	1.4	308.1	11.0	13.2
218.9	1.7	2.1	316.2	12.0	14.5
227.0	2.3	2.8	324.4	13.3	16.0
235.2	2.9	3.5	332.4	14.8	17.8
243.3	3.7	4.5	340.3	16.0	19.3
251.3	4.4	5.3	348.7	17.2	20.7
259.4	5.1	6.2	356.6	18.5	22.3
267.8	6.0	7.3	364.8	19.8	23.8
275.7	7.1	8.6	373.3	21.4	25.8

283.7	8.2	9.8	380.5	23.3	28.1
291.7	9.1	11.0			

**Table A.20** Experimental SimDist Data for WC-B1 Maltenes

<b>T</b> [°C]	<b>Distilled</b> Bitumen wt%	<b>Distilled</b> Maltenes wt%	<b>T</b> [°C]	<b>Distilled</b> Bitumen wt%	<b>Distilled</b> Maltenes wt%
185.0	0.01	0.01	407.0	20.8	25.0
262.0	4.2	5.0	440.0	24.9	30.0
304.5	8.3	10.0	472.0	29.1	35.0
340.5	12.5	15.0	504.0	33.2	40.0
372.5	16.6	20.0	531.5	36.5	44.0

**A3.2 Vapour Pressure****Table A.21** Experimental Vapour Pressure of WC-B1 Bitumen

<b>T [°C]</b>	<b>T<sub>uncer</sub>[°C]</b>	<b>P<sub>Raw</sub> [kPa]</b>	<b>r<sub>Mol</sub> [nm]</b>	<b>P<sub>Tran</sub></b>	<b>C<sub>T</sub></b>	<b>P<sub>Corr</sub> [kPa]</b>	<b>Uncer. [%]</b>
40.9	0.1	1.00	0.6	$5 \times 10^{-5}$	1	$5.34 \times 10^{-3}$	0.2
60.6	0.1	1.70	0.6	$5 \times 10^{-5}$	1	$2.08 \times 10^{-2}$	0.5
79.5	0.1	4.50	0.6	$6 \times 10^{-5}$	1	$6.27 \times 10^{-2}$	0.4

**Table A.22** Experimental Vapour Pressure of WC-B1 Maltenes

<b>T [°C]</b>	<b>T<sub>uncer</sub>[°C]</b>	<b>P<sub>Raw</sub> [kPa]</b>	<b>r<sub>Mol</sub> [nm]</b>	<b>P<sub>Tran</sub></b>	<b>C<sub>T</sub></b>	<b>P<sub>Corr</sub> [kPa]</b>	<b>Uncer. [%]</b>
30.3	0.1	0.83	0.6	$5 \times 10^{-5}$	1	$1.79 \times 10^{-3}$	2.1
39.9	0.1	0.87	0.6	$5 \times 10^{-5}$	1	$4.06 \times 10^{-3}$	0.2
40.1	0.1	0.91	0.6	$5 \times 10^{-5}$	1	$4.41 \times 10^{-3}$	1.0
46.0	0.1	0.92	0.6	$5 \times 10^{-5}$	1	$6.83 \times 10^{-3}$	1.7
59.7	0.1	1.36	0.6	$5 \times 10^{-5}$	1	$1.56 \times 10^{-2}$	0.3
60.1	0.1	1.42	0.6	$5 \times 10^{-5}$	1	$1.66 \times 10^{-2}$	1.2
61.0	0.1	1.44	0.6	$5 \times 10^{-5}$	1	$1.68 \times 10^{-2}$	0.2
79.4	0.1	3.62	0.6	$6 \times 10^{-5}$	1	$4.95 \times 10^{-2}$	0.1
80.0	0.1	3.66	0.6	$6 \times 10^{-5}$	1	$5.01 \times 10^{-2}$	0.6
80.4	0.1	2.77	0.6	$6 \times 10^{-5}$	1	$3.68 \times 10^{-2}$	10.4
100.0	0.1	9.52	0.6	$7 \times 10^{-5}$	1	$1.38 \times 10^{-1}$	2.7

**Table A.23** Experimental Vapour Pressure of WC-B1 85% wt Maltenes Residue

T [°C]	T <sub>uncer</sub> [°C]	P <sub>Raw</sub> [kPa]	r <sub>Mol</sub> [nm]	P <sub>Tran</sub>	C <sub>T</sub>	P <sub>Corr</sub> [kPa]	Uncer. [%].
40.9	0.1	1.74	0.7	4x10 <sup>-5</sup>	1	1.56x10 <sup>-4</sup>	0.9
60.5	0.1	1.31	0.7	4x10 <sup>-5</sup>	1	5.43x10 <sup>-4</sup>	0.7
80.2	0.1	1.16	0.7	4x10 <sup>-5</sup>	1	1.92x10 <sup>-3</sup>	0.4

**Table A.24** Experimental Vapour Pressure of WC-B1 78% wt Maltenes Residue

T [°C]	T <sub>uncer</sub> [°C]	P <sub>Raw</sub> [kPa]	r <sub>Mol</sub> [nm]	P <sub>Tran</sub>	C <sub>T</sub>	P <sub>Corr</sub> [kPa]	Uncer. [%].
60.0	0.1	2.08	0.7	4x10 <sup>-5</sup>	1	2.42x10 <sup>-4</sup>	0.5
80.0	0.1	1.81	0.7	4x10 <sup>-5</sup>	1	9.48x10 <sup>-4</sup>	1.0
95.0	0.1	1.48	0.7	5x10 <sup>-5</sup>	1	2.08x10 <sup>-3</sup>	0.1
110.1	0.1	1.26	0.7	5x10 <sup>-5</sup>	1	4.44x10 <sup>-3</sup>	0.3
125.1	0.1	1.11	0.7	5x10 <sup>-5</sup>	1	9.10x10 <sup>-3</sup>	0.5
159.8	0.1	3.10	0.7	5x10 <sup>-5</sup>	1	4.18x10 <sup>-2</sup>	0.2

### A3.3 *Liquid Heat Capacity*

Liquid heat capacity for Peace River maltenes was measured using a differential scanner calorimeter, analogue to the biodiesels, section A2.3

**Table A.25** Liquid heat capacity of WC-B1 maltenes

T[°C]	Cp [kJ/kmol.K]	T[°C]	Cp [kJ/kmol.K]	T[°C]	Cp [kJ/kmol.K]
-0.01	767.19	32.00	849.03	63.99	959.43
3.99	772.90	36.00	861.56	67.99	973.84
7.99	779.58	39.99	874.63	71.99	988.19
11.99	787.42	43.99	889.28	75.99	1001.97
16.00	799.67	47.99	901.77	79.99	1016.33
20.00	811.85	51.99	914.75		
24.00	825.02	55.99	929.69		

## **APPENDIX B: VAPOUR PRESSURE MEASUREMENT PROTOCOL**

The High Vacuum Vapour Pressure Measurement System, HV-VPMS, consists of two apparatuses: a degassing or sample preparation apparatus (DA) and a vapour pressure measurement apparatus (VPMA). The DA is used to prepare the sample for a faster and cleaner pressure measurement; it also can be used for primary fractionation of mixtures. The VPMA is used to measure vapour pressure and for secondary (deeper) vacuum fractionation. This appendix provides the necessary information and procedure steps for measurement of vapour pressure and fractionation of mixtures.

## TABLE OF CONTENTS

- B1. HV-VPMS Description
  - B1.1 Vapour Pressure Measurement Apparatus (VPMA)
  - B1.2 Degassing Apparatus (DA)
- B2. Assembling the HV-VPMS
  - B2.1 Cleaning Procedure for the Constituent Parts
  - B2.2 Assembling Procedure
- B3. Start Up
- B4. Apparatus Bake Out
- B5. Data Acquisition Set Up
- B6. Vapour Pressure Measurement
  - B6.1 Degassing
  - B6.2 Measurement
  - B6.3 Vapour Pressure Measurement Protocol
  - B6.4 Fractionation
- B.7 Data Processing
- B.8 Calibration Charts
- B.9 Leak Testing
- B.10 List of Parts
- References

### B1. HV-VPMS Description

The High Vacuum Vapour Pressure Measurement System, HV-VPMS, is shown in Figures B1. As can be seen, it comprises two different apparatuses, the VPMA (above) and the DA (below). Schematics of the individual parts of the apparatus can be found in Figures B2 and B9, respectively.



**Figure B.5** High Vacuum Vapour Pressure Measurement system (HV-VPMS); Vapour Pressure Measurement Apparatus VPMA (above) and Degassing Apparatus DA (below)

### *B1.1 Vapour Pressure Measurement Apparatus (VPMA)*

A schematic representation of the VPMA is shown in Figure B2. For a list of the different parts composing the VPMA, refer to Section B10

The VPMA contains a stainless steel (SS) Swagelok full nipple that is used as the sample vessel (S01) as shown in Figure B2 and B3. The nipple has ConFlat (CF) 133 fittings and has an approximate volume of 18 mL. The bottom part is sealed with a Swagelok CF133 blank and the upper part is connected to a VAT all metal angle valve Series 54 with a manual actuator. The combination of the sample vessel and the metal valve is known here forth as the sample chamber. Copper gaskets are used to seal the CF flanges and SS 8-32 x 0.75 in. bolts and nuts are used to tighten them.

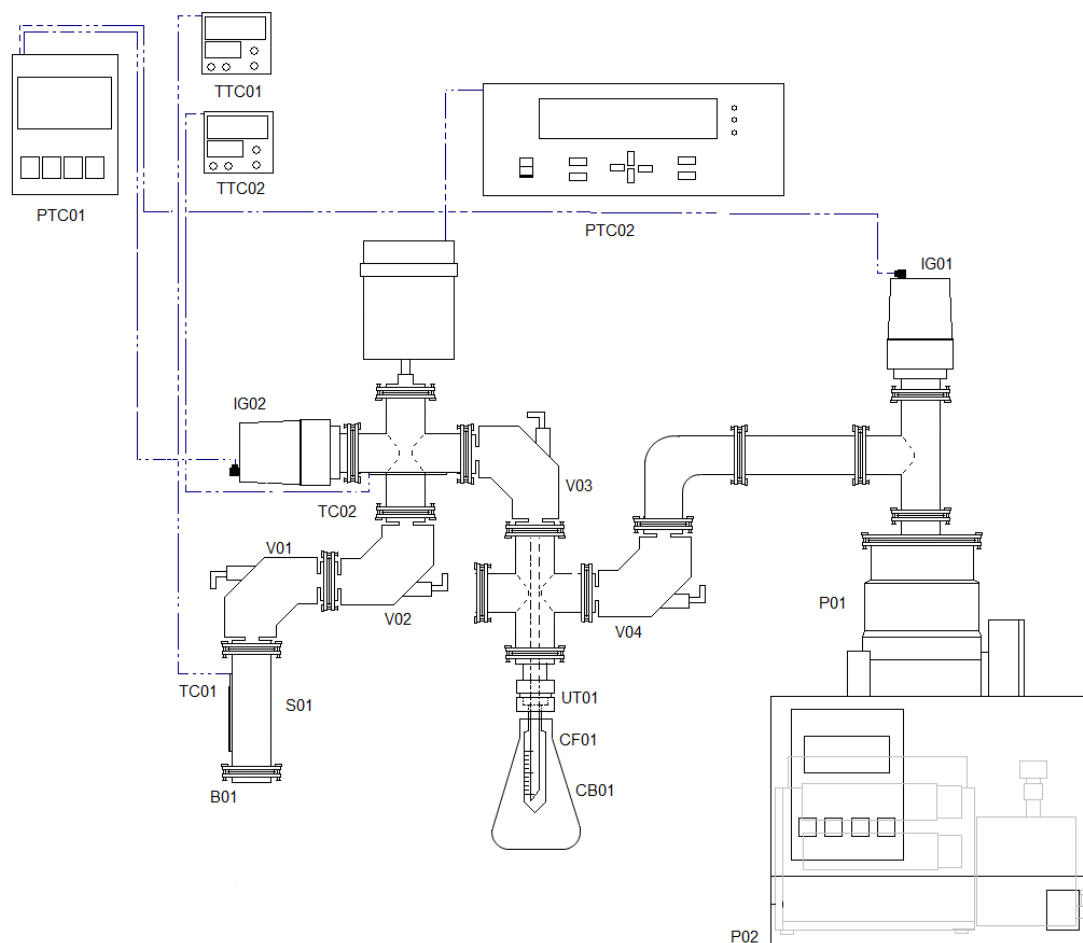


**Figure B6** Vapour Pressure Measurement Apparatus (VPMA). S01: sample vessel; V01 : all metal angle valve; TC01: J-Type Thermo couple; RTD01: RTD transducer; UT01: Swagelok UltraTorr fitting; CF01 : Pirex Cold Finger; IG01: Combined Pirani-Cold Cathode Ion Pressure Gauge; DG01: Diaphragm Pressure Gauge; PTC01: Pressure Transducer/Read Out; TTC01: Temperature Transducer/Controller; P01: Turbomolecular Pump; P02: Backing Diaphragm Pump

The sample chamber is connected to the rest of the VPMA through another VAT angle valve. The different sections of the apparatus are connected using stainless steel CF133 flanges, T's, elbows, and crosses, and are sealed with copper gaskets, specified to hold pressures down to  $1 \times 10^{-12}$  kPa. The VAT all-metal angle valves are used for isolation throughout the VPMA.

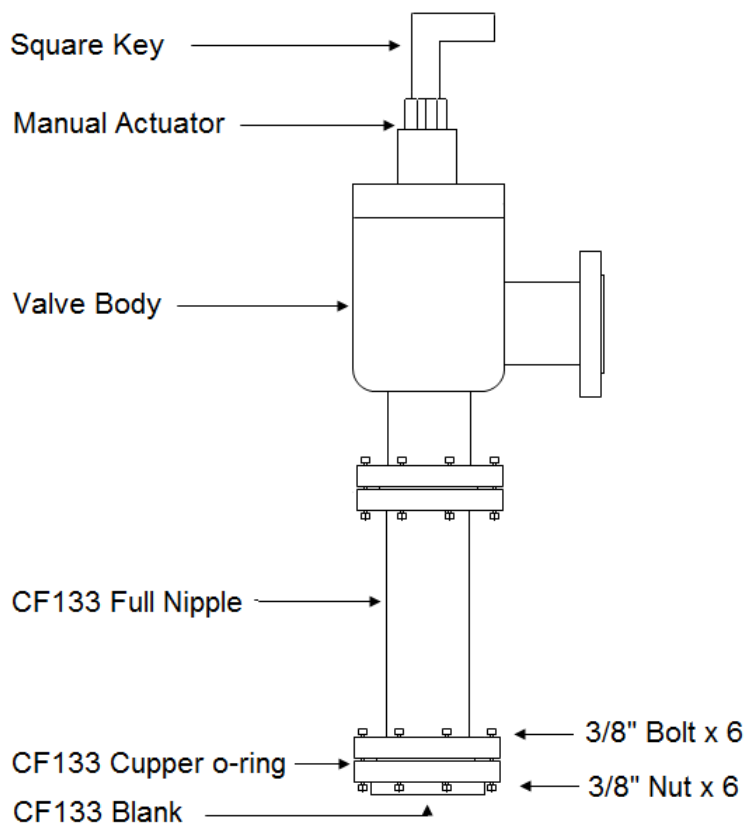


**Figure B7** Sample Chamber Schematic

The pressure on the sample chamber can be measured by two different gauges. First, an Inficon capacitance diaphragm gauge provided by CAPT (DG01 in Figure B2, and Figure B4), temperature controlled at 200 °C with a pressure range of 1 –  $1 \times 10^{-4}$  kPa and accuracy of 0.15%, given by the manufacturer. Pressure is displayed by a MKS PR4000 (PTC02) which has five significant figures, three decimal places.

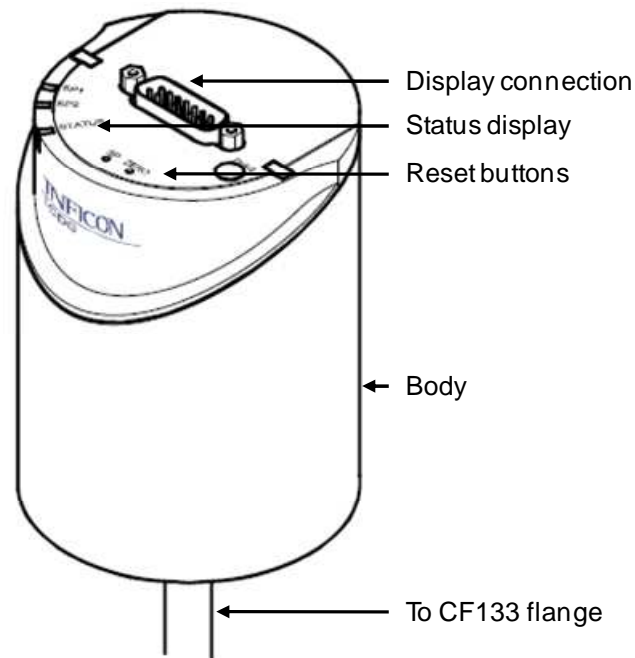


**Figure B8** Schematics of the Inficon diaphragm gauge (modified from Inficon [2008])

The second gauge is a Pfeiffer Compact FullRange™ Pirani-Cold Cathode gauge (IG02 in Figure B2, and Figure B5) with a pressure range of  $100 - 5 \times 10^{-7}$  kPa and an accuracy of 30% of the reading giving by the manufacturer. This gauge only works at temperatures below 60 °C. Pressure is displayed through a Pfeiffer DualGauge™ TPG262. The apparatus may work only with the DG01 by replacing the IG02 with a CF133 blank or by removing the electronic body of the IG02 (refer to Pfeiffer Vacuum, 2008, for detailed instructions in how to dismantle IG02).

Readouts of both DG01 and IG02 pressure gauges are converted on a digital file with LabView 8.6 © and can be obtained on an Excel file.

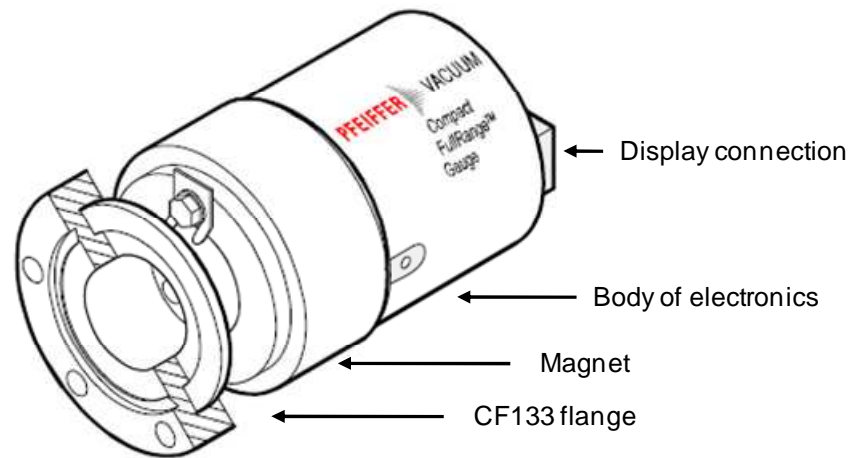


**Figure B9** Schematics of the Pfeiffer Compact FullRange™ gauge (modified from Pfeiffer Vacuum [2008])

Vacuum is provided by a Pfeiffer pumping station HiCube 80 Eco (P02 in Figure B2, and Figure B6), comprised by a HiPace 80 turbo-molecular pump which is backed up by a MVP 015-2 diaphragm pump. Start up, display and general control is provided by a DCU002 display and control unit which is included on the station. The pumping system is capable of reach a final pressure of  $1 \times 10^{-10}$  kPa based on manufacturer specification at a rate of 60 L/s, nitrogen.

The available vacuum provided by the system is monitored by a Pfeiffer Compact FullRange™ pressure gauge with KF flanges (rubber gaskets), IG01. The connection from the pump suction point to the gauge is shown in Figure B7. Note that if a CF FullRange™ gauge is available, the rubber gasket and CF-KF adapter is not required.

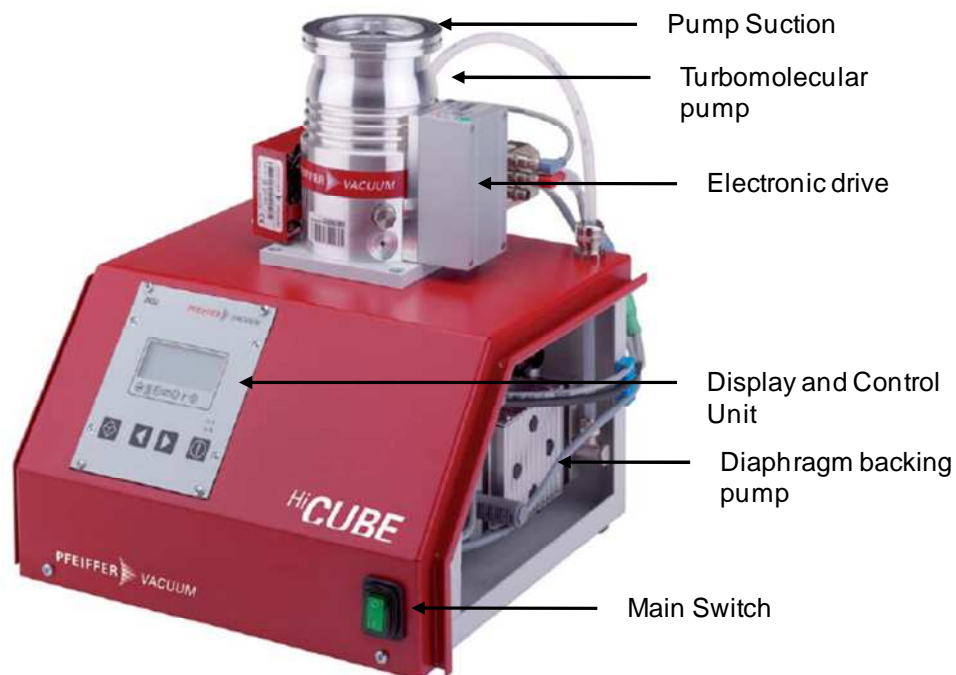


**Figure B10** Picture of the Pfeiffer HiCube 80 pumping station (modified from Pfeiffer Vacuum [2009])

The temperature of the system is controlled using Watlow SD displays auto-tuned on PID mode, coupled with J-Type thermo-couples, with a 0.1 C resolution. Heat is provided by electrical heat tape from ColePalmer. The VPMA has an operating temperature range from atmospheric temperature to 200 °C with the diaphragm gauge on, and up to 500 °C with no electronics.

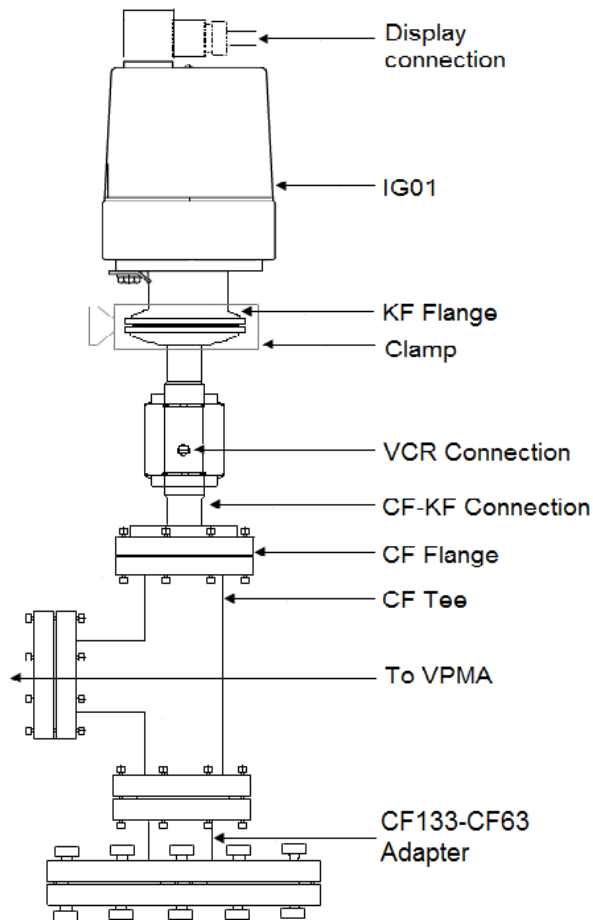


**Figure B11** Connection schematics from the pump station suction point to the Cold cathode-Pirani gauge with KF flanges

For fraction sample recollection, a custom made cold finger is used (Figure B8). It comprises a modified Pirex centrifugal tube with a 1/4" end, a modified CF133 cross with a 3/8" concentric tube silver soldered. The Pirex tube is fit to the cross via a 1/4" UltraTorr fitting by Swageok. The cold finger is submerged on an oil bath (500 mL Kimax Erlenmeyer with hydraulic oil – Figure B2, CB01) cool down with small pieces of dry ice (note that ice water can also be used to cool down the cold finger).

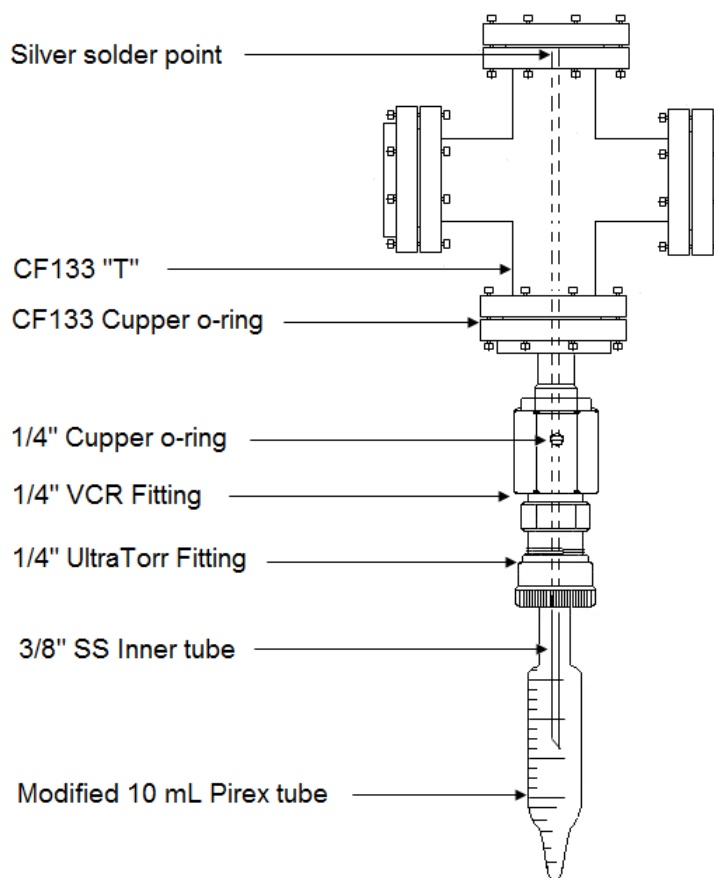


**Figure B12** Cold Finger schematic

### *D1.2 Degassing Apparatus (DA)*

The DA is shown in Figure B9. The DA contains a sample vessel (S02) analogue to S01, Figure B2. The vessel S02 is connected to a VAT all-metal angle valve. As with the VPMA, this is called the sample chamber as it is interchangeable with S01.

The pressure on the sample chamber is measured by a MKS Baratron 631B diaphragm gauge (DG02) with a pressure range of  $1 - 1 \times 10^{-3}$  kPa and accuracy of 0.5% of the reading giving by the manufacturer. Pressure is displayed by a MKS PR4000F display

(PTC02) (similar to Figure B4). Pressure readout is converted on digital file with LabView 8.6 ©

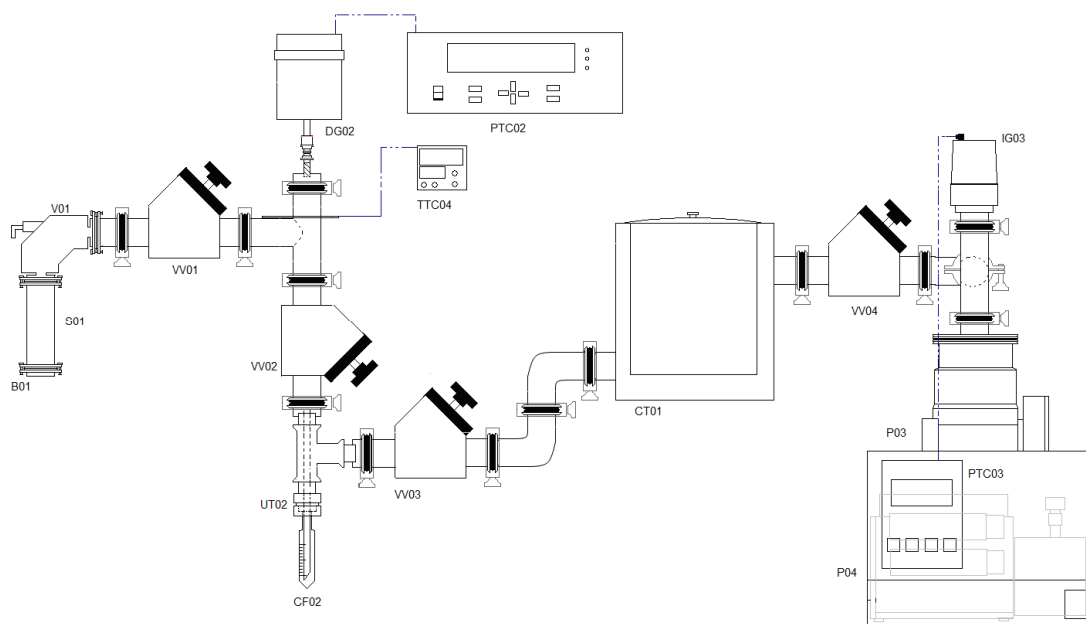


**Figure B13** Degassing Apparatus (DA): S01: sample vessel; V01: all metal angle valve; VV01: Viton sealed valve; UT02: UltraTorr fitting; CF02: Pirax cold finger; CT01: cold trap; IG03: Pirani-Cold Cathode ion gauge; DG02: diaphragm gauge; PTC02: pressure transducer /display for diaphragm gauge; TTC04: temperature transducer/controller; PTC03: pressure display for ion gauge; P03: turbo-molecular pump; P04: diaphragm pump

Vacuum is provided by Pfeiffer pumping station model TSH 071 E analogue to the HiCube 80 Eco pumping station used for the VPMA. The pump is protected against condensation by a LACO 3.5 quart 304 SS cold trap (CT01) operated with dry ice.

The different sections of the DA are connected using NW25 KF flanges, tees, and elbows, and are sealed with Viton o-rings, specified to hold pressures down to  $1 \times 10^{-6}$  kPa.

VAT Viton sealed on-line valves are used for isolation throughout the DA.

The temperature of the system is controlled using Watlow SD displays auto-tuned on PID mode, coupled with a J-Type thermo-couple, with a 0.1 C resolution. Heat is provided by electrical heat tape from ColePalmer. The DA has a temperature range from atmospheric temperature to 150°C. The apparatus can be baked out at temperatures around 200 °C subject to the maximum allowable temperature for Viton rubber (close to 220 °C).

For fraction sample collection a custom made cold finger is used (Figure B10). It comprises a modified Pirex centrifugal tube with a ¼” end, a modified NW25 KF “T” with a 3/8” welded concentric tube. The Pirex tube is fit to the cross via a ¼” UltraTorr fitting by Swageok. The cold finger is submerged on an oil bath (250 mL Kimax Erlenmeyer with hydraulic oil) cool down with dry ice.

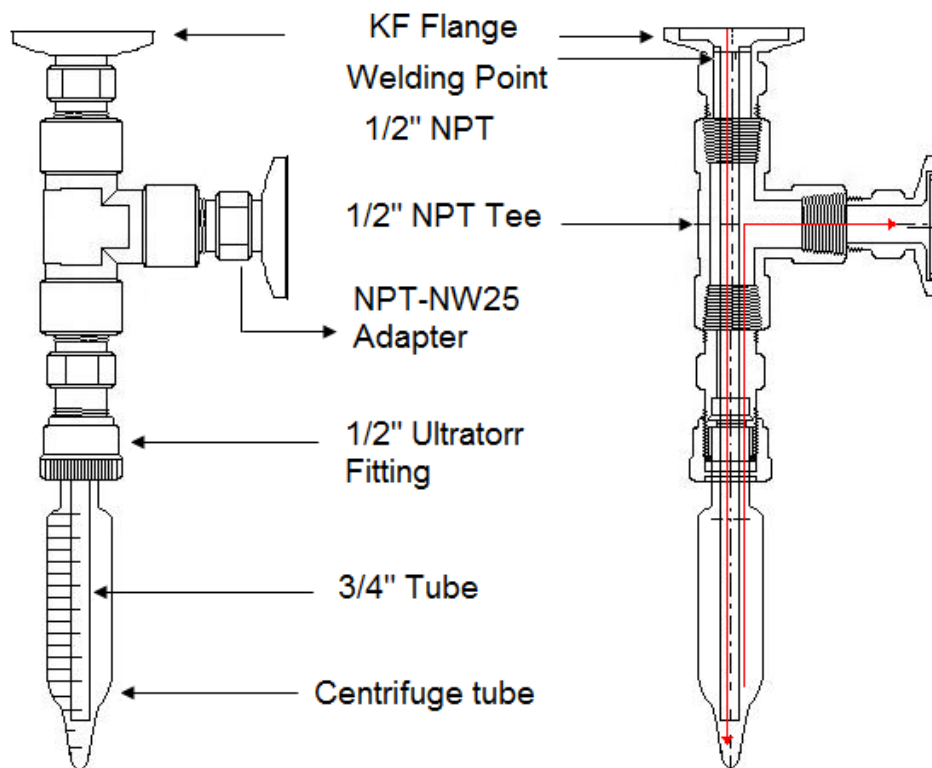


**Figure B14** DA Cold Finger schematic

## **B2 Assembling the HV-VPMS**

The HV-VPMS can be assemble and disassemble for inspection, cleaning, maintenance, leak testing, or replacement of parts. Sections B2.1 and B2.2 provide instructions in this regard. Always use powderless rubber gloves when manipulating the parts of the apparatus and when the inner surface of these is exposed. This will prevent natural oils in the hands to stick on the inner surface of the apparatus, reducing the ultimate pressure of the system.

### *B2.1 Cleaning Procedure for the Constituent Parts*

Clean the inner surfaces of the different sections of the apparatus before assembling. To do so:

- Use a cotton q-tip soaked with a convenient solvent (in most cases toluene works whenever organic compounds are being assessed) to scrub and clean the inner surface of the constituents
- Clean out the heavy solvent and cotton fibre remnants by washing out the part with a lighter solvent such as iso-propanol or acetone
- Dry the parts by blowing pressurized air or fume hood vacuum
- For the metal parts, bake out the parts at temperatures above 150 °C on a temperature controlled oven with vacuum, for at least 24 hours
- When the part is being exposed to ambient air, use a convenient lid to isolate them if the exposure time is short; otherwise use a zip lock bag to isolate the part
- To clean Ion Gauge internals, follow Section 5.2 of the BG 805 155 BE/C Pfeiffer manual [Pfeiffer Vacuum, 2008]

### *B2.2 Assembling Procedure*

The following procedure applies to the assembly of both apparatuses (VPMA and DA).

Different insights for each of the apparatuses are included whenever necessary:

- Put on powderless latex gloves to avoid natural oil contamination
- For the first part of the assembly, start from the sample vessel towards the pumping station (S01 or S02, Figures B2 or B9)

- Attach the different piping constituents (valves, tees, crosses, etc.) using copper o-rings CUCF133 for the VPMA. It is easier to do this assembly on a horizontal plane (a table). Put any two parts together with the metal o-ring and adjust bolts and nuts finger tight. Follow the same procedure with the DA, using Viton o-rings and metal clamps instead
- Install the different pressure gauges on a similar manner. Do not connect electronics to the read out
- Follow the above procedure all the way up to the UltraTorr fitting, UT01 and UT02 in Figures B2 and B9 for the VPMA and DA, respectively
- While on the horizontal plane, tighten the fittings. Make sure that the appropriate 3D direction is achieved on the whole assembly. To tighten KF flanges, finger-tighten the clamps; DO NOT use any mechanical leverage to tighten the clamps.

To tighten CF Flanges, it is recommended to tighten the bolts in the order shown in Figure B11; thus, a uniform pressure is applied on the metal o-ring, mitigating leaks

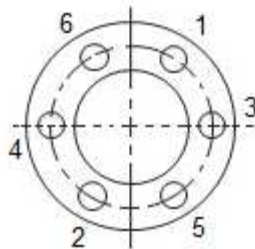


**Figure B15** ConFlat (CF) Flange Schematic- Recommended tighten up order

- Start the second part of the assembly from the pumping station towards the UltraTorr fitting
- Attach the different piping constituents (valves, tees, crosses, etc.) using copper o-rings CUCF133 for the VPMA and Viton o-rings for the DA. In this case, work on the working platform shown in Figure B1 or in the platform at which the apparatus will be parked. Connect all parts up to V04 for VPMA (Figure B2) and VV03 in DA (Figure B9). Tighten all connections up
- Connect both assemblies. The parts put together on the horizontal plane are heavy. It is recommended to install them with the help of another person
- Connect pressure gauges to their respective read out devices
- Install Pirex cold fingers to the UltraTorr connection. Make sure to tighten fittings properly, having in mind that by applying the wrong torque you can easily break the Pirex tube
- Install thermo couples to the apparatus. Use metal clamps to fix the devices to the pipes of the apparatus. Tighten the clamps taking care of not breaking the devices
- Wrap the pipes with the heat tape. Heat tape number 1 (HT01; 2 feet long) should wrap S01; HT02 (4 feet long) should go around the upper VPMA system (from V01 to V03) and HT03 (4 ft long) goes around most of the DA apparatus. Make sure you do not overlap heat tapes and that most of it lays in contact with metal
- Wrap the pipes with insulation tape. Make sure all heat tape surfaces are covered with the insulation tape. Use the insulation to tighten heat tape to the metal parts
- Submerge both Pirex tubes on an oil bath

### B3 Start Up

The following procedure can be used to start up the HV-VPMS. In essence, the procedure is analogue and equally applicable to the VPMA and DA systems:

- Turn on pressure readout devices. It will take between 10 to 20 minutes for the ion gauges to stabilize and about 2 hours for the diaphragm gauges to stabilize
- Turn pumps on (both Main Switch on and Display and Control unit DCU002, Figure B6). Follow the signals displayed on the DCU002 (Figure B12)

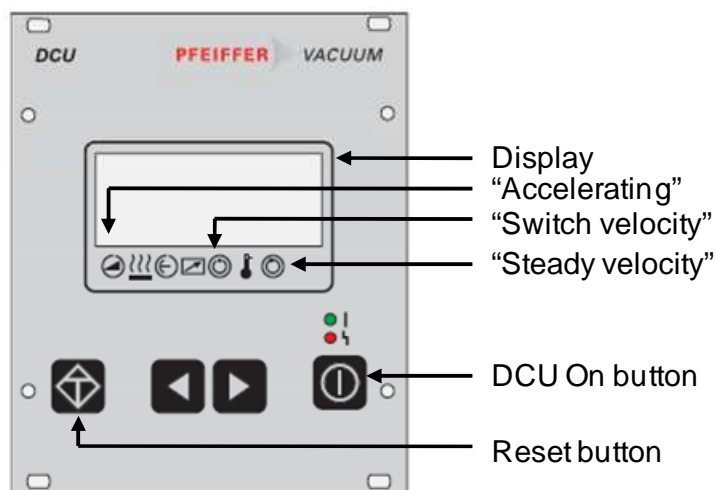


**Figure B16** DCU display and main constituents (modified from Pfeiffer [2004])

The “Accelerating” symbol should be displayed for about 10 to 20 minutes. Subsequently, the “Switch velocity” symbol should appear meaning that the molecular density inside the pump suction is low enough to turn the turbo pump on (automatically). This should last for about 2 minutes. Later on, the “Steady

velocity” symbol should appear. At the end of the pump turn on, the ‘Acceleratin” symbol should disappear

- Finally put dry ice in the cold trap and submerge some broken pellets on the oil baths. Be aware that initially foam may form inside the oil baths which makes the oil spill out of the Erlenmeyer. Submerge the bits carefully and wait till oil bath cools down a bit so you can put more bits more freely. Temperature on the oil bath should oscillate around 0 °C
- Temperature set up will depend on the procedure chosen, i.e., outgassing, pressure measurement, or fractionation

In case the turbo pump does not accelerate, it probably means that there is a major leak. You would need to disassemble the system and check for leaks (section B9). Less likely it can also mean that the diaphragms are wet. Please, refer to the PU 0012 BE/D operational manual for the diaphragm pump for instructions on how to replace the rubber diaphragms.

Gauges are pretty stable, but in case the gauges do not start up properly, please refer to their respective manuals [MKS, 2006; Pfeiffer, 2008; Inficon, 2008].

#### **B4 Apparatus Bake Out**

After the apparatus is assembled and before it is used, it needs to be baked out (outgassed). Note the time required cleaning and setting up the apparatus depends on how

clean the apparatus is; hence, by the incorporation of a separate degassing unit the outgassing time is significantly reduced (by 1 to 2 days work approximately).

While outgassing the VPMA, there is no need to keep dry ice on the system and you need to disconnect the electronics of IG01. With the pump running, increase the temperature of the TC02 (upper VPMA) to 200 °C and the TC01 to 190 °C. All of the valves should be open. Leave the system running for at least 48 hours. Use 150 °C for the outgassing of the DA.

Once the outgassing is finished, set TC01 to the initial temperature of the experiment, leave TC02 at 200°C, and set TC03 (DA apparatus) to 50°C. The system takes between 2 to 3 hours to reach steady state, depending on how well insulated it is.

To check if the outgassing procedure was successful, take pressure readings using LabView (section B5) for the open system (all valves open) and by closing different valves (V03, V04, and so on). If the recordings show a constant increase on the pressure, then a significant leak is present on the system and you need to check for leaks. If the system reached a higher pressure steady state in different runs (i.e. if you do the check out several times and every time the system reach a higher steady state) then the outgassing was incomplete and it needs to be done over again. Figure B13 shows the pressure profile of the system from atmospheric pressure to the ultimate pressure of the VPMA when the system was outgassed.

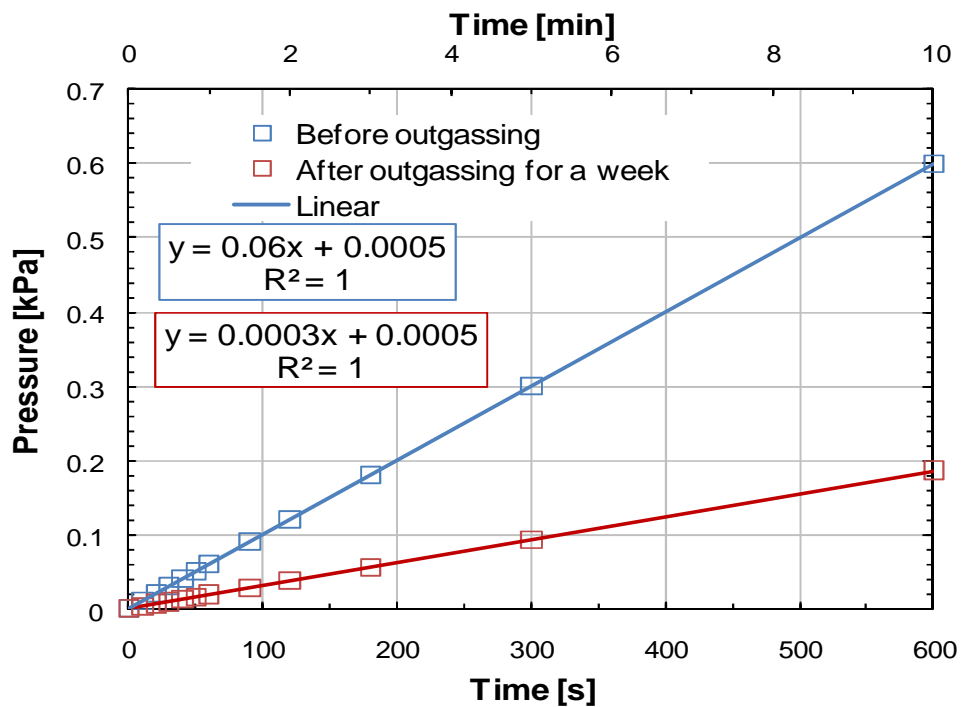


**Figure B17** Differences with non-outgassed and outgassed pressure profile

### B5 Data Acquisition Set Up

The following procedure can be followed to set up the data acquisition system:

- Double click the LabView shortcut on the desktop. LabView main window will open, Figure B14



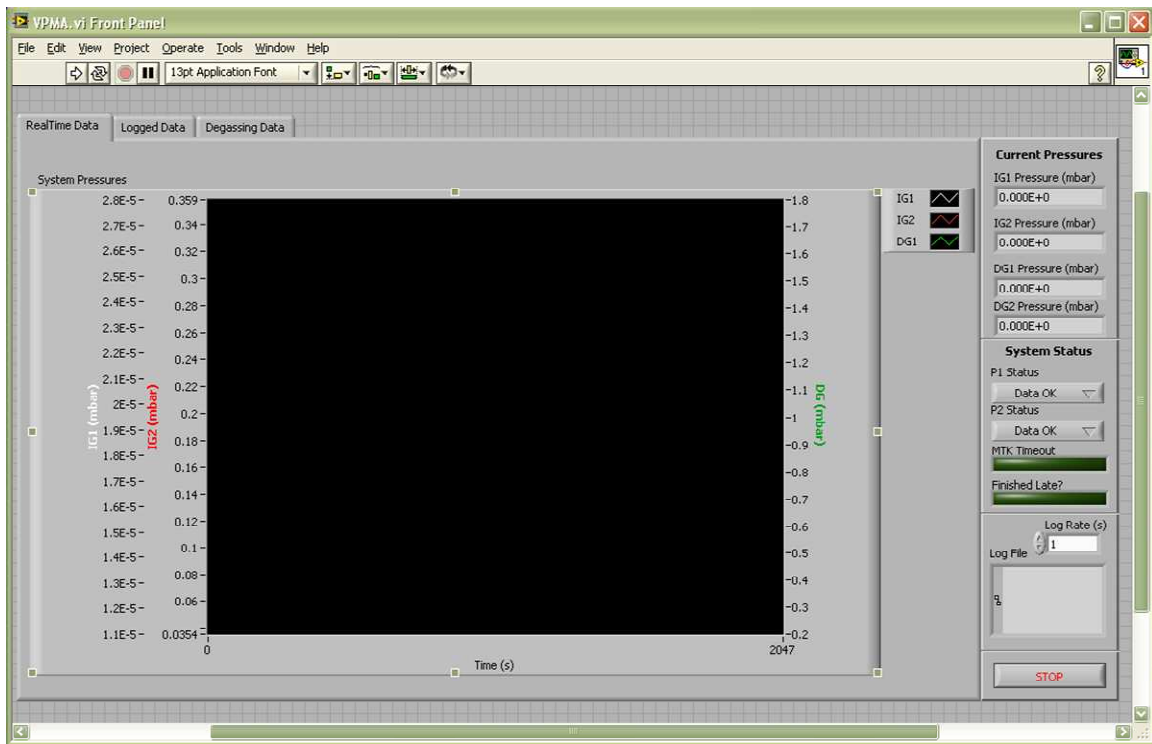


**Figure B18** LabView main window for HV-VPMS data acquisition

- Set the time frame as desired. Put the number of seconds per measurement in the “Log Rate” box in the low left corner of the main window, Figure B14, and hit Enter. For general pressure readings use 5 seconds; for more resolution, use 1 second (minimum value)
- Click on the “go” button . An “Open” window will open, Figure B15.

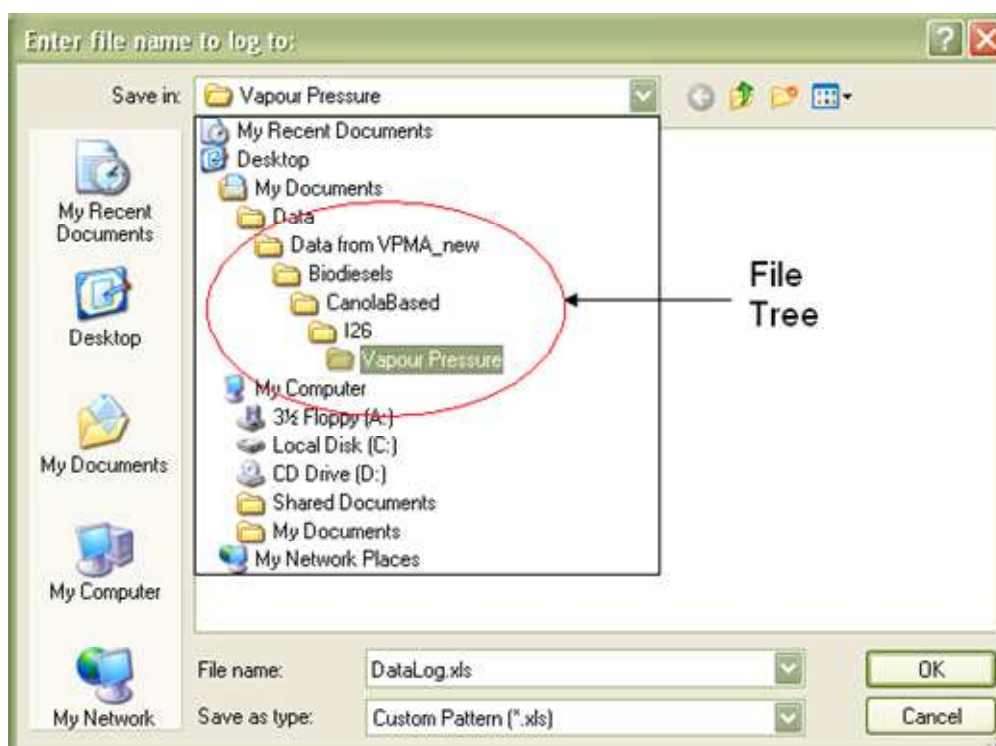


**Figure B19** LabView main window for saving files and the HV-VPMS “File Tree”

- Set up file destination and file name. Follow the ‘File Tree’ shown in Figure B15 and create an Excel file where the data is going to be logged. The name template generally used is:

Substance\_Temperature°C\_ddmmyy\_assaynumber

for instance, Hexadecane\_40°C\_101010\_01.xls

- Click on the “OK” button and you should be able to record data
- Adjust axis as desired or set them on auto-scale by right clicking the axis and choosing the autoscale option
- The data acquisition window contains three tabs, Figure B14. The first one is the real time data of IG01, IG02 and DG01 (Figures B2 and B9); the second tab is the

actual data that has been recorded of IG01, 02 and DG01 (depending on the log time selected); finally, the third tab shows the actual recorded data for DG02 (Figure B9)

## **B6 Vapour Pressure Measurement**

Once the system has been baked out, it is ready to be used. The degassing and vapour pressure measurement procedures followed by a proposed fractionation procedure is introduced as follows.

### *B6.1 Degassing*

The degassing apparatus is shown in Figure B9; however, for convenience sake, Figure B16 shows simplified schematics representation of the DA. Degassing can be performed using the VPMA as well but it would cause the impurities of the original sample to adhere on the inner walls of the apparatus. With the use of the DA, the VPMA remains clean. Based on Figure B16, the following procedure can be applied to degas a sample:

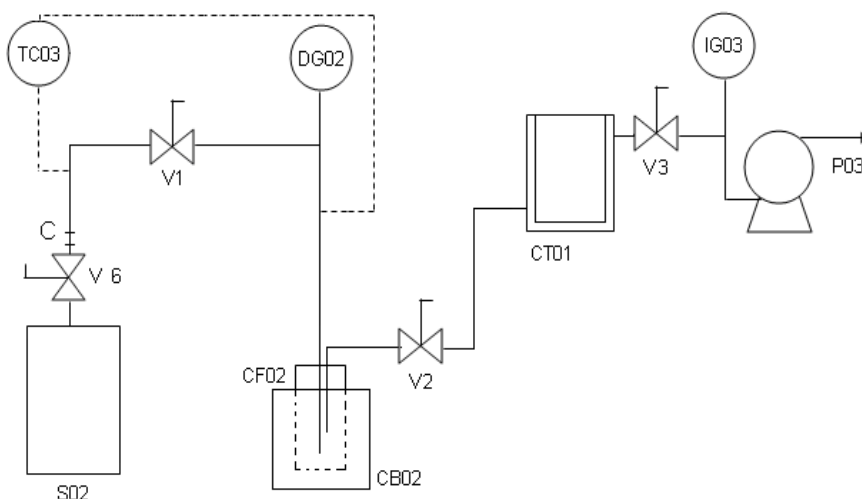


**Figure B20** DA simplified schematic

- Clean and bake out the sample chamber
- Pour the sample into the sample vessel by disconnecting the valve of the chamber, Figure B3
- Reconnect the valve to the sample vessel
- Connect the sample chamber to the DA through the CF flange close to VV01 at the “C” port
- Keep VV01 closed and VV02 and VV03 open
- Set DA temperature at a value close to 50 C
- Open valve V06
- Turn pump on and leave at least 45 minutes to settle down. If the pump is not accelerating you should check for leaks
- While the system is settling down, fill up the cold trap (CF01) with dry ice
- Start cycling when pressure readings are below  $1 \times 10^{-4}$  kPa (base line). Run cycles until the peaks are somewhat constant

Degassing cycles are performed by simultaneously opening VV01 and closing VV02 for 2 minutes and then simultaneously closing VV01 and opening VV02 (same order) until the pressure in the system reaches a value close to the base line (around 2 minutes, depending on the sample nature). An example of a cycle run on hexadecane is shown in Figure B17

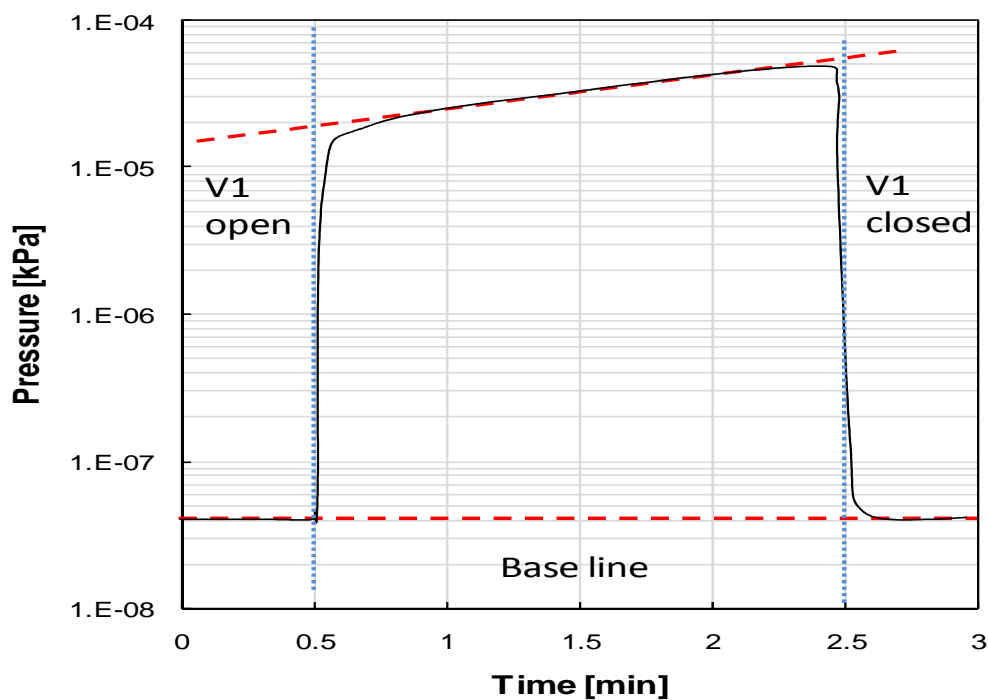


**Figure B21** DA degassing cycles for a hexadecane sample

After the degassing cycles have been completed:

- Close V06 and VV01 and disconnect the sample chamber from the “C” port

- Whenever the cold trap has no ice and there is a risk of major contamination within the pipes and pump, close VV03 until the dry ice is replaced or the pipes are cleaned

### B6.2 Vapour Pressure Measurement

The following procedure can be used to measure vapour pressure with the VPMA (Figure B2, simplified in Figure B18)

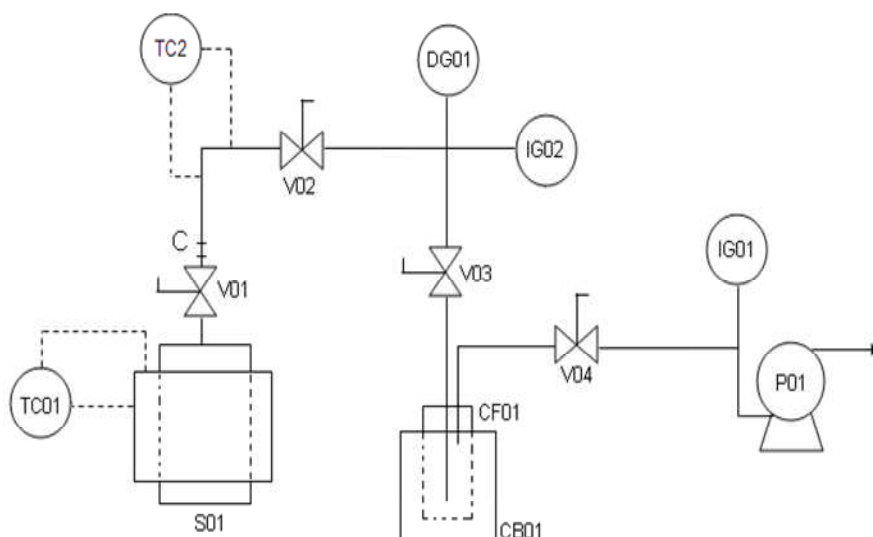


**Figure B22** VPMA simplified schematic

- Connect the sample chamber S01 to the VPMA. Make sure the valve V01 and V02 are closed
- Set the temperature of the sample chamber to the desired value
- Set the temperature of the upper part of the VPMA 200 °C to avoid major condensation on the pipes and ease gas mass diffusion

- Cool down the cold finger (CF01) by introducing dry ice into CB01. Follow the temperature decrease with a thermometer until it is close to 0 °C. Keep adding dry ice to keep this temperature steady. At the beginning of this step, it is important to introduce the pellets slowly and one at a time since the sudden CO<sub>2</sub> release in the hydraulic oil and the high temperature difference will generate the oil to foam and a major spill can occur. After the system has cool down, the fomay tendency disappears
- Turn the pump on leave 20 to 30 minutes to settle down
- Let the system run to be stable to within 0.2 °C and a base line lower than  $1 \times 10^{-8}$  kPa ( $1 \times 10^6$  kPa if the IG01 is connected through a KF flange, Section B1)
- Run cycles until the readings are constant

Cycles start by closing V02 and immediately afterwards opening V01. Run for 2 minutes and then close V01 and immediately afterwards open V02 for 5 minutes. Make sure that after a cycle and at the beginning of another cycle the base line is close to the initial value. Figure B19 shows an example of a measurement cycle on hexadecane at 25 °C.

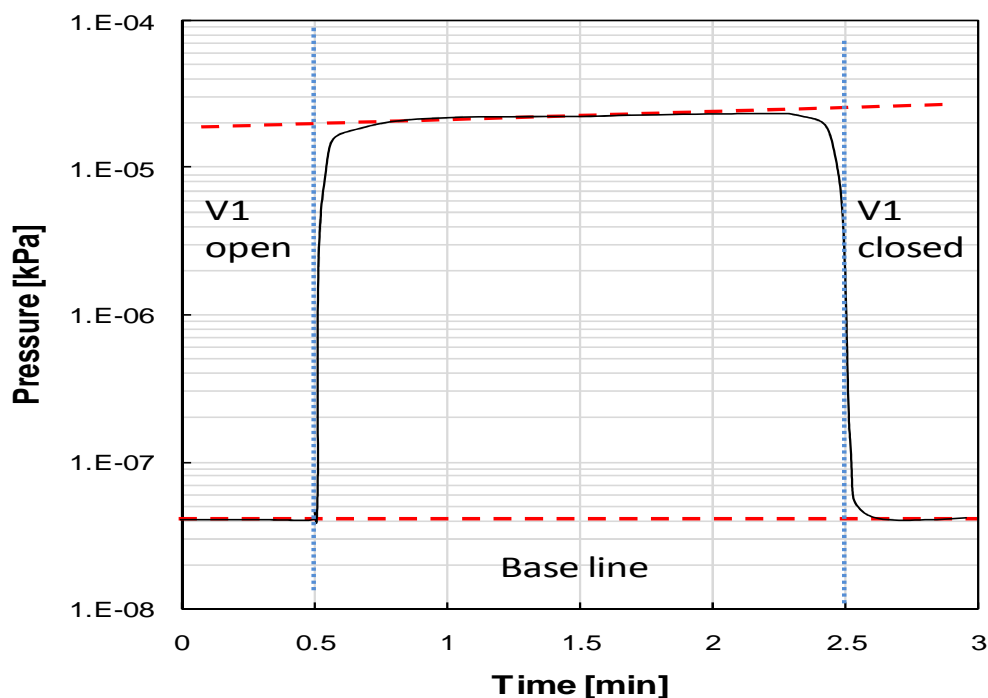


**Figure B23:** Vapour pressure measurement cycle

It usually takes an hour work to produce a single data point, meaning 2 to 3 days work to produce a duplicate P vs. T curve of 6 to 8 points plus 2 to 3 days of VPMA outgassing to prepare it for the next experiments. Hence, in practical terms, a week work is required to produce a vapour pressure curve for a substance. Note that during vapour pressure experiments the outgassing of sample chambers and degassing of samples can be carried over; thus, reducing working time for about a day.

### *B6.3 Fractionation*

The following procedure can be used to systematically fractionate mixtures using the VPMA (the DA can also be used for this purpose using an analogue procedure):

- Degas the sample (Section B6.1)
- Connect the sample chamber to the previously outgassed VPMA
- Set the upper temperature of the VPMA to a temperature 20 °C above the proposed temperature of the cut (let the sample chamber temperature controller off)
- Achieve a baseline lower than  $1 \times 10^{-8}$  kPa from the sample chamber to the pump (open valves V02 through V04, Figure B16)
- Cool down the cold finger (Section B6.2). Always keep the temperature of the cold finger as close to 0 °C as possible
- Open valve V01
- Slowly increase sample chamber temperature from atmospheric to the desired temperature (make 20 to 30 °C step increments, wait 20 to 30 minutes to stabilize and proceed to the next temperature step)
- Leave the system at the desired temperature while the cut is being collected in the cold finger
- Record volume changes to track the fractionation performance. It will also help determine when to stop the fractionation. A plot of volume vs. time should look like the Figure B20

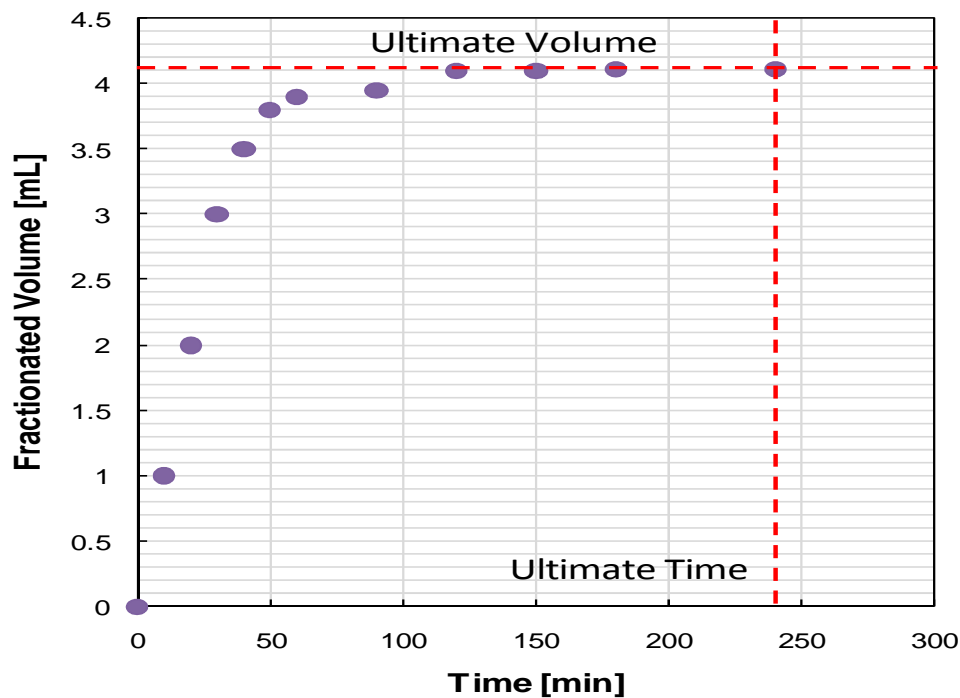


**Figure B24:** Volume vs. Time profile of fractionate crude oil – shown: Ultimate volume at which to stop the fractionation procedure at a given temperature at the ultimate time

- When no change of the volume is recorded or when the completion time has been reached (Figure B20), close valve V01 and left the system run for at least one hour to assure that no traces of the cut are left on the inner pipe contaminating the next cut
- Change temperature of the chamber and repeat the procedure for an extra cut

## B7 Data Processing

The data retrieved from the LabView interface is stored in an Excel template that needs to be processed, first, to format it, and second to obtain the vapour pressure of the pressure profiles of the cycles.

### Data Formatting

The original Excel template contains, from columns A to F, the Date and Time of the measurement and the values for IG1, IG2, DG1, and DG2, in mbar. It is suggested to add two sets of columns to this original template: first, include a transformation of the Date and Time format to a zero-referenced second's base. This will give a more traceable time and can be calculated in Excel through Equation B1 (where B refers to the Excel column B).

$$\theta^{i+1}[s] = \theta^i[s] + \Delta\theta$$

$$\Delta\theta = 3600 \times 24 \times \left[ \left( B^i - \text{Integer}(B^i) \right) - \left( B^{i-1} - \text{Integer}(B^{i-1}) \right) \right] \quad [\text{B.1}]$$

The second sets of columns refer to the difference between consecutive measurements in all of the gauges with respect to time. This will give an idea and an approximation to the derivative of the pressure profile with respect to time or, for cycling measurement, and idea of the leak rate. For this, use Equation B2.

$$\frac{dP}{d\theta} \approx \frac{\Delta P}{\Delta\theta} = \frac{P^i - P^{i-1}}{\theta^i - \theta^{i-1}} \quad [\text{B.2}]$$

### Pressure Profiles Processing

Once the pressure and time data points have been processed, a typical plot of pressure and pressure change vs. time looks like Figure B21

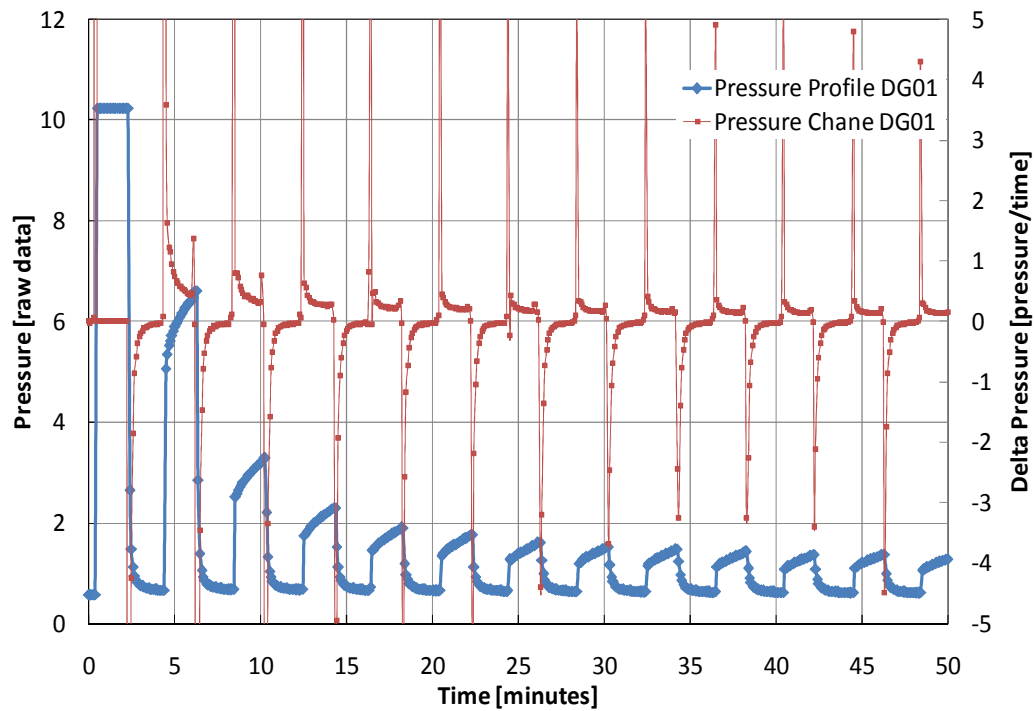


**Figure B25** Raw pressure profile of a single cycle using DG01

As can be seen in Figure B21, 13 cycles were run for this sample with the VPMA and DG01; the first cycle is out of range from the DG01, probably due to some trapped air. Subsequently, peaks were decreasing until they reach a somewhat constant behaviour. Also, note that the pressure change after a valve is closed tends towards zero while it tends towards a slightly higher value when the valve is open and the measurement is being performed. This indicates a very small leak on the system that needs to be corrected; finally note that the same leak rates were measured throughout the experiment regardless of the peak height.

To process the data, Figure B22 shows a single cycle out of Figure B21. A constant slope line (1) is drawn to extrapolate the pressure profile of the open cycle towards the opening

of the valve (2). The intersection of these two lines marks the initial pressure boost of the cycle without any leaks (at time zero of the cycle), or, in other words, the vapour pressure of the sample. A horizontal line (3) is drawn to help read the value of the chart.

Once the vapour pressure values have been extracted from each individual cycle and corrected using the calibration equations and plots (Section B8), a processed pressure profile is obtained, as shown in Figure B23. From this plot, it can be seen that the initial 8 cycles were used to purify the sample and the later 5 cycles were used to measure the vapour pressure. The latter is defined as the average of this 5 points.

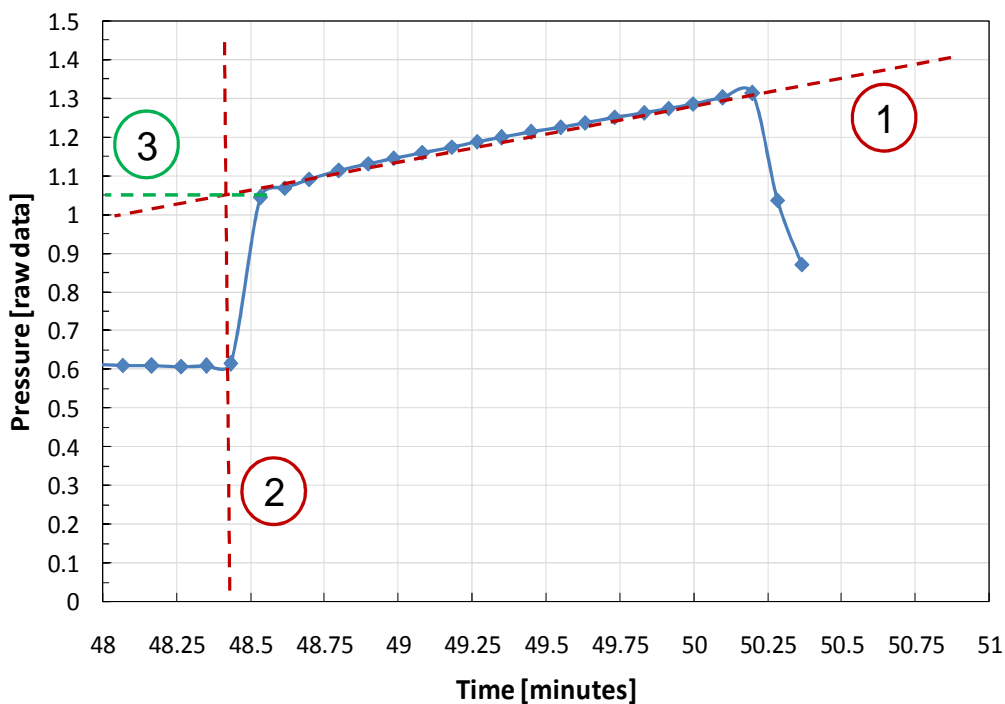


**Figure B26** Single pressure profile cycle processing

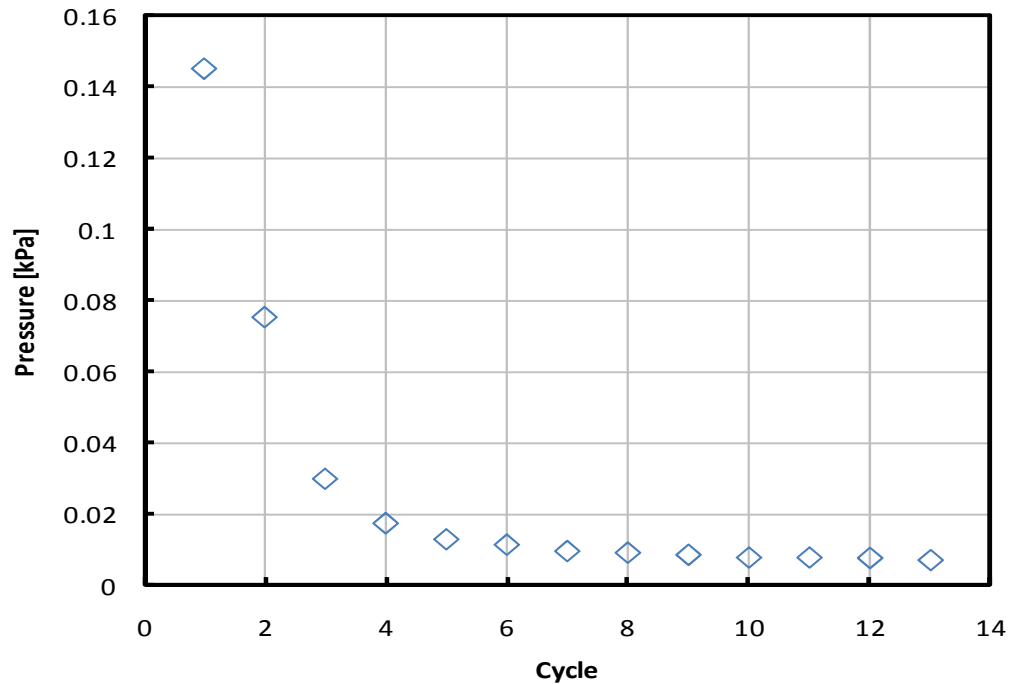


**Figure B27** Processed pressure profile

## B8 Calibration Charts

Calibration of pressure gauges and temperature probes (thermocouples) is introduced as follows:

### Thermocouple Calibration

All of the thermocouples were calibrated against a previously calibrated RTD at the laboratory. A 1:1 calibration ratio was found between the thermocouples and the RTD. In turn, the RTD was calibrated against a certified high precision thermometer (HPT - Automatic Systems Laboratories F250 Precision Thermometer Res. 0.025 C). The conditions were provided by a thermostated bath (FLUKE 6330 Calibration Bath). The calibration chart is shown in Figure B24 and is summarized in Equation B.1

$$T_{Calibrated}[^{\circ}C] = 0.99945T_{RTD}[^{\circ}C] - 0.1576 \quad [B.1]$$

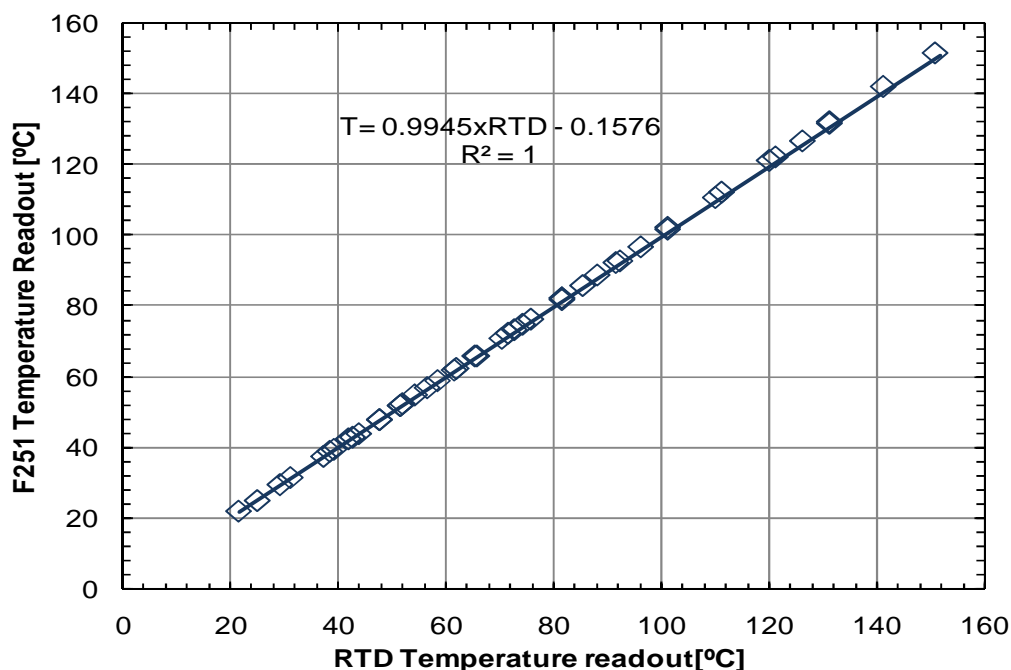


**Figure B28** Calibration chart for RTD against F251 HTP

### Pressure Gauge Calibration

Vapour pressure measurements on the VPMA and DA were taken with temperature controlled diaphragm gauges. For this type of gauge, a linear calibration is possible at pressures above  $10^{-2}$  kPa. However, below this threshold, a linear calibration is not representative and a logarithmic term may be required.

The first step was to calibrate the diaphragm gauges for the VPMA and DA (DG1 and DG2, respectively) at pressures above  $10^{-2}$  kPa, where the behaviour is expected to be linear. In this case, the Cold Cathode Pirani gauge (CCP) was calibrated to a reliable low vacuum diaphragm gauge available at the laboratory (GOR). The calibration data are

shown in Figure B.25 and were fitted with the following calibration equation with an AARD of 5.1%.

$$P_{GOR}[kPa] = 0.998P_{CCP}[kPa] + 0.243, \quad [B.2]$$

Subsequently, the diaphragm gauges DG1 and DG2 were calibrated against the CCP and back calculated to calibrated pressures using Equation B.2. This was necessary because the pressure ranges of the GOR and DG transducers do not overlap. Figure B.26 shows the calibration plot for DG1; these charts were linearly regressed with an AARD of 8.9%.

$$P_{GOR}[kPa] = 0.015P_{DG1} + 0.316, \quad [B.3]$$

$$P_{GOR}[kPa] = 0.0295P_{DG2} - 0.0027, \quad [B.4]$$

Equations B.3 and B.4 are the linear calibration of the diaphragm gauges DG1 and DG2 at pressures above  $10^{-2}$  kPa where  $P_{GOR}$  is replaced with  $P_{meas}$ , the calibrated measured pressure.

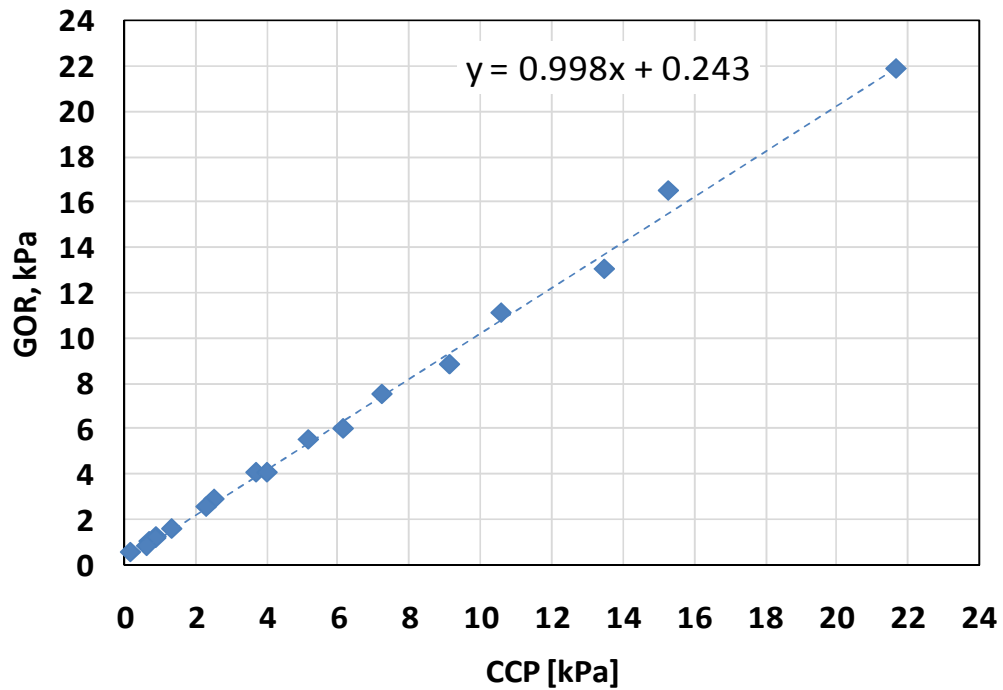


**Figure B.29** Calibration chart for Cold Cathode- Pirani gauge against GOR diaphragm gauge.

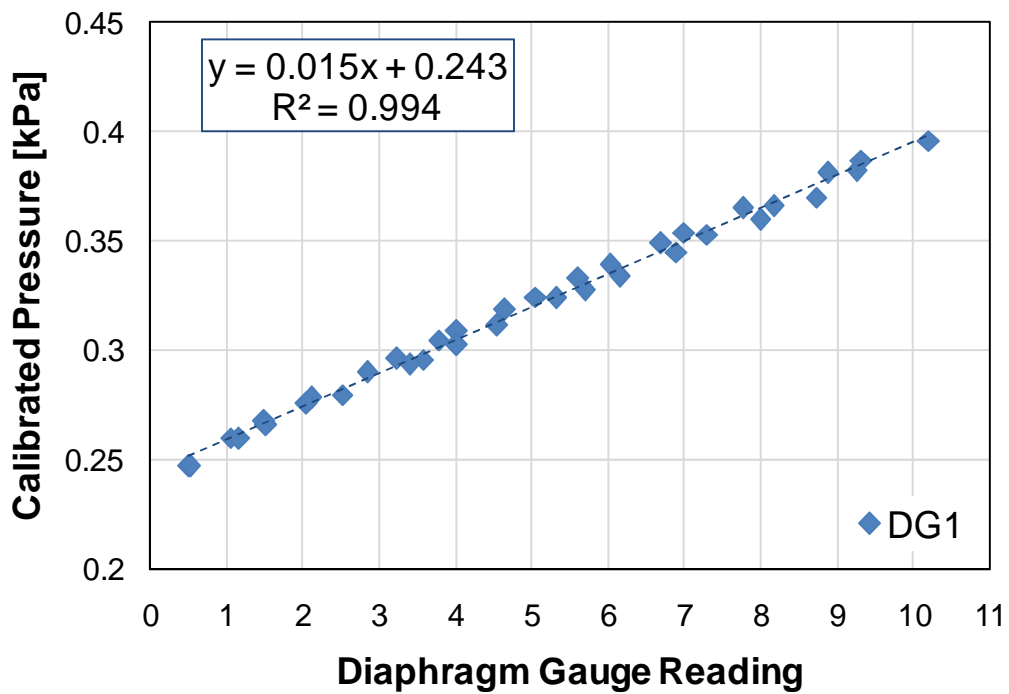


**Figure B.30** Calibration chart for DG1 diaphragm gauges.

The second step was to determine the calibration curves for pressures below  $10^{-2}$  kPa. In this case, the calibration was performed by comparing the measured vapour pressure of n-eicosane with literature data. Figure B.27 shows the experimental data (already corrected by Equations B.3 and B.4) against literature data.

The measured data deviate from the literature data at pressures below  $10^{-2}$  kPa. It is proposed to use a logarithmic expression to correct the pressure reading, accounting for the non-linear behavior of the diaphragm gauge at this pressure range. The calibrated pressure,  $P^*$ , was correlated as

$$P^*[kPa] = P_{DG1} \exp \left[ -22.344 \left( \frac{T_{NL}}{T} - 1 \right) \right], \quad [B.5]$$

$$P^*[kPa] = P_{DG2} \exp \left[ -10.461 \left( \frac{T_{NL}}{T} - 1 \right) \right], \quad [B.6]$$

where  $T_{NL}$  is the temperature, in K, at which the vapour pressure equates to  $10^{-2}$  kPa. The calibrated vapour pressures of eicosane are compared with the extrapolated literature data in Figure B.28.

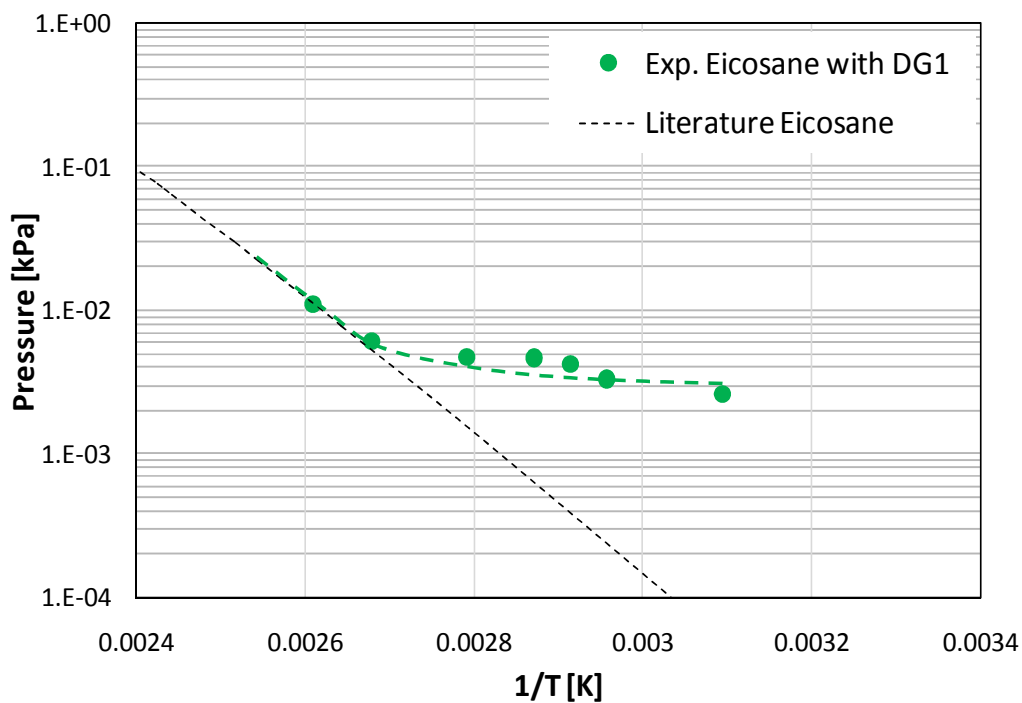


**Figure B.31** Experimental and literature data for eicosane measured with DG1 – dotted lines show the non-linear tendency of the data and do not represent any particular model.

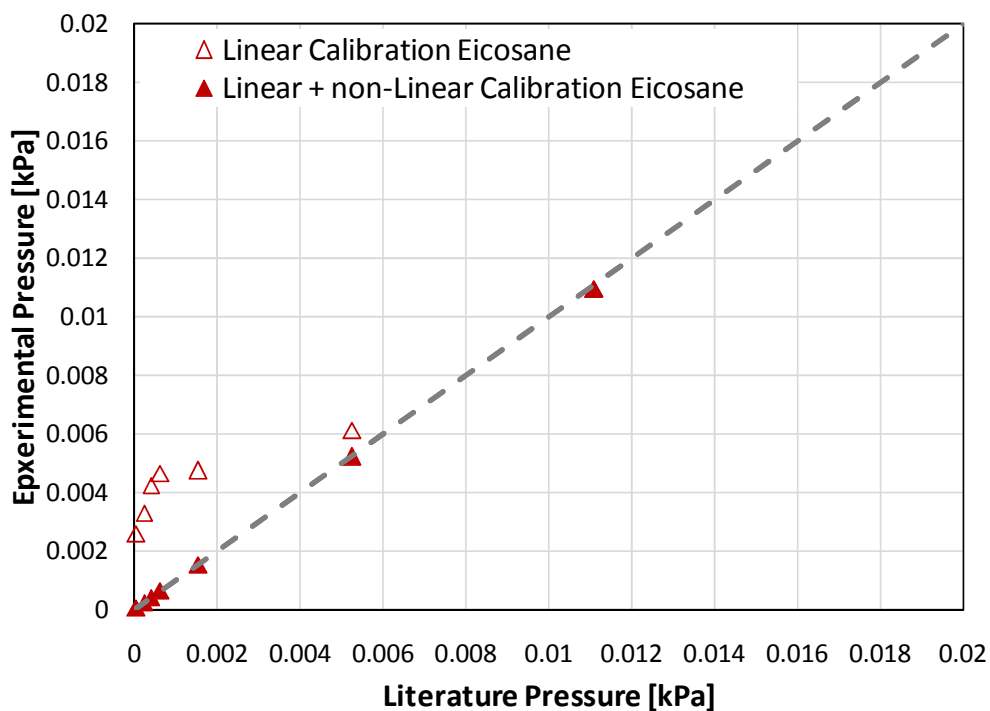


**Figure B.32** Literature and measured vapour pressure data of eicosane with linear calibration and with linear + non-linear calibration – dotted line represents is at 45°.

## B.9 Leak Testing

Leak testing is done through a Varian 979 leak detector with helium mass spectrometer (single dry mechanic pump) and a helium source. A schematics of the leak detector is shown in Figure B28

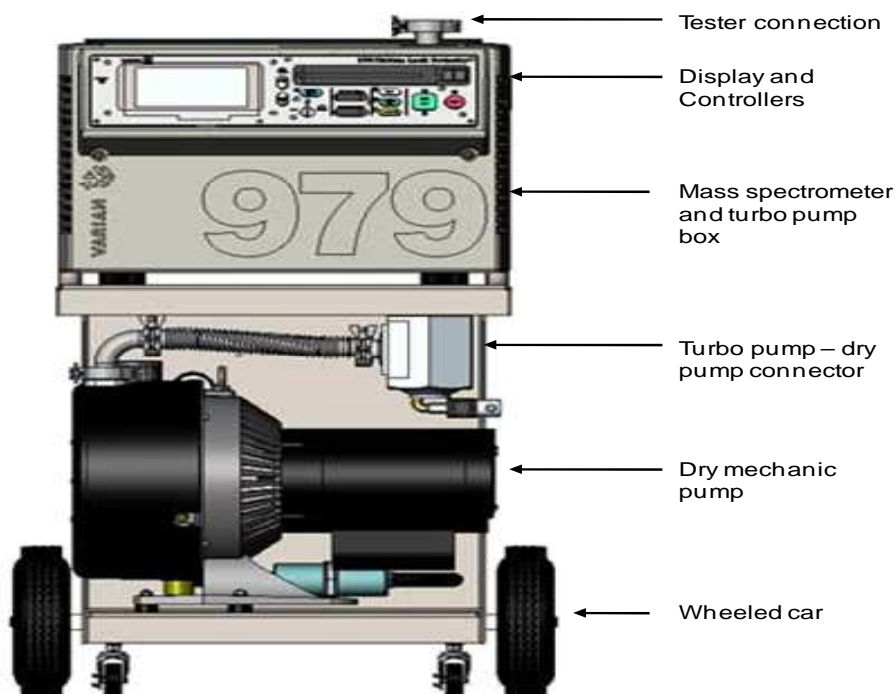


**Figure B33** Leak detector configuration with single dry mechanical pump (Modified from Varian [2003])

To perform a leak test you would need a helium bullet or tank. With that in mind, the following procedure can be used to perform the test (based on Figure B18):

- Close valve V05 and open all remaining valves
- Connect the leak detector from the tester connection to valve V03

- Turn on the leak detector (for further details please refer to the manual [Varian, 2003])
- Connect a hose to the helium bullet and open the regulator slightly to provide a very low helium flow. To prove this, put the hose near your skin and make the flow so that it is just noticeable
- With the hose from the helium bullet, sweep across all of the apparatus with special emphasis on the flanges and fittings, recording the leak rate from the leak detector display (or by sound if adjusted [Varian, 2003])
- If a big change in leak rate (or a stranding sound) occurs, that means that a significant leak is present at the region at which the hose is pointing

## B10 List of Parts

This section provides a list of the different parts comprising the HV-VPMS, Table B1

**Table B26** List of parts comprising the HV-VPMS

Description	Nominal Size	Ordering Number	Company
Full Nipple	CF133	JCF2N133	Swagelok
Blank	CF133	JCFR133	Swagelok
Copper Gaskets	CF133	JCFG133	Swagelok
Tee	CF133	JCF3T133	Swagelok
Elbow	CF133	JCF2E133	Swagelok
Cross	CF133	JCF4C133	Swagelok
Bolts and Nuts	SS 8-32x 0.75 in	54024-GE02	Chem. Store
All metal angle valve	16 (5/8")	54024-GE02	VAT
CDG200D Capacitance Diaphragm Gauge	DN16 CF-R	3CF1-653-2300	CAPT

---

Dry Ice Cold Trap	3.5 Quarts, 8” Tall, 8” Diameter	LIT-10025	LACO
-------------------	-------------------------------------	-----------	------

---

## References

Inficon, Capacitance Diaphragm Gauge CDG160D, CDG200D, Operation Manual tina53e1, **2008-04**

MKS Instruments, Inc., High Temperature Capacitance Manometer, Type 631B Absolute Manometer 631B-1/08, **2006**

Pfeiffer Vacuum, Pumping Operation with DCU PM 0547 BE/P (translated from Betriebsanleitung), **2004-10**

Pfeiffer Vacuum, Diaphragm Vacuum Pump with switchable Single Phase Wide Range Voltage Motor Operation Instructions PU 0012 BE/D (translated from Betriebsanleitung), **2006-01**

Pfeiffer Vacuum, TurboDrag Pump with Electronic Drive Unit TC 600 Operation Instructions PM 0504 BE/M (translated from Betriebsanleitung), **2007-02**

Pfeiffer Vacuum, Compact FullRange™ Gauge PKR 251, Operating Instructions BG 805 155 BE/C, **2008-04**

Pfeiffer Vacuum, HiCube 80 Eco Operational Instructions PT 0263 Be/B (translated from Betriebsanleitung), **2009-07**

Varian Vacuum Technologies, Model 979 Series Helium Mass Spectrometer Leak Detector, Operational Manual No. 699909979, Revision K, September **2003**

## APPENDIX C: SELECTED PROPERTY CORRELATIONS

The following Appendix summarizes critical properties and ideal gas heat capacity property correlations taken from the open literature. For further information refer to the original cited literature source.

### C.1 Critical Properties

Relevant critical property correlations for pure components include the Joback method for critical temperature and critical volume, and the Wilson-Jasperson method for critical pressure. The Joback method is shown in Equations C.1 and C.2 and Table C.1 and Wilson-Jasperson is shown in Equations C.3 and C.4 [Poling et al., 2001].

$$T_c = T_b [0.584 + 0.965 \sum_i n_i \Delta T_i - (\sum_i n_i \Delta T_i)^2]^{-1} \quad [\text{C.1}]$$

$$V_c = 0.001(17.5 + \sum_i n_i \Delta V_i) \quad [\text{C.2}]$$

where  $\Delta T_i$ [K], and  $\Delta V_i$ [m<sup>3</sup>/kmol] are group contributions, shown in Table C.1

**Table C.27** Constants for Joback methods for relevant molecular groups [Poling et al., 2001]

Group	$\Delta T$	$\Delta V$
CH <sub>3</sub> -	0.0141	65
-CH <sub>2</sub> -	0.0189	56
-CH=	0.0129	46
-COO-	0.0481	82

$$P_C = \frac{0.0186233T_C}{[-0.96601 + \exp(Y)]}$$

$$Y = -0.00922295 - 0.0290403N_r + 0.041(\sum_k N_k p_{cK} + \sum_j M_j p_{cJ}) \quad [C.4]$$

Where  $N_r$  stands for the number of rings on the molecule,  $N_k$  is the number of atoms of type  $k$  while  $M_j$  is the number of second order groups of type  $j$ .  $p_{cK}$  and  $p_{cJ}$  stand for the contributions of each group to the overall critical pressure. For a list of group contributions please refer to Poiling et al., [2010], Chapter 2, Section 2.2

Relevant critical property correlations for hydrocarbon pseudo-components components include those introduced by Lee and Kesler [Riazi, 2005], which are shown in Equations C.5 to C.6:

$$\begin{aligned} \ln P_C = & \\ & 8.3634 - \frac{0.0566}{SG} - 1 \times 10^{-3} T_b \left( 0.24244 + \frac{2.2898}{SG} + \frac{0.11857}{SG^2} \right) + 1 \times 10^{-7} T_b^2 \left( 1.46850 + \right. \\ & \left. 3.6480SG + 0.47277SG^2 - 1 \times 10^{-10} T_b^{30.42019} + 1.69770SG^2 \right) \quad [C.5] \end{aligned}$$

$$T_C = 341.7 + 8.11SG + T_b(0.4244 + 0.1174SG) + \frac{1 \times 10^5}{T_b}(0.4669 - 3.2623SG) \quad [C.6]$$

$$\omega = \frac{\ln\left(\frac{101.325}{P_C}\right) - 5.92714 + \frac{6.09648}{T_{br}} + 1.28862 \ln(T_{br}) - 0.169347 T_{br}^6}{15.2518 - \frac{15.6875}{T_{br}} - 13.4721 \ln(T_{br}) + 0.43577 T_{br}^6} \quad T_{br} < 0.8 \quad [C.6]$$

$$\omega = -7.904 + 0.1352K_W - 0.007465K_W^2 + 8.359T_{br} + \frac{(1.408 - 0.01063K_W)}{T_{br}} \quad T_{br} \geq 0.8$$

$$K_W = \frac{1.8T_b^{1/3}}{SG}$$

## C2 Ideal Gas Heat Capacity

Relevant ideal gas heat capacity methods for pure components are the modified Benson method [Bures et al., 1996] and the Joback method [Poiling et al., 2001]. Equation C.7 shows the Benson method whereas Equation C.8 shows the Joback method.

$$C_P^0 = \left( \frac{a^* + b^*T + c^*T^2 + \frac{d^*}{T^2} + e \left( \frac{f}{T} \right)^2 \exp\left[-\frac{T}{g}\right]}{\left(1 - \exp\left[\frac{T}{h^*}\right]\right)^2} \right) \quad [\text{C.7}]$$

$$C_P^0 = (a^{**} + b^{**}T + c^{**}T^2 + d^{**}T^3) \quad [\text{C.8}]$$

where  $a^*$ ,  $b^*$ , etc., are group contribution functions. For specific group contributions, refer to the literature source.